



HAL
open science

Evaluation of System-level Electromagnetic Hazards due to Environmental Stresses and Ageing –: Application to Shielded Cables and EMI-filter Ground Connections

Oskari Leppäaho

► **To cite this version:**

Oskari Leppäaho. Evaluation of System-level Electromagnetic Hazards due to Environmental Stresses and Ageing –: Application to Shielded Cables and EMI-filter Ground Connections. Electronics. INSA de Rennes, 2023. English. NNT: 2023ISAR0026 . tel-04701610

HAL Id: tel-04701610

<https://theses.hal.science/tel-04701610v1>

Submitted on 18 Sep 2024

HAL is a multi-disciplinary open access archive for the deposit and dissemination of scientific research documents, whether they are published or not. The documents may come from teaching and research institutions in France or abroad, or from public or private research centers.

L'archive ouverte pluridisciplinaire **HAL**, est destinée au dépôt et à la diffusion de documents scientifiques de niveau recherche, publiés ou non, émanant des établissements d'enseignement et de recherche français ou étrangers, des laboratoires publics ou privés.

COLLEGE MATHS, TELECOMS

DOCTORAL INFORMATIQUE, SIGNAL

BRETAGNE SYSTEMES, ELECTRONIQUE

INSA INSTITUT NATIONAL
DES SCIENCES
APPLIQUÉES
RENNES

THESE DE DOCTORAT DE .

L'INSTITUT NATIONAL DES SCIENCES
APPLIQUÉES RENNES

ECOLE DOCTORALE N° 601

*Mathématiques, Télécommunications, Informatique, Signal, Systèmes,
Electronique*

Spécialité : *Electronique*

Par

Oskari LEPPÄHO

Evaluation of System-level Electromagnetic Hazards due to Environmental Stresses and Ageing

Application to Shielded Cables and EMI Filter Ground Connections

Thèse présentée et soutenue à Angers, le 10 Mars 2023

Unité de recherche : IETR

Thèse N° : 23ISAR 09 / D23 - 09

Rapporteurs avant soutenance :

Frank LEFERINK Professeur, University of Twente
Bernd DEUTSCHMANN Professeur, TU Graz

Composition du Jury :

Président :	Philippe BESNIER	Directeur de Recherche, CNRS, INSA Rennes
Examineurs :	Françoise PALADIAN	Professeur des universités, Université Clermont-Auvergne
	Frank LEFERINK	Professeur, University of Twente
	Bernd DEUTSCHMANN	Professeur, TU Graz
	Olivier MAURICE	Ingénieur CEM (HDR), Ariane Group
Dir. de thèse :	Mohammed RAMDANI	Enseignant-Chercheur (HDR), IETR, ESEO
Co-dir. de thèse :	Frédéric LAFON	Master Expert CEM (HDR), Valeo
Co-encadr. de thèse :	Davy PISSOORT	Professeur, KU Leuven

Invité(s)

Richard PERDRIAU	Enseignant-Chercheur (HDR), IETR, ESEO
Priscila FERNANDEZ-LOPEZ	EMC Expert, Valeo
Marine HEULARD-STOJANOVIC	EMC Expert, Valeo

Intitulé de la thèse :

Evaluation of System-level Electromagnetic Hazards due to Environmental Stresses and Aging
Application to Shielded Cables and EMI Filter Ground Connections

Oskari LEPPÄÄHO

En partenariat avec :



The research leading to these results has received funding from the European Union's Horizon 2020 research and innovation programme under the Marie Skłodowska-Curie grant agreement No 812790 (MSCA-ETN PETER).

This thesis manuscript reflects only the authors' view, exempting the European Union from any liability. Project website: <http://etn-peter.eu/>



Document protégé par les droits d'auteur.

RÉSUMÉ EN FRANÇAIS

L'électronique automobile d'aujourd'hui évolue rapidement vers des solutions d'assistance à la conduite et de propulsion électrique. Un « hype cycle » [1] peut être utilisé pour analyser ces types de développements technologiques en cours. Les technologies d'assistance à la conduite et de propulsion électrique traversent le « fossé des désillusions » dans leur « hype cycle » [2] comme le montre la Figure 1. En effet, les limitations des technologies sont reconnues et l'industrie commence fermement à investir. L'objectif est de construire des solutions incrémentales concernant les problèmes découverts pendant la phase de désillusion.

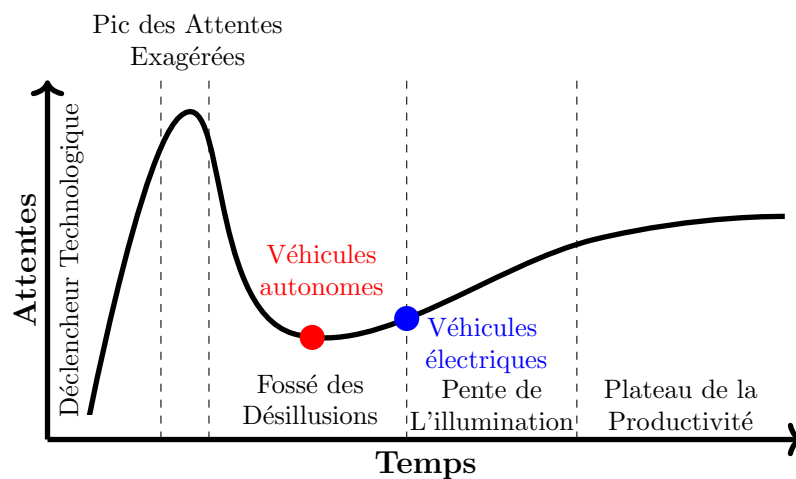


FIGURE 1 – Le « hype cycle » mettant en évidence l'avancement de véhicules autonome et électrique selon [2]. Image de fond par [3].

Pour industrialiser les nouveaux systèmes électroniques, les problématiques de compatibilité électromagnétique (CEM) liées au vieillissement d'un équipement doivent être solutionnées [4]. Les problématiques de CEM ne sont pas connues des automobilistes, mais restent connues des personnes ayant de l'expérience dans le domaine de l'électronique automobile. Les problèmes se présentent comme les obstacles de lancement des nouveaux produits sur le marché, ou comme une source des problèmes de qualité. Il y a quelques

exemples connus de systèmes automobiles qui sont confrontés à des problèmes de CEM, et en particulier les systèmes liés à la sécurité comme, par exemple, le module de commande de l'airbag [5].

Pour proposer une solution possible à certains de ces problèmes CEM, cette thèse est construite autour d'un sous-système électronique automobile, qui sont développés par les fournisseurs automobiles de rang 1, comme Valeo. Les chapitres sont divisés comme illustré en Figure 2. L'analyse des câbles blindés est abordée dans le Chapitre 1, la théorie d'efficacité de blindage des câbles est présentée ainsi que la mesure dans des conditions de laboratoire, mais également pour les essais environnementaux sous des conditions de stress thermique et de vibration. Des tests à court et à long terme hautement accélérés sont exécutés afin que le vieillissement soit pris en compte. Le Chapitre 2 présente une analyse similaire pour la résistance de contact des connexions de masse des circuits imprimés, qui sont souvent utilisés pour les filtres CEM. Pour finir et faire le lien entre la théorie et la pratique, la bonne gestion de risques de compatibilité électromagnétique est abordée dans le Chapitre 3. Ce chapitre aborde un exemple d'application des câbles blindés dans un système automobile. De la même manière, un autre exemple d'application est abordé sur les connexions de masse d'un filtre CEM. De cette façon, la nécessité de prendre en compte les contraintes environnementales est renforcée. Dans les sections suivantes, un bref résumé des principaux résultats par sujet est donné.

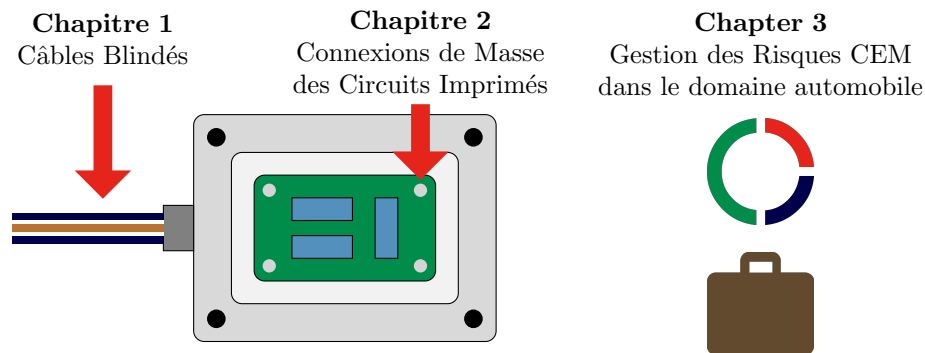


FIGURE 2 – Contenu de la thèse

Câbles Blindés

Dans cette section, les câbles blindés et leurs usages typiques pour le domaine automobile sont présentés. Ensuite, un aperçu de la cellule triaxiale environnementale développée est présenté ainsi que quelques résultats de vieillissement de câbles blindés. L'objectif est de déterminer la dépendance environnementale de l'impédance de transfert [6]

$$Z_T = R_T + j\omega L_T \quad (1)$$

et de ses composantes : résistance de transfert R_T et l'inductance de transfert L_T .

Les câbles blindés peuvent être répertoriés en trois catégories différentes comme illustré dans la Table 1. Les blindages homogènes donnent les meilleures performances, mais sont difficile à fabriquer et à installer. D'autre part, les blindages feuillard et tresse donnent des performances complémentaires. Plusieurs couches de blindage peuvent être combinés pour former les blindages multicouches [6]. Une blindage multicouche classique est construit à partir de feuillard et de tresse. En effet, leurs caractéristiques se compensent : la tresse donne une bonne performance à basse fréquence tandis que le feuillard donne une bonne performance à haute fréquence. Une autre combinaison classique consiste à enrayer une seconde tresse sur une première pour construire une double tresse.

Deux exemples d'application des câbles blindés pour le domaine automobile sont présentés dans la Table 2. Ils présentent les défis de l'industrie concernant une potentielle installation relative à l'assistance à la conduite ; une connexion d'une caméra à une unité de contrôle électronique (ECU), et une autre relative à la propulsion électrique ; une connexion de batterie de propulsion sur un onduleur de moteur électrique dans un véhicule électrique (VE).

Dans le cadre de l'évaluation des performances des câbles pendant leur vieillissement, une méthode d'essai dédié aux tests de vieillissement hautement accélérés (HALT) a été développée dans le but de caractériser l'impédance de transfert. Elle est basée sur la forme d'une cellule triaxiale environnementale comme illustrée dans la Figure 3. L'évaluation de ses performances a été publiée [7] dans le cadre de cette thèse.

Un résultat de mesure typique obtenu avec la cellule triaxiale environnementale est illustré dans la Figure 4. La partie constante entre 100 kHz et 1 MHz représente la résistance de transfert et la partie évoluant en fonction de la fréquence représente l'inductance de transfert. Ces deux paramètres dépendent de la température et les résultats sont variables à partir de 100 kHz. En basse fréquence, les longs câbles de connexion influent sur

TABLE 1 – Câbles blindés typiques

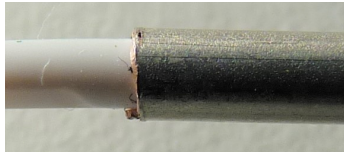
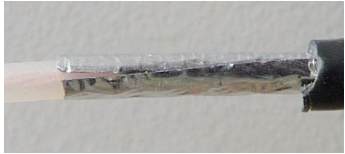

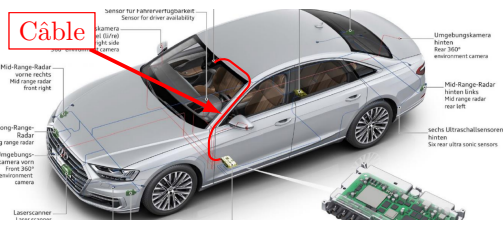
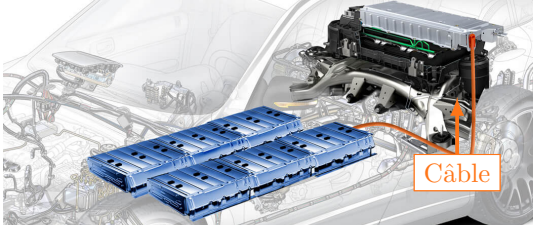
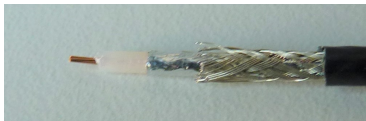

	Homogène	Feuillard	Tresse
			
Concept	Métal solide extrudé ou appliqué sur le diélectrique du câble	Feuillard solide ou recouvert de plastique enroulé sur le diélectrique du câble	Fils fins tressés sur le diélectrique du câble
Qualité	Blindage haute performance	<ul style="list-style-type: none"> • Performances limitées en basses fréquences • Bonnes performances en hautes fréquences 	<ul style="list-style-type: none"> • Bonnes performances en basses fréquences • Performances limitées en hautes fréquences
Effort	Difficile à fabriquer et à installer	Facile à fabriquer et à installer	Nécessite des machines de fabrication de haute-précision, facile à installer

TABLE 2 – Exemples d'applications de câbles blindés dans le domaine automobile

Caméra vers ECU ¹	VE Batterie vers Onduleur ²
	
	
Câble blindé impédance adaptée 50 Ω avec une tresse et un feuillard	Câble blindé haute tension avec un feuillard sur une tresse

¹La photo d'ensemble : Audi AG, Bordnetze Kongress 2018, ²La photo d'ensemble : DELFINGEN

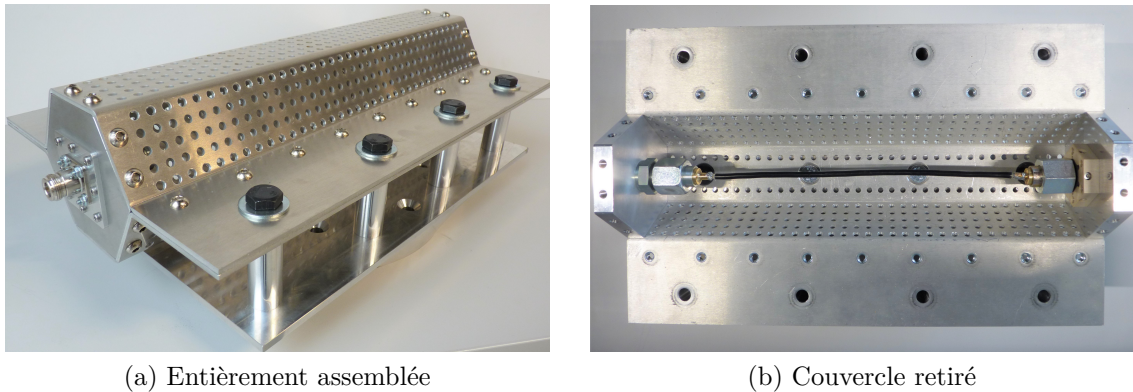


FIGURE 3 – Vue d’ensemble de la cellule triaxiale environnementale

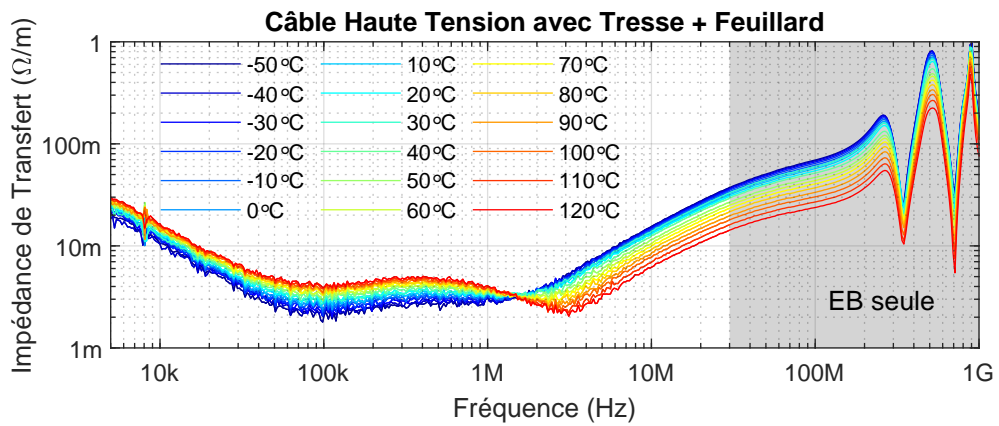


FIGURE 4 – Réponse typique d’impédance de transfert d’un câble blindé face aux variations de température

les résultats de mesure [8]. Au-delà de 30 MHz, la cellule triaxiale devient électriquement grande et la mesure directe d’impédance de transfert n’est plus possible. En revanche, l’efficacité de blindage (EB) peut être observée. Grâce à ses antirésonances, une impédance de transfert suffisamment fiable peut encore être extraite jusqu’à 1 GHz.

L’ensemble des résultats de vieillissement dans la Table 3 montre que la résistance de transfert est pratiquement insensible aux contraintes environnementales, excepté le câble coaxial. D’autre part, l’inductance de transfert dépend fortement des contraintes environnementales. Le câble haute tension est le meilleur et s’améliore avec les contraintes environnementales. En effet, son inductance de transfert a chuté de près de moitié de sa valeur d’origine. Au contraire, le câble LVDS s’est dégradé avec les contraintes environnementales, l’inductance a augmenté quarante fois de sa valeur d’origine. La plus grande

TABLE 3 – Impédance de transfert d'échantillons de câbles frais et vieillis

Câble	Type de Blindage	R_T (m Ω /m)			L_T (pH/m)		
		Frais	Vieilli	↑	Frais	Vieilli	↑
RG-55/U	Tresse + Tresse	7.8	8.0	+3%	7.2	10	1.4×
RG-58	Feuillard + Tresse	107	112	+5%	4.9	28	4.7×
RG-58C/U	Tresse	15.6	16.5	+6%	1100	1000	0.9×
Coaxial	Feuillard + Tresse	44.4	57.5	+30%	21	230	10×
LVDS	Feuillard + Tresse	20.8	21.7	+4%	2.1	84	40×
Haute Tension	Tresse + Feuillard	3.4	3.7	+8%	220	130	0.6×

différence entre les deux câbles est que le câble haute tension a une tresse serrée alors que la majorité des performances du câble LVDS viennent du feuillard est que la tresse est peu serrée. Ainsi, il a été mis en évidence que les blindages avec tresse résistent mieux aux contraintes HALT que les blindages avec feuillard.

Finalement, un câble blindé pour un capteur d'information (comme par exemple une caméra) illustré en Figure 5a a été étudié. L'étude a été publiée [9] dans le cadre de cette thèse. La comparaison des résultats de simulation d'immunité sur la Figure 5b montre l'importance de la prise en compte du vieillissement. Il est clair que le test d'immunité sera conforme pour un câble frais, tandis qu'avec un câble vieilli, le test ne sera pas conforme. Ainsi, il peut être conclu que les essais environnementaux sont importants pour découvrir la performance CEM d'un système automobile utilisant les câbles blindés pendant sa vie.

Résistance de Contact des Connexions de Masse des Circuits Imprimés

Dans cette section, les connexions de masse des circuits imprimés comme ceux de la Table 4 sont présentés. Ils sont souvent utilisés en tant que connexions de masse de filtres CEM. En effet, l'influence de la résistance de contact pendant et après les contraintes environnementales est importante pour les performances du filtre.

Deux installations typiques pour les applications automobiles sont présentées dans la Table 5. Ils présentent les défis de l'industrie concernant une potentielle installation relative à l'assistance à la conduite et une autre relative à la propulsion électrique. Le premier

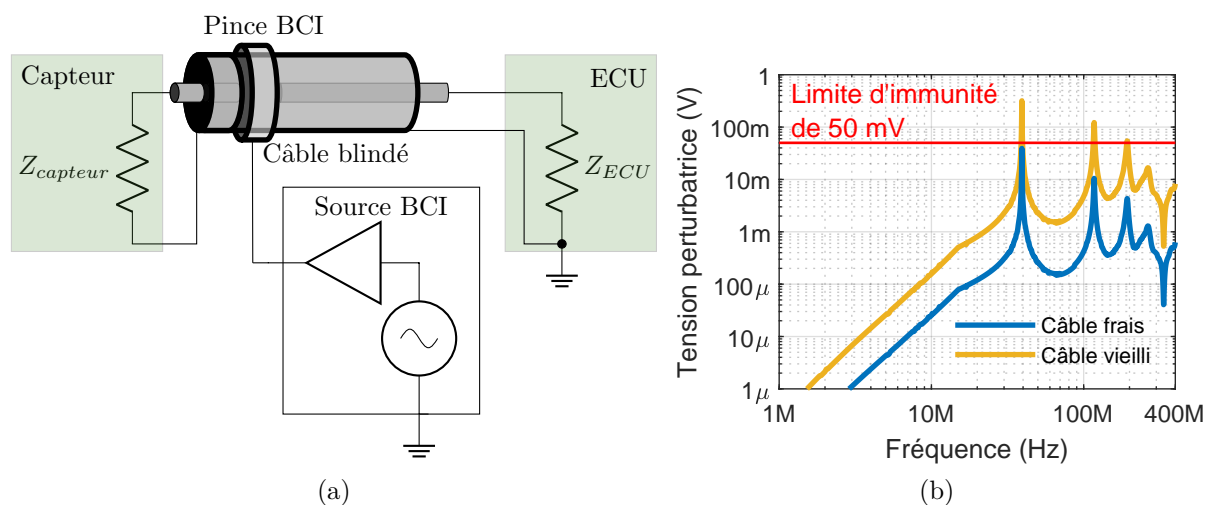


FIGURE 5 – Une représentation générique (a) d'un système automobile utilisant un câble blindé sur lequel des perturbations sont injectées et (b) un résultat de test BCI simulé sous SPICE avec un câble coaxial frais puis vieilli

TABLE 4 – Vue d'ensemble des contacts de masse typiques des filtres CEM


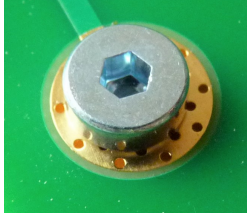

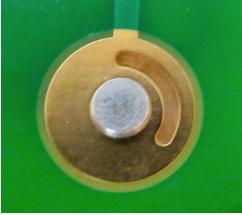
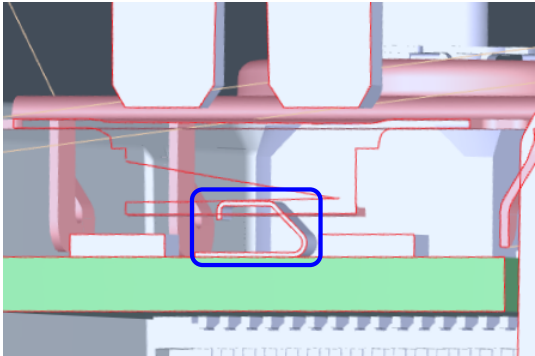
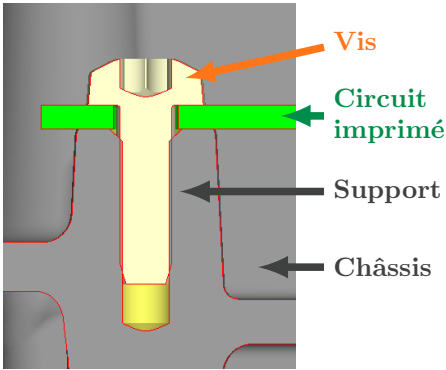
	Soudé	à Vis	à Ressort	Estampé [10]
				
Avantages	Bon contact électrique	Montage et démontage faciles	Facile à assembler	Assemblage rapide avec une grande surface de contact
Inconvénients	Difficile pour certains matériaux et gros objets dissipateurs de chaleur	Élément supplémentaire lors de l'assemblage final	Petite zone de contact, élément supplémentaire lors de l'assemblage du circuit imprimé	Outils spéciaux nécessaires

TABLE 5 – Exemples automobiles de contacts de masse de circuits imprimés

Ressort de mise à la terre à l'intérieur d'un ECU	Mise à la terre d'un filtre CEM de l'onduleur d'un VE
	
<p>Ressort en bronze phosphoreux étamé en contact avec une pièce en aluminium ou une pastille étamée d'un autre circuit imprimé</p>	<p>Plaquette de circuit imprimé étamée fixée à un support en fonte d'aluminium usiné avec une vis</p>

est un ressort de mise à la terre pour fermer le chemin du courant de blindage à l'intérieur d'un ECU et le deuxième est une vis de mise à la terre du filtre CEM de l'onduleur d'un VE.

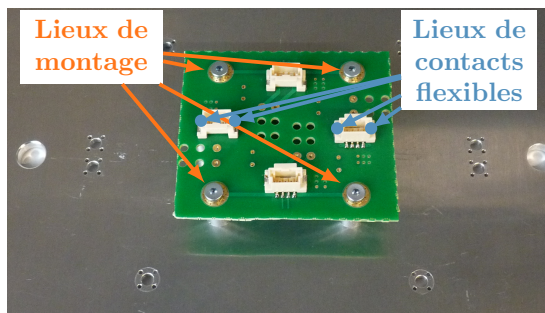
Dans le cadre de l'évaluation des résistances de contact de masse des circuits imprimés pendant leur vieillissement, une méthode d'essai pour les tests de vieillissement hautement accélérés (HALT) a été développée. Elle est basée sur la forme d'un banc d'essai simple comme illustré dans la Figure 6, les différentes versions étant développées pour ressembler à des cas d'utilisation automobiles typiques :

Circuit imprimé nu de petite taille : configuration que l'on trouve généralement dans les caméras et autres petits équipements avec uniquement des composants montés en surface.

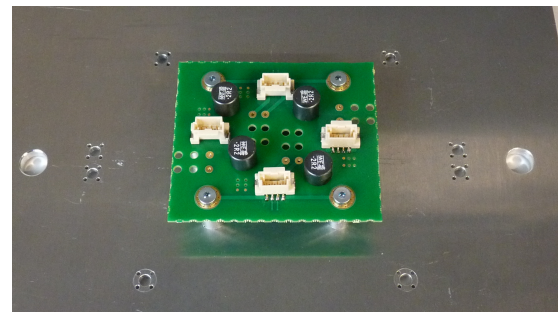
Circuit imprimé peuplé de petite taille : configuration de capteur similaire à celle ci-dessus, mais avec des composants d'alimentation plus imposants.

Circuit imprimé nu de grande taille : une carte mère ECU typique avec uniquement des composants montés en surface.

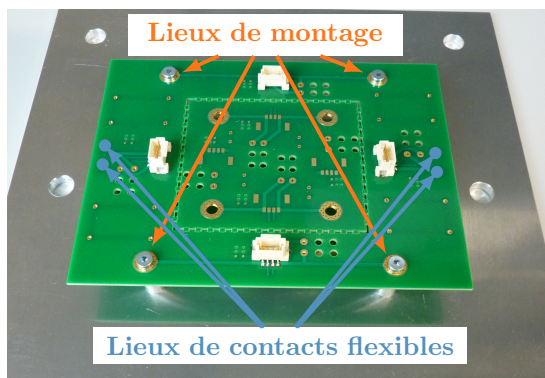
Circuit imprimé peuplé de grande taille : une grande carte de circuit d'alimentation ou une carte de circuit de filtre CEM d'un convertisseur de puissance haute tension dans un VE.



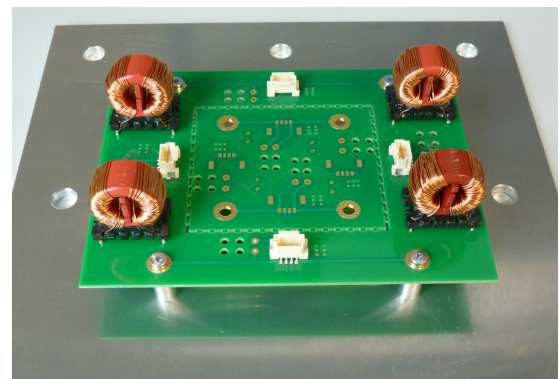
(a) Circuit imprimé nu de petite taille ($m = 19$ g)



(b) Circuit imprimé peuplé de petite taille ($m = 34$ g)



(c) Circuit imprimé nu de grande taille ($m = 61$ g)



(d) Circuit imprimé peuplé de grande taille ($m = 203$ g)

FIGURE 6 – Vue d'ensemble des différentes configurations de test de résistance de contact

Après les essais avec les bancs, il est présenté en Figure 7 que le vieillissement est un paramètre important. Il est présenté que la résistance d'un contact à vis est pratiquement insensible aux contraintes environnementales. La même conclusion peut être faite pour les contacts estampés sauf pour quelques échantillons, qui sont endommagés par de fortes vibrations. D'autre part, tous les contacts à ressort sont endommagés par des vibrations moindres. De plus, la valeur typique de résistance de contact à l'origine est plus grande que pour les autres types de contacts. De ce fait, la limite de défaillance a dû être augmentée à $100\text{ m}\Omega$. Ainsi, il a été mis en évidence que les contacts traditionnels comme les vis résistent mieux aux contraintes HALT que les autres types de contacts. Avec les contacts estampés, des performances similaires peuvent être obtenues, cependant la conception doit être excellente et le processus de fabrication bien contrôlé. Les ressorts peuvent très bien supporter les contraintes thermiques, mais ne sont compatibles qu'avec des niveaux de vibration très légers.

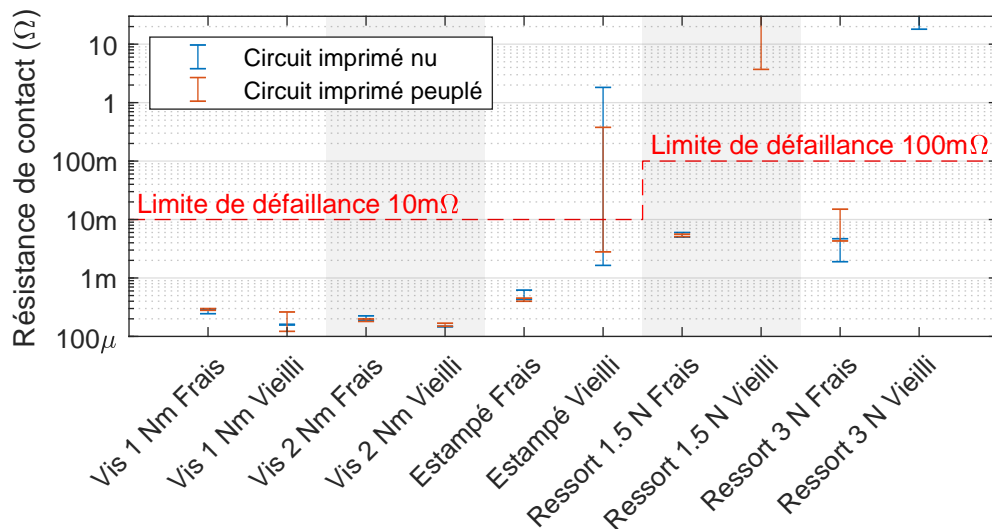


FIGURE 7 – Résistances de contact frais et vieillis

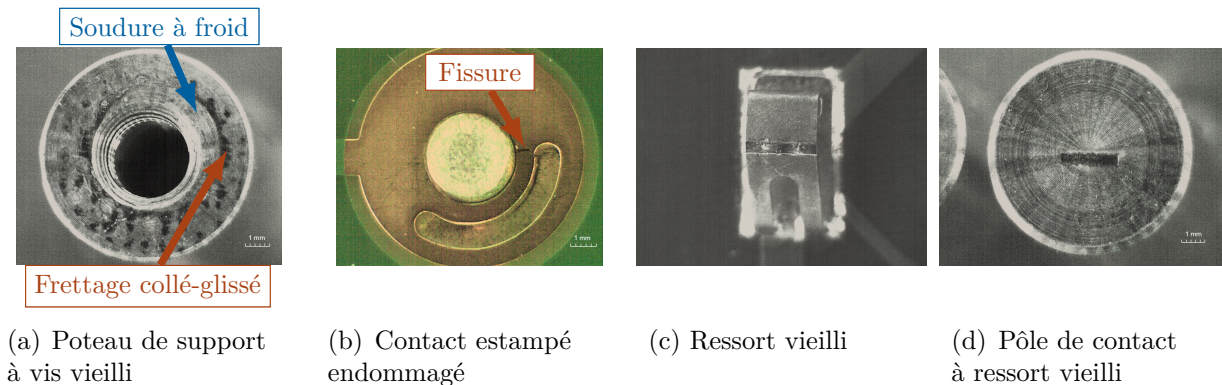


FIGURE 8 – Dommages sur les contact vieillis

Pour mieux comprendre le processus de vieillissement des contacts, certaines constatations visuelles présentées dans le Figure 8 sont analysées. La Figure 8a montre les dommages sur la surface de poteau de support à vis après le cycle de vieillissement. Deux zones importantes peuvent être reconnus : les marques noires indiquent un frettage collé-glissé et la zone brillante indique une éventuelle soudure à froid. Le Figure 8b montre une fissure dans le contact estampé et les Figures 8c et 8d montrent les deux corps de contact à ressort opposés avec des dommages importants sur la zone de contact.

Finalement, la susceptibilité d'un filtre CEM pour un onduleur d'un VE est étudiée comme illustré en Figure 9a. La comparaison des résultats de simulation d'atténuation de filtre est présentée en Figure 9b. Il est montré que les performances du filtre sont

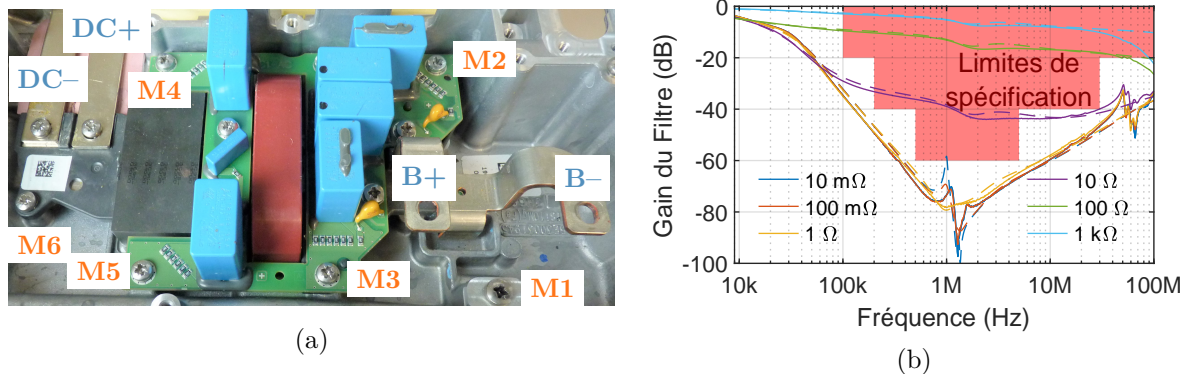


FIGURE 9 – (a) Filtre CEM d’un onduleur et (b) son atténuation en faisant varier les résistances de contact pour les points M2-M5

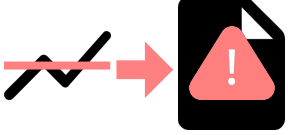

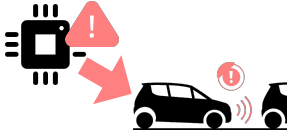
acceptables avec une résistance de contact maximum de 1Ω . Au-delà, les performances du filtre sont réduites de manière significative. Étant donné les résultats présentés dans la figure, il peut être conclu que le filtre est assez performant avec tous les autres contacts vieillis, à l’exception des contacts à ressort.

Gestion des Risques CEM et Conclusion

Étant donné que l’analyse des performances CEM tout au long du cycle de vie requiert des ressources conséquentes, elle doit être structurée pour obtenir un résultat optimal. Il se fait à l’aide de gestion des risques CEM. Le sommaire des différentes méthodes de gestion des risques CEM est présenté dans la Table 6. La gestion des risques CEM basée sur les règles est la plus répandue pour les produits standards. Dans les années à venir, certaines règles liées au vieillissement et aux contraintes environnementales sont susceptibles d’apparaître pour certains cas d’utilisations automobiles critiques, et pour les équipementiers axés sur la fiabilité. La gestion des risques CEM basée sur les risques repose sur l’expertise du fabricant du produit grâce à l’application de stratégies de conception et l’application de test correct pour faire face aux perturbations électromagnétiques (PEM) arbitraires. Enfin, la résilience EM se concentre sur la garantie de la sécurité du système électronique sous PEM arbitraire.

En conclusion, il a été démontré que les contraintes environnementales peuvent affecter les performances des câbles blindés et des connexions de masse des circuits imprimés. Dans les structures de câbles blindés, il a été conclu que la tresse était le type de blindage le plus performant, tandis que les feuillets montrent des faiblesses au stress vibratoire.

TABLE 6 – Résumé des objectifs de gestion des risques CEM

	CEM basée sur des règles	CEM basée sur les risques	Résilience EM
Applicable à	Des produits standards et systèmes bien connus	Nouveaux produits, systèmes complexes et défis émergents	Fonctions de sécurité ou de fiabilité d'un produit ou d'un système
Visuel			
Cause	PEM bien connues	PEM arbitraires	PEM arbitraires
Probabilité de	Performance CEM du produit ou système dans les limites standard	IEM	Dysfonctionnements dus à des IEM
Conséquences	Re-conception, coût des matériaux, délai de mise sur le marché	Défaillance du produit ou système chez le client	Dangers pour la sécurité ou autres risques de fiabilité
Évaluez la sévérité de	Perte financière	Perte financière et de réputation	Accident ou autre événement indésirable

Une analyse similaire pour les connexions de masse a montré que les écrous traditionnels sont très performants face aux contraintes environnementales hautement accélérées. En revanche, les connexions de masse avec des ressorts ont montré des défauts dus au stress vibratoire pouvant aller de vibrations légères à modérés.

Il est donc important de prendre en compte l'effet environnemental mentionné ci-dessus lors de la conception du produit. Quelques exemples automobiles ainsi qu'un cadre de gestion des risques sont fournis dans cette thèse et peuvent aider les ingénieurs de conception à le faire. Les défaillances CEM typiques résultant des retours de produits entraînent des situations de défaut introuvable qui sont extrêmement difficiles à résoudre, en particulier si elles sont liées à d'autres conditions environnementales que l'environnement ambiant du laboratoire. La prise en compte de ces contraintes environnementales et des performances CEM tout au long de la vie des produits permet aux entreprises d'améliorer la qualité de leurs produits.

ACKNOWLEDGEMENT

First and foremost, I would like to thank the European Union and the PETER project coordinators and supervisors to have made my research and this thesis possible. Our project was professionally lead by Professor Davy Pissoort, who also co-supervised my thesis.

Second, I would like to thank the pre-examiners Professor Frank Leferink and Professor Bernd Deutschmann for biting the bullet, and agreeing to review this thesis. I hope we will have a constructive discussion during the thesis defence.

At Valeo, Dr. Frédéric Lafon and his team provided a great opportunity and challenge to complete this thesis. Fred's deep expertise on automotive EMC and down-to-earth approach on more or less visionary ideas that I had for this thesis helped to concentrate the thesis topic in a way that it would best serve the future automotive EMC engineers. Dr. Priscila Fernandez-Lopez acted as my manager over the research project, but also as an academic mentor. It is due to her efforts in proof-reading that hundreds of smaller and larger omissions and errors in this thesis have been spotted, and I have had an opportunity to fix them. Dr. Marine Stojanovic-Heulard was the one to step-in to help if Priscila was unavailable or when I made some mistakes in my "engineering" French. Usually, those mistakes revealed my barbarian nature and complete vulgarity. I hope you managed to teach me a bit of manners, and French as a supplement. Marine also contributed her share in reviewing this manuscript and providing useful suggestions for improvement – in particular for the French summary.

A good Ph.D. thesis needs also some academic supervision. For me, that supervision came from two gentlemen from ESEO: Professor Mohammed Ramdani, my formal supervisor, and from Professor Richard Perdriau. It has been said that Richard and Mohammed come always as a pair, and I do not wonder why. Mohammed has an exceptional skill to see and manage large concepts and constructs. That combined with Richard's attention to detail ensures excellent results from projects that the two gentlemen supervise. This is also highlighted by the fact that the first student to defend his Ph.D. in our project is the one that Richard supervises.

I would like to thank all my co-authors of the publications that I made. Without your

input to the research direction, they would have not reached the level of quality they are now. The countless discussions we have had, and the revision I have made have strongly contributed to my academic writing skills.

I had the opportunity to visit some other Valeo sites during my work, and I would like to thank Dr. Marco Bonato from Valeo la Verriere for proposing to use their equipment for vibration tests and Marco Bencivenga and Ahmed Aachchak for practical arrangement and support during the tests. Special mention goes to the 'joker' Arnaud Maire for helping me to solve some issues related to vibration withstand of the triaxial cell developed in this thesis. Another important site visit for me was the visit to the Bobigny site hosted by Amin Frikha. There Bau Tran helped me to make the first swaged contacts and showed some other prototype manufacturing tricks. On more technical discussion, Cyril Dubuc helped to open the world of mechanical engineering of contacts, and provided good background for me to develop the test setup for the swaged contact.

During my secondments at University of York and KU Leuven I had the privilege to be guided both theoretically and practically by many experts in their field. I would like to thank Prof. Emer. Andy Marvin and Ass. Prof. John Dawson for their introduction to reverberation chambers. I appreciated especially Andy's down-to-earth approach on the problematic of electromagnetism. I enjoyed his innovative antenna designs and comparisons to acoustic problematic. In the end, it is just physics, so why wouldn't one benefit from insights that some other applications can bring. At KU Leuven, I got some excellent practical guidance to operate the highly accelerated life test setup from Klaas and Filip. Their straightforward approach of: "Now you know how to operate the machine, then you just need to figure out what you want to do with it." must have been perfected after practical experience with many former Ph.D. students. At KU Leuven, I also had the privilege to receive some important advice on adhesives from Korneel van Massenhove, guidance on using universal testing machine from Steven Fevery, and microscopic imaging services from Cédric De Schryver. Without all this help, I could have chosen a wrong path or would not have achieved the quality results that this thesis provides.

At Valeo, we hosted two ESRs from the project and numerous interns during my research project. I would like to thank my project colleagues Lokesh and Vasso for interesting discussions on our research topics and life in general. We spent memorable events both at work and exploring Paris, from Palace of Versailles to fashion week. Supervising Bouchra's internship was a nice experience, and I hope I was able to supply her with some provisions for the future. At least she got to experience a glimpse of both tightly

supervised and independent work at different phases of her internship, while providing some new insights for me and the company.

A small mention of gratitude is owed to Jesper Lansink Rotgerink for providing his braided cable figures to be used in this thesis. It saved me the time to make similar figures that would still not have been the same quality.

I would like to thank my parents Anja and Seppo for providing a stable foundation during my early study years. Without that foundation, I would not have reached this far. Also, I would like to thank my brothers Eemeli and Aatu. Our infrequent discussions with Eemeli on research and the example he set have been among the motivators for me to embark on an applied research career. Aatu, on the other hand, provided tangible help in having some of the first prototypes of the environmental triaxial cell manufactured and by giving practical insights on how the metal working process needs to be set to achieve meaningful parts.

I would like to thank all my colleagues at Danfoss Drives Gråsten, Vaasa, and Loves Park plants for the challenges and support they gave me before deciding to embark for the Ph.D. journey. It is very much due to the challenges that we solved together that I started to appreciate the common insight and structured thinking process that all my Ph.D. colleagues seemed to have. You may not know it, but it had a huge impact on me, and on how I wish to learn to view the world. So, thank you Henrik, Per, Søren, Andreas, and Anton to name a few of you.

Finally, it is time to thank my wife Eeva and son Väinö for enduring me during this research project. It has not been the easiest task, especially during the final phase of the thesis writing when I have been at home mainly to sleep. For Väinö, the time has brought many opportunities to learn new things and see magnificent structures like the Eiffel Tower and the Palace of Versailles, but also challenges of learning two languages at the same time. Quand tu peux lire ça, j'espère que tu peux apprécier les compétences que tu as acquis pendant notre séjour en France.

TABLE OF CONTENTS

Résumé en Français	5
Câbles Blindés	7
Résistance de Contact des Connexions de Masse des Circuits Imprimés	10
Gestion des Risques CEM et Conclusion	15
Acknowledgement	17
Introduction	25
Autonomous Driving Systems and EMC	27
Electric Vehicles and EMC	29
Environmental Testing	32
Thesis Outlook	33
1 Shielded Cables Under Environmental Stress and Ageing	35
1.1 Shielded Cable Performance Metrics	38
1.1.1 Shielding Effectiveness	40
1.1.2 Transfer Impedance	41
1.2 Test Methods at Ambient Laboratory Conditions	53
1.2.1 Triaxial Cell	54
1.2.2 Transfer Impedance Measurement Uncertainty with Triaxial Cell	56
1.3 Environmental Triaxial Cell	60
1.3.1 Design of the Triaxial Cell	61
1.3.2 RF Performance of the Triaxial Cell	65
1.3.3 Transfer of Thermal Energy	73
1.3.4 Transfer of Vibration Energy	76
1.4 Transfer Impedance as a Function of Thermal and Vibration Stresses	80
1.4.1 Thermal Stress	82
1.4.2 Vibration Stress	84
1.4.3 Combined Thermal and Vibration Stress	86
1.4.4 Thermal and Mechanical Ageing	88

TABLE OF CONTENTS

1.5	Conclusion on Shielded Cables	89
2	Circuit Board Ground Contacts Under Environmental Stress and Ageing	93
2.1	Theory of Electrical Contacts	95
2.1.1	Material Selection	96
2.1.2	Contact Pressure and Contact Area	97
2.1.3	Creep and Stress Relaxation	100
2.1.4	Oxidation of Contact Surfaces and Fritting	101
2.1.5	Plating of Contact Surfaces	102
2.1.6	Fretting	103
2.1.7	Conclusion on Electrical Contact Parameters	105
2.2	Contact Resistance Characterization	105
2.2.1	Contact Resistance Measurement under Environmental Stress . . .	108
2.2.2	Conclusion on Contact Resistance Measurements	117
2.3	Contact Resistance of Circuit Board Ground Contacts During Environmental Stress	118
2.3.1	Thermal Stress	119
2.3.2	Vibration Stress	122
2.3.3	Combined Thermal and Vibration Stress	125
2.3.4	Thermal and Mechanical Ageing	128
2.4	Conclusion on Circuit Board Ground Contacts	133
3	Risk-based EMC in Automotive Domain	135
3.1	Rule-based EMC	137
3.1.1	Shielded Cable Connection of a Sensor and an ECU	141
3.1.2	EMI Filter of a Powertrain Inverter	148
3.2	Risk-based EMC	158
3.2.1	Cost Optimization	160
3.2.2	Breakthrough Products	161
3.2.3	Complex Systems	161
3.2.4	Performance Updates with Software	163
3.2.5	Environmental Stress Dependency	164
3.2.6	Conclusion on risk-based EMC	170
3.3	Conclusion and Perspectives on EMC Risk Management	171

Conclusion	175
Bibliography	181
Appendices	201
A Transfer Inductance	202
A.1 Helical inductance	202
A.2 Hole inductance	203
A.3 Braid inductance	209
A.4 Skin inductance	211
B Field Strengths at Circular Triaxial Cell Cross-section	212
List of Publications	214

INTRODUCTION

Automotive world is at the edge of two major transitions: autonomous driving and electrification. Autonomous vehicles are expected to be a part of the solution for urban mobility. As people are concentrating on small areas of land in big cities, organizing an efficient traffic system becomes a challenge. Currently, it is not uncommon for workforce to spend two hours, or even more, in traffic every single working day. That decreases the quality of living in busy areas as the lost time in traffic could be used more productively. With connected autonomous vehicles it would be possible to setup a remote office in the car, or to use the commuting time to unwind with the help of in-car entertainment. Another global challenge comes from climate change, which could be partly solved by electric vehicles (EVs) depending on the future mix of electricity production. In addition, electric vehicles help to eliminate local emissions that cause health hazards to people living in urban environments.

A hype cycle [1] can be used to analyse technological developments in progress. Both autonomous and electric vehicle technologies are going through the "trough of disillusionment" in their hype cycle [2] as shown in Figure 10. It means that the limits of the current technology are being recognized, and the industry is starting to steadily invest in building incremental solutions for the problems discovered through the disillusionment phase. For autonomous vehicles, that is reflected in the following excerpts from industry influencers:

"It will probably be a while before private transport reaches high automation level."

(Uwe Burckhardt, Head of Test and Event at DEKRA Lausitzring [11])

"What must be true to get to zero preventable roadway deaths? We have concluded that seeing and processing about 100 Tb/s is one of these necessary requirements."

(Lawrence Burns, former General Motors VP of R&D [12])

"Whatever your feelings about driver-assistance tech, it's here to stay, and increasing in sophistication by the day."

(Matthew Avery, Director of Research at Thatcham Research, and Member of the Board at Euro NCAP [13])

One could easily foresee very similar statements to be given on vehicle electrification. While the basic building blocks of the electric power-train exist, there is still a huge amount of work left to properly industrialize the designs. Lack of experience in industrializing electric powertrains is evident in an extract of a recent recall that highlights insufficient design margin of a key component in a production EV:

"On affected vehicles, Direct Current ('DC') fast charging and repeated wide-open-pedal events can cause the high voltage battery main contactors to over-heat."

(Ford Motor Company in its Mustang Mach-E recall [14])

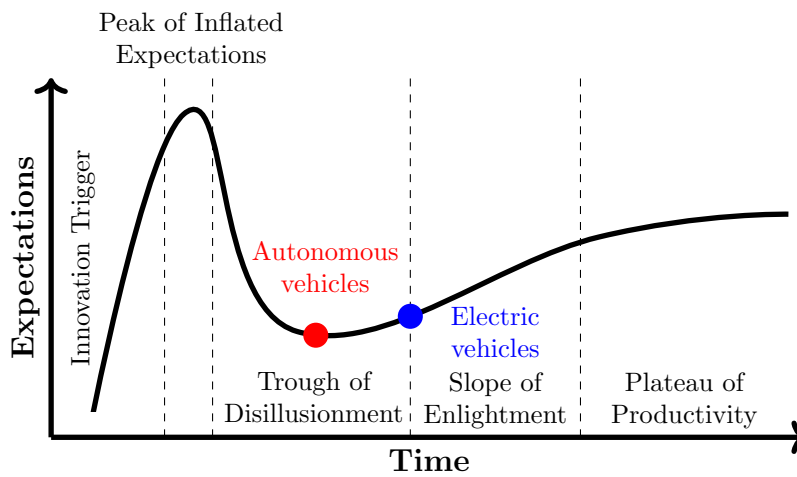


Figure 10 – A hype cycle highlighting the advancement of autonomous and electric vehicles according to [2]. Picture background by [3].

In addressing industrialization of the novel electronic systems, one key pillar is ensuring that electromagnetic compatibility (EMC) can be guaranteed through the lifetime of the vehicle [4]. These EMC challenges rarely break the news, but are well-known to those with experience in the automotive domain – as a hindrance for new product market introduction, and as one source of quality issues. There are some public examples of vehicle systems experiencing electromagnetic interference (EMI), even in safety critical systems, like the airbag control module [5]. Following two sections will discuss a subset of the challenges related to autonomous driving systems and electric vehicles, for which, this thesis searches for an answer. Finally, environmental testing section will discuss an approach to ensure that appropriate testing methods exist to evaluate solutions for the challenges presented in the preceding sections. This evaluation needs to extend to a

degree, where reliable estimation of technical performance is achieved through the lifetime of the vehicle.

Autonomous Driving Systems and EMC

To concretely introduce the problematic of autonomous driving systems, an example of an automated lane centring (ALC) system is taken. Its safety characteristics have been thoroughly evaluated in a project of the United States National Highway Traffic Safety Administration (NHTSA) [15]. The system consists of an advanced driver assistance system (ADAS) domain controller, various sensors, actuators, and data interfaces as shown in Figure 11.

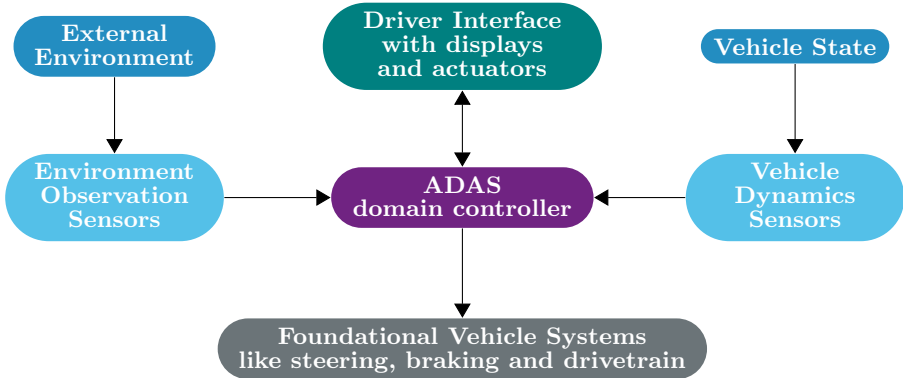


Figure 11 – A generic ALC system structure adapted from [15].

System level safety importance analysis of the ALC function reveals that the ADAS domain controller is EMC-wise the most important component to protect from EMI [16]. ADAS domain controller performs all high-level modelling and control of the ALC system, thus, being the most critical component in the system. This is highlighted in Figure 12 with a safety importance ratio for each module level. Sensing (10%) and actuating (10%) have low safety importance ratio as any sensor or actuator can be duplicated with relative ease, and their function can be sanity checked by either comparing the sensor data to expected values, or providing a test signal to the actuator and monitoring its effect. In contrary, verifying the correct function of the ADAS domain controller in real-time is more difficult with the only feasible options being competitive models and control algorithms running on different physical hardware and software structure, whose results are compared

against each other for the final decision. If an EMI event disturbs this process, it might be extremely difficult to recognize. Hence, a high safety importance ratio is assigned for the modelling (40%) and control (40%) parts. An example of a real-world EMI event is a case of a prototype vehicle, where the domain controller was not robust enough against electromagnetic disturbances (EMD) [17]. There, an unforeseen immunity issue was discovered only when the vehicle failed to stop at a red light during a demonstration. The cause of failure was later identified to be high disturbance level from the audiovisual equipment used to record and broadcast the demonstration.

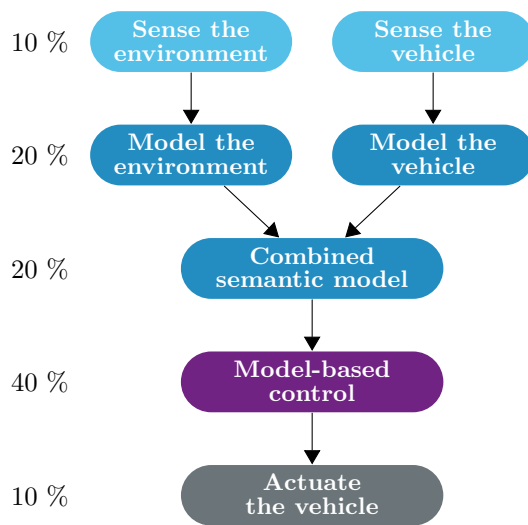


Figure 12 – A generic ADAS control structure with a safety importance ratio on the left for each level. Graph is from [16].

Currently, the functional safety approach standardized in ISO 26262 requires to comply only with traditional rule-based EMC standards in its hardware level specification [18]. As it will be shown in Chapter 3, this is not enough to properly ensure safety of complex autonomous driving systems. Instead, a risk-based resilience approach is needed. Resilience in this context means creating fault tolerant systems [19] that can handle unforeseen disturbances in addition to those defined in the state-of-the-art standards. Fault tolerance is commonly achieved by utilizing techniques and measures for systematic failure avoidance [20] – a concept more related to dependability and safety engineering than EMC. Thus, to achieve dependable safety function under EMD, a paradigm change in EMC engineering towards EM resilience is needed. Some early standardization work will be discussed in Chapter 3, but it is not at sufficient level to be applied in the automotive

industry at the moment. Thus, it is on the shoulders of individual companies to apply proper EM resilience into their designs leading to the first industry-wide challenge:

Industry Challenge

How to design autonomous driving systems that are robust against electromagnetic disturbances (EMD)?

This thesis concentrates on robustness of data communication between different modules performing the ADAS function. To safeguard this communication, different software and hardware means can be implemented ranging from error correction codes to correct possible bit flips due to EMD all the way to shielded communication cables to prevent EMD from entering into the signal paths in the first place. That leads to the second challenge of interference free data transmission:

Industry Challenge

How to achieve interference free data transmission between ADAS system modules, sensors, and actuators?

In this thesis, the performance of shielded communication cables in preventing the entry of EMD is evaluated through the approximated life of the vehicle. Further details on the characterisation plan are given in the Environmental Testing Section below.

Electric Vehicles (EVs) and EMC

The major challenge with EVs is the paradigm change in the applied voltage level compared to current state-of-the-art. Traditionally, passenger vehicles have relied on 12 V electrical architecture. Using such a low voltage has provided electrical safety benefits, but has also meant that high currents in the order of hundreds of amperes are needed, especially during the combustion engine start. In the event of a fault, the available short-circuit current from the electrical system is high enough to cause a risk of fire by overheating. In the United States it has been deemed that every fifth highway vehicle fire is due to the electrical system [21]. To conveniently achieve high enough power from the electric drivetrain, voltage needs to be increased into a higher level with the current

state-of-the-art being at 400 V, which will likely increase to 800 V in the near future. That is due to weight and cost reduction needs in the drivetrain components, improved overall efficiency, and fast charging requirements [22]. For average vehicles, this means that the used current is in the same order as the maximum currents used in legacy systems.

Typical high voltage components of an EV are shown in Figure 13. They are:

1. Charging port
2. On-board charger (OBC)
3. High-voltage (HV) battery
4. Electric drive unit (EDU) comprising of an electric motor and an inverter
5. DC-DC converter from high voltage to 12 V
6. Compressor for heat-pump

Charging port connects an external alternating current (AC) supply to the OBC, which transforms it to direct current (DC) for battery charging. This DC supply can be connected to the high voltage DC bus as shown in Figure 13, straight to the HV battery, or through the traction motor and inverter depending on system architecture [23]. There exists a connection from the charging port directly to the battery for DC fast chargers, but it is omitted in Figure 13.

Battery supplies the EDU as well as some auxiliary systems, like the DC-DC converter for charging the 12 V battery, and a heat-pump compressor for temperature control of the drivetrain elements as well as the passenger cabin. It is noteworthy that the 12 V battery is still needed as most of the automotive electronics is designed to work at extra low voltage (ELV). However, the requirements for 12 V battery are different from internal combustion engine (ICE) vehicles as it does not need to provide the high amperage starting current for ICE starter.

From commercial point of view, vehicle manufacturers (OEMs) have an incentive to standardize the interfaces for different HV components to benefit from offerings of several suppliers. On the other hand, larger suppliers have an incentive to develop added value offerings for using exclusively their components. One of those added values could be better EMC performance.

Controlling electric motors in a modern way means rapid switching of their supply voltage that generates a high-frequency common-mode (CM) voltage between motor windings and vehicle chassis. Charging and discharging inevitable parasitic capacitances with that voltage causes a CM current that can disturb other electronic equipments installed

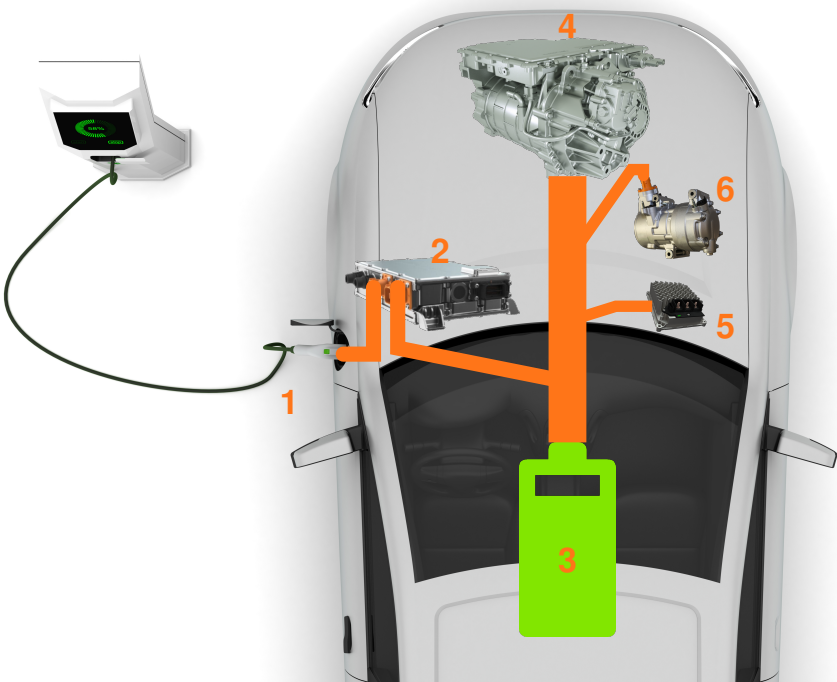


Figure 13 – A generic electric representation of main high voltage components in an electric vehicle. Base picture: © Getty Images/iStockphoto. Component pictures source: Valeo.

in the vehicle including the ADAS systems discussed in the previous section. This effect is supply voltage dependent, and changing from 12 V to 800 V means a significant increase of 36 decibels (dBs). Similar challenge is also seen in other high voltage infrastructure like the heat-pump compressor, OBC, and the DC-DC converter between the 800 V and 12 V systems. This leads into the first EV industry challenge:

Industry Challenge

How to manage the disturbance increase of 36 dB when moving to electric drivetrains?

CM current is usually controlled by conducting it in the grounding structure close to its initial path back to its source, and then coupled back to the high voltage circuitry through an EMI-filter. It is paramount to minimize the CM current loop area to avoid any radiation, and to minimize the ground impedance to avoid any voltage differential between

the chassis elements, called as ground bounce. For cable connections, it is commonplace to use shielded cables. While they increase the parasitic capacitance to ground, and hence the CM current amplitude if exposed to rapidly changing voltage components, they provide a low-impedance return path with small loop area that gives more advantages compared to the disadvantage of slightly increased CM current. The challenge in here is to ensure that the CM loop stays unchanged through the vehicle lifetime including service and accident damage repair, which leads to the last industry challenge of this thesis:

Industry Challenge

How to ensure continued performance of the common-mode loop design through the vehicle lifetime?

The scope of the common-mode loop design parameters in this thesis includes shielded cables and EMI-filter ground connections. Further details on the plan for their lifetime characterisation are given in the Environmental Testing Section below.

Environmental Testing

Assessment of through life performance of electronic components needs inevitably some form of testing. The goal of environmental testing is to ensure that the designed vehicle components endure the environmental stresses foreseen during the vehicle use. They are commonly accelerated by increasing the stress level to shorten the testing time. As the useful life of an automotive system is around ten years, and the development time of such a system is generally between one and three years, it is evident that test acceleration needs to be used during all development projects.

The industry challenges of the preceding sections are derived to the primary thesis challenge of environmental testing:

Thesis Challenge

Evaluate the effect of environmental stresses and ageing on shielded cables and EMI-filter ground connections

In the frame of this thesis, the objective is to:

1. Develop test setups for environmental characterisation of shielded cables and EMI-filter ground contacts
2. Characterise thermal and vibration response of shielded cables and ground connections
3. Test different samples to compare commonly available technological choices

Thus, the test time for a single device-under-test (DUT) is very limited. To overcome this challenge, highly accelerated life testing (HALT) is pursued [24]. It is normally used to evaluate the success of system integration of electronic products by stressing the system assembly at extreme levels to find any design mistakes that cause the system to perform worse than the fundamental performance limit of the technologies used in it. Now, instead of evaluating the system integration of a product, the fundamental limits of different technologies are pursued, and compared against each other. This leads to the second thesis challenge:

Thesis Challenge

Apply highly accelerated life testing (HALT) to evaluate different cable shielding and ground contact technologies in a rapid fashion.

Finally, the importance of the achieved results need to be demonstrated. To do this, the last thesis challenge requires finding examples that tie the results to the industry challenges:

Thesis Challenge

Demonstrate the results and their effects to functionality of automotive systems with real-world examples.

Thesis Outlook

To answer to the presented thesis challenges in the Environmental Testing Section, this thesis was launched as a part of an European Horizon 2020 project PETER [25]. To tie the seemingly independent work of solving environmental testing challenges of shielded cables and EMI-filter ground contacts better to the project and to the industry

challenges of autonomous vehicles, a further thesis challenge in EMC risk management was introduced:

Thesis Challenge

Contribute to the development of risk-based EMC approaches considering multi-parameter influences.

This thesis is structured around a generic automotive electronics subsystem that Tier 1 suppliers, like Valeo, develop for their OEM customers. The chapter division is illustrated in Figure 14. Analysis of shielded cables is discussed in Chapter 1. First, by revisiting the theory of cable shielding and its measurements in the laboratory environment. Then, extending it by taking into account the variation of temperature and mechanical vibration both as transient and as a long-term phenomenon i.e. ageing. Chapter 2 does the same treatment for circuit board ground contacts commonly used as part of common-mode EMI-filters. To tie these analyses closer to practice, Chapter 3 shows rule- and risk-based EMC approaches for two case studies from automotive domain. The first one uses a shielded cable between a sensor and an electronic control unit (ECU), and the second one is an application of an EMI-filter in an EV. At the same time, proper management of the EMC issues arising from these case studies is discussed. This aims to provide an answer to the last thesis challenge. There, the need to take the environmental effects into account as a part of the risk management process is reinforced, and the case studies are used to concretize dissimilarity of the different risk management approaches.

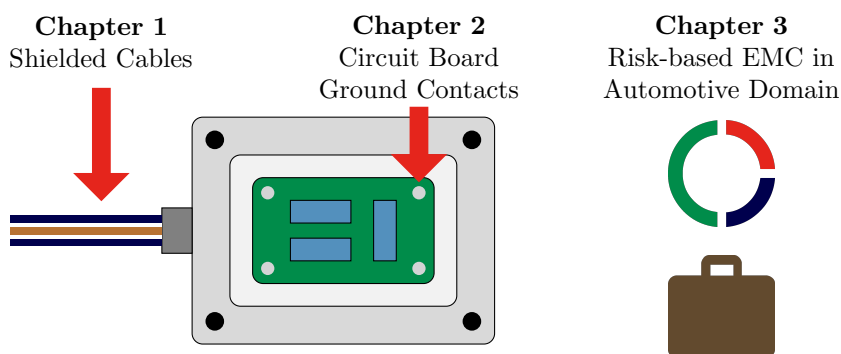


Figure 14 – Thesis scope

SHIELDED CABLES UNDER ENVIRONMENTAL STRESS AND AGEING

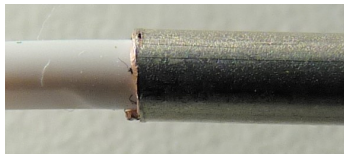
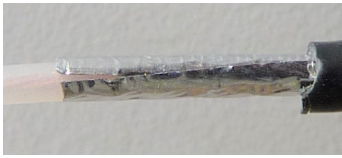

In search for an answer to the thesis challenges presented in the Introduction for shielded cables, this chapter presents the state-of-the art of shielded cable performance evaluation, and extends it to cover environmental stress and ageing. This is important to not only cover the performance evaluation when the cables are new and at laboratory conditions, but also when the cables have aged and are used in extreme environments as allowed by their specifications.

Typical cable shields come in three different variations as shown in Table 1.1. Solid shields offer the best performance, but are difficult to manufacture and install, whereas foil and braid shields offer complimentary performance. Multiple shielding layers can be combined together to form multi-layer shields [6]. A typical multilayer shield is formed from braid and foil shields as they compensate for each others' characteristics: braided shield provides good low-frequency performance, whereas foil shield provides good high-frequency performance. Another typical combination is to wind a second braid on top of the first one to form a double-braided cable.

As an example of automotive applications, two significant installations of shielded cables are presented in Table 1.2. They follow the industry challenges presented in the Introduction: camera-to-electronic control unit (ECU) cable in an advanced driver assistance system (ADAS), and an inverter connection to traction battery in an electric vehicle (EV).

For the camera connection, the cable is approximately two meters long, and routed from the top of the windscreen towards the A-pillar of the vehicle chassis, from where it is routed towards the floor of the vehicle where the ADAS control unit resides in this example. Note that, while the front camera location is fairly standard, different car manufacturers can have varying positions of the camera processing ECU, and thus, the cable routing and length can vary. The cable is impedance controlled to provide a high

Table 1.1 – Overview of typical cable shielding

	Solid	Foil	Braid
			
Structure	Solid metal extruded or applied on top of the cable dielectric	Solid or plastic-backed metal foil wrapped on top of the cable dielectric	Thin wires braided on top of the cable dielectric
Performance	High performance shield	Low-to-medium performance depending on foil winding strategy <ul style="list-style-type: none"> • Limited performance at low frequencies • Good performance at high frequencies 	Low-to-medium performance depending on braid construction <ul style="list-style-type: none"> • Good performance at low frequencies • Limited performance at high frequencies
Effort	Difficult to manufacture and install	Easy to manufacture and install	Needs high-fidelity manufacturing machinery, easy to install

data rate, and has a braid on top of a foil shield as shown in the picture in Table 1.2.

For the EV inverter connection, the high voltage cable is routed all the way from the traction battery into the the inverter that is situated on top of an electric motor forming an Electric Drive Unit (EDU). It is approximately 1.5 meters long, and routed along the chassis elements and the EDU side. Here, a rear-wheel drive configuration is shown, but a front-wheel drive version is very similar. The cable is not impedance controlled, but double insulated in a way that the centre conductor is insulated from the shield, and again the shield is insulated from the environment. In this way, any insulation failure that would expose parts of the cable under high voltage is likely to cause a short-circuit with the shield rendering action of circuit protectors, and resulting in the cable to be disconnected from any voltage sources while the outer insulation protects any user that could be manipulating the cable. For this purpose, the cable has a tight braid next to the inner conductor insulation that is combined with a foil on top of it for improved shielding performance.

Table 1.2 – Automotive examples of shielded cable applications

Camera to ECU ¹	EV Battery to Inverter ²
<p>Impedance controlled (50 Ω) shielded cable with a braid on top of a foil</p>	<p>High voltage shielded cable with a foil on top of a tight braid</p>

¹Overview picture: Audi AG, Bordnetze Kongress 2018

²Overview picture: DELFINGEN

Now, to analyse the performance of those shielded cables, some theoretical discussion is needed first. This is covered in Section 1.1 that discusses the performance metrics and modelling of shielded cables. Then, test methods to characterize cable samples are discussed in Section 1.2. However, these methods are intended to be applied to cables under normal laboratory ambient conditions. As it was highlighted in the Introduction, this approach is not enough for all industries. Thus, a further step to introduce a novel measurement method that can be used during environmental stresses is performed as described in Section 1.3. This new method is used to extract temperature and vibration amplitude dependency of transfer impedance for typical shielded cables. For which, the results are reported in Section 1.4. The chapter is finished with conclusions in Section 1.5. Afterwards, the results obtained in this chapter are used as an input for the automotive sensor-and-ECU case study in Chapter 3.

1.1 Shielded Cable Performance Metrics

Shielded cable performance metrics concentrate on defining the capability of the shield as an inhibitor of electromagnetic (EM) field coupling between the outside world and internals of a cable, separated by the cable shield [26]. The aggressor can be either inside of the shielded cable (an emission problem), or coming from the outside world (an immunity problem). The cable under analysis is commonly referred to as cable-under-test (CUT). There are two common ways to analyse the shielded cable performance:

Shielding Effectiveness (SE) defines a metric, which compares the system susceptibility to external electromagnetic field (or emissions from internal EM field) with and without shield as illustrated in Figure 1.1. The variables that are compared against each other can be various as shown in Section 1.1.1.

Transfer impedance approach decouples the problem in an internal and external solution linked by the transfer impedance. The internal solution takes into account the wave propagation inside the shielded cable, and the external solution takes into account the propagation between the shield and the external environment as illustrated in Figure 1.2. Now, the link between the domains is defined as transfer impedance

$$Z_T = \frac{V_{ext}}{I_{shield}}. \quad (1.1)$$

Here, the link is shown from the shield current I_{shield} in the internal system to the induced voltage V_{ext} in the external system. The same definition can be used in reverse to link I_{shield} to the induced voltage V_{in} in the internal system. A more thorough definition of transfer impedance is given in Section 1.1.2.

Shielding effectiveness used to be the more utilised metric due to availability of relatively straightforward experimental characterization methods. However, it is more difficult to implement in circuit analysis. Thus, a series of developments from the '90s up to today have concentrated on improving the experimental characterization of transfer impedance. The state-of-the-art of measurement methods are discussed in Section 1.2. Lately, transfer impedance has become the de-facto method for characterizing intrinsic cable shielding properties, whereas shielding effectiveness is still used to characterize complete cable assemblies, where the transfer impedance measurement methods are still lacking.

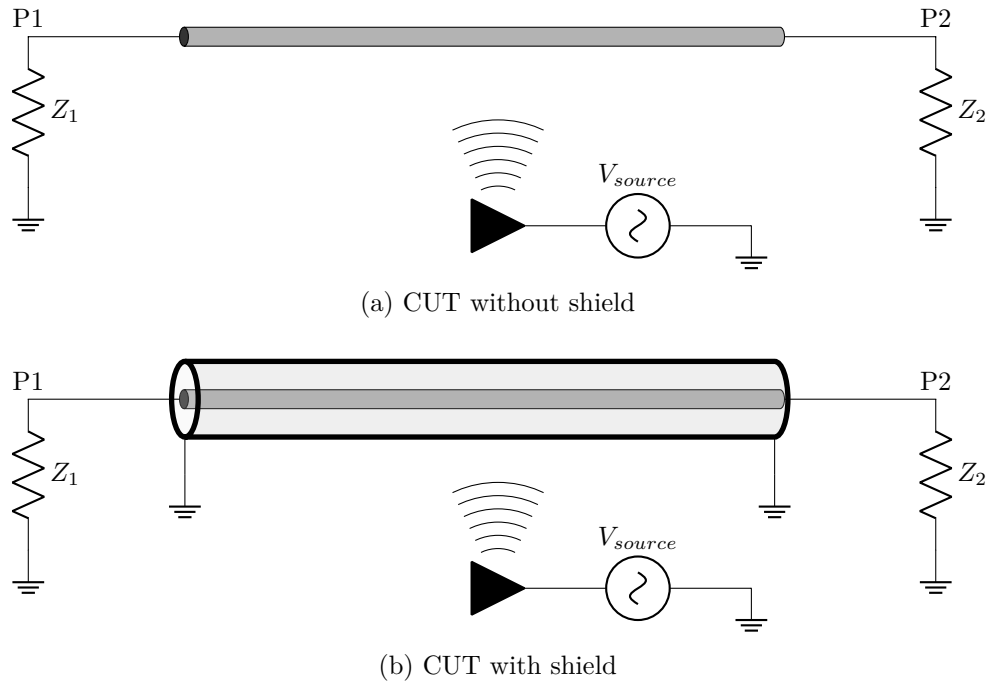


Figure 1.1 – Two test cases used to determine the shielding effectiveness of a shielded cable as a comparison between cases (a) and (b).

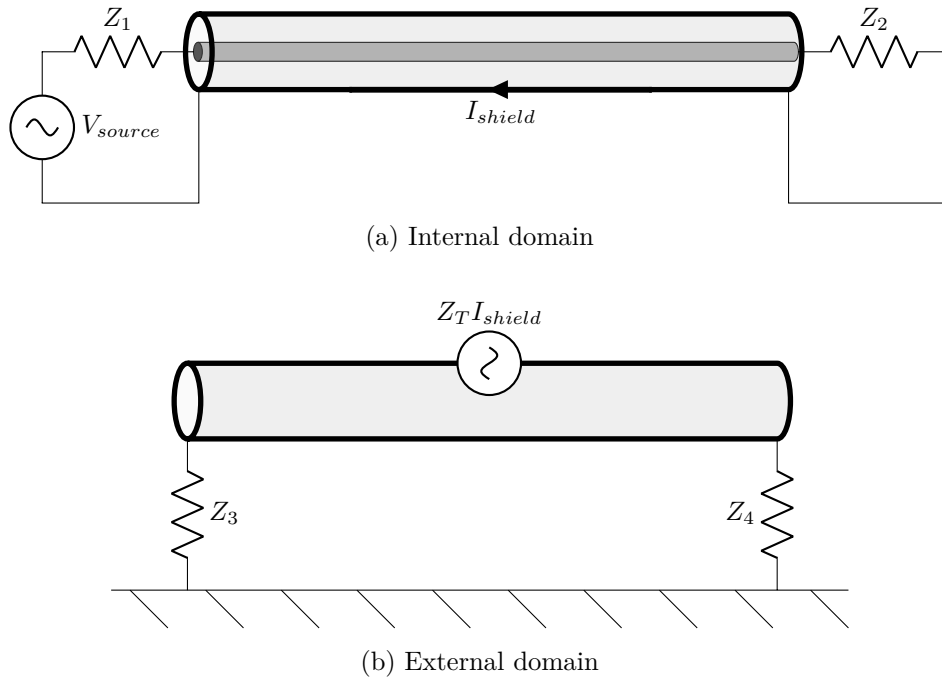


Figure 1.2 – Transfer impedance of a shielded cable linking the (a) internal and (b) external domains.

1.1.1 Shielding Effectiveness

Shielding effectiveness is a generic quantity to describe the performance of any electromagnetic shield. In this thesis, the focus is on the application to shielded cables, but the basic theory is shared among all shields.

There are three different definitions of shielding effectiveness [27]:

1. Electric shielding effectiveness SE_E :

$$SE_E = 20 \log_{10} \frac{|E_{unshielded}|}{|E_{shielded}|}, \quad (1.2)$$

where $|E_{shielded}|$ and $|E_{unshielded}|$ are the measured electric field strengths with and without shield, respectively.

2. Magnetic shielding effectiveness SE_M :

$$SE_M = 20 \log_{10} \frac{|H_{unshielded}|}{|H_{shielded}|}, \quad (1.3)$$

where $|H_{shielded}|$ and $|H_{unshielded}|$ are the measured magnetic field strengths with and without shield, respectively.

3. Electromagnetic shielding effectiveness SE_{EM} :

$$SE_{EM} = 10 \log_{10} \frac{2}{\frac{|E_{shielded}|^2}{|E_{unshielded}|^2} + \frac{|H_{shielded}|^2}{|H_{unshielded}|^2}}. \quad (1.4)$$

Electromagnetic shielding effectiveness is a special case of shielding aperture SA:

$$SA = 10 \log_{10} \frac{P_{unshielded}}{P_{shielded}}, \quad (1.5)$$

defined by the measured powers $P_{shielded}$ and $P_{unshielded}$ with and without the shield, respectively. The special case is achieved when loading of the shielded enclosure is zero at the measurement point.

For cables, simplified SE determination methods exist, as the internal domain can be considered as a transmission line. If utilizing any of the approaches described above, E-field, H-field or absorbed power values are commonly estimated by measuring voltage, current or power at P1 or P2 (see Figure 1.1), respectively to the desired field quantity.

This approach has resulted varying SE definitions with the most popular being one that relates shield current to the current in the internal domain as [28]

$$SE_I = 20 \log_{10} \frac{I_{shield}}{I_{in}} \quad (1.6)$$

to achieve a positive shielding effectiveness value roughly equal to that of Equation 1.3. Currents can be exchanged in the division to achieve a negative value for SE_I . This definition can be linked to transfer impedance by an experimentally verified formula [29]

$$Z_T = \frac{2Z_1}{l} \frac{\theta}{\sin \theta} 10^{-\frac{SE_I}{20}}, \quad (1.7)$$

when $Z_1 = Z_2$, l is length of the cable under analysis, and

$$\theta = \frac{2\pi f}{c} (\sqrt{\epsilon_r} + 1) \frac{l}{2} \quad (1.8)$$

is the propagation term.

As it is seen from Equation 1.7, defining transfer impedance in this way results in dependency of the cable length and frequency in a way that is not very straightforward. This is a result of SE_I being length dependent as I_{in} depends on the length of the cable. As such, this definition is not optimal, and should be in-fact used in reverse to derive shielding effectiveness from transfer impedance, when needed, as [30]:

$$SE_I = 20 \log_{10} \frac{Z_T l}{2} + 20 \log_{10} \frac{\sin \theta}{\theta} - 20 \log_{10} (Z_1). \quad (1.9)$$

In the next section, a method to derive per-unit-length transfer impedance that is dependent only on the physical parameters of the cable shield is presented.

1.1.2 Transfer Impedance

Transfer impedance for solid cable shields has been defined almost 100 years ago [26]. Soon after, significant work was performed to include the effect of small openings [31] and multiple shielding layers [6] to the total transfer impedance of the cable shields. Theory for transfer impedance of foil shields was introduced at the same time [6], and has not garnered much of public interest since. Theory of braided shield transfer impedance is the most recent one with the first theory derived based on the theory of small openings in a

solid shield [32] that was later extended to take the specifics of the braiding structure into account leading to some design rules to optimize the transfer impedance of single-braided shields [33]. This section discusses the theory of solid, foil wound, and braided shielded cables with an emphasis on braided shields due to their complexity. There are also more complex cable shielding structures, like double-braided shields [34], whose model has been recently improved [35], and twisted shielded cables [36]. Their theoretical discussion is omitted in this thesis.

Some recently published advancements in automotive cable shielding are revolving around electric vehicles. An aluminium pipe shield [37] has been proposed to be used so that the cable assembly is manufactured as a pre-formed part similarly to brake line assemblies. For automotive high-voltage system analysis, the first braid and foil coupling model has been recently presented [38], but there it was used only at low frequencies, and no thorough evaluation on its applicability nor comparison with transfer impedance (Z_T) measurements was given. In parallel to this thesis work, an ageing study on shielded cables was published [39], but it did not give results for transfer impedance – only for shielding effectiveness. To step back to the basics of the state-of-the-art, the background theory of transfer impedance is given next.

Transfer impedance of a generic shielded cable can be written as [6]

$$Z_T = R_T + j\omega L_T \quad (1.10)$$

that relates the shielded cable performance into two virtual circuit quantities: transfer resistance R_T and transfer inductance L_T . It can be expressed either as a quantity for a cable assembly with a unit in ohms, or as a per-unit-length quantity to be used with arbitrary cable lengths with a unit in ohms/m.

This shield performance metric can be extended by defining transfer admittance

$$Y_T = G_T + j\omega C_T, \quad (1.11)$$

where G_T is the transfer conductance of the shield, and C_T is the transfer capacitance of the shield. As most of the shields have relatively good coverage over the cable, and the dielectric between the openings of the shield is air or other good insulator, the transfer conductance is meaningful only for very high voltage cables, where measurable leakage current through the insulation could be observed. Good coverage of the shield also means that the transfer capacitance through the shield is small, and it can be neglected when

comparing to the effect of transfer inductance. Thus, in this thesis, only the two circuit quantities defining the transfer impedance will be explored further.

The main geometrical parameters for shields of Table 1.1 are introduced in Figure 1.3. A solid hollow cylinder shield in Figure 1.3a has the following parameters:

- D Shield outer diameter
- d Shield thickness
- l Length
- a Radius on inside of the shield
- b Radius on outside of the shield.

A typical helically wound foil shield in Figure 1.3b can be represented with the same parameters as the solid shield supplemented with:

- α_f Foil winding angle
- l_f Foil twist length.

Twist length is derived from the foil width b_f as

$$l_f = \frac{b_f}{\cos \alpha_f}. \quad (1.12)$$

A typical braided shield of similar size is illustrated in Figure 1.3c. The braid is rolled open in Figure 1.3d to better illustrate the key mechanical parameters critical in modelling of the braid:

- D Average diameter of the braid
- N Number of braid wires in a carrier ($N = 10$ in Figure 1.3)
- c Number of carriers ($c = 8$ in Figure 1.3)
- α Braiding angle ($\alpha = 37^\circ$ in Figure 1.3)

Number of carriers is the easiest to calculate from any cross-section of the braid, like the left or right end of the Figure 1.3d. Several other derivative parameters based on them are introduced throughout the following sections.

Transfer Resistance

Starting from the transfer impedance solution fulfilling Maxwell's equations, transfer resistance for a hollow cylinder (see Figure 1.3a) with an outer radius b and an inner

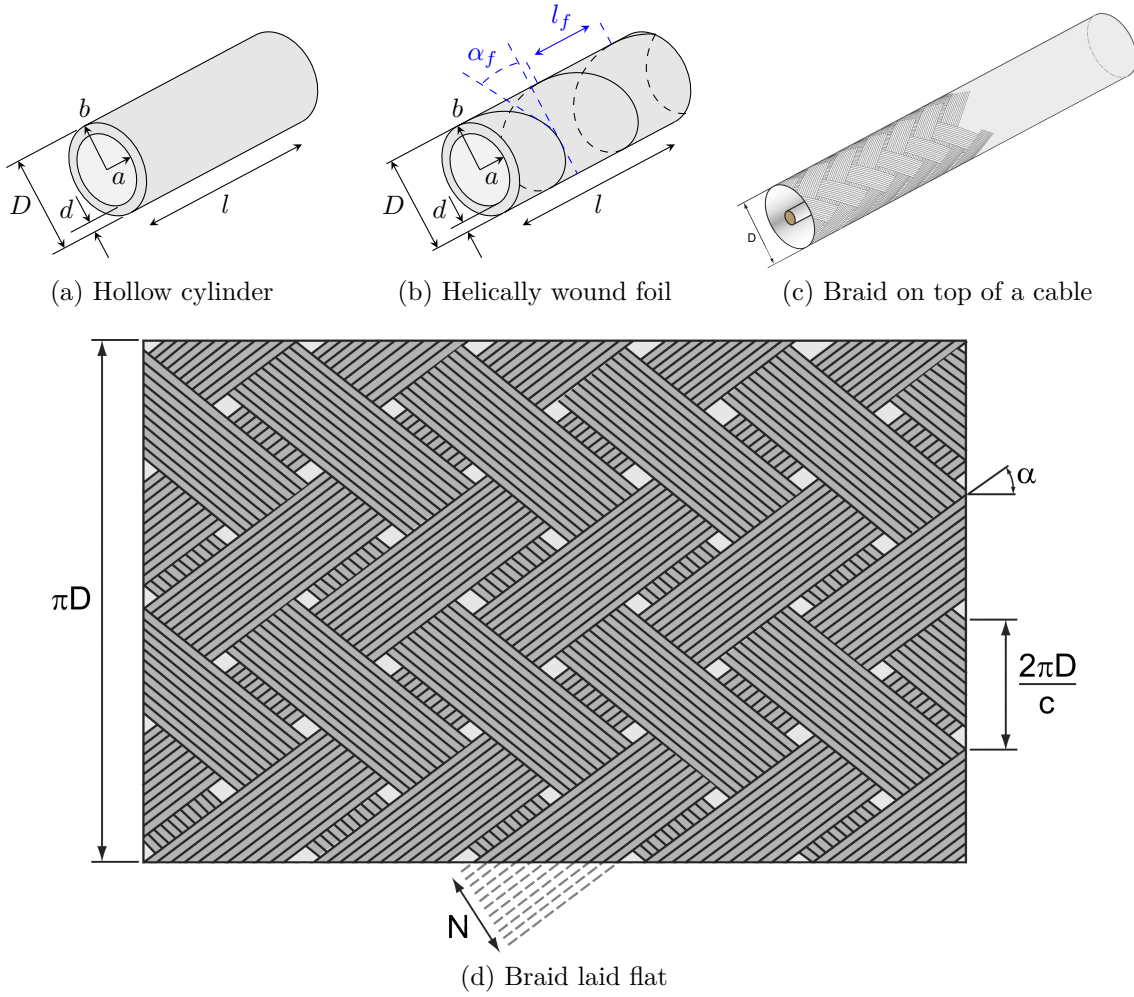


Figure 1.3 – Illustrations of typical solid, foil, and braided shields [40] on a cable.

radius a can be written as [26]

$$R_T(f) = \frac{1}{2\pi\sigma ab} \cdot \frac{1}{I_1(\gamma b) K_1(\gamma a) - I_1(\gamma a) K_1(\gamma b)}, \quad (1.13)$$

where

$$\gamma = (1 + j) \sqrt{\pi f \mu \sigma}, \quad (1.14)$$

is the cylinder's propagation constant [41], and μ and σ are permeability and conductivity of the shield material, respectively. The functions $I_1(x)$ and $K_1(x)$ are first order modified Bessel functions of first and second kind, respectively.

Equation 1.13 can be approximated with very good accuracy by [32]

$$R_T(f) = R_T(0) \frac{\gamma d}{\sinh(\gamma d)}, \quad (1.15)$$

where d is the thickness of the shield. Compared to equation 1.13 this approximate equation conveniently separates the transfer resistance of the shield at direct current (DC) from the frequency dependent skin-effect phenomena. The DC transfer resistance of a tubular shield

$$R_T^{solid}(0) = \frac{l}{\sigma A} = \frac{4l}{\sigma \pi (D^2 - [D - 2d]^2)} \quad (1.16)$$

is relative to the shield's length l and its cross-sectional area A that can be calculated from the shield thickness and outer diameter D .

For a helically wound foil shield (see Figure 1.3b), the DC transfer resistance calculation should be modified to take into account the extended shield length due to winding angle α_f [6]. The modified DC transfer resistance equation for the helically wound foil shield is:

$$R_T^{foil}(0) = \frac{R_T^{solid}(0)}{\sin^2 \alpha_f} = \frac{4l}{\sigma \pi (D^2 - [D - 2d]^2) \sin^2 \alpha_f}. \quad (1.17)$$

For a braided shield (see Figures 1.3c and 1.3d), the DC resistance calculation should be modified to take into account the cN individual braid wires [33]

$$R_T^{braid}(0) = \frac{l}{cN \sigma \cos(\alpha) A} = \frac{4l}{cN \sigma \pi \cos(\alpha) d^2}. \quad (1.18)$$

As the braid wires are not oriented straight towards the direction of the cable run, but angled, the braid wire angle α is needed to take into account the reduction of the effective cross-section. In addition, equation 1.15 is appropriate for homogenous shields, but tends to give too optimistic results for braided wire shields if braid wire thickness is directly inserted into Equation 1.15. A modification of the shield thickness [33]

$$d' = \frac{0.67d}{\sqrt{\cos(\alpha)}} \quad (1.19)$$

has been proposed, and will be used in this thesis.

It is to be noted, that the transfer resistance at DC, $R_T(0)$, is equal to the DC resistance of the shield i.e. $R_T(0) = R_0$. However, transfer resistance at high frequencies

is different from the AC resistance of the shield. This can be studied by solving the internal impedance of the shield and comparing it to its transfer impedance (as defined in Equation 1.15). The internal impedance of the shield is calculated following a hollow cylinder approach [26], where the return current is expected to flow externally to the shield:

$$Z_{cyl}(f) = \frac{\gamma}{2\pi\sigma b} \cdot \frac{I_0(\gamma b) K_1(\gamma a) + K_0(\gamma b) I_1(\gamma a)}{I_1(\gamma b) K_1(\gamma a) - I_1(\gamma a) K_1(\gamma b)}, \quad (1.20)$$

where the functions $I_0(x)$ and $K_0(x)$ are zeroth order modified Bessel functions of first and second kind, respectively. Comparing equations 1.13 and 1.20 it is seen that the Bessel functions in the denominator are the same, but the numerator of equation 1.13 is unity, whereas the numerator of equation 1.20 has another set of Bessel functions. To see the difference in frequency domain, these functions could be numerically evaluated and compared against each other, but especially equation 1.20 causes problems as some of the Bessel functions return too large values for double precision arithmetic before the multiplications and division.

Equation 1.20 can be simplified [26] to

$$Z_{cyl}(f) = \frac{\gamma}{2\pi\sigma b} \left(\coth \gamma (b - a) + \frac{\pi}{2\gamma} \left[\frac{3}{a} + \frac{1}{b} \right] \right) \quad (1.21)$$

at high frequencies. However, the fit with DC resistance is not very good. Operating only with a real part of the equations yields a better approximation at low frequencies with the cost of minor high-frequency inaccuracy

$$R_{cyl}(f) = R_0 \cdot \operatorname{Re}(\gamma d) \frac{\sinh(\operatorname{Re}(2\gamma d)) + \sin(\operatorname{Re}(2\gamma d))}{\cosh(\operatorname{Re}(2\gamma d)) - \cos(\operatorname{Re}(2\gamma d))}. \quad (1.22)$$

While accurate at low frequencies, this equation reintroduces the problem of double-precision arithmetic due to the hyperbolic functions returning very large values. However, noting that

$$\lim_{x \rightarrow +\infty} \frac{\sinh(x) + \sin(x)}{\cosh(x) - \cos(x)} = 1 \quad (1.23)$$

enables calculating values, when the real part of $2\gamma d$ gets significantly large.

Now, comparing the evolution of shield's resistance with increasing frequency as defined by the internal impedance Equation 1.22, and that of the transfer resistance

defined in Equation 1.15, it is seen that

$$R_{shield} \sim \gamma d \tag{1.24a}$$

$$R_T \sim \frac{\gamma d}{\sinh(\gamma d)}. \tag{1.24b}$$

As $\sinh(\gamma d)$ has larger absolute value of the first derivative with frequency than its argument, transfer resistance decreases as a function of frequency, whereas the shield resistance increases. This is meaningful also from the physical point of view: the magnetic field penetration through a homogenous shield decreases as a function of frequency. The corresponding results are plotted in Figure 1.4 with parameters given in Table 1.3. It is clearly seen that while all the three cases have varying DC-resistances, the high frequency resistance due to skin-effect is at very similar level. However, the difference between high-frequency transfer resistances is significant. Phase of the transfer resistance starts to vary as the skin-effect becomes important.

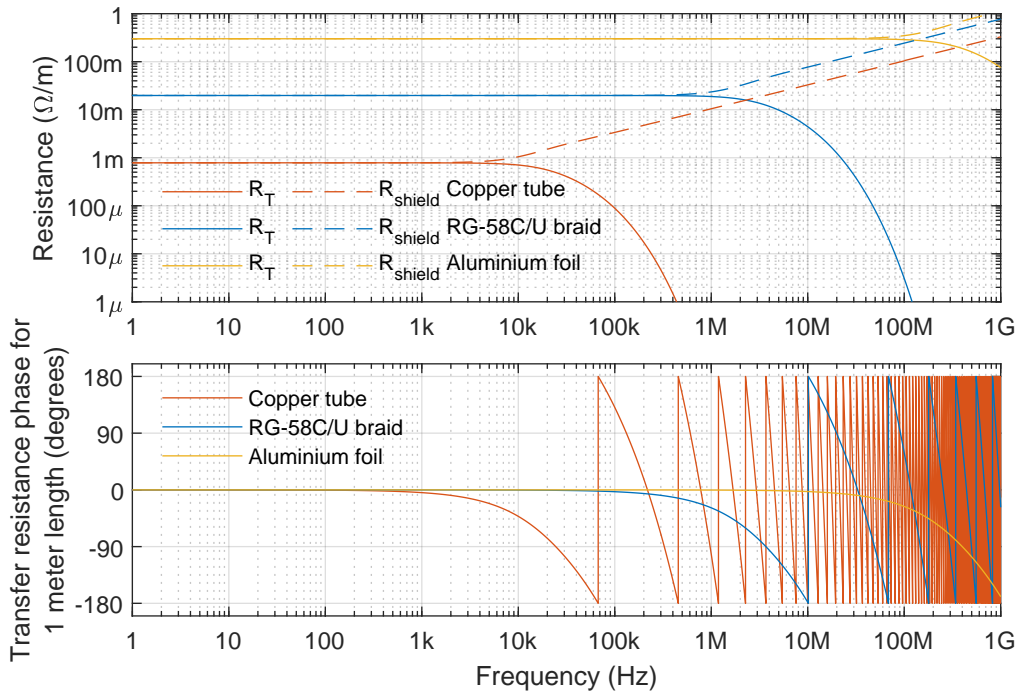


Figure 1.4 – Transfer resistance magnitude and phase as a function of frequency

Table 1.3 – Shield parameters used for the examples in Figure 1.4

Variable	Symbol	Value	Variable	Symbol	Value
Length	l	1 m	Braiding angle	α	35°
Permeability	μ	$4\pi \cdot 10^{-7}$ H/m	Winding angle	α_f	89°
Copper conductivity	σ_{Cu}	$\frac{1}{1.7241 \cdot 10^{-8}}$ S/m	Aluminium foil thickness	d_{foil}	10 μ m
Aluminium conductivity	σ_{Al}	$\frac{1}{2.82 \cdot 10^{-8}}$ S/m	Aluminium foil outer diameter	D_{foil}	3 mm
Copper tube outer diameter	D_{tube}	8 mm	Braid wire diameter	$d_{braidwire}$	110 μ m
Copper tube thickness	d_{tube}	1 mm	Total number of braid wires	cN	112

Transfer Inductance

Moving to transfer inductance, the treatment shown above for transfer resistance is adequate for all the closed tubes as the transfer resistance equations take into account diffusion of the magnetic field through the shield. If there would be any holes or perforations on the tube, the leakage inductance can be calculated as the hole inductance for braided shields.

For a wound foil shield, the solid shield approach would apply if the shield layers would touch each other perfectly. In practice, foil shields are made with non-noble materials, like aluminium or tin coated copper, that will oxidise from the surface. Thus, no good contact exists between the overlapping foil portions. The transfer inductance of a spiral-type foil winding structure can be modelled [6] as discussed in the helical inductance Section A.1, with an assumption of no overlap or gap between the turns. However, modern foil shields are commonly wound with certain overlap. No literature gives a state-of-the-art in modelling for that kind of a foil. That is contrary to braids, which have been studied in quite detail.

One of the latest overviews and comparisons of different braid models is done by Verpoorte et al. [40]. They recommend using a tripartite model

$$L_T = L_h + L_b + L_s, \quad (1.25)$$

where L_h is the hole inductance, L_b is the braid inductance, and L_s is the skin inductance. This is the basic model used in this thesis with each of the components discussed separately in Appendix A. For the inductance analysis, it is assumed that the permeability of all shield materials is that of a vacuum μ_0 for simplification of the equations.

Much of the transfer inductance determination for braided shields is based on analysing a single braid crossing as in Figure 1.5. Thus, some of its geometrical parameters together with equations for deriving them from the basic braid parameters shown in Figure 1.3 are given here for convenience.

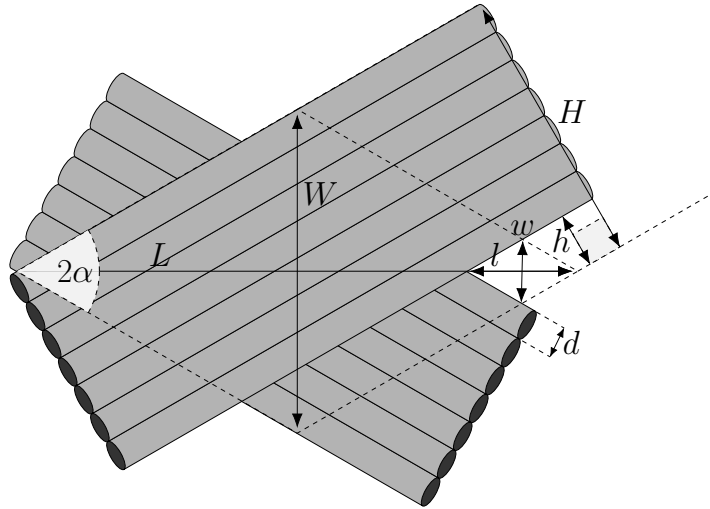


Figure 1.5 – One braid crossing and its dimensions

The braid crossing is defined by a rhombus of height H , length L , width W , an opening angle of 2α , and an area A . It has one rhomboidal hole of height h , length l , width w , and an area a . The hole has same opening angle of 2α as the larger rhombus. The equations

for the dimensions as a function of the basic braid parameters are:

$$W = \frac{2\pi D}{c} \quad (1.26a)$$

$$L = \frac{2\pi D}{c \tan \alpha} \quad (1.26b)$$

$$H = \frac{2\pi D \cos \alpha}{c} \quad (1.26c)$$

$$A = \frac{WL}{2} = \frac{2\pi^2 D^2}{c^2 \tan \alpha} \quad (1.26d)$$

$$h = H - Nd = \frac{2\pi D \cos \alpha - cNd}{c} \quad (1.26e)$$

$$w = \frac{h}{\cos \alpha} = \frac{2\pi D \cos \alpha - cNd}{c \cos \alpha} \quad (1.26f)$$

$$l = \frac{h}{\sin \alpha} = \frac{2\pi D \cos \alpha - cNd}{c \sin \alpha} \quad (1.26g)$$

$$a = \frac{wl}{2} = \frac{(2\pi D \cos \alpha - cNd)}{c^2 \sin 2\alpha}. \quad (1.26h)$$

If the rhomboidal shape of the braid crossings with a hole is to be preserved, the braiding angle is limited depending on the other braiding parameters. An example in Figure 1.6 shows a case, where the braiding angle can be 48° at maximum. After that angle, the hole dimensions become negative meaning over-braiding of the cable. Over-braiding is excluded from the scope of this thesis.

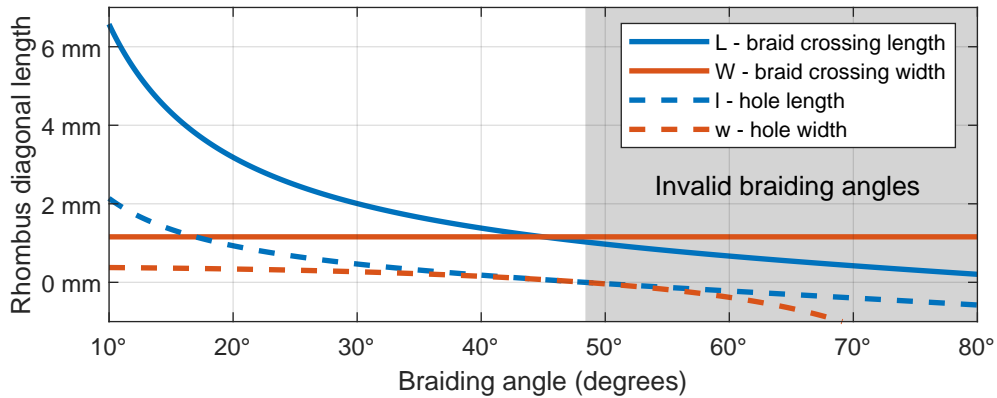


Figure 1.6 – Rhombus dimensions as a function of braiding angle with $D = 2.95$ mm, $d = 110$ μ m, $N = 7$, $c = 16$

The theoretical definitions of transfer inductance parameters in Appendix A contain still some modelling uncertainties. That is why they have been modified to fit better to experimental data as will be shown in the following section. It will become evident that the experimental model is more practical to use until the theoretical treatment of the modelling uncertainties is improved.

Experimental model

As can be observed from explanation in the previous section, the nature of a braided shield is complex, and there are still some insufficiencies in the theoretical models. To compensate for them, Kley developed an experimental model based on a large set of measured braids to compensate for features that are difficult to analyse theoretically [33]. In this section, his experimental model is briefly discussed.

The model can be divided into three parts:

$$Z_T = R_T + j\omega L_T + (1 + j)\omega L_S \quad (1.27)$$

transfer resistance R_T , transfer inductance $L_T = L_h + L_b$ as a sum of hole and braid inductances, and skin inductance L_S , where the last comprises of a real and imaginary part to describe the additional complex skin-effect phenomena not taken into account in transfer resistance calculations. The transfer resistance per metre is

$$r_T = \frac{4}{\sigma\pi c N d^2 \cos(\alpha)} \frac{d'\gamma}{\sinh(d'\gamma)}, \quad (1.28)$$

which is equal to Equation 1.18, when the braid wire diameter correction in Equation 1.19 is used. The transfer inductance per meter is

$$l_T = \frac{\mu_0}{c} \left[0.875 \frac{\pi}{6} (2 - \cos \alpha) (1 - G)^3 e^{-\tau_H} - \frac{0.11}{N} \cos(2k_1\alpha) \right], \quad (1.29)$$

where coefficient

$$k_1 = \frac{\pi}{4} \left[\frac{2}{3} G_0 + \frac{\pi}{4} \right]^{-1} \quad (1.30)$$

and attenuation constant

$$\tau_H = 9.6G \sqrt[3]{\frac{B^2 d}{D_m}} \quad (1.31)$$

with average diameter of the braid $D_m = D_0 + 2.5d$ being a function of the dielectric

diameter D_0 . It can be divided into hole inductance

$$l_h = \frac{0.875\mu_0\pi}{6c} (2 - \cos \alpha) (1 - G)^3 e^{-\tau_H}, \quad (1.32)$$

and braid inductance

$$l_b = -\frac{0.11\mu_0}{cN} \cos(2k_1\alpha), \quad (1.33)$$

equivalently to the theoretical derivation in Appendix A. Finally, skin inductance per metre is

$$\omega l_S = \frac{1}{\pi\sigma\delta} \frac{1}{D_m} \left[10\pi G_0^2 \cos(\alpha)(1 - G)e^{-\tau_E} - \frac{3.3}{2\pi G_0} \cos(2k_2\alpha) \right]. \quad (1.34)$$

The three inductance parameters derived for an example case with theoretical and Kley's experimental equations are shown in Figure 1.7. While hole inductance values are close to each other, the braid inductances are vastly different. For the example case, the skin inductance, which has a loss-component, and whose best theoretical definition is based on Kley's experiments, defines the transfer impedance at lower inductive frequency range. For Kley's model, it is superseded by braid inductance above 10 MHz. This is contrary to the theoretical model, where skin inductance dominates up to 1 GHz, and is only then superseded by hole inductance. In conclusion, the state-of-the-art cable models cannot be yet explained completely by physical phenomena. As it will be shown in Section 1.3.2 when comparing different measurement results to models, Kley's model based on experimental data is still the best available model to date for braid modelling.

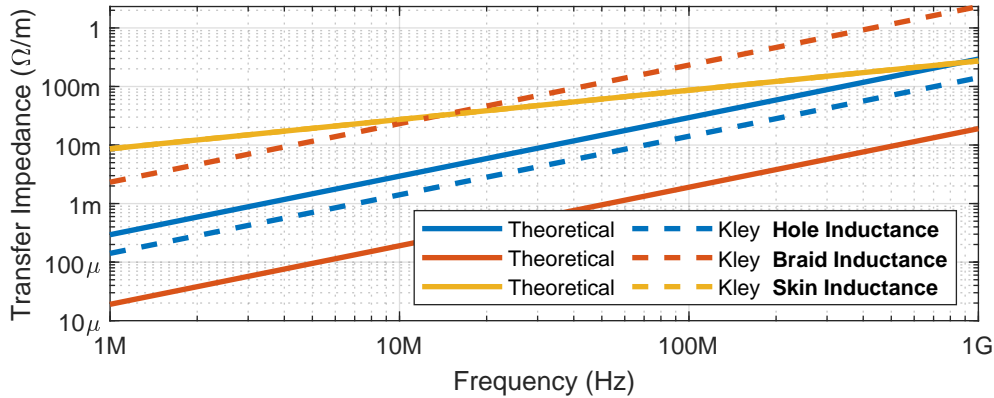


Figure 1.7 – Contribution of theoretical and Kley inductances on transfer impedance for $D = 2.95$ mm, $d = 110$ μ m, $N = 7$, $c = 16$, $\alpha = 35$

As a part of his work to arrive at a more practical model for single braided shields,

Kley also developed further the test methods to experimentally determine the transfer impedance [8]. His contributions were mostly on the triaxial cell, which is discussed in the next section, and also developed further in this thesis.

1.2 Test Methods at Ambient Laboratory Conditions

There is a large variety of different test methods available for shielding effectiveness and transfer impedance determination of shielded cables and shielded cable assemblies. An effort to list most of them has been done earlier [42], where authors mention the complexity of current standardization environment and question the need for all the method variations. Thus, no further effort is made in the frame of this thesis to map the complete test space. Only three most used methods relevant for the shielded cable samples measured in the frame of this thesis are briefly reviewed, and one of them is analysed more deeply. The latter is evidently the triaxial method that will be further developed to withstand environmental stresses in Section 1.3.

Shielding effectiveness can be determined with any method capable of illuminating the cable or cable assembly with a controlled electromagnetic field. The challenge is that most of these methods provide either a partial illumination, like methods involving an anechoic or a semi-anechoic chamber, or they provide too homogeneous illumination representing a plane wave from a single direction like the triaxial or a TEM cell. Thus, shielding effectiveness characterisation is shifting towards reverberation chambers that provide statistically equal illumination from any direction, and thus, effectively represent plane waves arriving from all directions [43].

Determining the transfer impedance of a shielded cable needs a well-defined illumination as the transfer impedance is calculated based on the induced voltage in the inner conductor and the shield current as shown earlier in Equation 1.1. The voltage and current are interchangeable, so that same value of transfer impedance is observed if shield voltage and the current in the inner conductor are used instead.

Classical ways to measure transfer impedance of shielded cables are line-injection [44] and triaxial [8] methods. The former is based on building an impedance matched transmission line with the cable shield acting as a return path. The latter is described in section 1.2.1. There are other methods, and variations of the presented methods, like quadraxial cell [28], direct current injection [45] and ground plate method [46], but they are either too labour-some to use, like the quadraxial cell method, or are more directed

towards shielded connector measurements [42], like the latter two. Thus, they will not be discussed further in this thesis.

After a proper measurement method has been selected, uncertainty in the measurement results needs to be analysed. Section 1.2.2 discusses typical measurement errors due to the unideal construction of the triaxial cell as well as due to the connecting cables and the measurement instrument, which is a vector network analyser (VNA) in this case.

1.2.1 Triaxial Cell

The triaxial cell structure for measurement of transfer impedance has existed for considerably long [47], and it is standardized by the IEC [48]. A schematic of the cell is shown in Figure 1.8. A cable-under-test (CUT) of length L_C with a shield diameter a , characteristic impedance of $Z_{0,in}$, and a propagation constant of $\beta_{in} = 2\pi/\lambda_{in}$ is tested in a triaxial cell that has a diameter of b . As the cable is installed in the triaxial cell, its shield together with the outer walls of the triaxial cell forms a transmission line with a characteristic impedance of $Z_{0,out}$ and a propagation constant β_{out} that depend slightly on the cable jacket permittivity. The cable is terminated with an impedance R_1 that is shielded inside an adapter connecting the CUT to the centre-pin of the P2-connector. This part is commonly designed in such a way that its characteristic impedance $Z_{0,out,adapter}$ is $50\ \Omega$ that is matched with a common measurement system impedance $Z_0 = 50\ \Omega$ forming the outer circuit of the test system. The RF-source voltage V_{source} can be connected to either of the ports, but it is here connected to P1, which forms the inner circuit together with the CUT.

The transfer impedance of the CUT in the cell is measured with the help of a signal generator and a spectrum analyser, or with a VNA. The former usually results in a better dynamic range for the measurement, whereas the latter is more straightforward to setup as only one instrument is needed. In both cases, the target of the measurement is to characterize the transmission S-parameter between ports 1 and 2 (see Figure 1.8) as a function of the incident voltage wave V_1^+ and the observed voltage wave V_2^- , when port 2 is matched

$$S_{21} = \left. \frac{V_2^-}{V_1^+} \right|_{V_2^+=0}. \quad (1.35)$$

To determine the transfer impedance from the ratio of the measured amplitudes, the voltage at the inner circuit needs to be first written as a function of the incident and

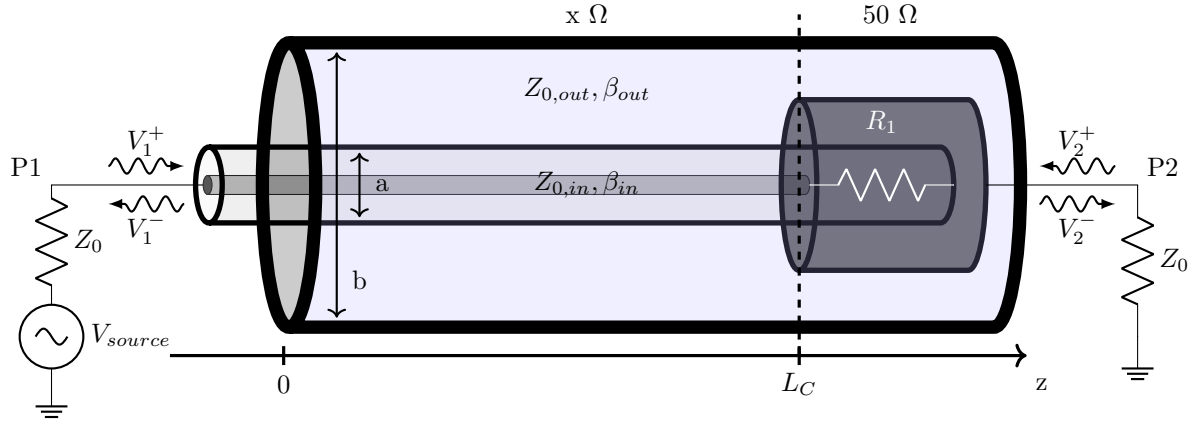


Figure 1.8 – Schematic of a Triaxial Cell

reflected waves [41]

$$V_1(z) = V_1^+ e^{-j\beta_{in}z} + V_1^- e^{j\beta_{in}z}. \quad (1.36)$$

Then, the current in the inner circuit can be defined as

$$I_1(z) = \frac{1}{Z_{0,in}} (V_1^+ e^{-j\beta_{in}z} - V_1^- e^{j\beta_{in}z}). \quad (1.37)$$

For electrically short samples

When the propagation effects do not need to be taken into account, the exponents $j\beta z \Rightarrow 0$ and Equation 1.36 is reduced to a simple location independent voltage

$$V_1 = V_1^+ + V_1^-. \quad (1.38)$$

Then, the Figure 1.8 schematic can be reduced to one shown in Figure 1.9, and the transfer impedance can be written as

$$Z_T = \frac{V_2^-}{I_1}. \quad (1.39)$$

Solving for the current I_1 based on the simplified Equation 1.37 results

$$I_1 = \frac{V_1^+ - V_1^-}{Z_0} = \frac{V_1^+ - \Gamma V_1^+}{Z_0} = \frac{2V_1^+}{R_1 + Z_0}, \quad (1.40)$$

where Z_0 is now the Port 1 impedance and

$$\Gamma = \frac{R_1 - Z_0}{R_1 + Z_0} \quad (1.41)$$

is the reflection coefficient [41] at the load resistor R_1 . Now, the transfer impedance becomes

$$Z_T = \frac{(R_1 + Z_0) V_2^-}{2V_1^+} = \frac{R_1 + Z_0}{2} S_{21} \quad (1.42)$$

and normalized to unit-length

$$z_T = \frac{R_1 + Z_0}{2L_C} S_{21}, \quad (1.43)$$

where L_C is the length of the cable-under-test.

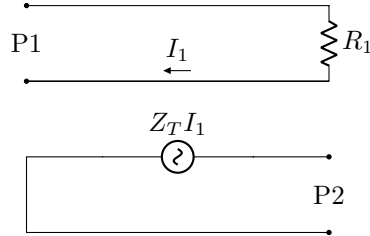


Figure 1.9 – Simplified Schematic of a Triaxial Cell

Two of the most typical test configurations modify the Equation 1.43 by only setting different values for R_1 . To maximize the dynamic range, the shield current I_1 needs to be maximized by setting $R_1 = 0$. To maximize the validity range of Equation 1.43, any reflections arising in the test setup need to be attenuated as well as possible. Then, setting $R_1 = \{Z_0, Z_{0,in}\}$ matches it either with the test system impedance or the characteristic impedance of the CUT.

1.2.2 Transfer Impedance Measurement Uncertainty with Triaxial Cell

There are four major contributions on the uncertainty of the transfer impedance measurement with a triaxial cell:

1. Non-ideal construction of the triaxial cell
2. Cable placement in the triaxial cell and other issues from sample preparation

3. Dynamic range of the VNA/spectrum analyser and other measurement errors from them
4. Performance of the test cables placed in between the VNA and the triaxial cell.

The systematic error from non-ideal construction of the triaxial cell is a result of the cable couplings at the ends of the cells that introduce both additional contact resistances and impedance discontinuities. The former having an effect on the low-frequency measurement result, and the latter on the high frequency measurement result as the wave reflection is not happening only at the short-circuited end of the cell. Cable placement in the triaxial cell causes a random error as the cable will not be exactly centred and its location will slightly change between consecutive setups. The same applies to other random errors done during sample preparation. Finally, performance of the external measurement equipment together with the connecting cables is usually the most significant parameter affecting the accuracy of the measurement, if low values of transfer impedance are measured. Here, a combination signal generator – spectrum analyser gives the best dynamic range, but in terms of measurement speed and configuration agility, a VNA is usually preferred. The effect of the test cables will be discussed in Section 1.3.2.

The best way to analyse error caused by non-ideal construction of the triaxial cell would be to perform 3D FEM simulation on the entire designed triaxial cell structure, and compare the achieved S-parameter results to the ones of an ideal design. However, this approach needs high-performance computing resources that were not available during this thesis, and thus, a simpler approach on comparing some key design parameters and measurement results will be done in Section 1.3.2. As a conclusion from there, the newly designed cell can be considered as an ideal triaxial cell up to 1 GHz.

To evaluate the effect of the cable sample preparation and placement, a small test with three different samples of the same cable was performed. The results in Figure 1.10 show a larger sample-to-sample uncertainty for transfer inductance determination than for transfer resistance. The 3σ -uncertainties covering 99.7% of future measurements are given in Table 1.4. Excellent repeatability is seen for transfer resistance, while decent repeatability is achieved for transfer inductance. If the triaxial cell needs to be used when it is electrically long, the transfer inductance needs to be extracted from an anti-resonance point, and uncertainty in its value is slightly higher. In this test, the variation of the measurement result could be either from variation of the measured parameters between the cable samples, or due to the sample preparation and installation. A further effort to separate these sources of measurement uncertainty was not performed.

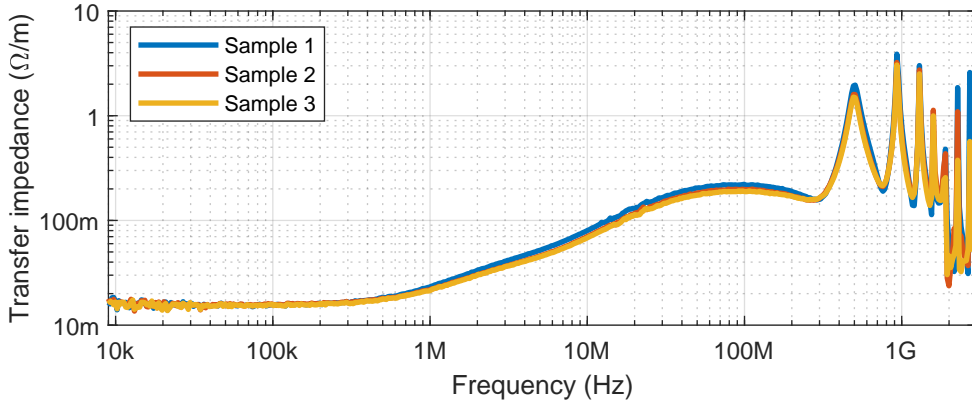


Figure 1.10 – Sample-to-sample measurement uncertainty

Table 1.4 – Sample-to-sample measurement uncertainties

Characteristic	Uncertainty (3σ)
Transfer resistance	3%
Transfer inductance	30%
Transfer inductance from an anti-resonance point	40%

Uncertainty caused by the VNA is studied for a Rohde & Schwarz ZNL6, which was used during all the environmental tests. The results in Figure 1.11 are reported for both transfer impedance and measured transmission coefficient S_{21} that are linked by Equation 1.43. They show that for a typical cable sample, like the braided cable (results of Figure 1.24), the VNA measurement uncertainty does not limit result accuracy. On the other hand, for samples with very low transfer impedance, like the copper-pipe reference (results of Figure 1.22), the measurement uncertainty due to VNA alone is significant passing 10%, 30%, and 100% uncertainty limits at many frequencies. In fact, it is so significant that the instrument datasheet [49] did not specify uncertainty down to those levels, but they needed to be estimated from the data sheet values.

The upper plot in Figure 1.12 shows the transmission coefficient uncertainty information extracted from the VNA data sheet. In addition, it shows a curve fitting made with that data, and the three uncertainty levels used in Figure 1.11. Only the first 10% uncertainty level can be directly deduced from the data sheet values, whereas for the other two, extrapolation of the data sheet values needs to be used. Extrapolation is done by

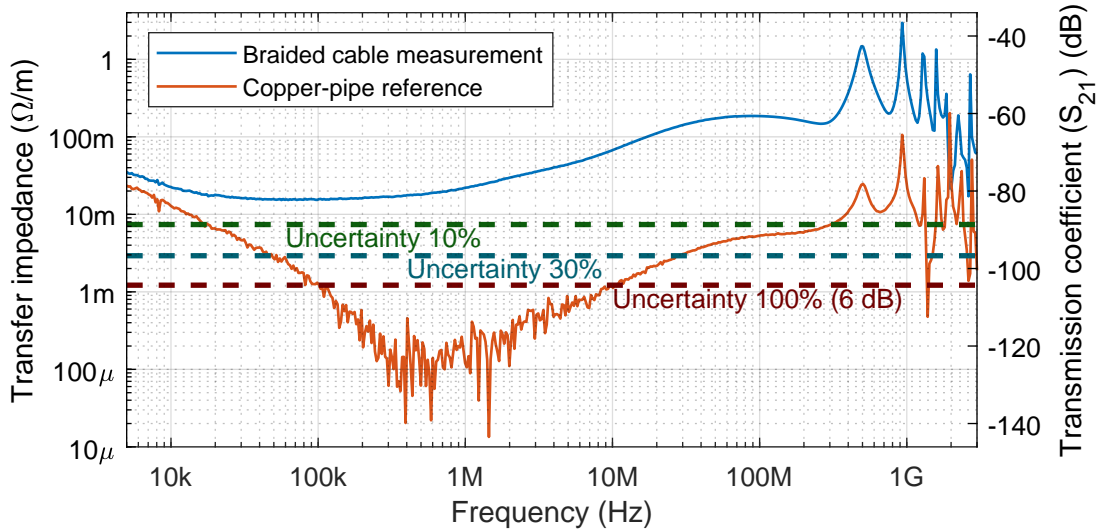


Figure 1.11 – Measurement uncertainty of transfer impedance with an R&S ZNL6 VNA

fitting a two-term exponential curve to the data sheet values. It is of a form

$$f(x) = ae^{bx} + ce^{dx}, \quad (1.44)$$

where coefficients $a = 7.528 \cdot 10^{-6}$, $b = -0.1303$, $c = 0.07748$, and $d = 0.002908$ have been determined by non-linear least squares method. The lower plot of Figure 1.12 shows the transfer impedance measurement error derived by Equation 1.43 from the transmission coefficient measurement. The three uncertainty levels used in Figure 1.11 are again highlighted.

In general, the measurement uncertainty can be deemed to be manageable. While it is not a significant issue for typical shielded cables, and expresses typical variations of an installation in the case of sample-to-sample variations, shields with excellent performance, like copper-pipe reference sample, slide to unmeasurable range at low frequencies. It is seen that the 100% (6 dB) uncertainty range with VNA measurement offers a practicable limit for the measurements. Below it, noise floor of the equipment makes the results unusable.

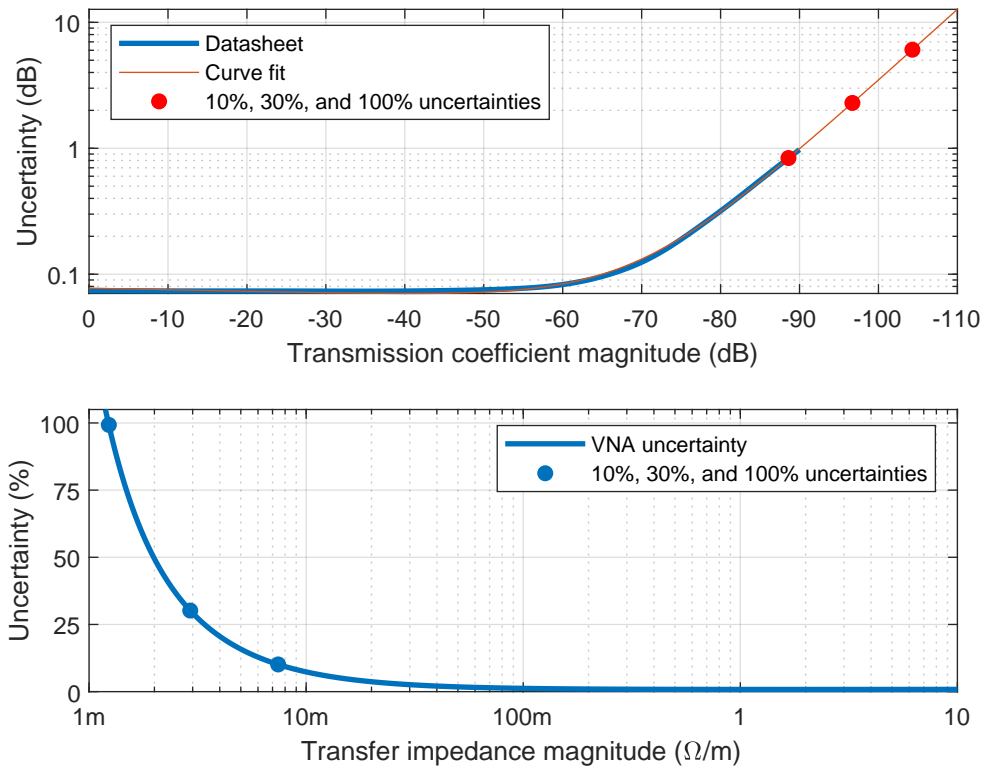


Figure 1.12 – Measurement uncertainty extracted from R&S ZNL6 VNA data sheet

1.3 Environmental Triaxial Cell

Test methods introduced in Section 1.2 have one common deficit: they are not very well suited for measurements that are not performed at ambient laboratory conditions. While reverberation chamber and line injection methods could be foreseen to include thermal stress during measurements, there is no easy way to apply dynamic mechanical stress, like vibration to the cable sample without affecting the reliability of the measurement result. For the triaxial setup these goals are easier to reach, and thus, this section discusses a modification of the triaxial cell method to enable testing during thermal and vibration stresses. Major part of the content in this section has been published in [7].

This discussion is divided into several subsections, so that first, an overview of the mechanical design of the new environmental triaxial cell is given in Section 1.3.1. Then, its radio frequency (RF) performance is compared to a commercial cell in Section 1.3.2, after which, the stability of the transfer impedance measurement is verified over a wide range of temperatures and random vibration levels in the same section. Finally, transfer

of thermal and vibration energies from the test chamber to the CUT are evaluated in Sections 1.3.3 and 1.3.4, respectively.

1.3.1 Design of the Triaxial Cell

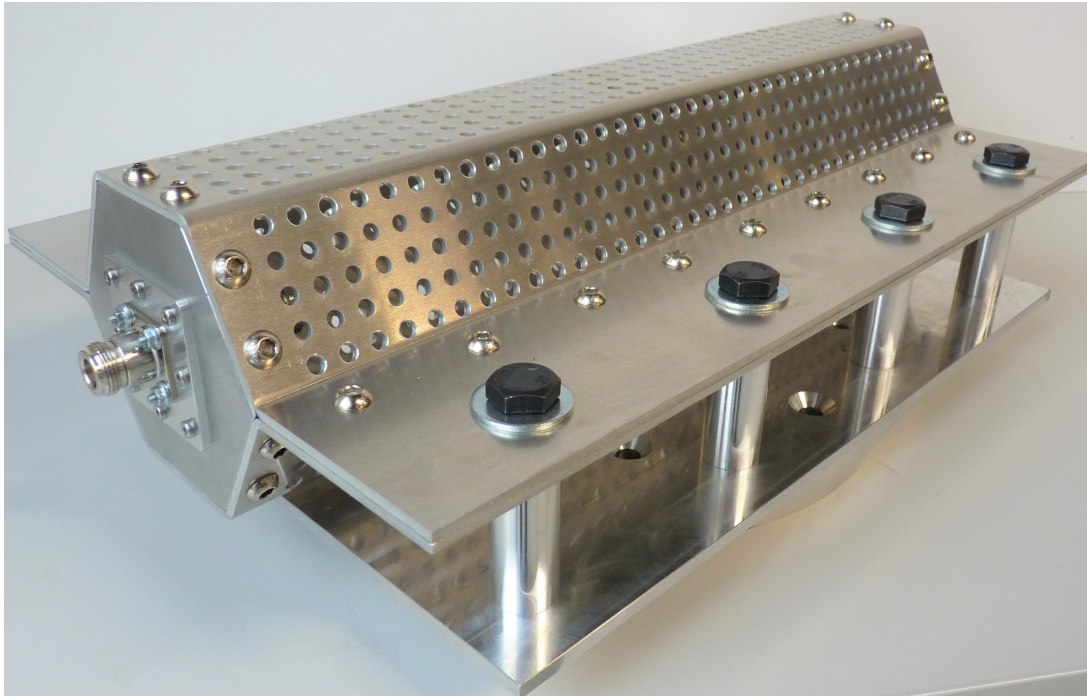
At the start of the cell design, several design objectives were gathered to ensure that the cell would fulfill its purpose. In the following, all of them are listed and discussed one-by-one to give reasoning on why they were selected, and on how the cell design takes them into account:

1. Robust structure to withstand thermal and vibration stress
2. Possibility to flow air through the cell to heat or cool the cable sample
3. Frequency range from 0 to 1 GHz
4. Cable sample easily changeable
5. Possibility to connect different test leads
6. Reasonable cost-of-manufacture

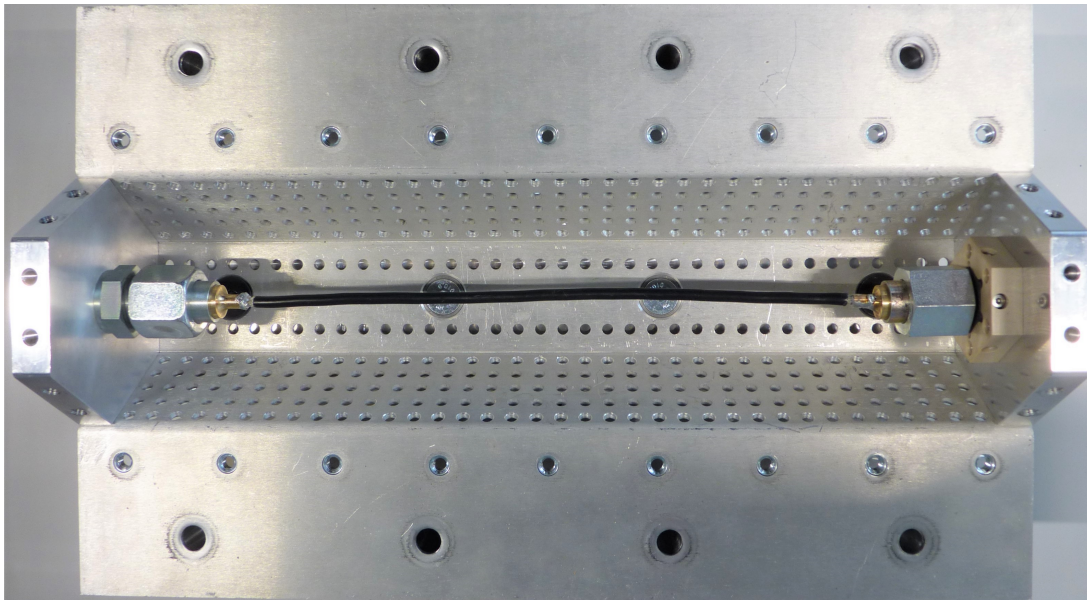
To respond to the objectives 1 and 2, while keeping in mind the cost constraint of objective 6, the shell of the triaxial cell was made from 3 mm thick aluminium with perforations of 5 mm in diameter placed in a 10-by-10 mm grid. The RF-performance analysis in Section 1.3.2 shows that this design fulfils the objective 3. Moreover, to enable objective 4, the cell shell was designed to be split into two. This was done by using nearly identical halves bolted together. To enable straightforward sheet-metal manufacturing process, cell cross-section was changed from round to hexagonal. This provided the benefit of straightforward mounting point locations at the sides and bottom of the shell. The sides were supported by aluminium posts, and the bottom was supported by an aluminium bar. The resulting overall design is shown in Figure 1.13. To further design for objectives 4 and 5, the termination design is discussed next.

Terminations have their own design objectives in addition to the global objectives defined above:

1. Low contact resistance from cable shield mounting to
 - (a) the shell of the triaxial cell for the short-circuited termination
 - (b) centre-pin of the N-connector for the floating termination
2. Robust mechanical support for the CUT



(a) Fully assembled



(b) Cover removed

Figure 1.13 – Overview of the complete environmental triaxial cell

Different termination methods were graded to help in the selection of the best one to fulfil the design objectives. The grading results in Table 1.5 are not the absolute truth as different termination technologies can have different realisations with changing strengths and weaknesses. However, it helped in selection of the ferrule technology as the best available termination method for the design in this thesis.

Table 1.5 – Comparison of the cable shield termination methods

Characteristic	Soldering	Connector	Pressure	Ferrule
Initial contact resistance	+ + +	- -	-	+ +
Contact resistance stability	+ + +	- - -	-	+ +
Mechanical robustness	+ +	+	+ +	+ + +
Ease of sample change	- - -	+ + +	+ +	+

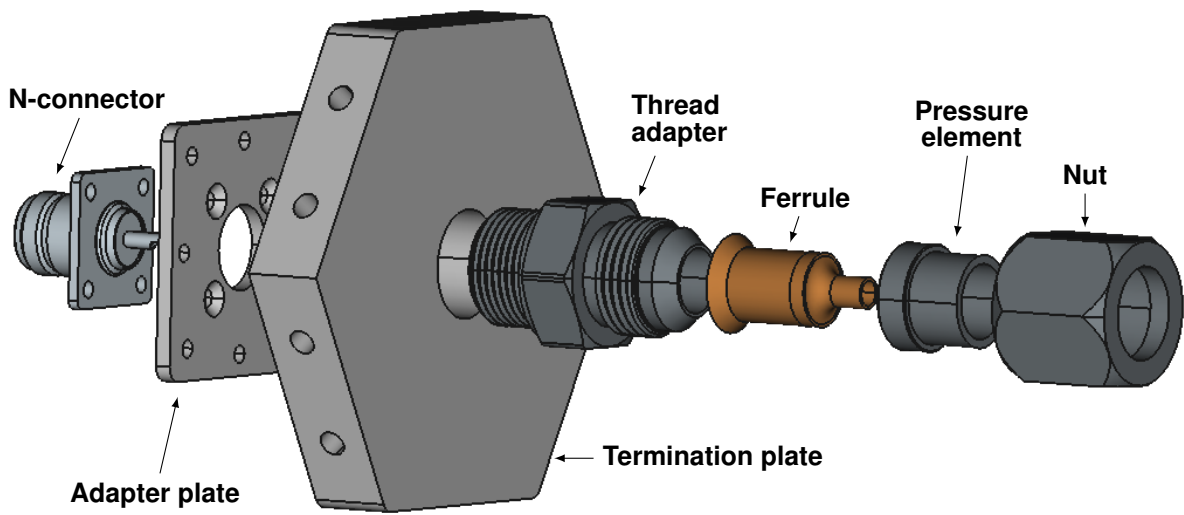
+ + + Excellent, + + Very Good, + Good, - Fair, - - Poor, - - - Bad

The practical termination design started with finding an adapter to connect the ferrule to the termination plate both mechanically and electrically. A hydraulic flare fitting was selected due to robust mounting hardware, availability of commercial-off-the-self (COTS) products, and a good contact cross-section for high electrical conductivity. A 37° JIC flare was used, but other available angles would work similarly.

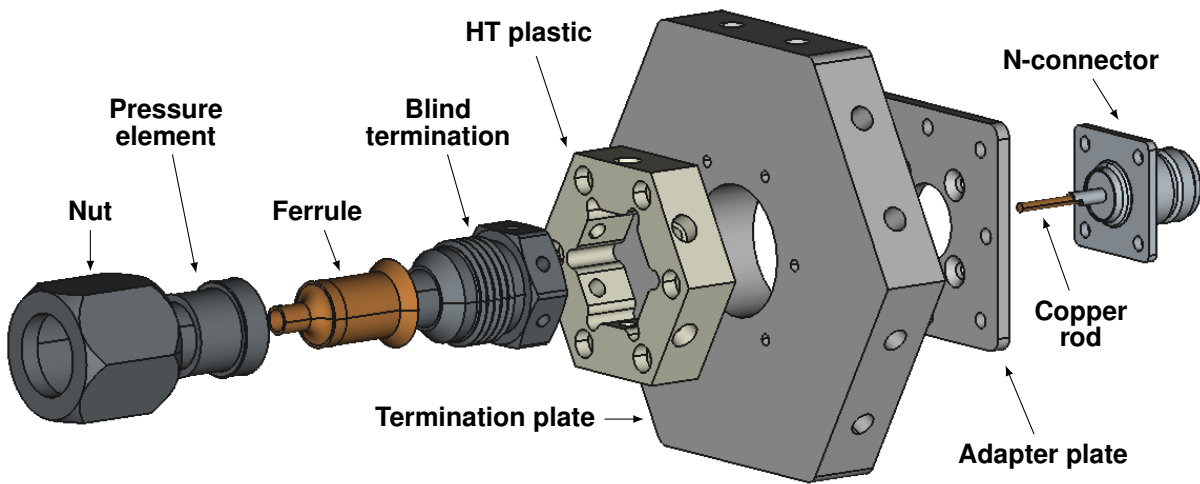
Now, the termination plates shown in Figure 1.14 needed to be relatively thick (15 mm) due to the thread adapter that was fastened to the threads on the termination plate as in Figure 1.14a. In addition, the cell shell was mounted at the termination plate edges necessitating sufficient thickness for reliable bolt holes.

The short-circuited termination was built from a threaded adapter screwed on the termination plate. The adapter had a JIC-flare at the other end as shown in Figure 1.14a. Ferrule was mounted to it with a pressure element and a nut. On the other side of the termination plate, an adapter plate was used to mount the N-connector to avoid interference with the centre thread of the termination plate.

A very similar design was used for the floating termination as in Figure 1.14b. Instead of a thread adapter, a blind termination was used, and supported by a piece of electrically insulating polyether ether ketone (PEEK) plastic, which is suitable for high-temperature (HT) use. The blind termination had circumferential holes drilled into it for mounting it to the HT plastic, and one axial hole to connect it electrically to the centre pin of the N-connector. There, a copper rod was brazed with silver-tin alloy for a robust contact. Then, a small portion of the copper rod between the blind termination and the N-connector



(a) Short-circuited termination



(b) Floating termination

Figure 1.14 – Exploded view drawings of the terminations

centre pin was replaced with a flexible copper braid to avoid stress-fracture of the copper rod. The combination of a blind termination, copper rod, adapter plate, and an N-connector was assembled outside the test system, and then dropped through the hole in the termination plate into its place. Using a flexible piece in the middle of the copper rod enabled this way of manufacturing without tight tolerance requirements on the length of the assembly.

Finally, the ferrules were crimped and soldered to the cable sample for optimum electrical contact and mechanical robustness as shown in Figure 1.15. For most of the cables, the dielectric does not withstand high crimping forces, and thus, crimping is more about bringing the shield and ferrule surfaces close together for optimum soldering process. Especially the low melting point dielectrics like polyethylene (PE) do not withstand soldering heat for long periods of time, and thus, the surfaces to be soldered should fit neatly together for rapid soldering. To aid that, the ferrule should be warmed up first with a high-power soldering iron, after which, the braided shield can be quickly warmed up while adding tin alloy to form a good solder joint. Following a successful design and assembly of the environmental triaxial cell, its performance needs to be verified as will be discussed in the next section.

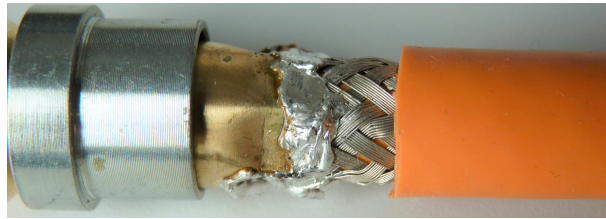


Figure 1.15 – A crimped and soldered ferrule on a cable sample

1.3.2 RF Performance of the Triaxial Cell

First, the performance of the triaxial cell design was evaluated by 3D finite-element method (FEM) simulation. There, the effect of the hexagonal cross-section was compared to a circular one, which is the most commonly used. The E- and H-field distributions at 1 GHz at port 2 without the termination assembly are shown in Figure 1.16. The comparison shows that the field distribution between the circular and hexagonal designs is very similar. When scaled with the free-space impedance $\eta = 377 \Omega$, the H-field results in Figure 1.16b match the E-field results in Figure 1.16a. This is due to the

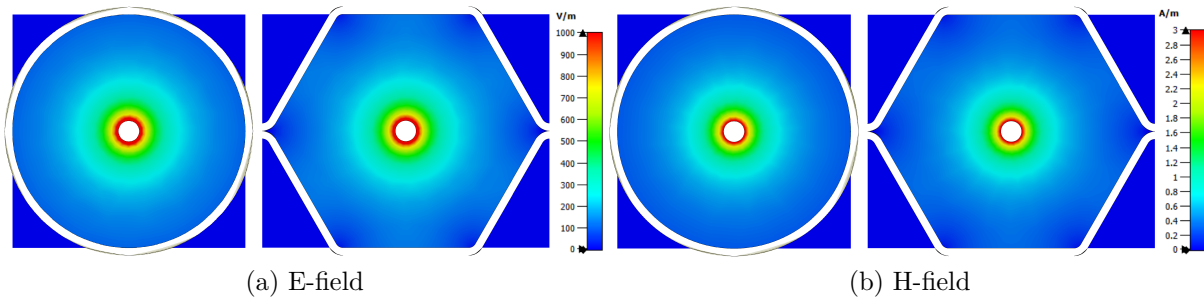


Figure 1.16 – Field magnitude on the cross-section of circular and hexagonal triaxial cells

infinite waveguide boundary condition of the simulation program. As will be explained in Appendix B, the real wave impedance varies along the triaxial cell as it is an RF resonator, not a waveguide.

To gain some assurance on the performance of the perforations with the hexagonal structure, a field distribution plots of E- and H-fields for various configurations are given in Figure 1.17 including a theoretical solution for the circular case calculated as shown in Appendix B. To achieve a dense representation of the field quantities, a local mesh is used to reduce the interpolation error around the evaluated axis. The location of the plot axis is selected in such a way that it intersects a hole in the perforation. That result can be compared to distributions of solid hexagonal and circular designs. As is shown in Figure 1.17, the field amplitudes are the same close to the cable sample, and show some differences close to the shell of the triaxial cell. The analytically calculated H-field distribution has an offset from the simulation results due to different boundary conditions that could not be equalized easily. As it was explained in Section 1.1.2, the transfer impedance measurement depends on the field strength applied close to the cable, and thus, all the methods shown in Figure 1.17 will give equal results.

At ambient laboratory conditions

At ambient laboratory conditions, the developed environmental triaxial cell in Figure 1.18a was compared to a round commercial cell [50] in Figure 1.18b. Two different comparisons were done:

1. Transfer impedance measurement performance using RG-58C/U as a CUT
2. Reflection measurement between the CUT shield and the cell wall (Port 2) using a copper tube as a CUT

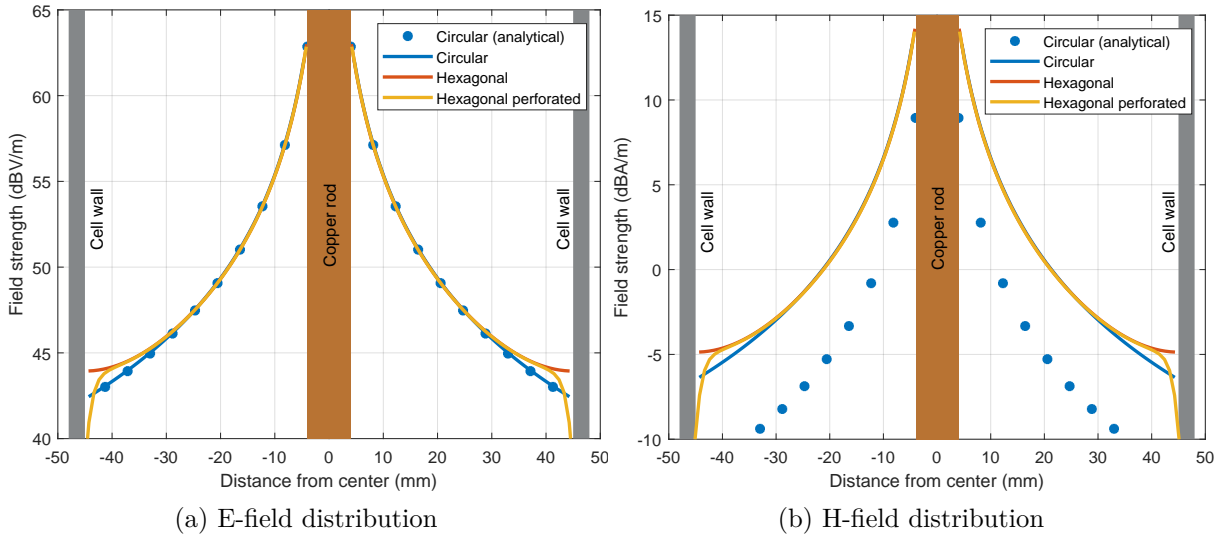


Figure 1.17 – Field distribution plots of different designs

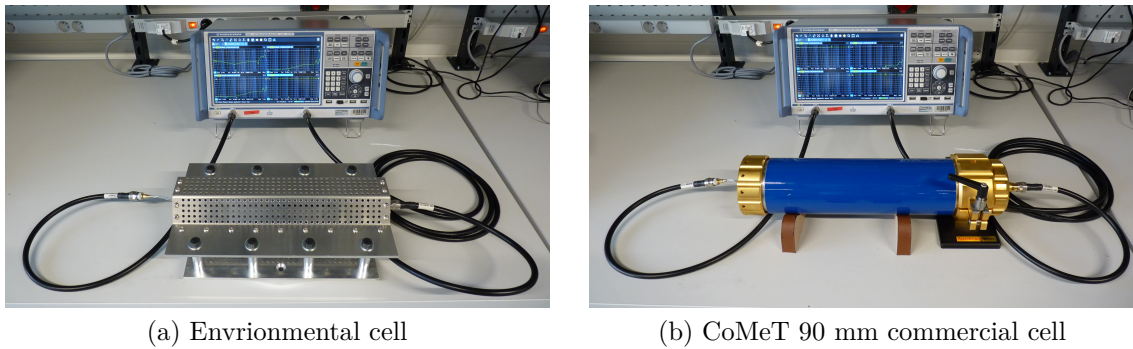


Figure 1.18 – Test setup overviews with the environmental and commercial triaxial cells

As it will be shown below, these comparisons confirm adequate performance of the new cell.

For transfer impedance, the comparison is given in Figure 1.19. Commercial cell gives a slightly higher transfer resistance as it connects to the cable shield with a pressure contact plates that provide optimal contact pressure only for very specific cable samples. For others, like the sample used, the cable diameter falls between two sizes of the pressure plates, and either the slightly loose contact is tolerated, or the cable diameter is increased by using copper tape or equivalent at the contact region. Either one of these approaches leads to slightly increased resistance measurement. For transfer inductance, both of the cells give a very similar measurement result. As the sample lengths are very close to each other: 30 cm in the commercial cell and 25 cm in the new cell, the resonance points of

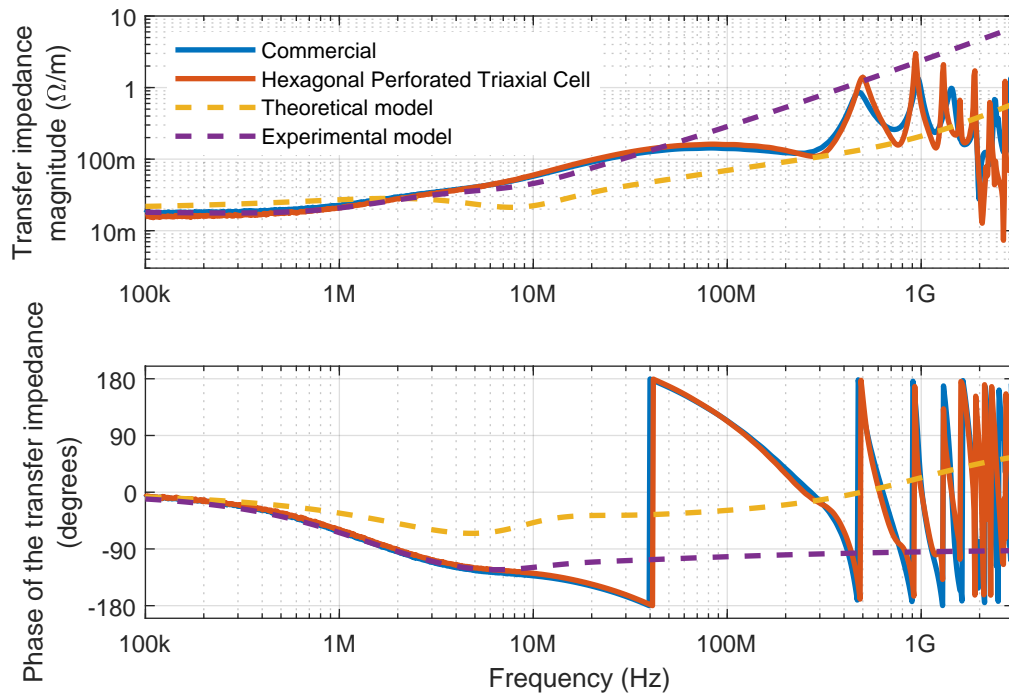


Figure 1.19 – Transfer impedance measurement comparison with an RG-58C/U cable

the measurement results are very similar.

Comparing the results to the two models from Section 1.1.2, it is seen that the experimentally derived model fits better to the results. The more theoretical approach seems to underestimate transfer inductance in this case. Moreover, the model confirms that the transfer impedance can be estimated from the anti-resonance peaks of the triaxial setup up to 1 GHz. For the new setup, the anti-resonance peaks seem to coincide slightly better with the model than for the commercial one.

Very similar results are seen for the phase of the transfer impedance. The experimentally derived model fits the results perfectly up to 10 MHz, above which the results start to deviate due to the electrical length of the triaxial cell becoming significant. Overall, this highlights a very successful division of the shield's inductance to hole, braid and skin portions as they all have a different effect on the phase of the transfer inductance. Here, major portion of the inductance is given by braid inductance. This can be observed from the negative phase shift similarly to magnitude. Phase of the theoretical model does not match the measurement that well.

For reflection measurement, the comparison is given in Figure 1.20. Magnitude wise,

the new cell gives better reflection coefficient up to 1 GHz. Above that, considerably large resonance points appear, where power is lost in the cell. Observing the phase of the reflection coefficient, it is seen that the reflection at the new cell does not happen completely at the end of the cell after 1 GHz. Instead, only part of the input power is reflected at the cell end, and a major part is either reflected earlier or radiated out of the cell. This is visible from the sudden phase-shift of the reflection coefficient. It still shows partial power reflecting from the cell end up to 2 GHz. The likely location for most of the reflected power is at the interface, where the blind termination begins. Another reason for the observed effect could be radiation from the perforation, but neither of the phenomena was studied more in detail in this thesis. Thus, the copper rod and the termination plate create a microwave resonator at those high frequencies. Overall, the new cell provides correct illumination of the cable up to 1 GHz.

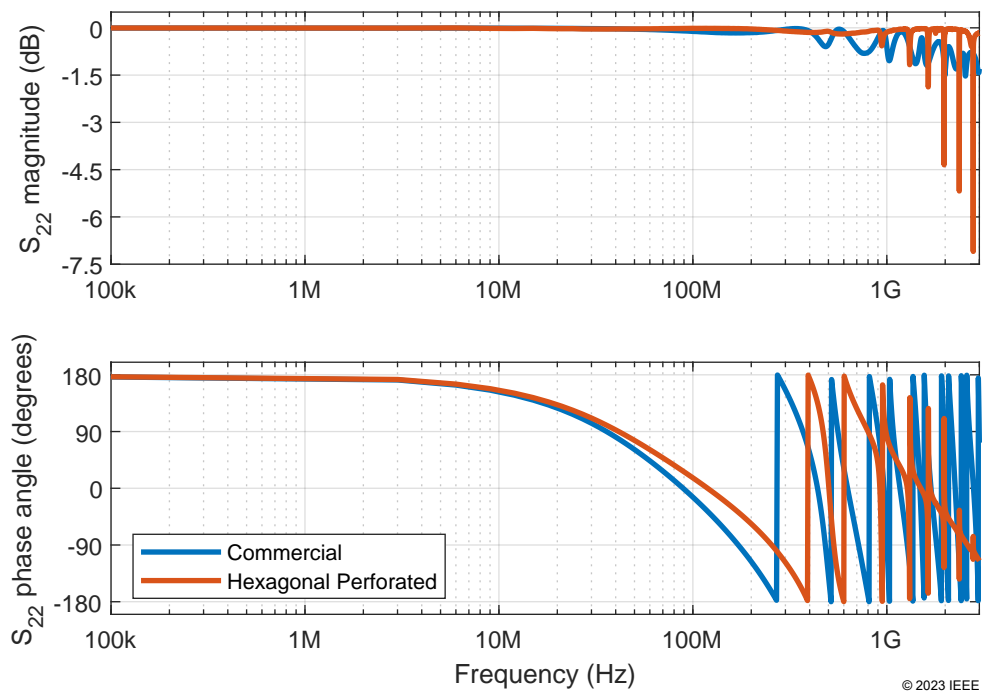


Figure 1.20 – Reflections at the outer circuit with a 8-mm copper pipe

During HALT stress

Performance of the new triaxial cell was evaluated also under highly accelerated life test conditions. These conditions are more thoroughly discussed in Section 1.4. This

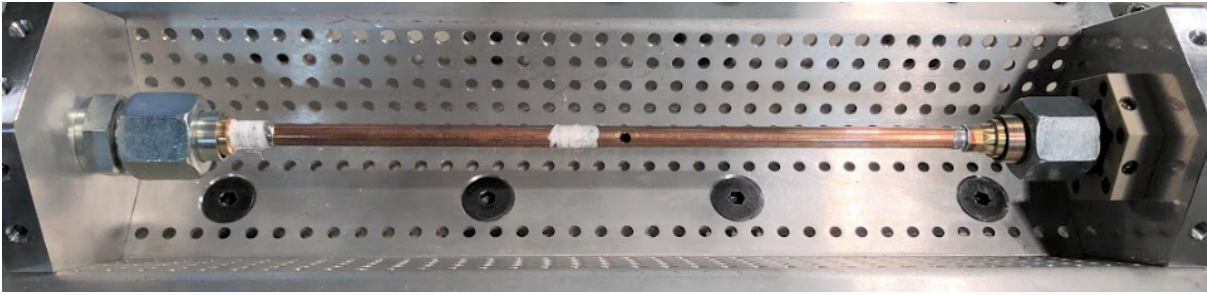


Figure 1.21 – A copper pipe CUT with a 4 mm hole drilled onto it in the environmental triaxial cell

evaluation allows to perform analysis on the stability of the measured transfer impedance results during the HALT tests. Most of the tests were done with a solid copper pipe as in Figure 1.21 that had one 4 mm hole drilled onto it to provide a stable transfer inductance to act as an appropriate reference.

Temperature step results from -50°C to 120°C with 10°C steps are in Figure 1.22. They were done with the above solid copper pipe that has one 4 mm hole drilled onto it. Now, two general differences are seen compared to the results at laboratory ambient, and to the transfer impedance model of a solid shield at ambient temperature as described in Section 1.1.2 taking into account the additional hole inductance:

1. Increased DC coupling due to longer test cables causes erroneous measurement results at low frequencies [8].
2. Between 100 kHz and 10 MHz the measurement results are close to the VNA noise floor, and affected by it as discussed in Section 1.2.2.

Excluding the above, it is seen that the transfer inductance measurement is not dependant on temperature between -50°C and 120°C . For transfer resistance, a similar evaluation cannot be done due to it being masked by the DC coupling phenomenon.

Temperature cycling results are in Figure 1.23. They were performed with the same sample as the temperature step results above with exactly the same results and conclusions. Thus, rapid temperature cycling between -50°C and 120°C does not have an effect on the measurement accuracy of the transfer inductance.

The vibration dependency results are in Figure 1.24. They were performed with a RG-58C/U cable sample as the reference. The reference sample was changed as it was observed that the centre conductor of the previously used copper pipe did not stay in place during vibration tests causing vibration dependent measurement results that were not due

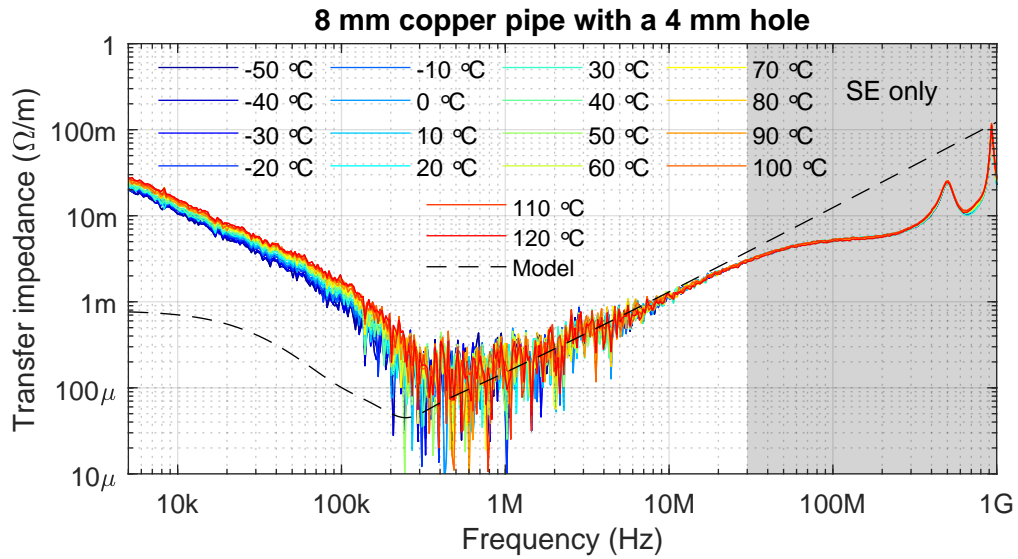


Figure 1.22 – Thermal response of the environmental triaxial cell with a copper pipe sample that has one 4 mm hole on it

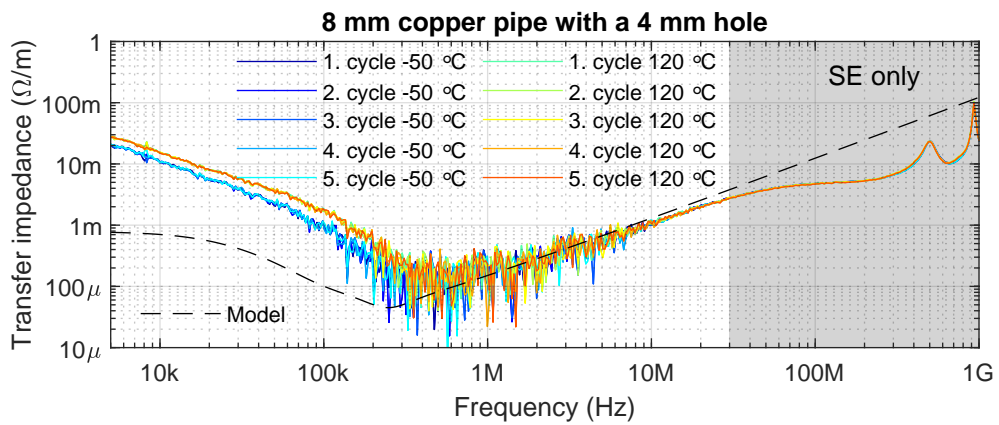


Figure 1.23 – Cyclic thermal response of the environmental triaxial cell with a copper pipe sample that has one 4 mm hole on it

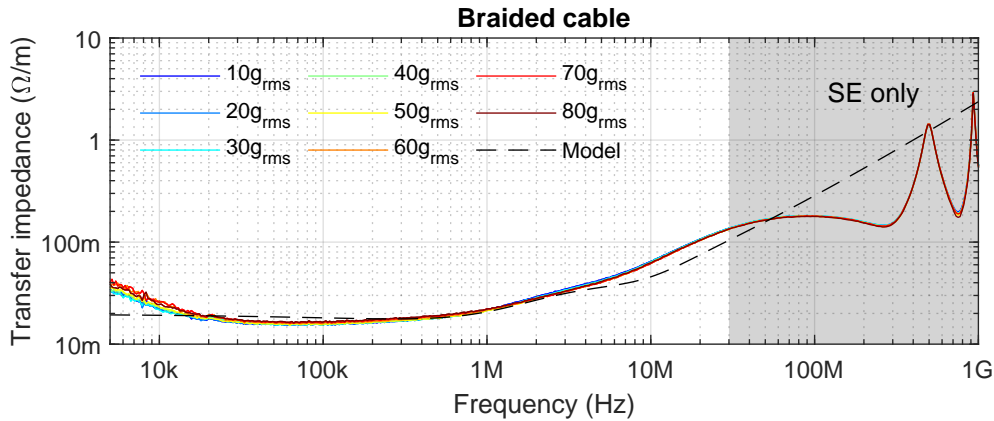


Figure 1.24 – Vibration response of the environmental triaxial cell with a braided cable sample

to the triaxial setup. The results of RG-58C/U cable show that neither the measurement of transfer resistance or transfer inductance is dependent on vibration amplitude. Due to higher transfer resistance than that of the copper pipe above, DC coupling disturbs the measurement results only up to 30 kHz.

The combined thermal cycling and vibration results are in Figure 1.25. As it will be seen in Section 1.4, the transfer impedance of RG-58C/U cable will depend on temperature, and it could not be used as a proper reference for combined thermal and vibration testing. The best available sample was the copper pipe used for the thermal tests above. It did not show perfect independence on vibration magnitude, but had similar dependency on it between pure vibration, as well as, combined vibration and thermal tests. It can be determined with reasonable certainty that the transfer inductance measurement result with the new triaxial cell is not susceptible to combined thermal cycling and vibration. The results show also a single result at 60g_{rms} and 120°C that has an indication of a loosened test cable. That is seen as an increased test cable resistance over the section of the results, where DC coupling dominates. The immense stress to the test setup during the combined test broke it several times due to either detached test cable from the N-connector, or due to the inner conductor soldering breaking either from the termination or at the N-connector centre-pin. After each failure, the setup was repaired and the tests were resumed at the position, where the failure was observed.

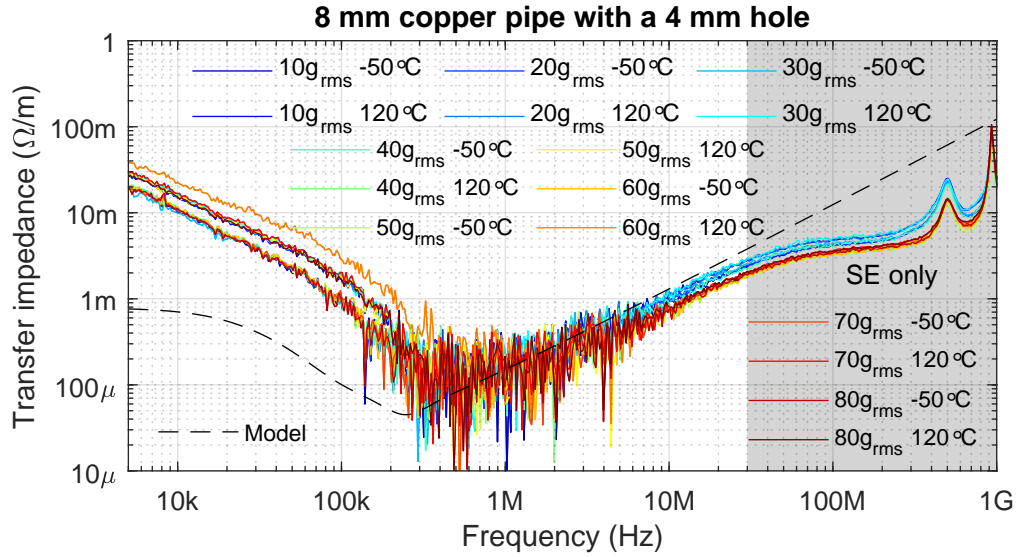


Figure 1.25 – Combined thermal cycling and vibration response of the environmental triaxial cell with a copper pipe sample that has one 4 mm hole on it

1.3.3 Transfer of Thermal Energy

Transfer of thermal energy to the cable sample was evaluated while the triaxial cell was mounted into a Hanse Environmental VTC-16 HALT test system. Three test cases were formed to see the differences in thermal response of the cable jacket and the ferrule at the short-circuited end:

1. No incoming air guidance as in Figure 1.26a
2. Some air guidance as in Figure 1.26b
3. Maximum practicable air guidance as in Figure 1.26c

Then, a test with an RG-58C/U cable was performed with these different configurations together with two thermocouples and a chamber temperature sensor attached as shown in Figure 1.27. In addition, the inlet air temperature from the top of the chamber was measured. Thermal responses to a single cycle are reported in Figure 1.28 with different cases corresponding to the configurations shown in Figure 1.26.

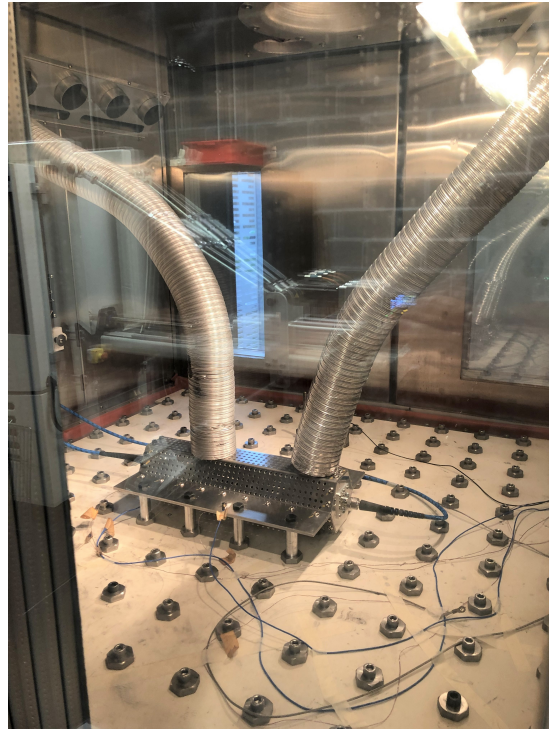
To have a better understanding of the thermal responses, a simple first-order low-pass filter

$$T_{filt}(i) = \alpha T_{inlet}(i) + (1 - \alpha) T_{filt}(i - 1), \quad (1.45)$$

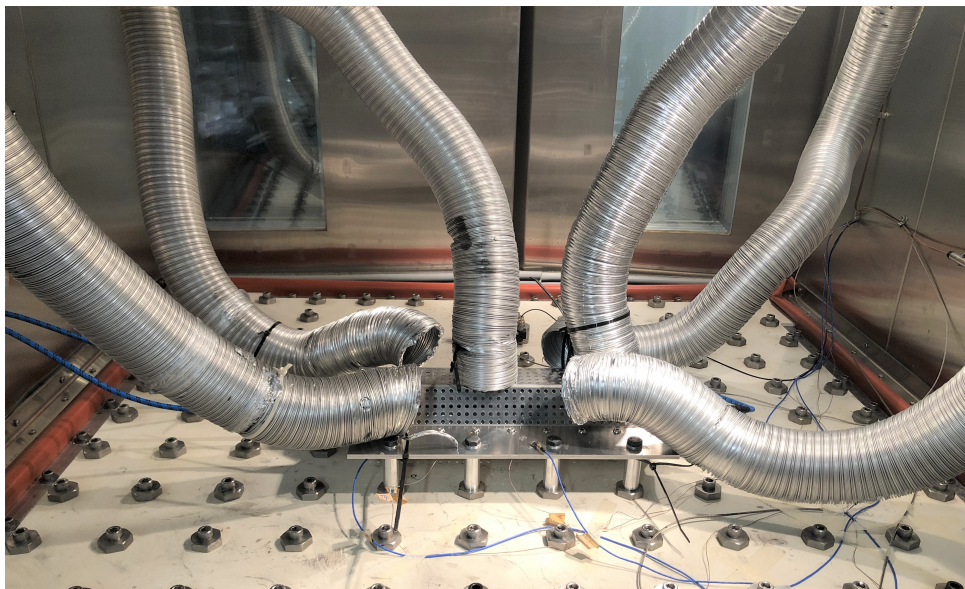
with the chamber air-inlet temperature T_{inlet} measured at the top of the chamber as the



(a) No air guidance



(b) Some air guidance with two pipes



(c) Maximum practicable air guidance with six pipes

Figure 1.26 – Different configurations for thermal energy transfer in the HALT chamber

input variable, was used to approximate the thermal response time constants

$$\tau = \frac{1 - \alpha}{\alpha} \Delta t, \quad (1.46)$$

where Δt is the time between the consecutive samples $i - 1$ and i . The approximations are shown in Figure 1.28 as dashed lines.

Time constants between the configurations were between 40 seconds and 3 minutes for the cable jacket, and from 2 minutes and 15 seconds to 3 minutes 50 seconds for the ferrule. Temperatures can be considered to be stabilized after five time constants have passed [51]. To retain an adequate testing time, the configuration with six pipes was selected for further tests, and a slight compromise was made so that the ferrule temperature will not be completely stabilized at the end of each test cycle.

As can be seen in Figure 1.28, chamber control on inlet-air temperature was adjusted for a large overshoot during rapid heating and minimal overshoot during rapid cooling. As the chamber adjustment is an involved process, and the test time was limited, it was decided not to try to adjust the set-points. It is to be noted that the inevitable thermal gradient of tens of degrees will cause some additional stress to the cable, which is actually beneficial in finding any weak spots during transient thermal stress.

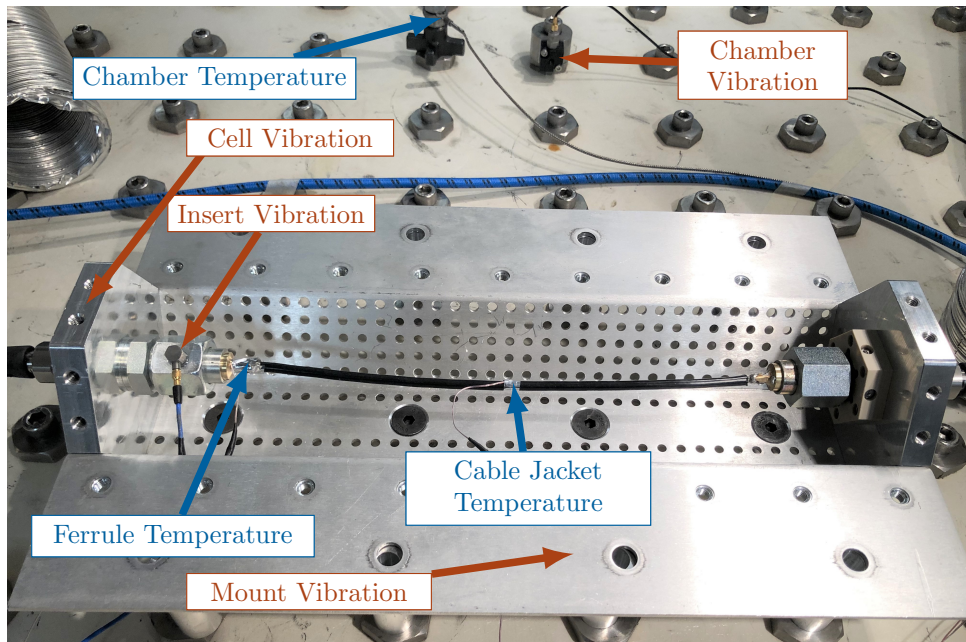


Figure 1.27 – Thermal and vibration sensor locations

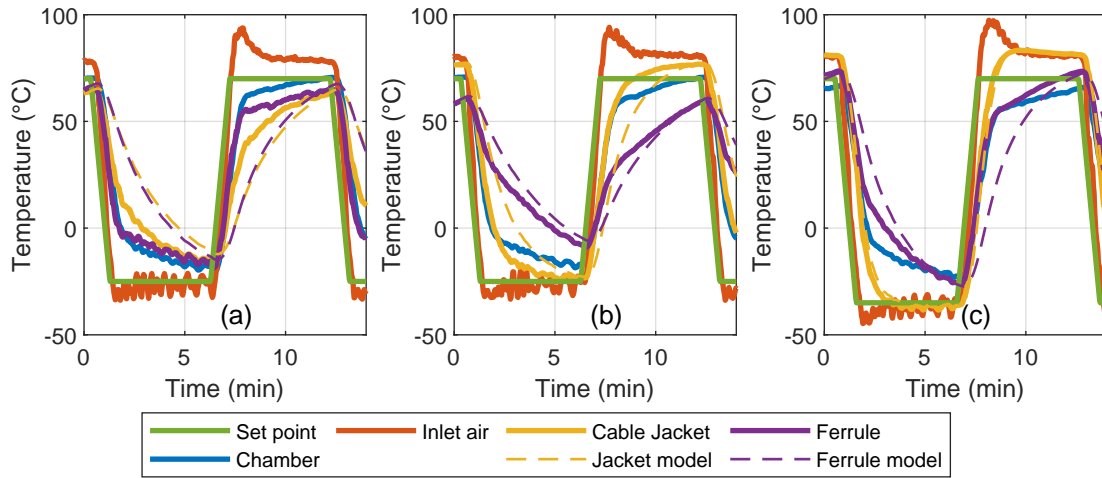


Figure 1.28 – Thermal responses of the configurations in Figure 1.26

1.3.4 Transfer of Vibration Energy

Vibration energy transfer analysis is done by comparing accelerations measured with piezoelectric acceleration sensors [52] at different sensor locations shown in Figure 1.27. HALT test systems commonly use non-coherent (random) vibration input that has very little extractable information except negative and positive maximum acceleration levels without doing further mathematical processing as can be seen from Figure 1.29. Calculating a mean of the signal, it is found to be very close to zero. After that, an RMS value will give more information on the effective amplitude of the acceleration stress, very similarly to electrical signals. However, for mechanical stress, the frequency of the acceleration is also important as different parts tend to be susceptible for stresses at different frequencies. Large, flexible parts tend to act as low-pass filters attenuating high frequency components that are above their self-resonance frequency (SRF), while being susceptible to stress inflicted at or close to SRF. In contrary, small, stiff parts just transmit low frequency vibration, but can be susceptible to vibration happening at higher frequencies. Thus, it is necessary to analyse different frequency components existing in the acceleration experienced by the test system and the cable-under-test.

Power spectral density (PSD) [53] is the main tool to analyse the frequency content of acceleration signals. It is a modification of Fourier Transform in such a way that random data taken with different sampling intervals can be compared against each other

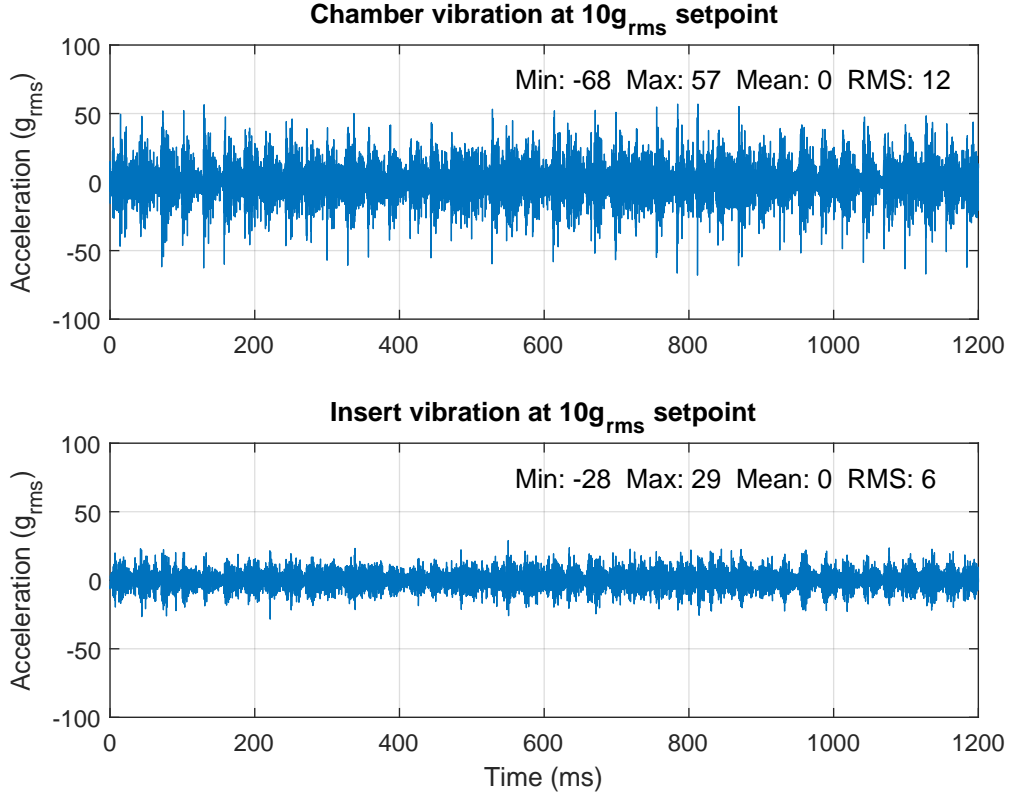


Figure 1.29 – Accelerations at $10g_{rms}$ setting for two sensor locations of Figure 1.26

effectively. For discrete-time signals, power spectral density is defined as

$$\text{PSD}(\omega) = \sum_{k=-\infty}^{\infty} r(k)e^{-j\omega k}, \quad (1.47)$$

which is a discrete time Fourier transform (DTFT) of $r(k)$, and where

$$r(k) = \text{E} \{y(t)y^*(t - k)\} \quad (1.48)$$

is the covariance function of the signal $y(t)$ sampled at multiples of unity. The expected value of the signal is

$$\text{E} \{y(t)\} = 0 \quad \forall t. \quad (1.49)$$

Star denotes a complex conjugate, and k is lag between two samples. The sampling interval of Equation 1.47 can be changed to arbitrary time interval T_s by time expansion

of DTFT

$$\text{PSD}(\bar{\omega}) = T_s \sum_{k=-\infty}^{\infty} r(k) e^{-j\bar{\omega}T_s k}, \quad (1.50)$$

where $\bar{\omega}$ is discretely sampled angular frequency spectrum instead of a continuous angular frequency spectrum ω . To deal with the infinite sum, limit theory is used to redefine Equation 1.50 as

$$\text{PSD}(\bar{\omega}) = \lim_{N \rightarrow \infty} E \left\{ \frac{T_s}{N} \left| \sum_{t=T_s}^N y(t) e^{-j\bar{\omega}t} \right|^2 \right\}, \quad (1.51)$$

when the number of samples N approaches infinity. The actual value of the signal's PSD will be obtained with infinite number of samples, which is not very practicable. As there are only N samples available, a best available approximation of the actual PSD [54] is achieved by:

$$\text{PSD}(\omega) \approx \frac{T_s}{N} \left| \sum_{t=T_s}^N y(t) e^{-j\omega t} \right|^2 \approx \frac{T_s}{N} \cdot \text{FFT}(y(t)), \quad (1.52)$$

which is called a periodogram. The fast Fourier Transform (FFT) is usually calculated as a single-sided spectrum, in which case, all the frequency components except the DC component and the Nyquist frequency need to be multiplied by two.

Applying Equation 1.52 to the time-domain results in Figure 1.29 together with same results at higher vibration setting level of $80g_{rms}$ results in the power spectral densities shown in Figure 1.30. It is seen that the amplitude of the table vibration is higher, and has a dominant frequency at over 2 kHz, whereas the insert vibration is lower in amplitude, and has the highest power around 800 Hz. The PSD frequency content difference between low and high amplitude is negligible, and can mostly be explained by the error caused by a limited sample size. Further power spectral densities are shown in Figure 1.31. There, the vibration power measured next to a cell mounting bolt dominates. It shows very high peaks at 1.5 kHz, 2 kHz, and 5 kHz. Also, the RMS-value is higher than either the setting or the table measurement almost doubling the setting value. However, it is clearly seen that this vibration energy at high frequencies is not transferred well to other parts of the triaxial cell. The measurement point at the cell top, close to the insert measurement shown in Figure 1.30, has comparable spectral content and amplitude with the insert measurement.

At the end of the tests, it was noted that the momentary acceleration results of the chamber vibration sensor were saturated at high vibration levels. This was troubleshot with the chamber manufacturer to be a result of a manufacturing configuration error.

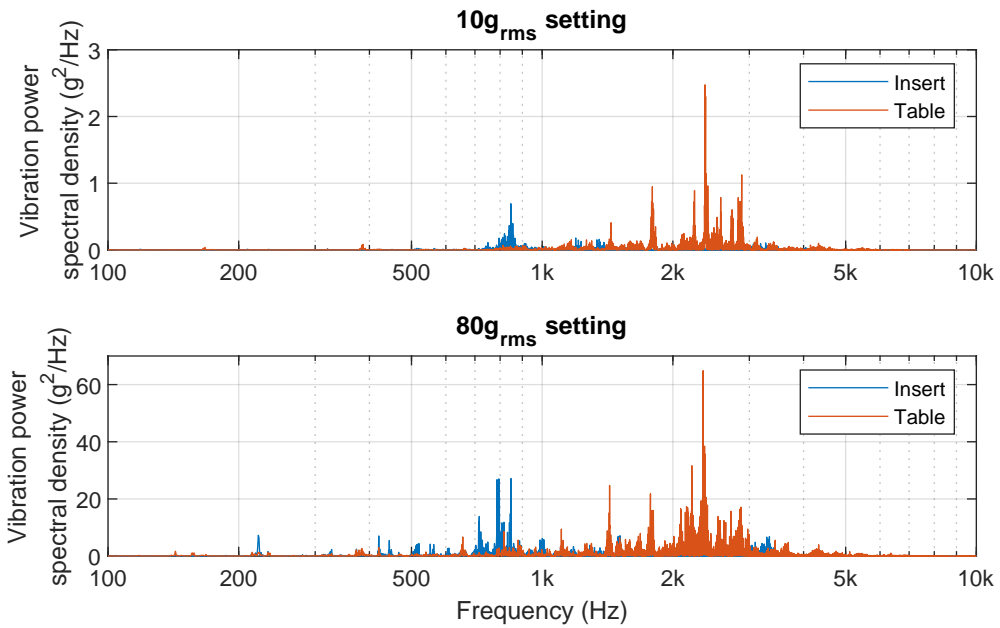


Figure 1.30 – Accelerations at 10g_{rms} and 80g_{rms} settings for insert and table sensor locations of Figure 1.26 with a copper pipe sample

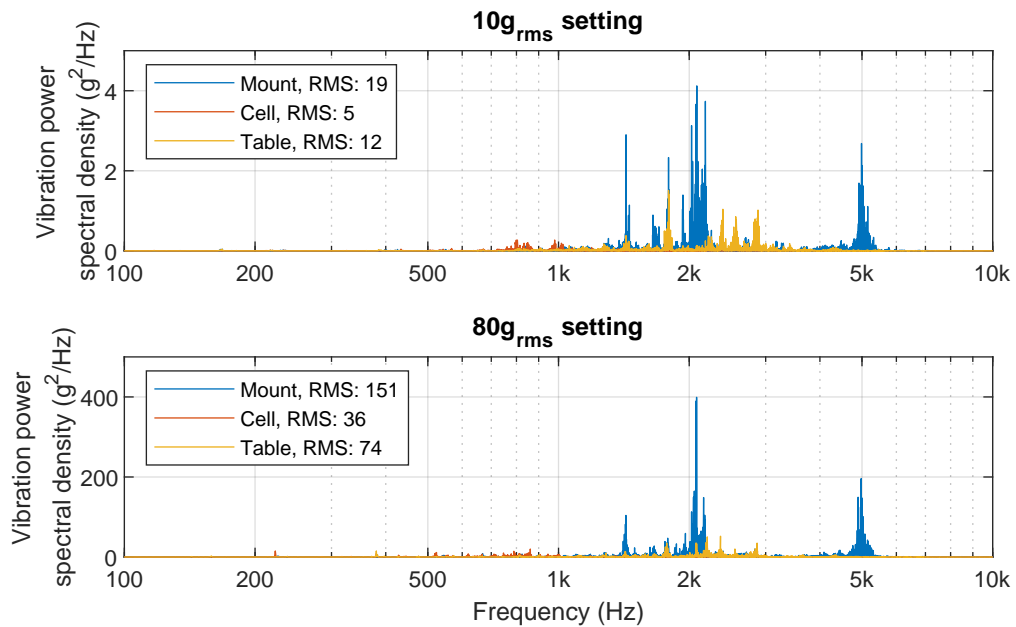


Figure 1.31 – Accelerations at 10g_{rms} and 80g_{rms} settings for bolt, cell and table sensors of Figure 1.26 with an RG-58C/U cable sample

However, it seemed not to have an effect on the actual vibration level as the saturation happened after the control signal had been extracted from the measurement.

As a conclusion, the triaxial cell will have an effect on the spectral content and the amplitude of the random vibration signal. However, it was shown that a very good vibration transfer to the mounting locations of the cell is achieved. The triaxial cell with a 25 cm mounting interval represents a typical cable mounting, and the triaxial cell is still more rigid than most of the typical structures used for cable mounting. Thus, it is concluded that the designed cell is suitable for generic vibration testing, but care needs to be taken if it is applied into specific high frequency vibration tests.

1.4 Transfer Impedance as a Function of Thermal and Vibration Stresses

This section gathers some key results of different shielded cables tested under environmental stress that were previously published in [7]. The environmental stress was realized using a highly accelerated life test (HALT) environment. For temperature and vibration, its advantage is relatively fast test time, but it comes with a compromise on accuracy in test parameters. While at high accuracy temperature chambers the specimens could be contained within 1°C of the set temperature, in HALT errors of at least 5°C need to be tolerated. For vibration, a slightly increased error in the vibration amplitude measurement is expected due to thermal dependency of the sensors, but also due to the glue mounting of the sensor behaving differently at different temperatures.

The HALT test cycle is presented in Figure 1.32. There are four different test phases:

A) Quasi-static thermal tests

- Temperature steps from ambient temperature to -50°C, and then to 120°C, or to the minimum and maximum tolerable temperature of the CUT according to its data sheet, whichever was more limiting
- No vibration

B) Dynamic thermal tests i.e. thermal cycles

- Five cycles between the temperature extremes used in the previous phase with a 5-minute dwell-time at each extreme
- No vibration

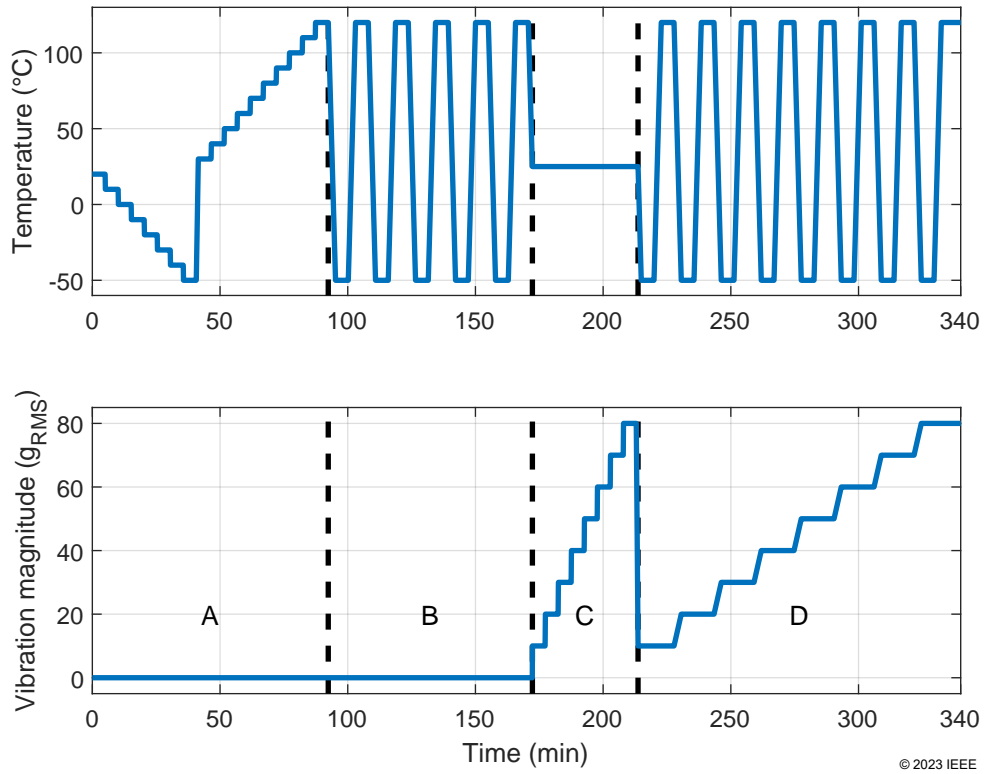


Figure 1.32 – HALT cycle temperature and vibration level setpoints

C) Quasi-static random vibration tests

- Ambient temperature
- Increasing vibration level with a $10g_{rms}$ step up to $80g_{rms}$ with a 5-minute dwell-time at each level

D) Combined thermal cycles and vibration test with dynamic thermal stress and quasi-static random vibration

- A cycle between the temperature extremes used in phase A with a 5-minute dwell-time at each extreme for each vibration level
- Increasing vibration level with a $10g_{rms}$ step up to $80g_{rms}$ with a 10-minute dwell-time at each level to enable one full thermal cycle per vibration level

Typical temperature and vibration responses of the setup were discussed in sections 1.3.3 and 1.3.4.

Pictures of the evaluated cable types are collected in Figure 1.33. The RG-55/U in Figure 1.33a is a standard double-braided cable aimed at application requiring excellent

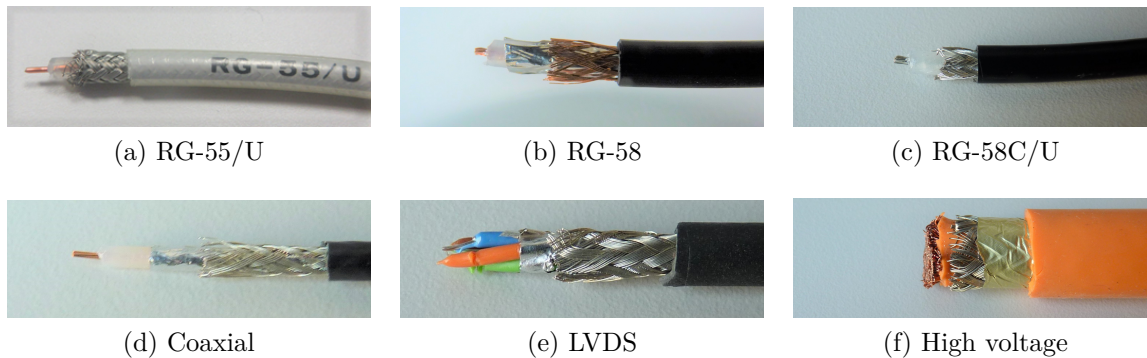


Figure 1.33 – Overview of the evaluated cables

shielding effectiveness. The RG-58 in Figure 1.33b is a generic low-cost coaxial cable with a sparse braid on top of a foil shield, and RG-58C/U in Figure 1.33c is marketed as a higher performance version of the same generic specification with a single braid. The coaxial and LVDS cables in Figures 1.33d and 1.33e, respectively, are used for high-speed data transmission in automotive applications. Their shielding structures are similar with a braid on top of a foil shield. Finally, the high voltage cable in Figure 1.33f with a foil shield on top of a tightly wound braid is typically used in electric vehicles.

The following sections discuss the specific results for CUTs in Figure 1.33 so that in section 1.4.1 the effect of quasi-static and dynamic thermal stress is discussed. Then, in section 1.4.2 the effect of random vibration is discussed. The dynamic thermal stress combined with random vibration is the last transient stress discussed in section 1.4.3. Finally, the ageing effect of the stress cycle is discussed in section 1.4.4 by comparing the transfer impedance test results at ambient conditions before and after the complete test cycle. Two representative quantities of the transfer impedance are extracted: transfer resistance at low frequencies, and transfer inductance at higher frequencies. The extraction frequencies for these two quantities per cable are in Table 1.6. For three cables: RG-58, coaxial, and LVDS, transfer inductance needed to be extracted from the shielding effectiveness region of the measurement.

1.4.1 Thermal Stress

For thermal stress, static and dynamic stresses are discussed. Static stress dependency means the transfer impedance change during quasi-static thermal stress, whereas dynamic stress is during thermal shock events. A typical response of shielded cable transfer im-

Table 1.6 – Extraction frequencies for transfer impedance environmental dependency

Cable	f for R_T extraction	f for L_T extraction
RG-55/U	50 kHz	30 MHz
RG-58	10 kHz	500 MHz
RG-58C/U	50 kHz	10 MHz
Coaxial	300 kHz	960 MHz
LVDS	300 kHz	930 MHz
High voltage	300 kHz	10 MHz

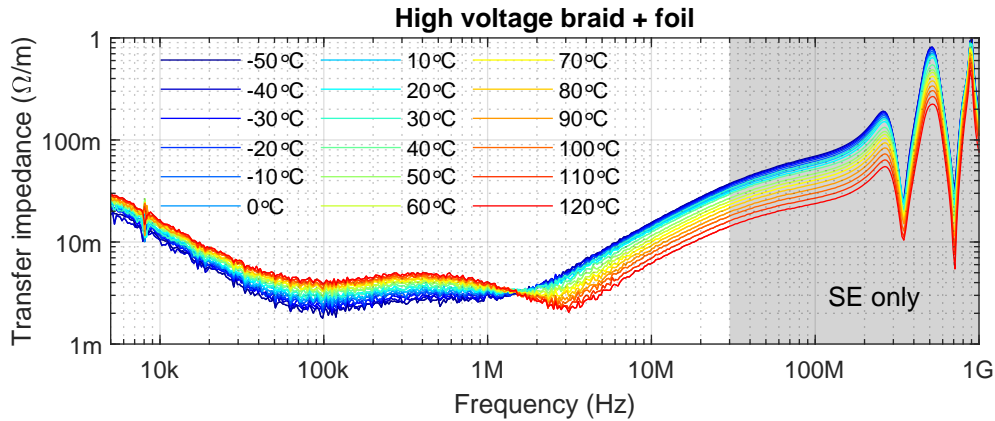


Figure 1.34 – Typical shielded cable transfer impedance response to temperature variations (Phase A of Figure 1.32)

pedance to quasi-static temperature variations is shown in Figure 1.34. The cables of Figure 1.33 were tested within their specified temperature ranges, and the temperature dependency of transfer resistance and inductance was extracted into Table 1.7.

Transfer resistance thermal dependency is generally between that of a copper, which is 0.40%/°C, and an eutectic Tin-Lead alloy, which is 1.0%/°C [55]. This is an expected behaviour for a tinned wire braid. However, the foil and braid combination of the coaxial cable sample showed reduced thermal dependency that could be due to the braid wires being copper with impurities like nickel-chromium alloy. The thermal dependency of its resistance is one tenth compared to copper at 0.04%/°C.

Thermal dependency of transfer inductance was less homogenous. Shields with bare braids displayed more modest changes than the ones with foil. Notably, it was observed that most of the shields had a negative temperature coefficient of transfer inductance. It

Table 1.7 – Transfer impedance thermal dependency (Phases A and B of Figure 1.32)

Cable	Shield Type	R_T (%/°C)	L_T (%/°C)	R_T (%/cycle)		L_T (%/cycle)	
				T_{min}	T_{max}	T_{min}	T_{max}
RG-55/U	braid+braid	0.44	0.11	-0.2	-0.5	3.3	1.1
RG-58	foil+braid	0.58	0.79	0.3	0.0	-10	-8.1
RG-58C/U	braid	0.48	-0.28	-0.1	0.1	-0.4	0.5
Coaxial	foil+braid	0.32	-0.48	-0.2	0.2	4.7	2.9
LVDS	foil+braid	0.42	-0.81	0.3	0.0	-4.9	-5.5
High voltage	braid+foil	0.41	-0.40	1.0	0.9	-2.7	-3.6

means that for them the braid inductance, or equivalent of that of the foil, is dominating the total inductance, whereas for the positive temperature coefficient would mean that the hole inductance dominates. Generally, the changes in inductance were at least a magnitude higher than what could be explained by thermal expansion of the cable dielectric. Thus, a further study would be needed to characterize the parameters having an effect on this inductance dependency.

The last two columns of Table 1.7 characterize the cyclic dependency measurement results of transfer resistance and inductance. It is to be noted that the temperature control was within $\pm 5^\circ C$ with five cycles measured. Thus, any value lower than the respective percentage change as a function of temperature is negligible. By applying this rule, it is seen that only the high voltage cable has significant resistance change over the first cycles. This could be related to lost connection with the foil shield over the braid. Inductance wise all the tested cables show some dependency to thermal cycling. Interestingly, the coefficient signs cannot be predicted from the quasi-static temperature dependency of the transfer inductance. However, similarly to temperature dependence, the shields that have a foil element show higher dependency on thermal cycles than the ones with pure braids. A response of the high voltage cable is shown in Figure 1.35 as an example of the dynamic thermal stress response.

1.4.2 Vibration Stress

Vibration stress test was done with a table-controlled random-vibration sweep from $10g_{rms}$ to $80g_{rms}$. Typical frequency content and vibration energy transfer is discussed in section 1.3.4. Vibration dependency results are gathered in Table 1.8.

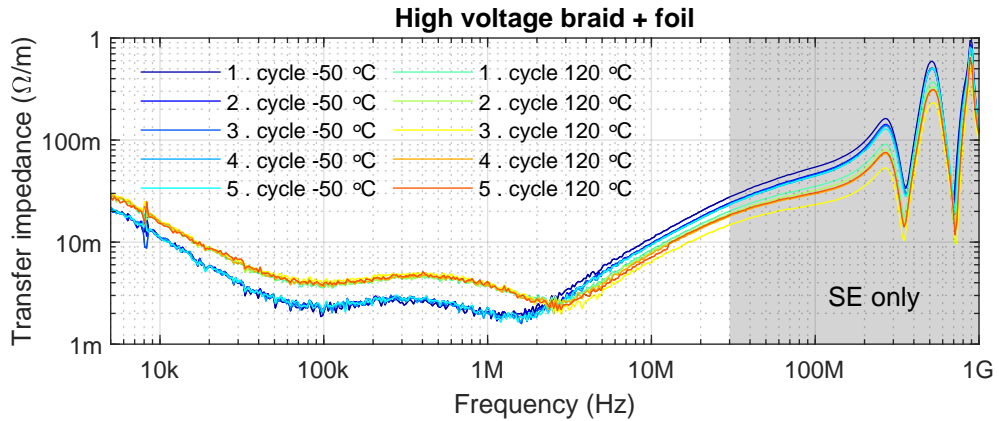


Figure 1.35 – Typical shielded cable transfer impedance response to thermal cycles (Phase B of Figure 1.32)

Table 1.8 – Transfer impedance vibration dependency (Phase C of Figure 1.32)

Cable	Shield Type	R_T (%/ g_{rms})	L_T (%/ g_{rms})
RG-55/U	braid+braid	-0.01	0.61
RG-58	foil+braid	0.00	exponential
RG-58C/U	braid	0.11	-0.06
Coaxial	foil+braid	1.31	exponential
LVDS	foil+braid	0.12	8.51
High voltage	braid+foil	-0.06	0.19

Transfer resistance results show generally limited dependency on vibration amplitude with the exception of the coaxial cable with a foil and braid shield. There, the transfer resistance is linearly dependent on the vibration amplitude. On the other hand, the transfer inductance results show different levels of vibration dependency. Some cables, like the RG-58C/U, are practically vibration independent, and some cables, like the RG-55/U, show modest dependency of vibration. Then, there are cables, whose transfer inductance is highly dependant on vibration amplitude, like the foil and braid shielded LVDS cable. Finally, two cables showed an exponential transfer inductance degradation, which is an indicator of shielding failure. Typical transfer impedance evolution for such a case is shown in Figure 1.36.

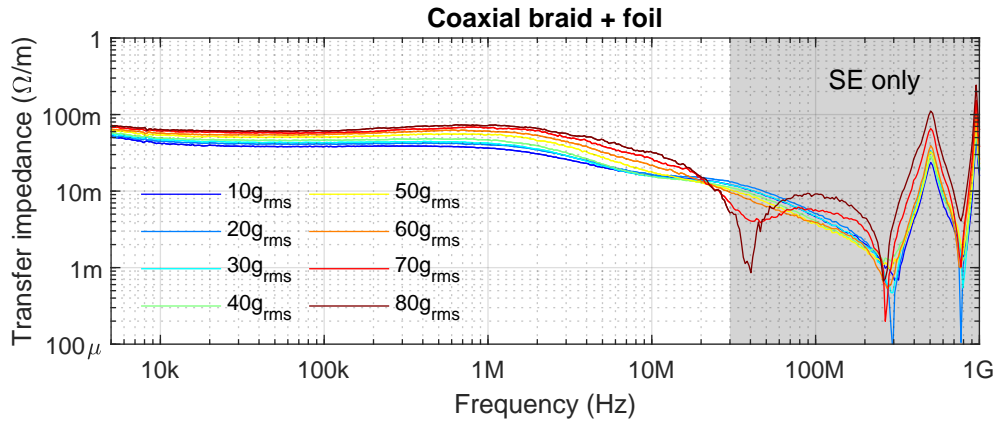


Figure 1.36 – Typical shielded cable transfer impedance response to random vibration with a failure at high vibration level (Phase C of Figure 1.32)

1.4.3 Combined Thermal and Vibration Stress

The last test with combined thermal cycling and vibration is more of an ageing test than a dynamic response one. However, some interesting dynamic observations could be done from the results shown in Table 1.9:

1. Transfer resistance of pure braid shields had slightly higher vibration amplitude dependency at low temperatures, while shields with foil were more dependent at high temperatures
2. Some foil and braid shields showed exponential dependency of both transfer resistance and inductance to vibration amplitude at high temperatures indicating shielding failure, but no such effect was observed at low temperatures.
3. There was a large variation on transfer inductance stress dependency, as some cables barely showed changes, and others showed almost two decades of inductance change over the tested vibration amplitude interval.

Generally, the results were a combination of the cyclic thermal and vibration tests. The two cables that showed signs of failure during pure vibration tests failed more clearly during the combined test. An example of such increasing stress, and an eventual failure at high vibration level can be seen from the transfer impedance graph of a coaxial cable in Figure 1.37.

Table 1.9 – Transfer impedance combined thermal cycle and random vibration dependency (Phase D of Figure 1.32)

Cable	Shield Type	R_T (%/g _{rms})		L_T (%/g _{rms})	
		T_{min}	T_{max}	T_{min}	T_{max}
RG-55/U	braid+braid	0.03	0.01	0.00	0.06
RG-58	foil+braid	0.03	exp.	1.19	exp.
RG-58C/U	braid	0.04	0.02	0.04	0.17
Coaxial	foil+braid	0.11	exp.	9.65	exp.
LVDS	foil+braid	0.01	0.05	20.10	52.90
High voltage	foil+braid	0.07	0.12	-0.18	-0.28

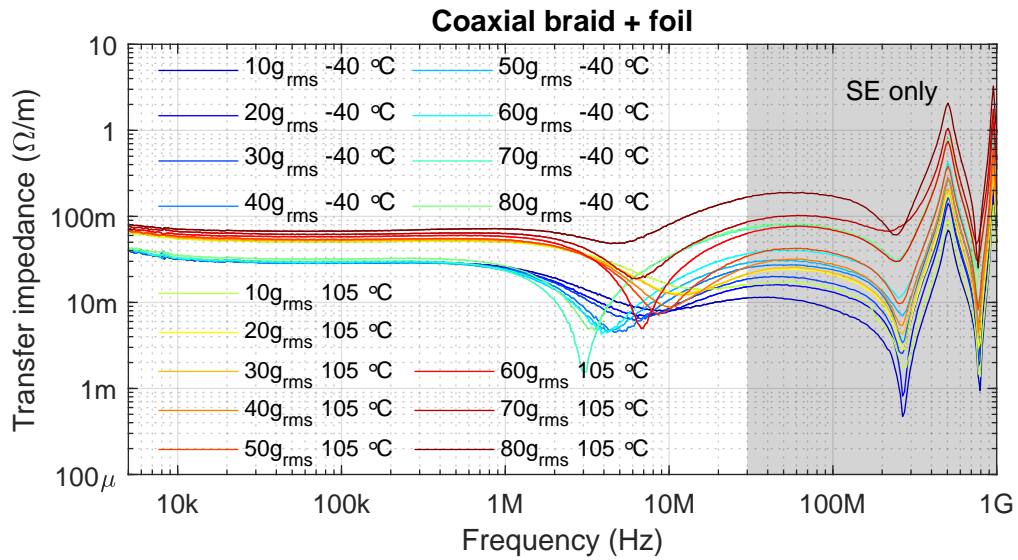


Figure 1.37 – Typical shielded cable transfer impedance response to random vibration with a failure at high vibration level (Phase D of Figure 1.32)

1.4.4 Thermal and Mechanical Ageing

The effect of thermal and mechanical ageing for the tested cables is evaluated by comparing the transfer impedance measurement results taken at the beginning of the tests at ambient temperature, to those taken after the completed test cycle, once the test setup had been cooled down back to ambient temperature. From Table 1.10 it is seen that measured ageing of transfer resistance is close to the measurement uncertainty for all cases, except the coaxial foil and braid shield. From transfer inductance point of view, all the three cables with a foil and braid shield suffered significant transfer inductance increases due to the applied environmental stresses. Interestingly, the high voltage braid and foil shield worked better, and even a reduction of the transfer inductance was seen as shown in Figure 1.38. This could be either related to different materials used in the construction of the cables, or it could mean that the foil on top of the braid will see less stress, and is less likely to break. A more in-depth study would be needed to find out which reason is the major contributor.

The LVDS cable, whose measurement result is also in Figure 1.38, was dissected in search for explanations for the increased transfer inductance. The cable with jacket and braid removed is shown in Figure 1.39. Figure 1.39a shows some signs of stress on the braiding, but no broken braid wires. Thus, the effect of braid ageing to the transfer impedance is likely limited. On the other hand, Figure 1.39b shows the damage inflicted on the foil. It was ripped at both ends, and multiple smaller rips were observed all along the cable. It is likely that the ripped foil is the reason for the observed transfer inductance increase.

Table 1.10 – Transfer impedance of fresh and aged samples

Cable	Shield Type	R_T (m Ω /m)			L_T (pH/m)		
		Fresh	Aged	↑	Fresh	Aged	↑
RG-55/U	braid + braid	7.8	8.0	+3%	7.2	10	1.4×
RG-58	foil + braid	107	112	+5%	4.9	28	4.7×
RG-58C/U	braid	15.6	16.5	+6%	1100	1000	0.9×
Coaxial	foil + braid	44.4	57.5	+30%	21	230	10×
LVDS	foil + braid	20.8	21.7	+4%	2.1	84	40×
High voltage	braid + foil	3.4	3.7	+8%	220	130	0.6×

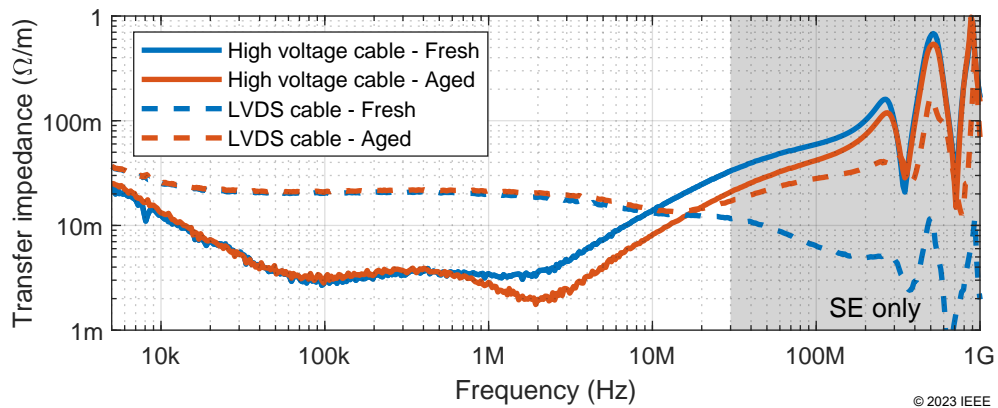


Figure 1.38 – Fresh and aged transfer impedance measurement comparison

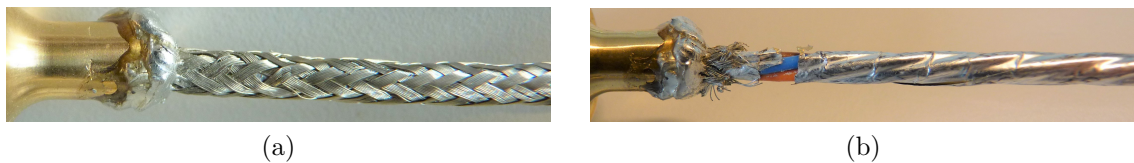


Figure 1.39 – LVDS cable with (a) jacket and (b) braid removed after the test cycle

1.5 Conclusion on Shielded Cables

Shielded cables are an excellent component for protecting signals from EMI. However, some of their performance parameters can suffer from environmentally induced stresses. This chapter discussed the concepts of shielding effectiveness and transfer impedance, and demonstrated how they can be derived from electromagnetic theory. Typical methods to measure either SE or Z_T were discussed, and triaxial method was selected to be developed further to accommodate environmental testing of shielded cables. Modifications to the existing triaxial structure were made so that increased airflow through the cell was guaranteed, and its robustness against vibrations was ensured. Finally, the cell was used in highly accelerated life test conditions to stress multiple different cable samples under quasi-static and transient thermal stress, random vibration, as well as, combined transient thermal stress and random vibration.

The novel environmental triaxial cell design demonstrated good measurement performance up to 1 GHz. Further improvements could be directed to improving the impedance characteristics of the cavity at the floating end. The cell allowed air to circulate around the cable sample and, when used with air guides, provided rapid thermal response. The cell

sustained vibration relatively well with the weakest spots being either the CUT soldering to the N-connector centre-pin, or test cable mountings at the N-connector interface.

During thermal stress, transfer resistance of the shields behaved similarly as the conductivity of its material. Highest variation was 58%/100°C. Transfer inductance variations were not consistent, but seemed to depend on the shield construction. Highest variation was 80%/100°C (one case of directly, and one inversely proportional). During thermal cycling, transfer resistance was practically independent of the cycle amount for the tested cables. However, the transfer inductance was affected up to a 5% increase, or a 10% decrease per rapid thermal cycle between the maximum and minimum operating temperatures of the respective cable.

Half of the tested cables were immune to random vibration but, from the other half, two cables showed exponential transfer inductance increase over the vibration amplitudes suggesting that the cable shielding failed when high vibration energies were used. In addition to the failures, one cable exhibited a linear dependency of transfer inductance on vibration amplitude. The transfer impedance increase of 85% per $10g_{rms}$ was significant. In combined testing, the same trend continued, but now the weaker cables showed exponential behaviour on their transfer resistances, too. In addition, the highest linear dependence was 529% per $10g_{rms}$.

After the environmental tests, the measurement results of aged cables were compared to the results taken before the tests on the fresh samples. For all the other cables except the coaxial cable with a foil and braid shield, the transfer resistance change was within measurement uncertainty. The aforementioned cable exhibited a 30% increase in transfer resistance indicating a broken foil or even some snapped braid wires. Transfer inductance wise only RG-58C/U cable did not show any signs of ageing. Rest showed ageing ranging from improved performance of the high voltage cable to 40-times multiplication of the transfer inductance of the LVDS cable.

Based on these results, there is a need to study the foil shields more in detail to understand their behaviour under environmental stresses. Some old models for foil shields exist, but they would need to be first verified properly against cable samples wound with modern foil winding practices. In addition, a physics-based model for foil ageing would be beneficial.

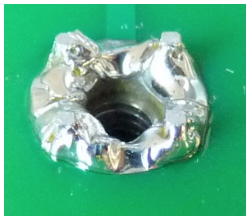
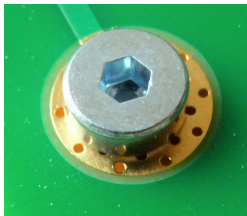

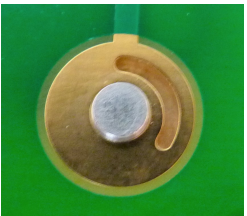
As it was shown that there can be both dynamic and ageing related changes in the shielding performance, when the cables are subjected to environmental stresses, it is evident that these need to be taken into account during product design. The results in

this chapter can be used as a baseline for temperature and vibration dependent transfer impedance definition using the relative changes of transfer resistance and inductance as a generic model for each of the cable tested cable types. This is the approach that will be taken in Chapter 3, where the system immunity against conducted disturbances injected to the cable shield is analysed. However, before diving into the applications, a similar analysis as for shielded cables in this chapter is given to EMI filter ground contacts in the next chapter.

CIRCUIT BOARD GROUND CONTACTS UNDER ENVIRONMENTAL STRESS AND AGEING

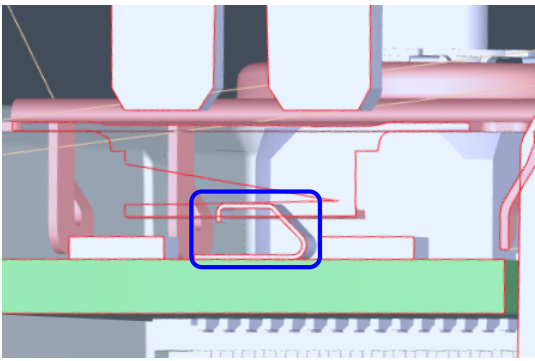
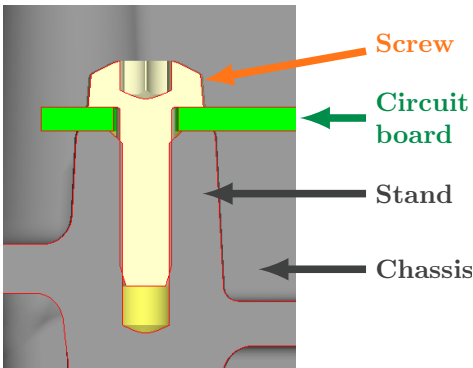
This chapter analyses the performance of some typical grounding structures used to connect EMI-filters to the common reference potential of the system. This reference potential is usually the chassis ground. Typical ground contacts can be made with various different methods, and some common ones are shown in Table 2.1 with their main advantages and disadvantages highlighted.

Table 2.1 – Overview of typical EMI-filter ground contacts

	Solder	Screw	Spring	Swaged [10]
				
Advantages	Good electrical contact	Easy assembly and disassembly	Easy to assemble	Fast assembly with large contact area
Disadvantages	Difficult for some materials and large heat sinking objects	Screw is extra hardware during final assembly	Small contact area Spring is extra hardware during circuit board assembly	Special tools needed

In automotive, the most important EMC-related electrical connections have been made with wiring harnesses in the past. They have been the main culprit on conducting any captured radiated emissions from the environment to the different electronic control units of the vehicle. However, with the current trends highlighted in the introduction of this thesis, the future brings a new set of electrical connections with high importance for the EMC of the vehicle: the ground contacts of EMI-filters and EM shielding structures. Table 2.2 highlights two common use cases of circuit board grounding in modern vehicle electronics.

Table 2.2 – Automotive examples of circuit board ground contacts

Grounding spring inside ECU	EV Inverter EMI-filter grounding
	
<p>Tin-plated phosphor bronze spring contacting an aluminium part or a tin-plated pad of another circuit board</p>	<p>Tin-plated circuit board pad secured to a machined cast aluminium stand with a screw</p>

A grounding spring is used inside an automotive electronic control unit (ECU) to connect the circuit board ground to the casing of the ECU. This is especially important, when using shielded cables for high-speed data transmission as described in Chapter 1. Now, the ground return current of the high frequency signal needs to be well controlled also inside the ECU casing from the connector to the circuit board. Ideally, shielded connectors with both the signal conductor and the shield structure soldered into the circuit board would be used, but it is often not possible due to manufacturing concerns. A second best approach is to use grounding springs to connect the connector body to the circuit board as is shown in the ECU example of Table 2.2.

Another typical ground contact is a circuit board pad connected to the equipment casing by a screw as shown in the EV inverter EMI-filter example in Table 2.2. There, the aim is to conduct the capacitive leakage currents from the motor and motor cables

back to the high voltage DC-bus of the inverter. Here, a reliable contact is needed to prevent disturbances caused by the returning ground currents. If the EMI-filter ground contact would be broken, a significant high frequency common-mode (CM) voltage would be seen between ground and the high voltage circuitry elsewhere. This could result in e.g. a malfunction of a Battery Management System (BMS) [56].

To define the basics of reliable electrical contacts, a theoretical discussion on the characteristics of electrical contacts is given in Section 2.1. To determine quality of electrical contacts in practice, contact resistance measurements are needed. They are discussed in Section 2.2. For a thorough through-life characterisation of electrical contact quality, some form of environmental stress testing is needed. In the frame of this thesis, a test setup for highly accelerated life testing (HALT) was developed and its characteristics are also reported under Section 2.2. To demonstrate typical findings in HALT, a performance evaluation of three typical circuit board ground contacts used in automotive industry is done in Section 2.3. Finally, a conclusion on the contact analysis is given in Section 2.4.

2.1 Theory of Electrical Contacts

Generally, electrical contacts have been studied as tribological systems with contact resistance being either the main focus of the study [57], or a secondary quantity to extract mechanical parameters that would otherwise be difficult to measure [58]. The basic parameters of any mechanical contact, including an electrically conducting contact, are material of the contacting elements, contact area, and pressure discussed in Sections 2.1.1 and 2.1.2. An important special parameter for electrical contacts is plating of the contact surfaces discussed in Section 2.1.5. In addition to contact fundamentals, stress effects influencing the electrical contact quality are discussed. These include creep and stress relaxation in Section 2.1.3, oxidation and fritting as a counteracting phenomenon in Section 2.1.4, and fretting in Section 2.1.6.

All of the following sections give only an overview of the different aspects influencing electrical contact resistance for brevity. The reader is invited to visit the mentioned references for a more thorough understanding on the subjects. One major cause of failure for electronic contacts: corrosion, is omitted in this thesis. An assumption is made that the analysed electrical contacts are within sealed environments, where entry of water or other corrosive agents is limited.

2.1.1 Material Selection

On the first sight, selecting materials for electrical connections seems straightforward: pick copper or aluminium that is as pure as possible and move on. This is the case for circuit boards, wires, and many other electrical and electronics components. However, the ground current return paths of systems, to which common-mode EMI-filters are connected, can be complex. It is common that those current paths are designed mainly from mechanical standpoint, and electrical conductivity of the paths is an afterthought.

Copper is generally considered as a good electrical conductor, but this applies only to very pure copper that is used for electrical components. This pure copper is specified to have conductivity according to the International Annealed Copper Standard (IACS). Copper resistivity increases with impurities, and even a small amount of wrong impurity can dramatically reduce conductivity of the alloy. Adding only 0.04% of phosphorus will reduce conductivity of copper to 80% IACS [59]. This effect, along with the effect of some other common impurities, is shown in Figure 2.1.

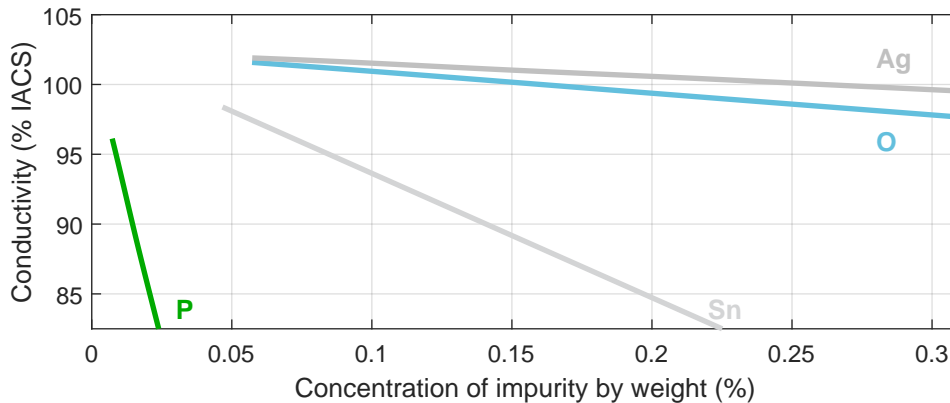


Figure 2.1 – Effect of impurities on the resistivity of copper [59]

Aluminium and its alloys are used as electrical conductors due to their low price and weight. In automotive, A319 alloy is commonly used in casting of structural parts [60]. It has 7% silicon content, and trace amounts of other metals. Its electrical conductivity is approximately one half of pure aluminium [61] as highlighted in Figure 2.2.

In contact analysis, conductor material knowledge is most important in extracting the bulk material resistance from the actual contact resistance in the measurement results as explained in Section 2.2. For complex geometries, the resistance contribution of the ground structure can be easier to simulate with 3D FEM if the material properties are

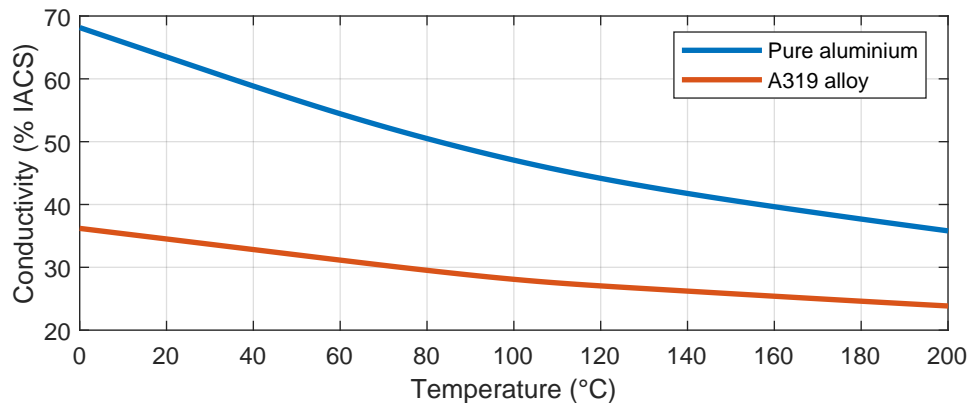


Figure 2.2 – Conductivity of aluminium as a function of temperature [61]

known, than to directly measure it. Some surface properties, like hardness, will also vary with material selection, and they become important, when analysing contact tribology in the following sections.

2.1.2 Contact Pressure and Contact Area

Two fundamental pillars of an electrical contact between two conductors are contact area and pressure. They determine the effective cross-section of the contact, and thus, contribute significantly to the final contact resistance.

The real contact area contributing to contact resistance is not the contact area, where the conductors are visibly touching [62]. Instead, the contact area can be divided into several subparts, each of which is equal or smaller than the preceding area as in Figure 2.3 [63]:

1. Apparent contact area
 - Area, on which the two conductors seem to touch each other
2. Actual contact area
 - Area, on which the two conductors actually touch each other
 - Usually centred around bolts or other pressure elements
3. Load-bearing area
 - Area that supports the weight of the top conductor
 - Area that provides a counter force to the normal force applied by the pressure elements

- Experiences elastic and plastic deformation
4. Quasi-metallic contact area
 - Area that is covered by a sufficiently thin insulation film to allow tunnelling of electrons, and thus, electrical conduction
 5. Metallic contact area
 - Area, where main conduction between connecting bodies happens
 - Structure resembles that of a solid metal piece if the contact bodies are made of the same material

Now, it is typically only the *metallic contact area* that significantly contributes in determining electrical resistance of the contact. As this interface resembles a solid metal piece, the contact resistance is not so much about the resistance of the contact areas themselves, but about *constriction resistance* due to current concentrating on small areas of metallic contact between the contact members. An exception to this being the case where majority of current conduction happens due to tunnelling at quasi-metallic contact areas, but it is not relevant for common electrical contacts. Now, as the metallic contact area is proportional to the elastic and plastic deformation caused at the contact surfaces, it becomes necessary to analyse the effect of contact pressure on the contact resistance.

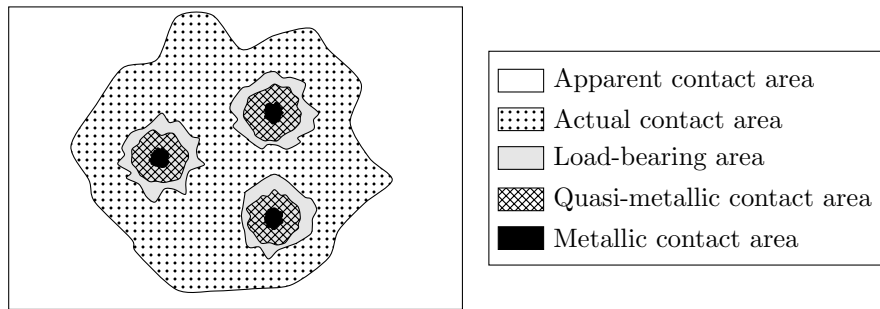


Figure 2.3 – Different parts of a rectangular contact area [62]

The applied contact pressure will deform the contact surfaces elastically and plastically [63]. This leads to forming of the different contact areas described above. The sizes of the areas are proportional to contact pressure. The size change of the metallic contact area can be seen from contact resistance dependency on contact pressure in Figure 2.4. There, contact resistance asymptotically reaches a constant value as the contact pressure is increased. On the other hand, if the contact pressure is decreased, there is an

asymptotic pressure limit below which the contact is not conducting any more due to oxide build-up. This limit depends on the properties of the conductor material, and the difference between noble and ordinary elements is discussed in Section 2.1.5.

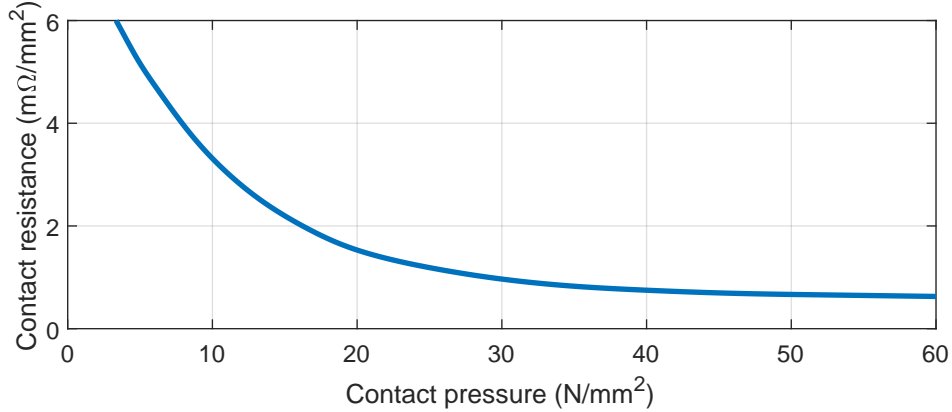


Figure 2.4 – Effect of contact pressure on contact resistance of a copper-to-copper busbar contact [59]

Determining the contact pressure is not always a straightforward task. For example, when using a torque wrench to tighten non-lubricated bolts the uncertainty of the contact force is $\pm 35\%$ [64], which is in addition to the uncertainty caused by the torque wrench accuracy. In case of other contacts, specific methods need to be used. Like for practical springs, where either complex analytical calculations or 3D-FEM needs to be conducted during the spring design as any practical measurement mean would either require design changes or would prevent electrical conduction through the interface. Fairly recently, new methods like pressure sensitive films [65] and piezoelectric sensors [66] have been developed for contact pressure determination. However, they were not used during this thesis.

The contact force in a bolt contact [64]

$$F_N = \frac{T}{Kd} \quad (2.1)$$

is calculated from tightening torque of the bolt T , the nominal bolt diameter d , and the nut factor K , which tells about lubrication of the threading. A typical nut factor for a zinc plated bolt joint is $0.332 \pm 20\%$ [64]. It is common to use contact pressure

$$P_N = \frac{F_N}{A} \quad (2.2)$$

as a universal quantity to represent contact force over different contacts as it illustrates better the forces deforming the surface asperities of the contacts.

To arrive at properly deformable surface asperities, specific surface roughness with sharp peaks is needed. This is especially important, when at least one of the contact surfaces is aluminium [67]. Very similar rules for surface preparation apply for copper joints, but precision with which they are applied is not as critical as for aluminium [59]. This is due to the soft nature of copper oxide and its ability to slightly conduct electricity.

Finally, it is important to take care on the longevity of the applied contact force through the lifetime of the contact. The design of the mechanical contact parameters including environmental effects, like temperature variation, is important as illustrated for bolted contacts in [64]. Other appropriate mechanical design rules need to be followed as well. If the contact is susceptible to temperature changes, a small amount of thermal cycling, like the five cycles used in this thesis, is enough to uncover this dependency [67]. Similarly, if the contact is susceptible to mechanical shock or vibration, a modest exposure time is enough to indicate this vulnerability [67], again enabling accelerated tests if needed.

For soft materials, like pure aluminium, some additional phenomena needs to be taken into account [68]: shear stress related to opening of a contact can lead to momentarily reduced contact resistance as enough tangential shear can effectively break more of the oxide layer between contacts than what was initially broken as the contact was made. This effect cannot be observed with harder materials, like copper. Also, stress relaxation of the contact is significant issue for soft materials, and is related to creep discussed in the next section. To limit stress relaxation for aluminium, a maximum mean pressure to the contact elements should be less than 60 N/mm^2 for contacts that are operated at temperatures up to 80°C .

2.1.3 Creep and Stress Relaxation

In addition to cyclic thermal stresses that can change contact pressure in a short amount of time, creep and stress relaxation are important factors in decreasing contact performance for some materials. Creep means cold flow of a metal or other material under constant stress or pressure. As typical mounting structures impose a mounting force to a limited area, the material under stress tends to flow to minimize the stress from this mounting force. If the mounting force is kept constant, the flow of material is called creep. Stress relaxation is a similar macro effect to creep, but instead of being measured under constant stress, it is a measure of stress decrease under constant strain. In bolted joints

either effect can occur, or they can occur simultaneously. [69]. The terminology between creep and stress relaxation is relatively new, and some of earlier sources might use the terms interchangeably.

Stress relaxation on soft metals, like aluminium, is more of an issue [67] than with harder conductors like copper [59]. The amount of stress relaxation and its effect depends on the design of the contact. Even in a well-designed aluminium joint, stress relaxation will happen. However, primary stress relaxation very soon after tightening the joint contributes to the bulk of the contact pressure change, whereas long-term stress relaxation can be considered insignificant [70]. This is the reason for some everyday guidance given for aluminium parts, like the instructions of re-tightening alloy wheel bolts after driving one hundred kilometres. If soft aluminium conductors are used, a similar re-tightening procedure should be followed for electrical contacts after approximately 1000 hours [67].

Creep and stress relaxation do occur for other materials than metals, too. A particular interest regarding this thesis is flame retardant epoxy reinforced with woven glass fibres as it is used as the structural material for printed circuit boards. It displays insignificant stress relaxation, when used well below its glass transition temperature T_g , but high stress relaxation and creep close to it [71]. A margin of 20°C or more to the glass transition temperature is recommended.

Although stress relaxation will decrease contact pressure of the joint, contact resistance of a well-designed electrical contact does not change [67]. This is due to the fact that the previously formed contact spots are kept under reducing pressure until they are completely broken at very low pressures. Thus, further analysis of both creep and stress relaxation is excluded in this thesis.

2.1.4 Oxidation of Contact Surfaces and Fritting

Different metals have different tendencies to form oxides when being in contact with an atmosphere that contains oxygen. Some of these oxides are non-conductive, like aluminium oxide Al_2O_3 ($\rho > 10^{12} \Omega\text{m}$) [72], and other conductive or semi-conductive, like copper oxide CuO ($\rho \sim 1 \Omega\text{m}$) [73]. In any case, when they are present in an electrical contact, they hinder its conductivity. Proper preparation of the contact surfaces by removing any accumulated oxides helps in ensuring good quality electrical contacts.

For aluminium surfaces, oxide formation is very rapid and the oxide is very hard [67]. Thus, the contact surfaces should be prepared as flat, but with high surface roughness to ensure that the formed oxide layer is penetrated by the peaks of the rough surface giving

good metal-to-metal contact spots.

For copper surfaces, the importance of oxide removal is smaller. In fact, it has been shown that some oxide growth in the contact surfaces can reduce the contact resistance by introducing a larger, though only slightly conducting, contact area [68].

Even if there is an insulating oxide layer in the contact, it is possible that electrical conduction is achieved after voltage is applied. The oxide layer can be broken either by arcing or fritting. Arcing will generally destroy the contact and is related to cases, where high contact voltages of tens to hundreds of volts with large enough short-circuit current is present, like in the electric vehicle powertrain. This destructive behaviour is not taken into account in this thesis. Fritting, on the other hand, is a phenomenon, where a sufficiently thin oxide layer or other tarnish is broken down by the electric field formed in the contact without significant arcing [74]. For permanent contacts, it can happen the first time the contact is mated and significant current is flowing through it, but as the oxide layer is broken the first time, subsequent fritting events are not observed [75]. Thus, fritting is more important phenomenon for intermittent contacts like those in relays and will not be taken into account in this thesis.

The component production (e.g. casing of an electrical system) and sub-system assembly (e.g. automotive ECU) can have significant time-delay in between, and most controlled atmosphere requirements for components in-between are considered excessive. Moreover, no surface preparation should be done at sub-system assembly level as it increases assembly times. Thus, removing oxides immediately before joint assembly is not feasible. Instead, proper roughness of the contact surfaces or plating with appropriate material as discussed in the next section should be specified to ensure an immediate and a long lasting electrical contact.

2.1.5 Plating of Contact Surfaces

Plating materials are generally used to prevent the base metal corrosion, and to lower the contact resistance of the joint. One way for contact resistance reduction is to use softer plating materials that enable larger contact area. This is the case for example with tin plated copper where the tin plating doubles the contact area of the copper contacts with same contact pressure [76].

Another feature of the plating materials is the behaviour at low contact loads. The main difference is between noble and non-noble metals as the noble metals do not form an oxide layer on top of them [76]. They can be used with very low contact forces as the

contact load does not need to break the tarnish film as illustrated in Figure 2.5, where noble silver plating has a defined contact resistance at zero contact force, but non-noble tin does not.

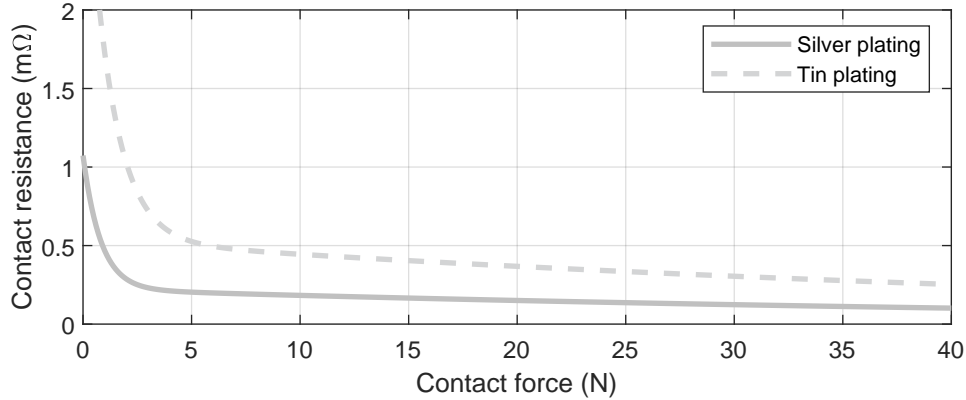


Figure 2.5 – Contact resistance comparison as a function of contact force between silver and tin platings [76]

It would seem obvious to always use soft and noble plating materials like gold to minimize the contact resistance, but cost, creep, and environmental concerns are the major challenges here. Noble metals are generally more expensive than their non-noble substitutes, and attaching them reliably on the surface of other conductors needs harsh chemicals, like cyanide in case of gold plating. Also, under constant contact pressure, the softer plating materials tend to creep causing reduced contact pressure, and a possible disconnection if creep has not been accounted for.

2.1.6 Fretting

Fretting is contact surface wear due to microscopic movements of contact bodies, usually between 1-100 μm . It can be divided into three different regimes [77]:

Stick regime is characterized by a linear relationship between the tangential force and the contact displacement. Within this area, the contact bodies are stressed, but stay together. The fretting scar is minimal, but can have surface cracks due to stresses subjected by the tangential force. For most materials, no significant changes in electrical performance happen in this region.

Stick-slip regime is characterized by a hysteresis loop in the tangential force - displacement graph. This means that the contact bodies move significantly at the higher

tangential forces. The fretting scar has two clearly identifiable parts: a stick zone in the middle, and a slip zone surrounding it. At the slip zone, there are significant surface cracks that get detached. If detaching happens, the particles get usually crushed and oxidized under the contact. These oxidized particles are non-conductive, and can accumulate to create a non-conductive fretting scar changing the electrical performance of the contact.

Gross-slip regime is characterized by a similar hysteresis loop as the stick-slip regime, but with a drop in the tangential force with high displacements. This indicates that the contact has moved from static to kinetic friction, and all areas of the contact bodies are in relative motion to each other. The surface does not show cracks any more, but signs of plastic shear. This evidently will detach particles from the surfaces that again get crushed and oxidized under the contact. Now, this oxide layer can cover the whole contact surface, and lead to an electrically isolated contact. However, it is to be noted that constant movement of the oxide and freshly detached metal particles causes most often an intermittent electrical contact.

Fretting has been studied extensively for connectors and other contacts conducting functional signals [78]. For power contacts, some limited studies have been performed [79] as well as for circuit breakers [80], where fretting was observed due to power cycling, a similar situation that is relevant for EV powertrains that experience many cyclic power loads during their lifetime - especially in city traffic. For power contacts, the deterioration of the contact leads to eventual arcing. In SELV-systems these are micro-arcs [81]. In low voltage systems, the phenomenon remains without much of attention. Reason could be due to destructive arcing effects for which causal relationship with fretting cannot be backtraced.

Fretting studies on plated contacts have shown that fretting at stick-slip regime results an infinite contact lifetime, whereas fretting at gross-slip regime causes always a contact failure [82]. Contact failures happen faster with non-noble coatings due to formation of oxide debris. Noble coatings need to be consumed first to uncover non-noble materials underneath that are able to produce oxide debris during wear. As the under-platings are not generally designed for conducting electricity, the contact failure is imminent after the noble material has been consumed.

Overall, if fretting is limited to stick-slip region, it is not a problem for EMI-filter ground contacts discussed in this thesis. In case of gross-slip fretting, that can be the case especially for spring grounding structures, care needs to be taken to design the

contact materials in such a way that the electrical contact lasts for the lifetime of the vehicle without fretting induced failures.

2.1.7 Conclusion on Electrical Contact Parameters

Several parameters of electrical contact performance were discussed in this section. It was highlighted that the most important design parameters for initial contact resistance are:

- Selection of the material for the contacting bodies - each material has its optimum contact pressure
- Selecting the correct contact pressure for the materials used in the contact
- Ensuring sufficient metal-to-metal contact area in the joint that can be very different of the apparent contact area

Then, during the lifetime of the electrical contact, the above parameters should be controlled against threats coming from the environment and mechanical ageing. These threats are:

- Thermal stresses reducing or increasing the contact pressure
- Creep and stress relaxation reducing the contact pressure
- Oxidation reducing the effective metal-to-metal contact area
- Fretting wear of the contact bodies and possible oxidation in case of non-noble materials.

It was shown that designing a reliable electrical contact is simple if there are no other constraints on the way. Taking a large enough contact area with hard materials and sufficient contact pressure can provide a very reliable electrical contact. However, many times there are financial, as well as, space and assembly constraints that limit the available options and prevent making all contacts ideal. Then, the challenge becomes from making the right compromise between contact performance against other design requirements. It is there, where the following analysis is very important.

2.2 Contact Resistance Characterization

Contact resistance characterization needs depend on the contact design. The approach will be slightly different if regularly broken contacts (relays, etc.), sliding contacts, or con-

tinuous contacts will be evaluated. In addition, the contact characterization setup will need to be built differently depending on the amount of external stresses that need to be taken into account. In this section, the basics of contact resistance characterization under external stresses are discussed, and typical means of resistance measurement are covered. Finally, a test system for system level contact characterization under environmental stresses is introduced.

In contact characterization under external stress, there are different levels of detail on which the studies can take place as illustrated in Figure 2.6. Traditionally, physics level tests are done within tribological domain of mechanical engineering. There, the contact normal force F_N , vibration frequency f , displacement of the contact members relative to each other δ , and ambient temperature T_{amb} are controlled. The aim is to have complete control of the parameters affecting the phenomena of electrical contact degradation described in the section above [83]. This information is most useful for initial design of an electrical contact, but might hide some effects of the real contacts, like design elements affecting the normal force of the contact during stress scenarios. Thus, an application level test has been devised [78], where a real contact is tested, but as many stress parameters as possible are independently controlled. Again, it will be difficult to link the controlled stresses to the actual stresses that the electrical contact will be subjected to during its typical lifetime usage scenario. For this purpose, this thesis introduces a system level test, where the external macro-parameters, like ambient temperature T_{amb} , the change rate of the ambient temperature $\partial T_{amb}/\partial t$, and acceleration $\partial^2 x/\partial t^2$, are controlled. In this case, all the typical contact stress characteristics are determined by the system design. This system level is the scope of this thesis, and has not been explicitly performed in the past. However, it is to be noted that most of the system level accelerated life tests (ALT) include this type of contact test implicitly. Thus, if the system test plan has been properly built, and the contact performance monitored through the tests, contact failures have been covered.

Typically, contact resistance measurement is simple. A test current is conducted through the contact-under-test (CUT) and voltage is measured over it. Then, contact resistance is determined as

$$R_{contact} = \frac{U_{contact}}{I_{test}} \quad (2.3)$$

In practice, there are a few details to take into account. If the test current is conducted through the same leads with which the contact voltage is measured (2-wire measurement in Figure 2.7a), resistance of the leads, and eventual contact resistance to the sample,

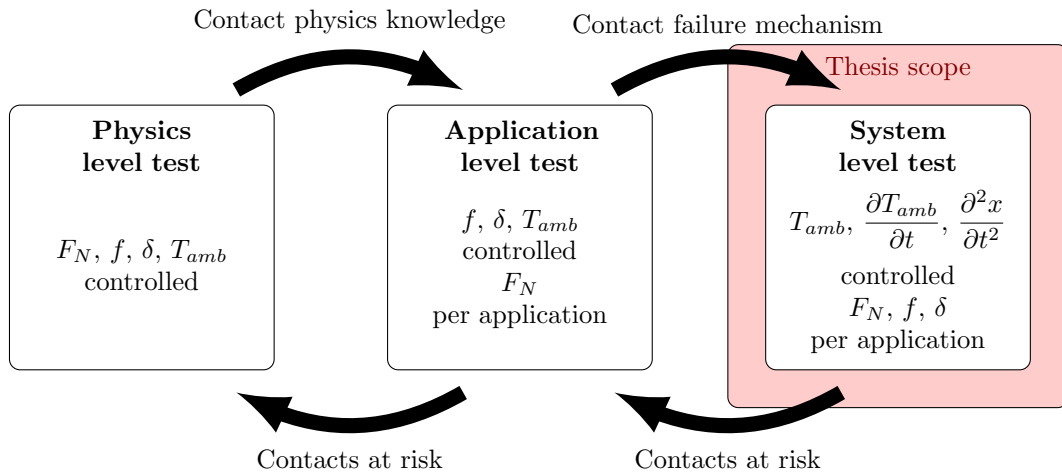


Figure 2.6 – Different levels of contact characterization tests

are added to the measurement results. In most cases, they are in between few hundred milliohms and a few ohms. A common way to circumvent this issue is to use separate leads and contact points for the test current injection and the contact voltage measurement on the contact bodies (4-wire measurement in Figure 2.7b). By this way, the voltage measurement is performed only over the CUT, and a correct resistance value can be measured. Now, the last challenge for measuring very low resistances is the accuracy and noise level of the voltage measurement. This is usually compensated by increasing the measurement current. However, the measurement current should be of the same magnitude as the current to be used in the application. Otherwise, there is a risk of heating up the CUT with the measurement current, which would provide artificially high resistance values compared to the real application.

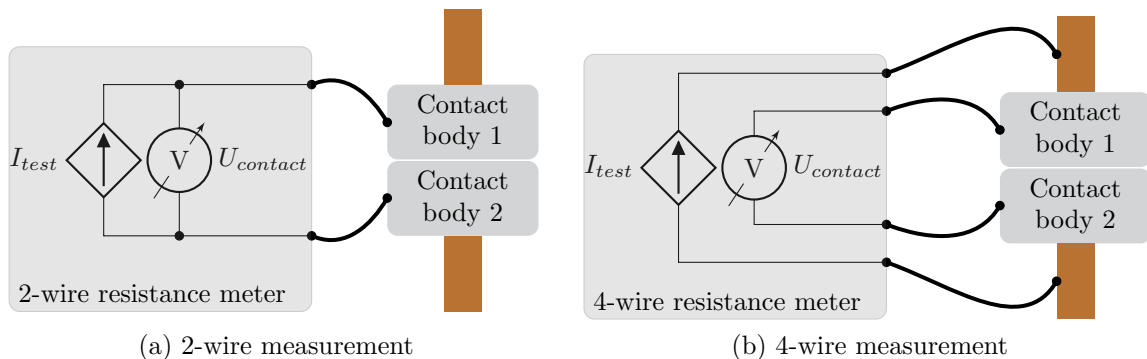




Figure 2.7 – 2- and 4-wire contact resistance measurement setups

In the frame of this thesis, two different 4-wire resistance measurement devices were used. As can be deduced from their parameters in Table 2.3, Aim TTi BS407 micro-ohmmeter can be used to measure very low levels of contact resistance, but it is slow as thermal electromotive force (EMF) compensation needs to be done manually [84]. On the other hand, the Agilent data acquisition (DAQ) system can measure relatively fast, and does automatic thermal EMF compensation, but cannot measure accurately below 10 m Ω [85]. Micro-ohmmeter has to be used to measure all the contacts introduced in Table 2.1, except springs, due to their low contact resistance. Springs have a higher contact resistance, and can be measured with the DAQ.

Table 2.3 – 4-wire resistance meters

Equipment	Aim TTi BS407	Agilent DAQ 34980A + 34921A + 34921T
Picture		
Smallest resistance range	1999 $\mu\Omega$	100 Ω
Measurement current	250 mA	1 mA
Measurement accuracy	0.1% \pm 8 $\mu\Omega$	0.01% \pm 4 m Ω
Practical measurement frequency	1/min	1/s

2.2.1 Contact Resistance Measurement under Environmental Stress

In measuring contacts between circuit boards and chassis structures the challenge is to connect reliably to the chassis structure during environmental stress. To simplify the measurement interface, it was decided to measure two contacts in series. This way, the 4-wire resistance measurement interface could be completely contained within the circuit board.

The aim of the tests was to represent different types of real products that have different mounting patterns, and whose circuit boards have components of vastly different masses. To do that, a collection of different test setups was devised as shown in Figure 2.8:

Small bare board represents a circuit board typically found in cameras and other small sensor equipment with only surface mount components.

Populated small board represents a similar sensor circuit board as above, but with some heavier power supply components.

Large bare board represents a typical ECU mainboard with only surface mount components.

Populated large board represents a large power supply circuit board or an EMI-filter circuit board of a high voltage power converter in an electric vehicle.

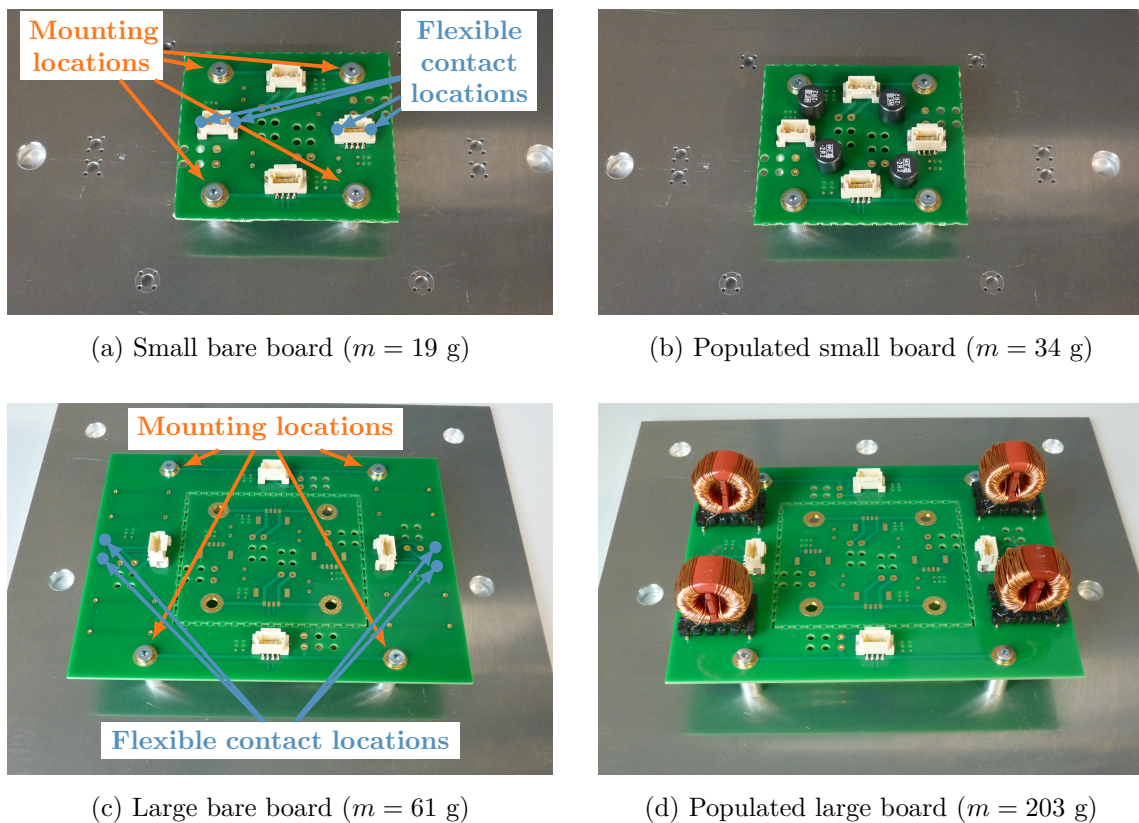


Figure 2.8 – Overview of the different contact resistance test setups

Locations for testing two types of electrical contacts were foreseen as shown in Figure 2.8: those used for mounting, and those providing some amount of flexible movement. Typical examples of mounting type of contact are screws and soldering. On the other hand, flexible contacts are usually some type of springs or conductive foams.

Figure 2.9 shows the test current path and voltage measurement traces in one of the contact pairs for a large and a small circuit board. Now, the most important part to

ensure is the contact between a circuit board mounting pole and the base plate. This contact needs to be significantly more reliable than any of the tested contacts between the mounting pole and the circuit board to ensure reliable test results. The design of the contact has a reservation for double mounting with screw and solder. However, a proper soldering method was not found in the frame of this thesis due to the preheating requirements posed by the aluminium base, and a short time frame of the flux effectiveness for the solder paste available. Thus, only screw connection had to be used. The M4 screws of class 10.9 were tightened to 3 Nm torque, and the mounting poles were verified to provide a maximum of $110 \mu\Omega$ of resistance between two circuit board mounting points.

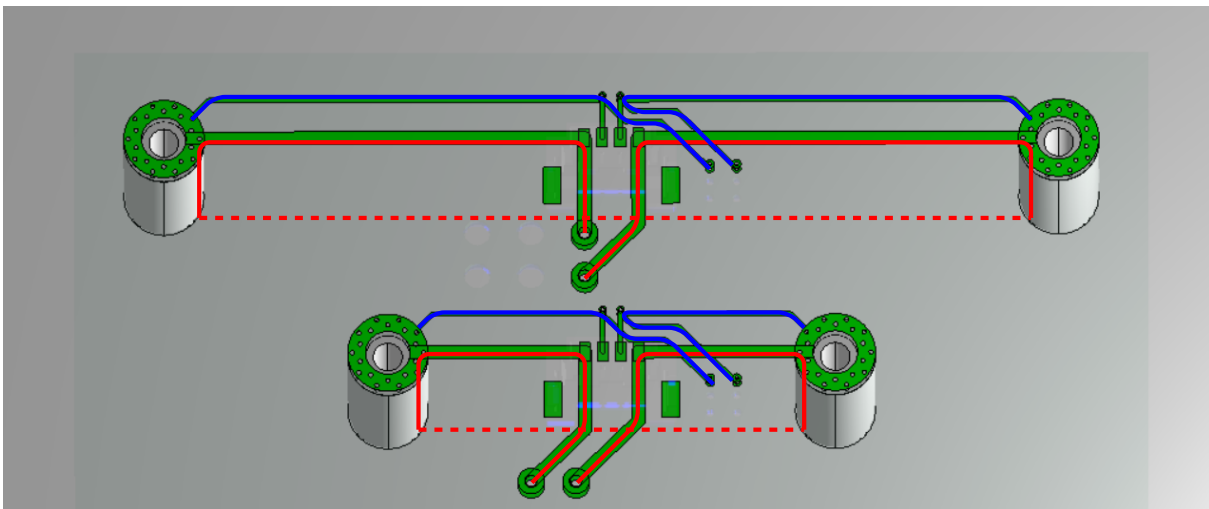


Figure 2.9 – Test current paths in red and voltage measurement traces in blue for the large and small circuit board mounts

A similar HALT cycle as described in Section 1.4 for shielded cables was used also for the circuit board ground contacts. The dwell-time at each test point had to be increased from five to ten minutes due to manual measurement configuration that needed more than five minutes for a complete data capture at each test level. The cycle shown in Figure 2.10 covers a typical automotive electronics application temperature range, which was from -40°C to 130°C for phase A. Then, five thermal cycles between -40°C and 125°C were conducted in phase B with $100^{\circ}\text{C}/\text{min}$ change rate request. Above 100°C , the change rate request had to be lowered to only $10^{\circ}\text{C}/\text{min}$ to prevent activation of thermal protection of the test chamber. This had only a limited effect on the harshness of the test as the inlet air had an overshoot well above the set point at that moment. In phase C, the vibration

stress testing was performed at controlled 25°C temperature stepping up vibration level in $10g_{rms}$ steps. The test system was brought into its limits, and thus, some measurements were done up to $80g_{rms}$, and some up to $90g_{rms}$ depending on the test setup performance. In Figure 2.10, the $90g_{rms}$ variation is shown. In phase D, the stresses of phase B and C were combined.

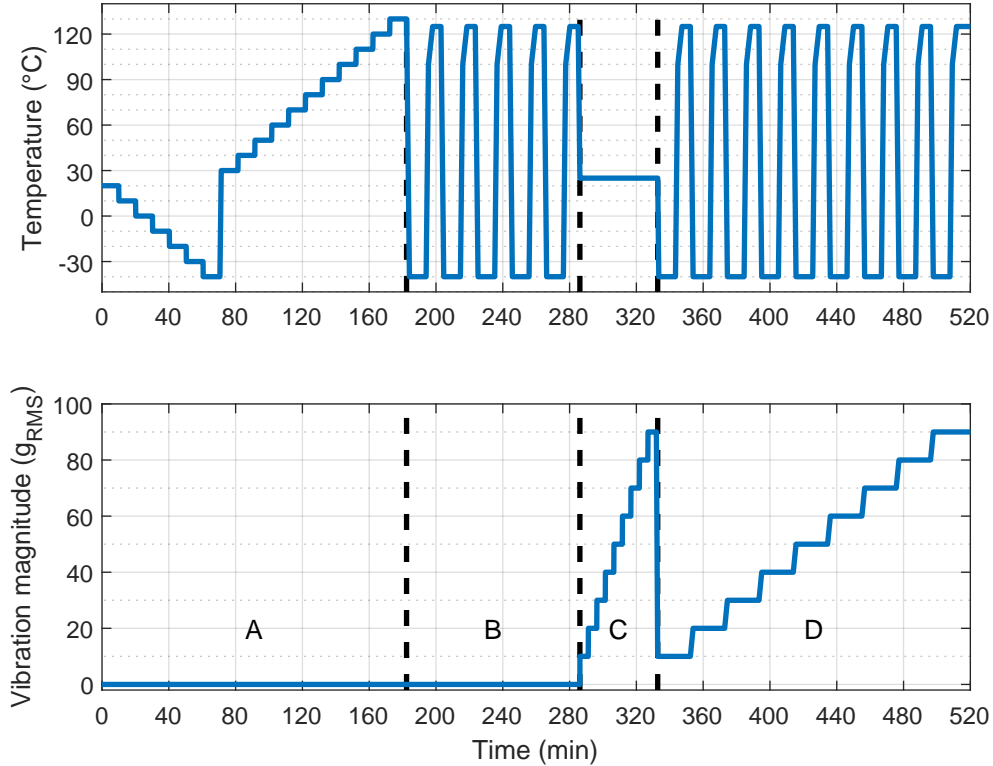


Figure 2.10 – HALT stress cycle for contact resistance tests

During the tests in HALT-chamber, four different contact resistance setups were installed simultaneously to speed-up the tests. Figure 2.11 shows a typical test configuration with equally distributed setups and air guides to ensure as uniform stress to the samples as possible.

Tested Contacts

The contacts tested in the frame of this thesis are shown in Figure 2.12. Two variants of screw and spring contacts were tested, whereas only one variant of a swaged contact was used.

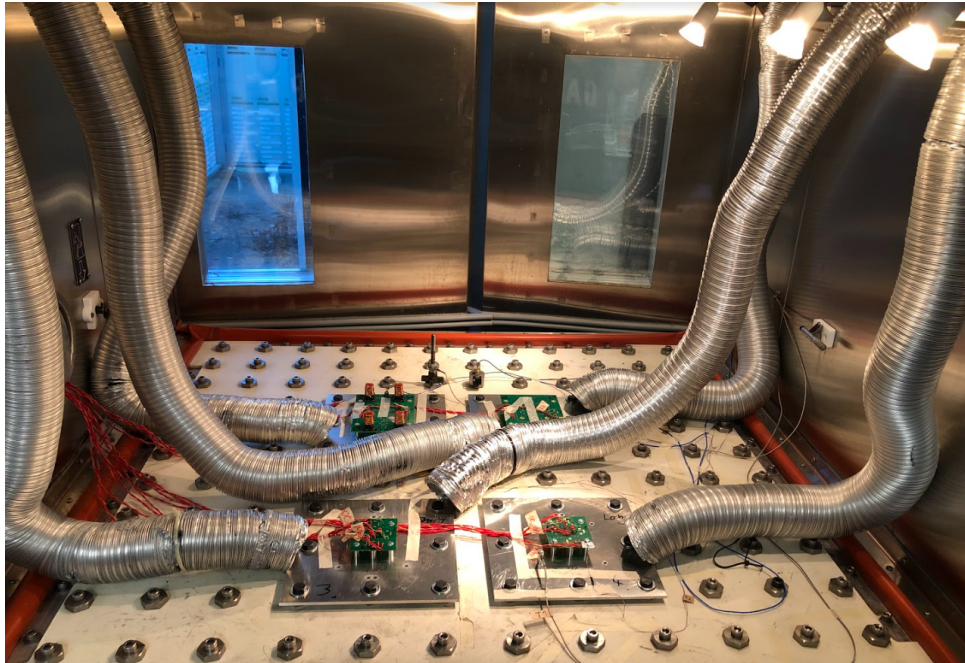


Figure 2.11 – Four contact resistance test setups installed in the HALT chamber



(a) Screw contact

(b) Swaged contact

(c) Spring contact

Figure 2.12 – Overview of the evaluated contacts

Table 2.4 describes properties of the different contacts. For screws, contact force and pressure were estimated based on Equations 2.1 and 2.2, respectively. For swaged contacts, some proprietary formulas were used to estimate the contact pressure. A maximum value was used for both the contact force and the contact area during pressure determination. For the spring contacts, contact force was estimated based on datasheet values, and the minimum contact pressure was determined based on the area of the fretting scar in an aged contact. Contact pressure at the beginning of the tests is expected to be up to ten times larger. Thus, the initial contact pressure was at the same level for all the contacts, and the contact resistance differences came more from differences in contact area and surface parameters.

Table 2.4 – Properties of tested contacts

	Screw 1 Nm	Screw 2 Nm	Swaged	Spring 1.5 N	Spring 3 N
Tightening torque	1 Nm	2 Nm	-	-	-
Contact force	750 N	1500 N	400 N	1.5 N	3 N
Contact area	50 mm ²	50 mm ²	18 mm ²	1 mm ²	1 mm ²
Contact pressure	15 $\frac{\text{N}}{\text{mm}^2}$	30 $\frac{\text{N}}{\text{mm}^2}$	20 $\frac{\text{N}}{\text{mm}^2}$	1.5 $\frac{\text{N}}{\text{mm}^2}$	3 $\frac{\text{N}}{\text{mm}^2}$
Contact material 1	AlSi1Mg	AlSi1Mg	AlSi1Mg	AlSi1Mg	AlSi1Mg
Contact material 2	ENIG	ENIG	ENIG	4 μm Sn over 2 μm Ni	4 μm Sn over 2 μm Ni

Transfer of Thermal Energy

Thermal energy transfer to the circuit board and its mounting structure was analysed, when they were mounted in a Hanse Environmental VTC-16 HALT test system. From the experience gained during the triaxial setup analysis in Section 1.3.3, only one configuration needed to be built with the air guidance arranged as shown in Figure 2.11.

The results of the thermal response measurements in Figure 2.13 show that the circuit board temperature follows closely the air temperature that is conducted to the chamber. The mounting locations and their corresponding contact poles that are placed close to the air stream from the air guides follow the chamber air temperature. However, the contact poles not in straight air stream lag behind the chamber air. Overall, the temperature re-

response is adequate taking into account the relatively large thermal mass of the aluminium plates, where the contact poles are mounted. As the circuit board follows the inlet air temperature, the contacts see a large thermal gradient during cyclic tests.

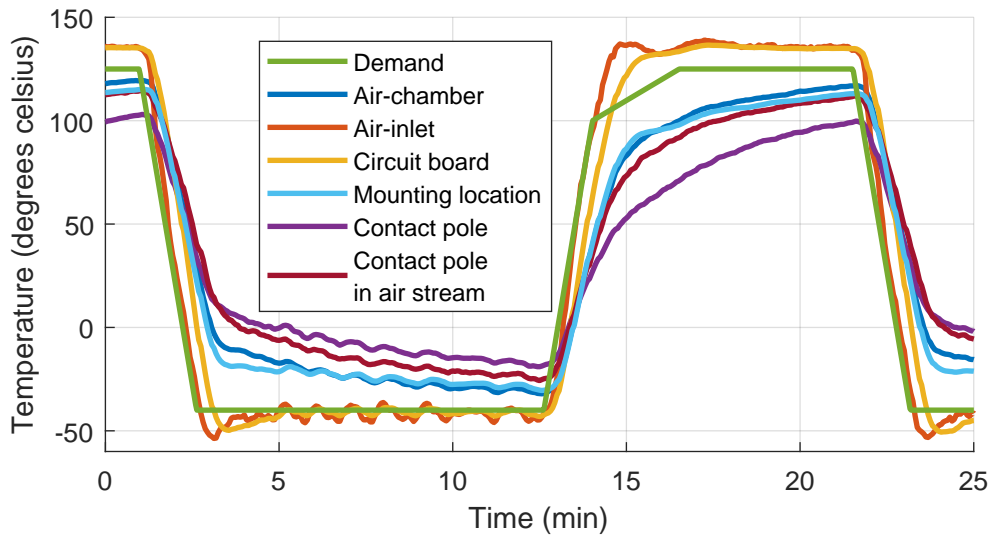


Figure 2.13 – Thermal response of the contact bench in HALT

Transfer of Vibration Energy

Similarly to thermal energy transfer, transfer of the vibration energy was analysed when the circuit boards and the mounting structures were mounted in a Hanse Environmental VTC-16 HALT test system. Here, several points needed to be analysed as there were four distinct test configurations with different masses as shown in Figure 2.8. Due to the limited time for the tests, only the larger circuit boards were analysed for the vibration response as the smaller boards can be assumed to be adequately represented by the data recorded close to the mounting locations of larger boards. Vibration amplitude in time domain together with the vibration power spectral density (PSD) was analysed similarly as explained for shielded cables in Section 1.3.4.

There were two significant locations of the circuit board, where acceleration measurements were needed: close to the mounting points, and between them, where flexible contacts could be tested. The acceleration sensor weight of 2 g was small enough to not have a significant effect on the behaviour of the circuit board. The time-domain responses at $10g_{rms}$ -level are in Figure 2.14. They were recorded during combined thermal

and vibration test at 125°C due to data capture issues on one test during pure vibration phase, which prevented proper comparison between different configurations. However, the results at high temperature are representative of the ones at lower temperatures. As could be expected based on the results in Section 1.3.4, vibration amplitude close to the mounting points was higher than that of the chamber vibration sensor. The amplitude measurement at the flexible contact test locations provided unexpected results: vibration amplitude with the populated circuit board was one half of that with the bare board. An explanation for this behaviour could be that the large chokes, which were mounted with epoxy glue all around the component bottom to the circuit board, actually made the circuit board more rigid, and damped the high frequency vibrations transmitted through the mounting points. This theory is amplified, when observing the PSD plots in Figure 2.15. With bare board, high resonance peaks are seen around one and two kilohertz, whereas similar resonance peaks are seen only above 2 kHz for the populated boards. This indicates that the populated board is more rigid than the bare board.

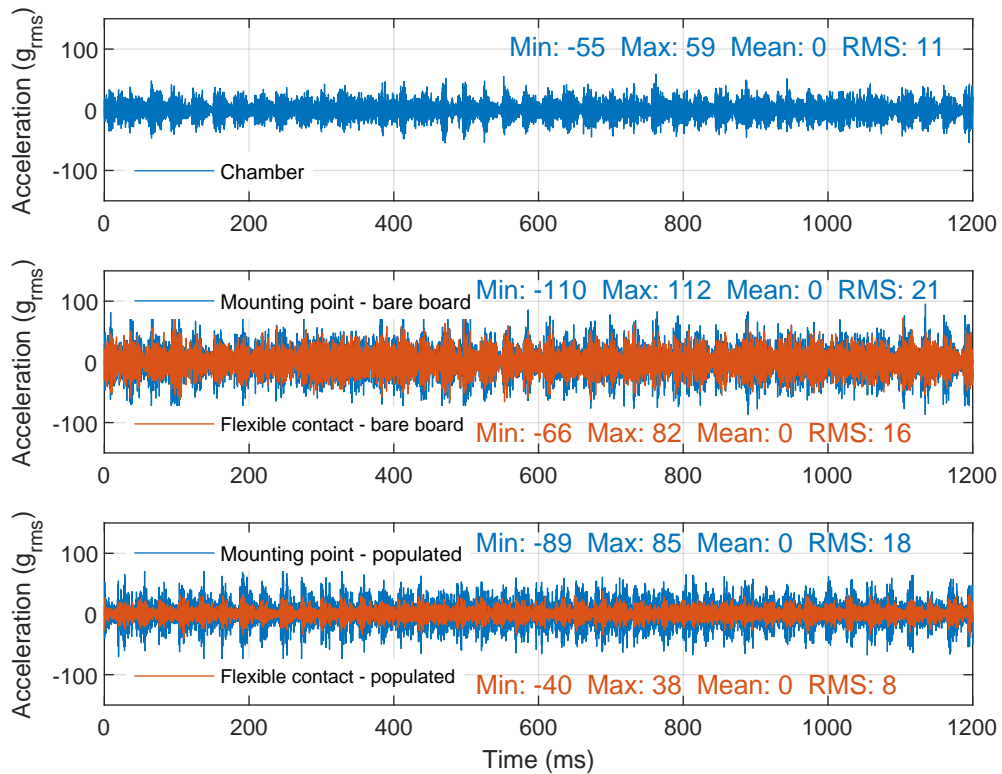


Figure 2.14 – Time domain vibration response of the circuit board ground contact measurement setup in HALT

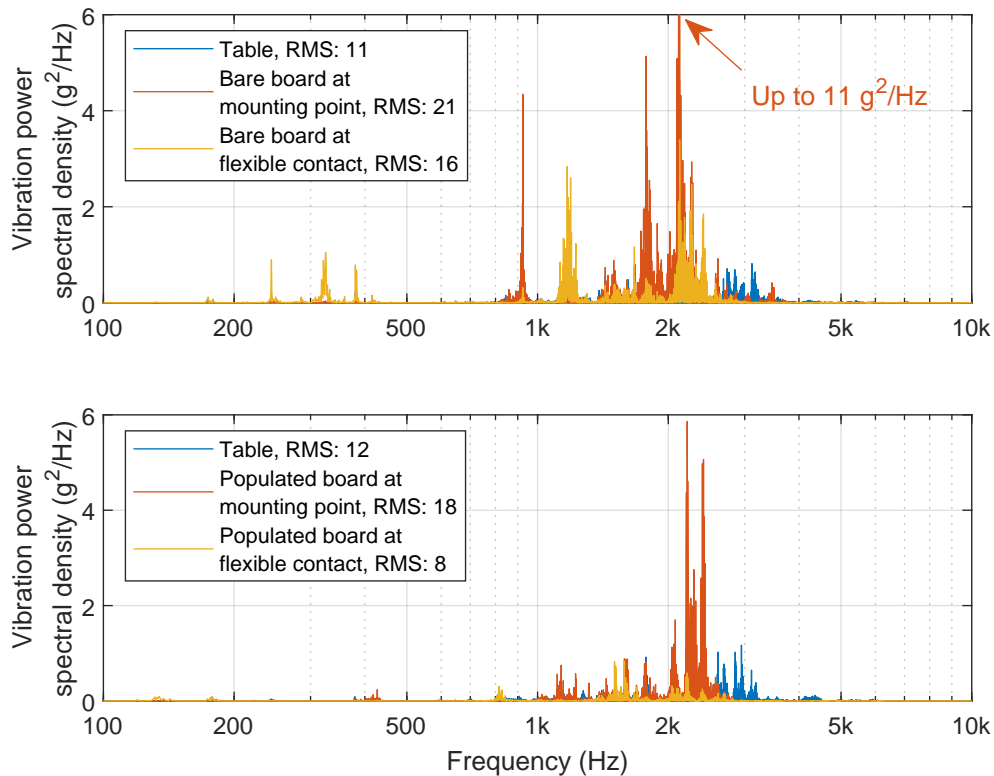


Figure 2.15 – Power spectral density plots of the time domain responses

Overall, the vibration energy was adequately transferred to the circuit boards under test. Amplification of the vibration amplitude up to twice the control point was seen for measurement points close to the mounting points. At flexible contact location, a smaller amplification was seen for a bare board sample, and a slight attenuation was seen for the populated circuit board. Also, it was evident from the PSD plots that the vibration energy was concentrated to lower frequencies at flexible contact test location compared to the mounting point. This is an expected result.

Measurement Uncertainty and Reliability

From measurement uncertainty point of view, the two equipment used (see Table 2.3) differ significantly. With the micro-ohm metre, a 10 % measurement uncertainty is achieved from 100 $\mu\Omega$ upwards, whereas the lower limit for the same uncertainty with the DAQ-system is 50 m Ω . Thus, it is clear that the DAQ-system cannot be used for most of the contacts as its measurement uncertainty is too high at low resistance values.

It was planned to verify the contact resistance measurement reliability during HALT by measuring a soldered contact, but a reliable soldering process for joining the contact poles made from Al6082 to the circuit board was not found during this thesis. However, as will be seen from the results in Section 2.3, the bare screw contact with sufficient mounting torque provided a reliable mounting of the contact poles to the aluminium base plate. Resistance from pole-to-pole measurement path of some selected screw and swage poles before and after the HALT cycle is shown in Figure 2.16. It can be deemed that the contact pole resistance decreased during HALT stress similarly to what will be shown for the screw contacts in Section 2.3. Thus, the pole-to-base screw connection is reliable enough for the measurements done in the frame of this thesis.

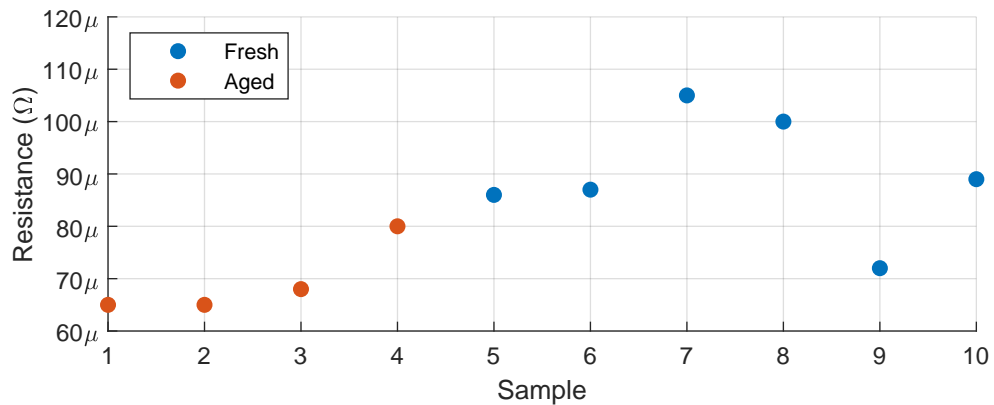


Figure 2.16 – Series resistance of two contact poles and the base

2.2.2 Conclusion on Contact Resistance Measurements

In the beginning of the section an argument was built to favour the measurement of system level contact parameters instead of physics or application level parameters. This approach enables using HALT and other system level accelerated stress testing methods to determine the reliability of electrical contacts in automotive electronics. For the circuit board ground contacts in the scope of this thesis, two different measurement systems were available: a micro-ohm metre and a data acquisition unit. The micro-ohm metre can be used to measure very low contact resistances, like those of typical ground contacts, but it has a low-pass filter and manual EMF compensation that limit the dynamic of the measurement. On the other hand, the data acquisition unit can be used to capture contact resistance data relatively fast, being able to capture momentary resistance changes during

environmental stress. However, due to its high measurement uncertainty at low resistance values it is usable only for relatively bad contacts.

As can be deduced from above, measuring low contact resistances fast, but reliably is a great challenge. If successful measurement approach could be defined, that would allow for better determination of instantaneous contact resistances during the environmental stresses. Prospective high-speed micro-ohm metres exist [86], but for effective use, they would need to be integrated with the temperature and vibration level measurements to correlate changes in contact resistance to transients happening in temperature or vibration amplitude. It was not done in the frame of this thesis, but it is a clear path forward for better system-level contact characterization.

A reliable test system needs a good jig to properly transfer the environmental stresses to the contacts. A circuit board based test system was designed for this thesis, and it was verified to properly expose the tested contacts to thermal and vibration stresses used within HALT tests. An out-of-the-ordinary observation was done for the populated circuit boards that actually imposed less vibration stress to the spring contact locations in the middle of the circuit board, compared to a bare board. The reason was deduced to be the mounting of the large components with epoxy glue that both prevented them from disintegrating during the tests, but also made the circuit board more stiff.

2.3 Contact Resistance of Circuit Board Ground Contacts During Environmental Stress

This section discusses the measurement results of HALT stress tests for contacts as described in Section 2.2.1. To evaluate the effectiveness of the contacts, a limit value for the contact resistance was applied. A default limit of 10 m Ω [83] was applied to screw and swaged contacts, but springs were expected to have a higher initial contact resistance as shown in test report for the spring family [87]. Thus, a higher 100 m Ω failure limit was applied for them.

Although there were two contacts in series, it is very rare that both fail at the same time. For that reason, it is justifiable to account the total measured contact resistance to the weaker contact. With maximum error, the real contact resistance is one half of the measured value.

2.3.1 Thermal Stress

Thermal stress testing was performed in two phases: A and B of Figure 2.10. First, a temperature sweep from -40°C to 130°C was done while contact resistance was recorded every 10°C step. Then, five thermal cycles between -40°C and 125°C were conducted. Resistance measurements were done at the extreme temperature levels: a minimum of -40°C shown with blue colour in the following figures, and a maximum of 125°C is shown with red colour.

Screw contact resistance dependency on thermal stress is shown in Figure 2.17. The temperature sweep shows a rising trend as a function of temperature for all the contact samples. On average, the contact resistance rises by $2\%/10^{\circ}\text{C}$. Some of the contacts that were mounted with a lower 1 Nm torque show a non-linearity in their contact resistance that is due to initial settling of the contact during which the contact resistance rises slightly. During cyclic thermal stress, all contact resistances increased over the stress cycles. An average increase was $8\%/cycle$.

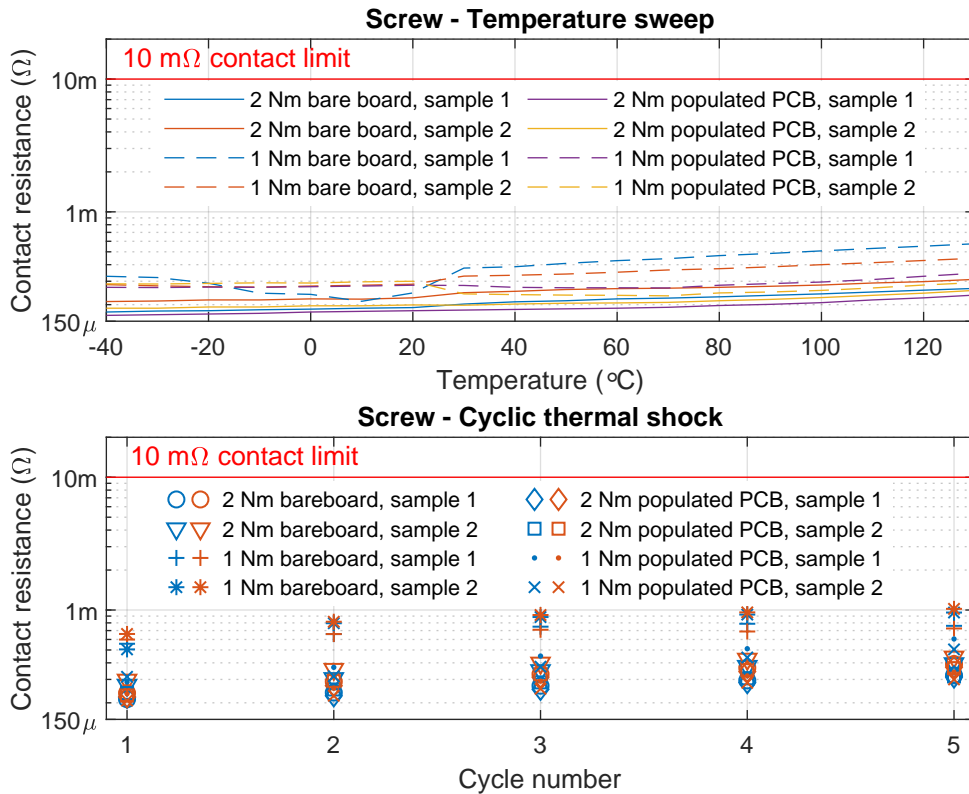


Figure 2.17 – Screw contact resistance during thermal stress

Swaged contact resistance dependency on thermal stress is shown in Figure 2.18. The temperature sweep shows a rising trend as a function of temperature for all the contact samples. The bare board sample 1 has somewhat higher contact resistance from the beginning than the other samples. On average, the contact resistance rises by 2%/10°C, which is the same amount as for screw contacts. During cyclic thermal stress, all contact resistances increased over the stress cycles. An average increase was 11%/cycle, which was slightly higher than that of the screw contacts.

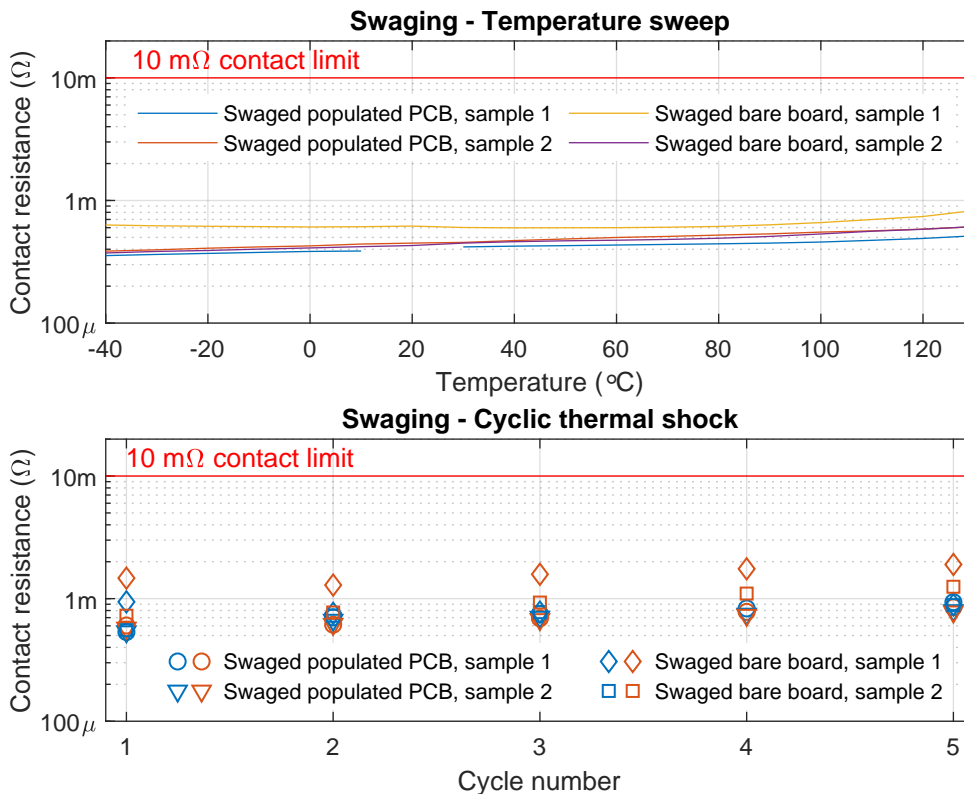


Figure 2.18 – Swaged contact resistance during thermal stress

Spring contact resistance dependency on thermal stress is shown in Figure 2.19. There is a high sample-to-sample variation below 10 mΩ due to the DAQ accuracy issues, but as the values are a decade lower than the contact performance limit, this inaccuracy was accepted. Moreover, the high force contact sample 2 on populated circuit board demonstrated contact resistance at low milliohm range, which was below the measurable range. The temperature sweep does not show a clear trend on any of the spring contacts. The higher contact force sample 1 with populated circuit board shows an increased contact

resistance over 100°C. This could be due to lost contact force from softening of the circuit board, but the result is inconclusive, because the same cannot be observed for other contacts. During cyclic thermal stress, no average changes in contact resistance over the thermal cycles was observed. However, some of the contact resistances clearly depended on the phase of the cycle. The high force spring on a bare board sample 2 demonstrated a large contact resistance increase during rapidly increasing temperature that then stabilized during constant temperature phase, and temporarily reduced during rapidly decreasing temperature. On the other hand, sample 1 of the same spring contact configuration demonstrated an opposite behaviour. In addition, there were spring contacts, like the ‘low force bare board sample 2’, whose contact resistance stayed stable over the cyclic stress. Thus, no conclusive performance observation could be done other than noting that all the contacts stayed functional over the thermal stresses.

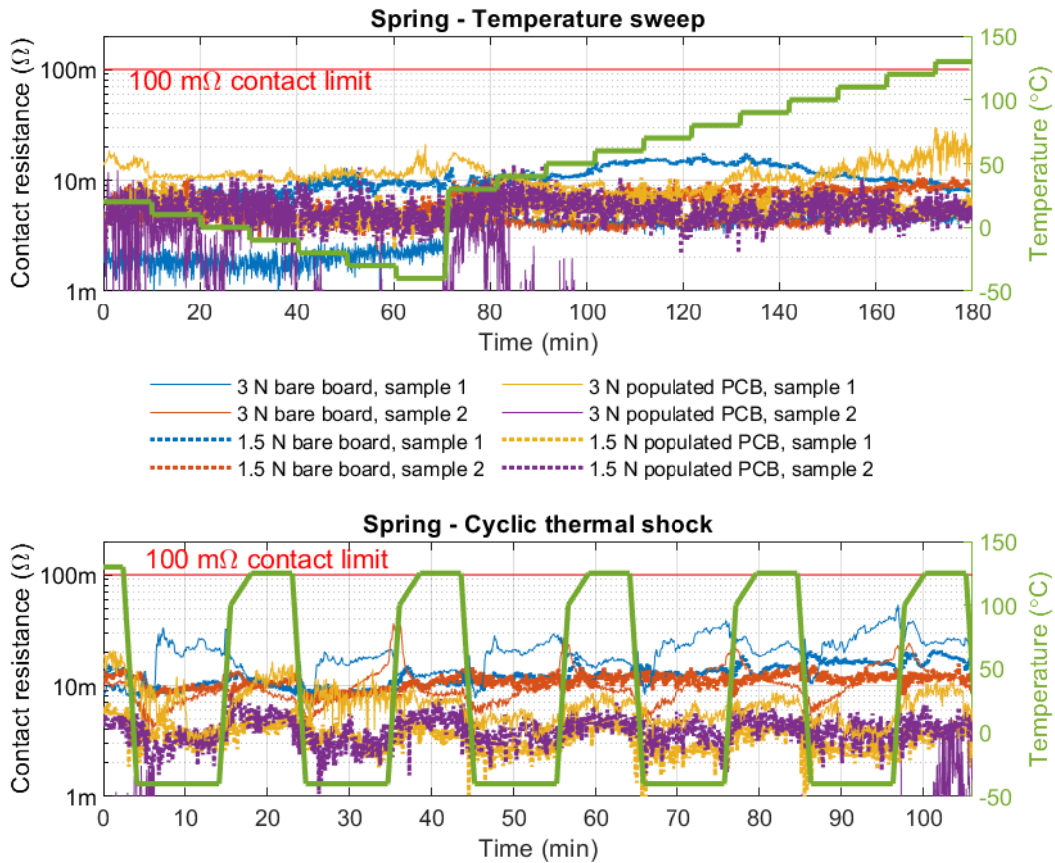


Figure 2.19 – Spring contact resistance during thermal stress

Overall, all the contacts performed well during thermal tests, but some increase of contact resistance was seen during thermal cycles for screw and swaged contacts. This could be due to slight loosening of the contact and could be amplified during long term cyclic thermal stress. Thus it is important to apply a correct amount of lifetime thermal cycles for those contacts during design verification. In automotive use cases that number is definitely larger than five that was used in this test. However, the thermal gradient is normally not as high as the 100°C/min used in this test. This thermal gradient is also expensive to achieve due to need of high power heating elements and liquid nitrogen cooling. Thus, in the future, it is recommended to use other methods like refrigerated thermal chambers for the cyclic thermal evaluation with more cycles. Spring contacts demonstrated a higher initial contact resistance than the screw and swaged contacts, but no evidence on their thermal ageing could be gathered. Thus, they seem to perform better over thermal stress cycles, but it was observed that momentarily their contact resistance can be affected by large thermal gradients.

2.3.2 Vibration Stress

Vibration stress testing (phase C in Figure 2.10) was performed at controlled 25°C temperature while the contact resistance of the contacts was recorded at every 10 g_{rms} step of vibration amplitude. Some measurements were recorded up to 80 g_{rms} , and some up to 90 g_{rms} level depending on the setup performance.

Screw contact resistance dependency on random vibration amplitude is shown in Figure 2.20. At low vibration levels there was a variation between decreasing, constant, and increasing contact resistance depending on the contact, but once the vibration amplitude was increased, all contacts demonstrated decreasing contact resistance indicating that the applied contact pressure from screws and the harsh vibration caused increase of either the asperity spots or their size. An average reduction in contact resistance of -8%/10 g_{rms} was observed.

Swaged contact resistance dependency on random vibration amplitude is shown in Figure 2.21. Initially, up to 50 g_{rms} or 60 g_{rms} , contact resistance decreases indicating that the pressure applied between the swaged aluminium pole and the gold-plated copper barrel on the circuit board together with vibration increases either the amount or size of the contact asperities. An average decrease of contact resistance by -9%/10 g_{rms} was observed up to 50 g_{rms} . However, a clear change to increasing contact resistance is seen over 60 g_{rms} , which indicates that the contact is stressed above its best performance area.

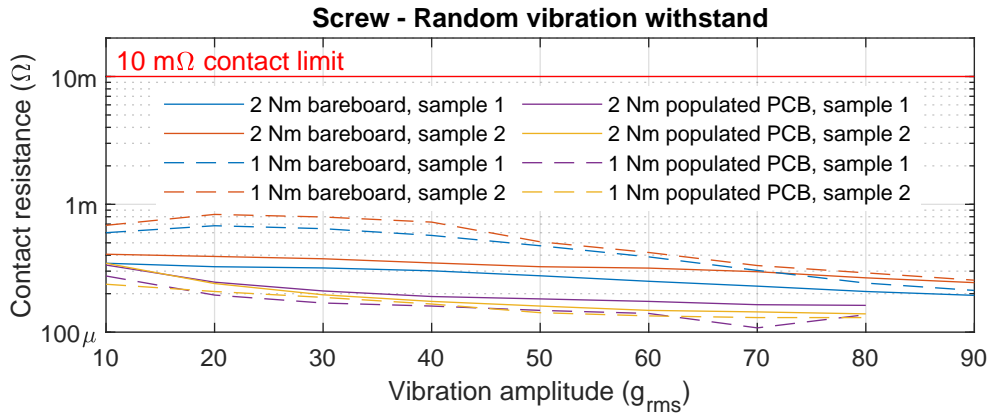


Figure 2.20 – Screw contact resistance during vibration stress

An average increase of contact resistance by 30%/10 g_{rms} was observed between 60 g_{rms} and 90 g_{rms} . At the highest 90 g_{rms} vibration level, the ‘bare board sample 1’ contact fails. Further failure analysis is shown in Section 2.3.4.

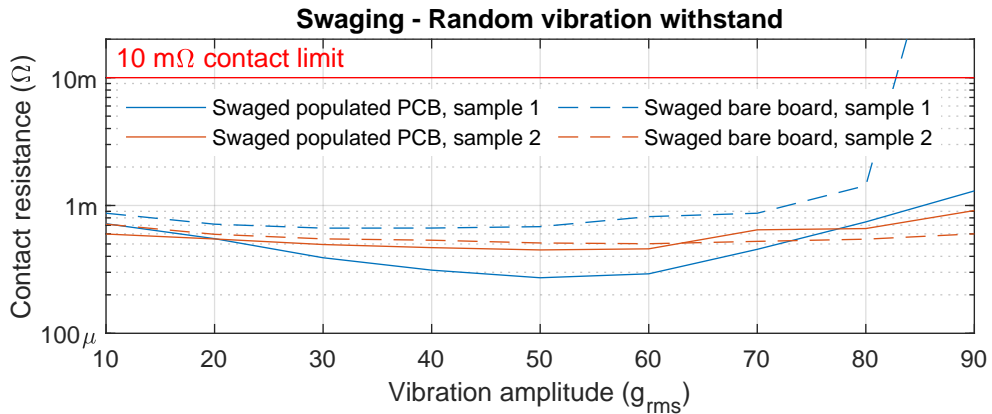


Figure 2.21 – Swaged contact resistance during vibration stress

Spring contact resistance dependency on random vibration amplitude is shown in Figure 2.22. All spring contacts failed during the vibration test, but failure levels were fairly different. First contacts failed already at a low 10 g_{rms} vibration level, and failures mounted as the vibration amplitude was increased. The last spring failed at 50 g_{rms} level. As the vibration stress was removed at the end of the test, none of the contacts returned back to working state. A typical result of worn down contact areas and broken springs is shown in Figure 2.23. It illustrates well that the vibration stress applied was over the

design limit of the springs and a more robust design is needed to match the vibration withstand levels of screw or swaged contacts. Further analysis of the wear pattern on the intact, but aged, spring contact is shown in Section 2.3.4.

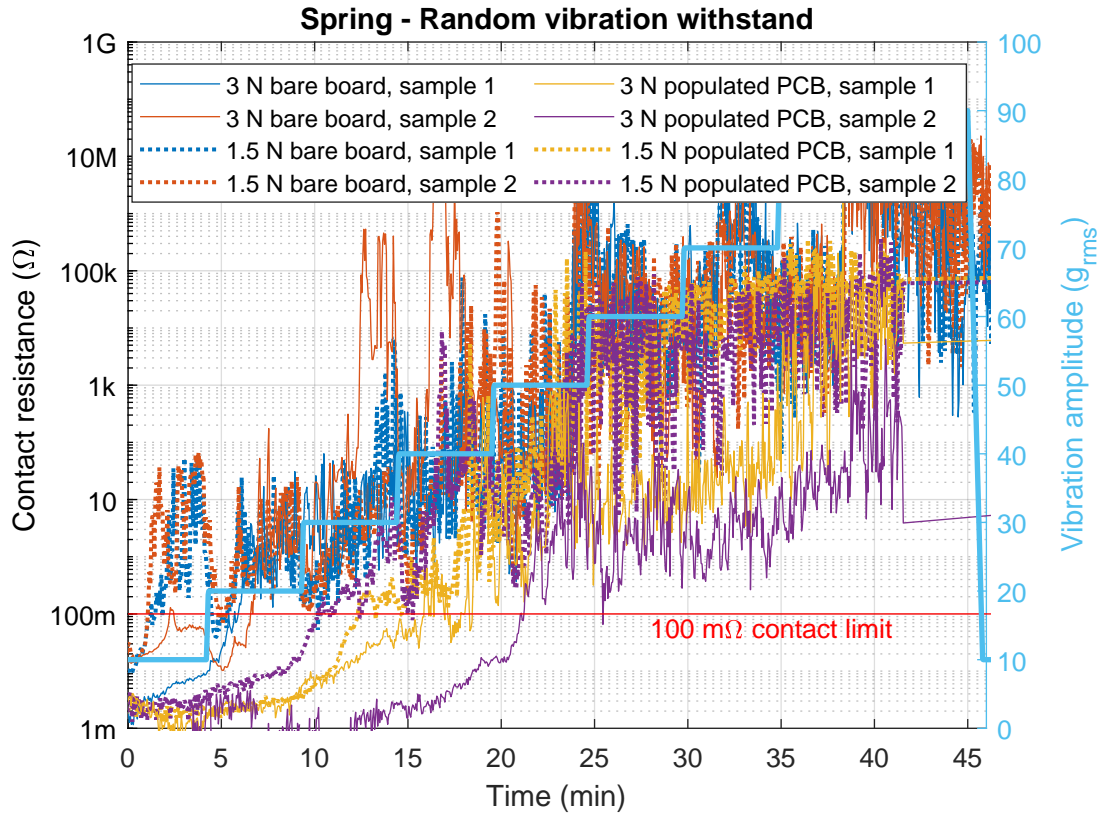


Figure 2.22 – Spring contact resistance during vibration stress

During vibration, a clear order of technical performance between the contacts was established. The performance of the screw contacts actually increased as the vibration level was increased. This is likely due to sufficient mounting torque that ensured good contact pressure, which was able to cause the formation of new contact spots and/or enlarging of the old ones, when combined with vibration stress. For swaged contacts similar performance was seen up to $60g_{rms}$, after which a fairly rapid performance degradation was seen on all contacts eventually leading to a failure of one contact sample at the highest $90g_{rms}$ vibration level. The worst performance was achieved with spring contacts that all failed during vibration between $10g_{rms}$ and $50g_{rms}$ levels. In conclusion, the screw contact can be used in any vibration situations, a swaged contact can be used over low to medium vibration amplitudes, and the tested spring contact cannot be recommended to be used

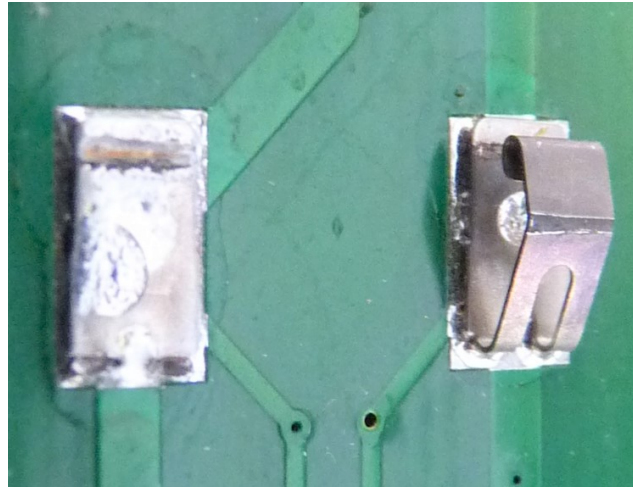


Figure 2.23 – Spring contacts after vibration stress - one spring has broken out, and the other has severe wear marks on its contact surface

in any vibration environments without design changes. If its vibration performance variability could be reduced by e.g. different plating materials, the spring contact could be recommended for use in low vibration environments.

2.3.3 Combined Thermal and Vibration Stress

In combined thermal and vibration stress tests (phase D in Figure 2.10), the previous cyclic thermal and vibration stresses were applied simultaneously to see if the stress combination would accelerate some failures. The contact resistance was measured at different vibration steps of $10g_{rms}$ increment up to $80g_{rms}$ or $90g_{rms}$ depending on setup performance at two different temperatures: at a minimum of -40°C shown with blue colour in the following figures, and at a maximum of 125°C shown with red colour.

Screw contact resistance dependency on combined thermal cycling and increasing random vibration is shown in Figure 2.24. Again, as was the case for the triaxial measurement setup in Chapter 1, some configurations of the test bench started to be at the edge of their performance. Namely, connectors were used to connect the measurement wires to the circuit boards under test to speed-up the test preparation in the beginning. However, some faults due to connector issues were noticed, and later tests were made with measurement wires soldered on the circuit boards. Unfortunately, not all the tests could be redone with soldered measurement wires due to time limitations on the HALT chamber availability. However, as it will be shown in Section 2.3.4, none of the screw contacts

failed during these tests, and the missing measurement results are an annoyance without hiding any important details. At moderate vibration levels up to $40g_{rms}$, screw contacts demonstrated a slightly increasing contact resistance, most likely due to thermal cycling, with an average increase of $5\%/cycle$. At high vibration levels, the ageing effect of thermal cycles was negated and the contact resistance decreased by $-10\%/10g_{rms}$ between $40g_{rms}$ and $90g_{rms}$ resulting lower and more tightly bound group of contact resistances than in the beginning of the tests.

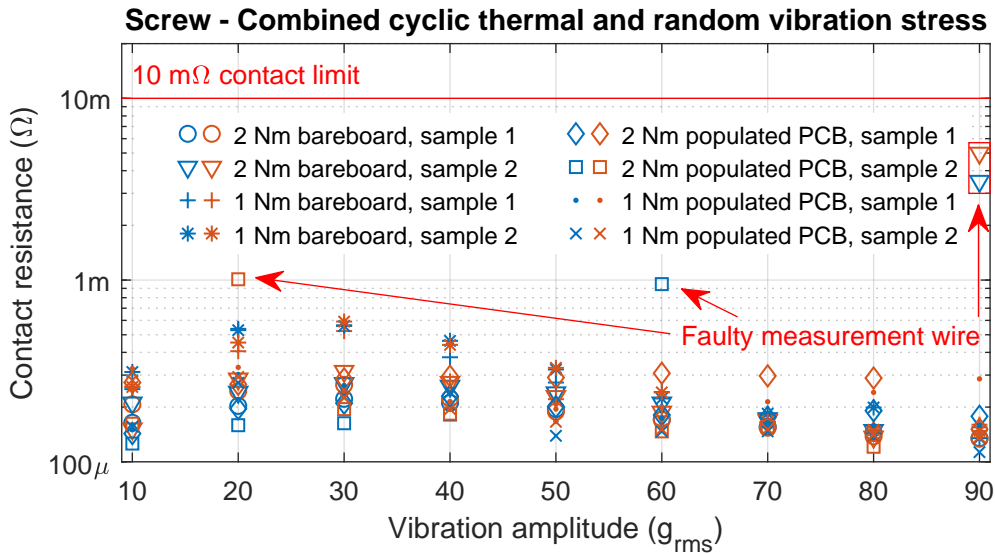


Figure 2.24 – Screw contact resistance during combined thermal and vibration stress

Swaged contact resistance dependency on combined thermal cycling and increasing random vibration is shown in Figure 2.25. The contact that had failed at the end of the vibration tests initially failed the contact performance limit, but during mild and medium vibration at low temperatures, its contact resistance reduced to an acceptable level. This indicates that at cold temperatures the circuit board shrinkage was large enough to increase contact pressure and lower contact resistance, despite damage caused in vibration. Then, at high temperatures the circuit board expanded and the electrical contact failed to a relatively high resistance level. In addition to the already failed contact, a second contact of ‘populated circuit board sample 2’ failed at $80g_{rms}$ level. For the contacts that did not fail, no clear trend of contact resistance over the stress amplitudes could be determined. The measurement results varied slightly, but ended up with similar values at the beginning and the end of the tests.

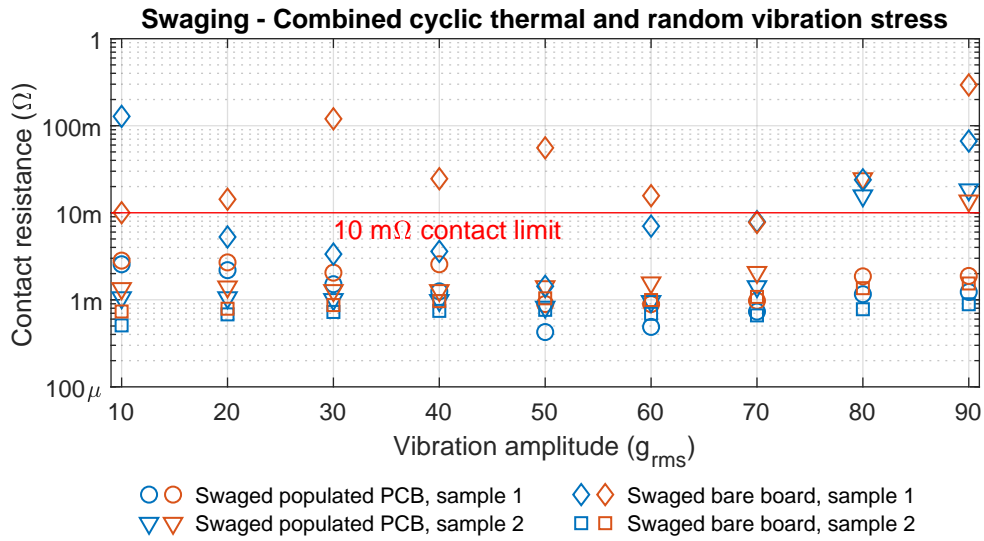


Figure 2.25 – Swaged contact resistance during combined thermal and vibration stress

Spring contact resistance dependency on combined thermal cycling and increasing random vibration is shown in Figure 2.26. It is to be noted that all the spring contacts started this test from a failed level, and thus, no significant conclusions can be done from these results. Due to limited HALT chamber slot, there was no time to replace the springs and their contact poles to redo just the combined cyclic thermal and vibration test with fresh spring contacts. If that would have been done, it is likely that similar phenomena as in vibration test Figure 2.22 would have been observed. Now, the most interesting observation that can be done from Figure 2.26 is that during rapid thermal transients, especially when decreasing the temperature, the contacts that were mechanically intact exhibited fairly low contact resistance values with the best ones even reaching the area of good contact resistance. This signifies the large span of possible contact resistances that can be measured with damaged springs, which can sometimes make failure analysis difficult as in certain situations a clearly failed spring contact can exhibit acceptable contact resistance values.

Overall, during combined cyclic thermal stress and random vibration, results from pure vibration tests were amplified. The screw contacts performed again the best, and their contact resistance decreased even further from the vibration tests, although at low vibration levels the thermal cycles actually increased the contact resistance over a few cycles. The swaged contacts came second in performance evaluation with a second contact failing at high vibration level. However, the remaining contacts that were intact did not

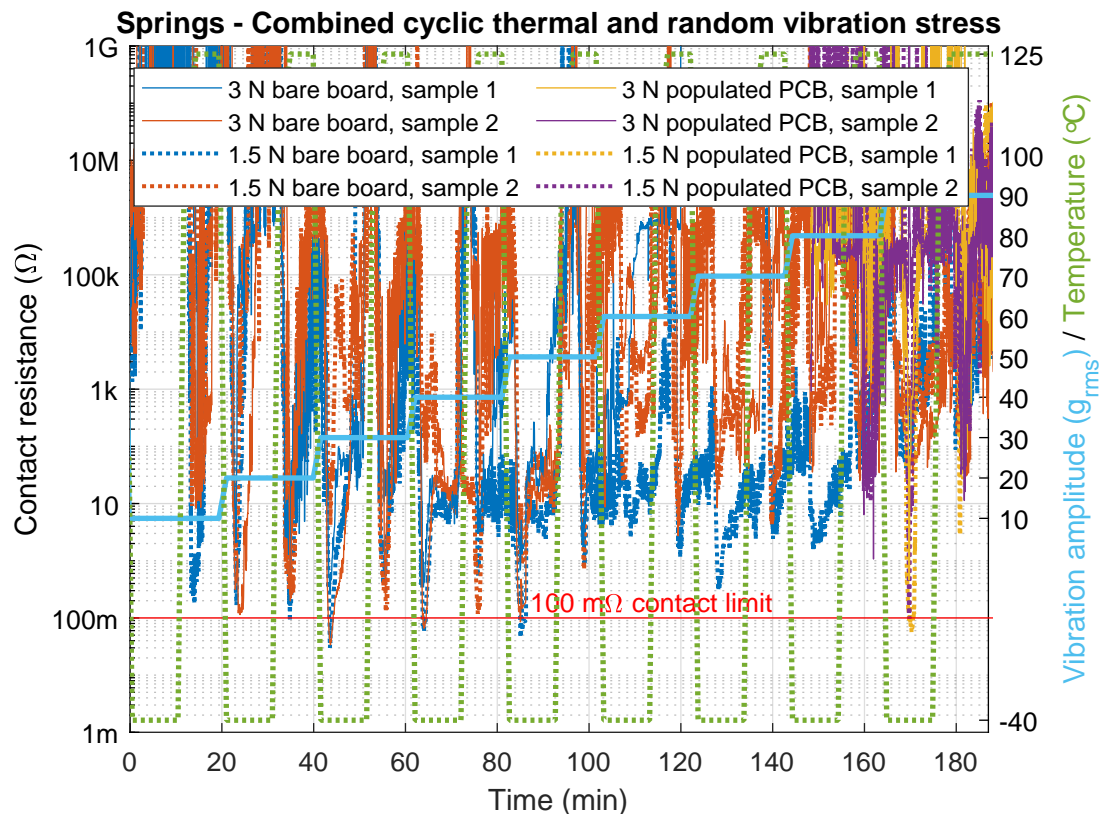


Figure 2.26 – Spring contact resistance during combined thermal and vibration stress

demonstrate any ageing over the stress cycle. Finally, all spring contacts started the test from a failed state, and no great conclusion can be made for them. If test time would have allowed replacing the springs with fresh ones for this test, the results would have likely followed the ones of the pure vibration test. However, an interesting note can be made that even if all the springs had failed, some of them returned to acceptable contact resistance state under thermal transients. This signifies the fact that it can be sometimes difficult to recognize a failed contact as it can return to conducting state under a specific set of environmental conditions. This has been recognized to be a challenge for other contacts, too [88].

2.3.4 Thermal and Mechanical Ageing

In this section, the contact resistances of fresh and aged contacts are compared. The ageing stress cycle was the one described in Figure 2.10. After a global view on contact

performance has been discussed, typical findings on contact surfaces are discussed with the help of microscopic images. Further analysis could be done with more advanced methods, but was not pursued as the equipment for those analyses was not available in the frame of this thesis. For fretting scars, performing scanning electron microscopy (SEM) would provide more accurate images on the surface and could possibly extract surface topographical data. Comparing that data between fresh and aged results could provide more insights on the severity of surface scarring. Energy-dispersive X-ray spectroscopy could be used on the scarred surfaces to determine the atomic material composition of the scars. This analysis could be especially interesting for the gold-plated circuit board pad that had wear marks. It could be determined if any aluminium deposits from the mounting pole have been transferred onto the gold plating. Finally, cross-sectional analysis of the swaged contact could provide more information on the reasons of failure, and on the exact failure mechanism.

The global ageing results are in Figure 2.27 as measured at ambient temperature before and after the ageing stress. The error bars in the figure show the difference between minimum and maximum measured values. Screw contacts start with a low value of contact resistance in hundreds of micro-ohms, and end up with even lower values that are very close to the resistance offset of the measurement setup meaning that no significant contact resistance exists in the connection at the end of the ageing cycle. Swaged contacts performed slightly worse when fresh, and experienced clear ageing over the ageing cycle. While the intact contacts had still acceptable contact resistance, damaged contacts discussed in the sub-section below had a contact resistance well above the contact failure limit. Contact resistance with fresh spring contacts was at a similar level as that for the intact aged swaged contacts. As could be seen in previous sections, all the spring contacts failed during the tests, and that is confirmed by the ageing test results: measured contact resistance was above the contact failure limit for all the aged spring contacts.

Aged screw contact

Microscopic images of fresh and aged screw contacts are shown in Figure 2.28. The fresh pole shows some machining imperfections, but no damage, and the fresh circuit board pad has an excellent surface. Even though the contact resistance measurements did not reveal it, the aged pole has quite some oxidation damage on it. It is most likely due to stick-slip fretting. A reason, why the contact resistance values kept improving over the ageing cycle, could be the bright area of the contact that looks very much like a large

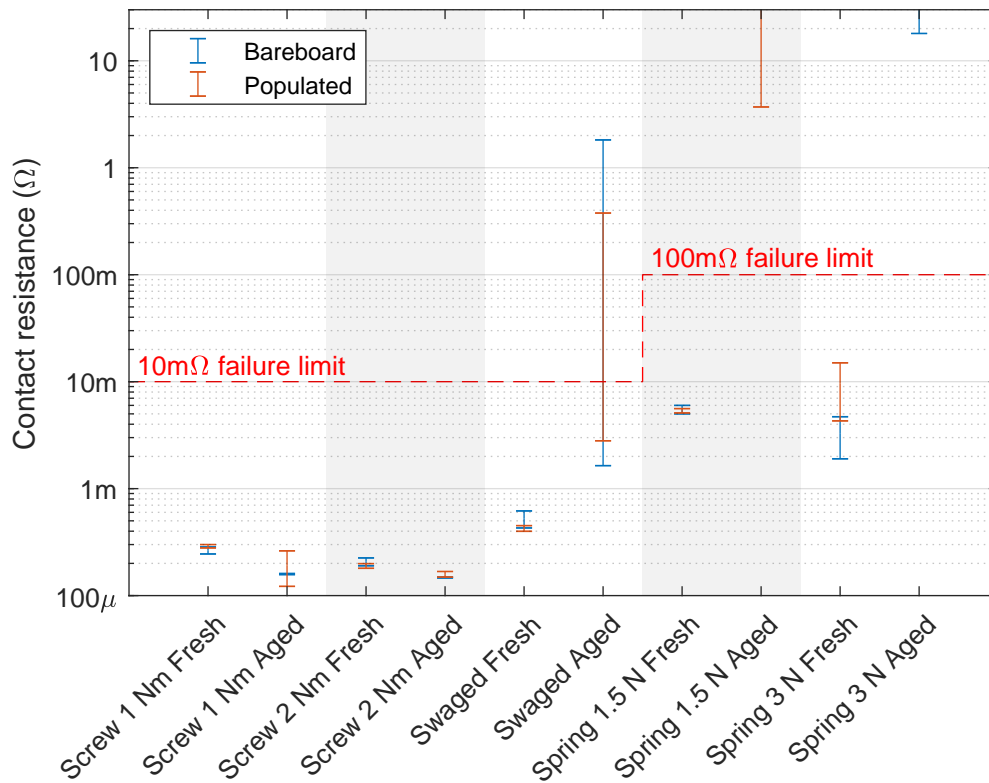


Figure 2.27 – Contact resistance of fresh and aged contacts

contact asperity spot formed by cold welding.

Aged swaged contact

Microscopic images of intact and damaged swaged contacts are shown in Figure 2.29. The intact contact looks like a new one, whereas the damaged contact has a clear break at the end of the stress relief. Zooming to that, the breakage of the copper layer is clearly visible, and the contact was held together with just some glass fibre strings of the circuit board core. The next phase of the failure analysis would be to mould the intact and damaged connections to epoxy, and do a cross-section comparison of the two contacts to perform a more detailed damage analysis. However, proper equipment for that was not available in the frame of this thesis, and no further damage analysis is done.

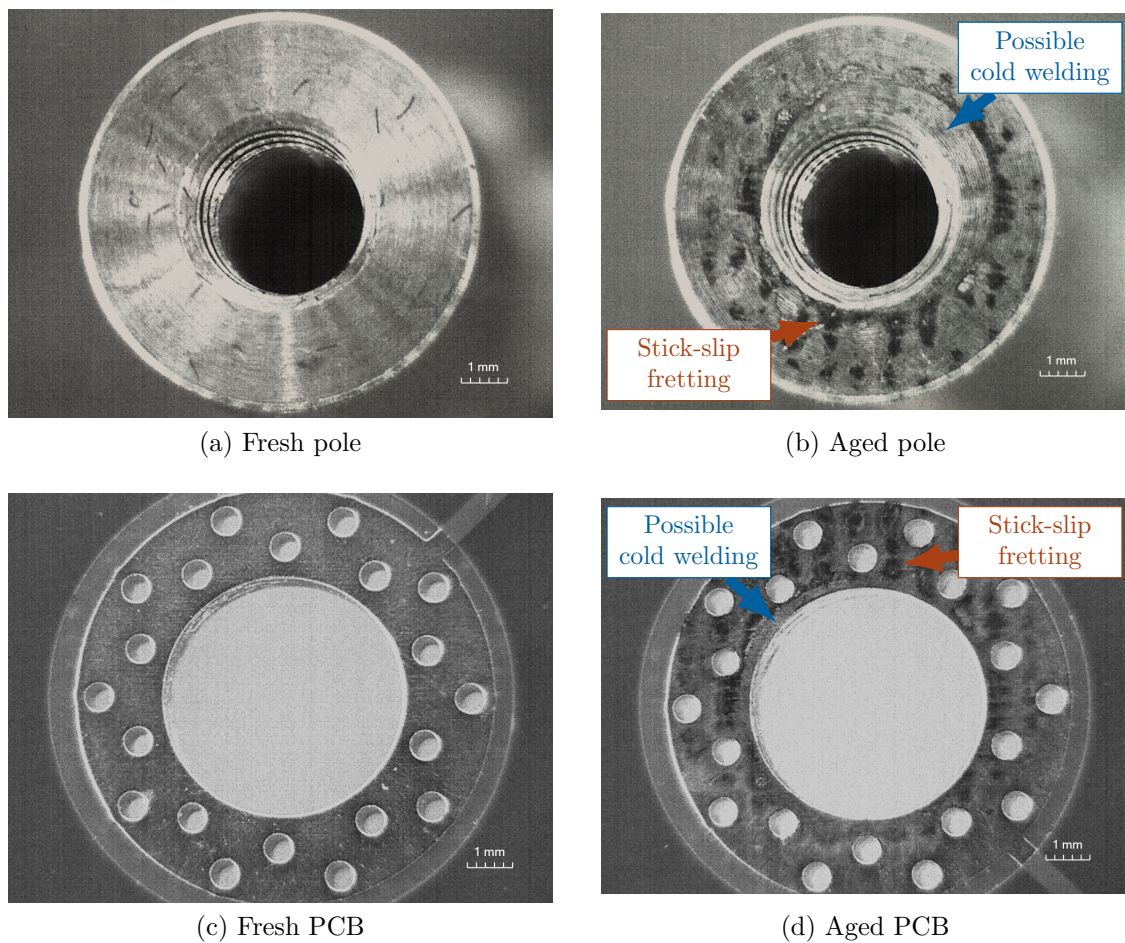


Figure 2.28 – Fresh and aged screw contact surfaces

Aged spring contact

Microscopic images of fresh and aged spring contacts are shown in Figure 2.30. Both the aged spring and pole show significant loss of material at the contact area in addition to oxide debris. The zoomed pictures of fresh and aged poles at the spring contact area signify the difference. Wear shown is likely due to gross-slip fretting (see Section 2.1.6) at the contact area, which leads to quick destruction of the contact surfaces as seen in here. The contact pressure values reported earlier in Table 2.4 were calculated based on the dimensions of the fretting scar. After wear, contact pressure is at such a low level that even without oxide debris in the scar, the electrical contact formed would be bad.

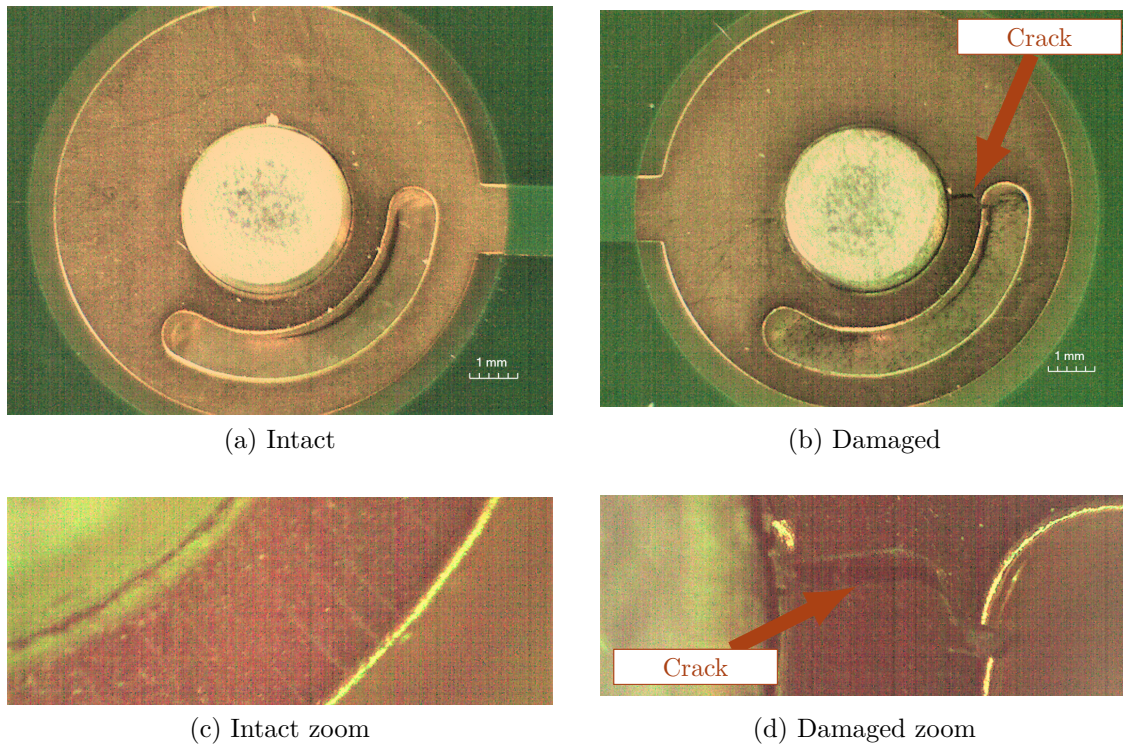


Figure 2.29 – Intact and damaged swaged contacts

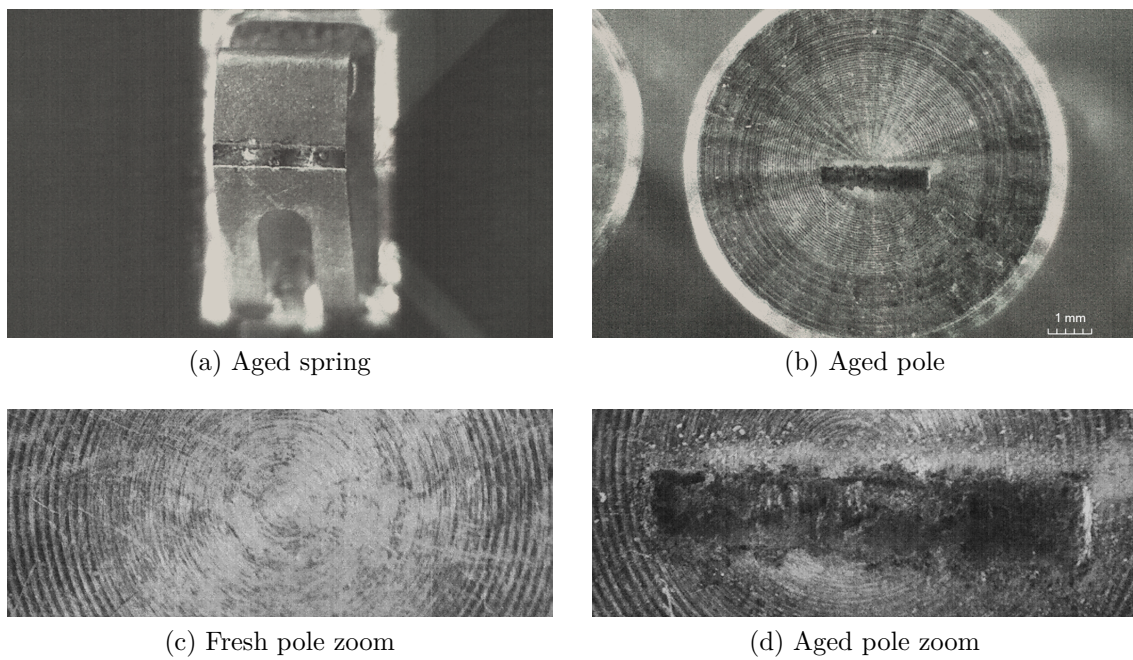


Figure 2.30 – Fresh and aged spring contact surfaces

2.4 Conclusion on Circuit Board Ground Contacts

Phenomena behind electrical contact are quite complex, even though at first, it might seem like a simple problem of bringing two metallic parts to touch each other. Different selection of materials, mechanical design parameters, and external stresses have an effect on the final value of contact resistance, which is the main measure of contact performance for electrical contacts. Optimizing only one parameter is not enough to ensure good contact resistance through the lifetime of the contact, but a compromise between all contact parameters needs to be achieved. When all are equally good, the best contact performance is achieved.

In this chapter, a new test setup to evaluate system level electrical contact performance against external stresses, like temperature and mechanical vibration was developed. The test system is targeted to evaluate ground contacts of circuit boards that are often used for common-mode EMI filters, and whose analysis has been neglected before. Bulk of the electrical contact research has concentrated on sliding contacts that are used in electrical machines and mechatronics, and on contacts used in connectors. However, there is similar problematic to connector contacts with EMI filter ground contacts as they are effectively single-insert connectors that are put together during system assembly, and opened at maximum during service intervals, if ever. This mechanical break can behave similarly to a connector, and can be subjected to faster ageing in electrical performance than rest of the EMI filter.

To highlight typical results of contacts used for EMI filter grounding, three contacts were analysed: a screw contact, a swaged contact, and a spring contact. Screw contact was the most reliable of the tested contacts with no failures over the test cycle. In fact, during vibration, contact resistance even dropped at high vibration levels. Only during cyclic thermal stress, slight performance degradation was observed. Swaged contact performed the next best. Its performance degraded slowly over all the tests, except vibration at low-to-medium amplitudes, where slightly increased performance was seen. At high vibration levels, a few of the contacts failed due to rupturing of the circuit board at the stress relief. This indicates that the contact was either swaged with too high force, or there are additional improvements needed in the stress relief design. However, further mechanical analysis to improve the contact is not in the scope of this thesis. Spring contact performed the worst. While all of the spring contacts were below the contact resistance limit during thermal tests, a significant variation in contact resistance could be seen during thermal

shocks for some of the contacts. During vibration tests, all spring contacts failed. First failures happened at the modest $10g_{rms}$ level, which indicates very weak performance, and continued up to $50g_{rms}$ level indicating average performance. No contact returned into good conduction state after removing the highest vibration level. However, during combined thermal cycling and random vibration some contacts entered briefly an area of good electrical performance during thermal transients. Best improvement was seen during falling temperature. On the other hand, some springs had broken mechanically at this point.

In conclusion, it was shown that a traditional screw contact can perform reliably over the imposed stresses. It is to be noted that only M4 screw with property class 10.9 was tested. It was tightened below its specifications, but close to the maximum torque that can be used with a circuit board, and to a value half of that. Both of the mounting torques still provided contact pressures needed for very good electrical contact. Using different screws and mounting torques could result very different results on the longevity of the contact. However, it was illustrated that with proper mechanical design, excellent through-life results can be achieved with screw contacts. For swaged contacts, some compromises needed to be done during building the prototypes, which could have had an effect on the longevity of the broken contacts. However, it was also demonstrated that a well-built swaged contact will experience only limited ageing during the HALT cycle that was used. A more thorough understanding of the mechanical design and manufacturing parameters of the swaged contacts is needed in the future to ensure proper electrical behaviour. It is possible that the current design has very narrow margins of manufacturing, which means that either excellent tooling needs to be used to ensure uniform contact performance, or some improvements in the contact design are needed to widen the manufacturing margins. Albeit the initial higher contact resistance, spring contacts worked well during thermal stresses, but failed in vibration. Design improvements including higher contact force and use of different plating materials could be beneficial to improve the performance of the spring contacts. However, in installations where vibration stress does not exist, they would perform adequately as such.

In the next chapter these results will be applied into practical example together with the shielded cable results from the previous chapter. In addition, a risk management approach to take these results into account during product development is proposed.

RISK-BASED EMC IN AUTOMOTIVE DOMAIN

In this chapter, the results of the previous two chapters are integrated into typical automotive EMC problems, and approaches to manage these issues are presented. As the current regulation [89] does not explicitly require car manufacturers (OEMs, i.e. original equipment manufacturers) to take into account the effects of ageing or environmental stresses, it is left on the shoulders of individual OEMs and their suppliers to handle the through-life EMC performance of their products.

Depending on the viewpoint, it can be considered either a failure in standardization or an intentional omission to avoid over-regulation, that any through-life EMC performance requirements are left out in the regulation. However, this *rule-based EMC* approach is the global state-of-the-art, and is discussed in Section 3.1 with two automotive design examples:

- A shielded cable connection between an automotive sensor and an electronic control unit (ECU)
- An EMI filter of an electric vehicle (EV) traction inverter.

Automotive OEMs and their suppliers have relied on further risk management as a part of their quality efforts to properly address through-life EMC of their equipment. The amount of extra resources put into this work has been dependant on the actor, and their business targets. Some have invested significantly, while others have done next to nothing. In either of the cases, no publicly available data exists either due to the results that are considered as a competitive advantage, or due to ignorance. However, in many cases the process that has been followed to achieve these results has followed closely a *risk-based EMC* approach discussed in Section 3.2. There, two examples of application are given based on the same examples that were used in Section 3.1, and on the results of Chapters 1 and 2.

In addition to risk-based EMC, automotive domain, among other industries, is in the need of an innovative approach to manage the electromagnetic interference (EMI) risks in increasingly complex safety related electronics, like advanced driver assistance systems (ADAS) and eventual autonomous vehicles. The best available framework to deal with this problematic is *electromagnetic (EM) resilience* [20]. However, it is still in its infancy, and much of further research is needed to provide efficient tools for its application. Thus, it is discussed only in the perspectives part of Section 3.3.

To illustrate different coverage that is achieved with the above mentioned EMC management approaches, Figure 3.1 collects them together presenting different relative coverages of all EMC issues. Ideal design goal would be to address totality of the EMC issues, but it is not economically feasible in most of the cases, and could be technically impossible, too. The simplest way to manage these issues is to rely on industry standard practices: the *rule-based EMC*. Depending on how well the existing standards cover the product in question, there is a chance that either over- or under-engineering results from application of the rule-based method. To alleviate this issue, *risk-based EMC* has been introduced. Its goal is to take into account the specifics of the designed product and its intended environment to avoid over-engineering, and to cover more of the EMC issues specific to the product implementation that the existing product standards might not cover. While correctly applied risk-based EMC can cover most of the EMC issues a product would encounter during its lifetime as discussed in Section 3.2, it is not very well fit for products that need to provide safety functions, or other functions with high dependability requirements. This is due to its intrinsic focus on EMC. For safety related products, design needs to start from ensuring the safety of the function that the product is providing, and then to analyse the space of EMC issues that can interfere with this safety function. Depending on the product, this solution space could approach all EMC issues, but it is mostly just a small subset of all the EMC issues that a product will encounter. Solutions for these issues need to start from a mindset of how the safety issue is alleviated, which does not necessarily mean solving the EMC issue similarly as with rule- or risk-based methods. It means that EMI might occur, but the system can still remain safe to use. This approach is called *EM resilience*.

Some previous work in the automotive domain has recognized the need for a risk-based EMC approach [90] due to rapidly developing electrification, connectivity, and driver assistance technologies. A 'goal-based' approach has been proposed [91], effectively combining the risk-based EMC and EM resilience approaches of above. However, as

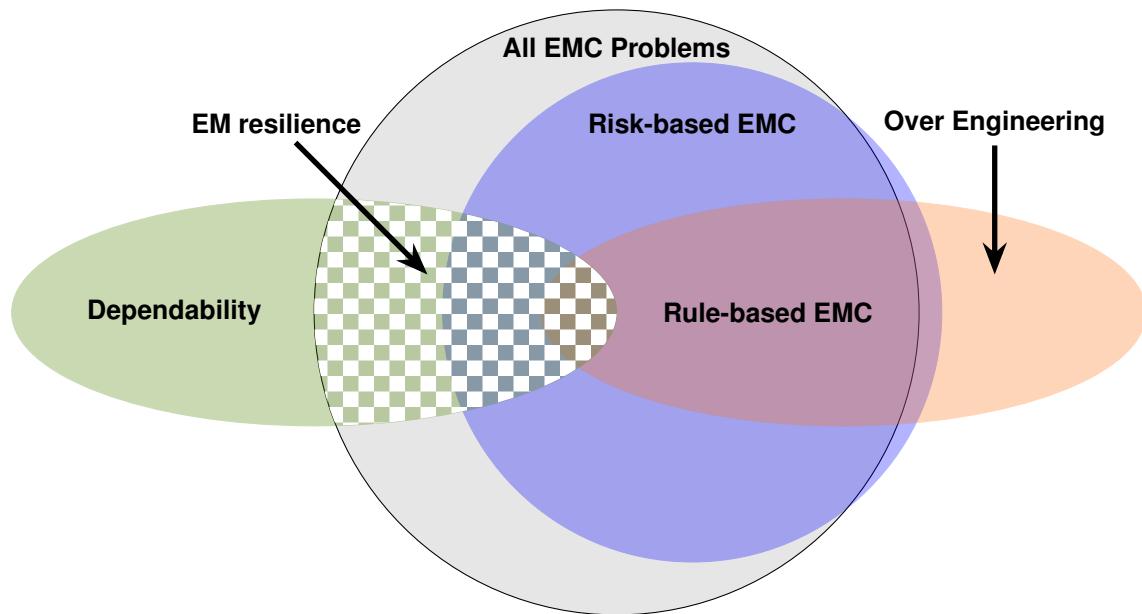


Figure 3.1 – Facets of EMC risk management as an Euler diagram

discussed above, their focuses differ to a great extent, although some goal-based assurance methods could be used in both to demonstrate their efficiency. Thus, they are better treated separately.

In the following sections, a generic introduction covering most industry applications is given first. Then, specific attention is given to the automotive domain.

3.1 Rule-based EMC

Rule-based approach uses a set of rules to ensure that sufficient level of electromagnetic compatibility is achieved. Those rules are ought to ascertain that the probability of EMC issues is reduced to an appropriately low level. This level is such that no significant quality issues can be detected due to EMI, but some small EMC issues might remain in the design. Rules can come from different sources. At least self-imposed, competitor derived, customer specified, and society imposed rules exist. Most common ones to comply are the societal rules expressed in national and international standards for standard products, and a combination of standards and customer specifications for customer specific or one-off designs.

To cover largest international markets, industrial equipment manufacturers need to

comply with several different standard requirements. For electronic equipment, most of them are derived from the requirements of International Electrotechnical Commission (IEC). There, the most important EMC standardisation is done within the International Special Committee on Radio Interference (CISPR), and within the IEC 61000-series. At local level, an EMC directive [92] and European Norms (EN) apply within European Union, and Federal Communications Commission (FCC) and Industry Canada (IC) rules apply in North America. For smaller markets, there exists likes of UK-CA for United Kingdom, China Compulsory Certificate (CCC), and Regulatory Compliance Mark (RCM) for Australia, among many others. As the local standards are often either direct or modified copies of the international requirements, they are not discussed in more detail here. In automotive domain, United Nations Economic Commission for Europe (UNECE) sets the most stringent requirements for passenger vehicle EMC performance in its regulation 10 [89]. That regulation is complemented by standards from CISPR and International Standardization Organization (ISO).

In international standardisation, there are generally three levels of documents based on the maturity and purpose of the documentation. International Standards (IS) are normative, and after a certain delay, usually transformed into EN in Europe. Technical Specifications (TS) are less mature than IS, but can still be used as normative elements. They are rarely developed further in the national domains, but are often used in contracts between suppliers and their customers in areas where other standardization is lacking. Technical Reports (TR) provide information on the basis of standardization, and are often related to a specific set of IS and TS. They help readers to understand the background for selections made in the IS and TS they cover, and can be a valuable asset in finding best ways to comply with them.

One of the important pillars in international standardization is the policy of consensus. Representatives from each participating country gather together to draft the standard, after which, it is sent for commenting and eventual approval rounds to all the national bodies of participating countries. It is there, where different societal actors with technical and commercial interests in the topic discuss and vote for the standard's content. Policy of consensus also means that all the major technical issues in the proposed standard need to be adequately resolved. More often than not, it means making a compromise between technical and economical aspects for the benefit of the society. This process of making compromises is sometimes referred to as 'horse-trading' due to inconsistent nature of the solutions it has provided in the past. Great trust is placed on the standardization

committee members to prevent inconsistencies by self-assessing the compromises being made, and ensuring consistency of the end result.

For complex series produced products that are integrated from many sub-assemblies, like modern cars, it is common that the manufacturer of the final product, the OEM, imposes a set of requirements specific to their product. As the approach to provide a product fulfilling its EMC requirements might differ from manufacturer to manufacturer, the imposed limits to their subcontractors will vary, too. These limits are usually documented in the OEM standards for large companies, or in smaller requirement documents for smaller companies. As the documents provide information on the approach that the OEM has taken for system level EMC management, they are often considered confidential.

Note that the consensus approach applied in international standardization fits best for average products that fall within the standard's limits. For a specific product, a situation can develop, where not all of the requirements are sensible. If this is the case for a product marketed in Europe, the risk-based EMC approach described in the next section is an easy solution as the EU EMC directive [92] allows for its use. In other cases, like the case of naval ships, product supplier might need to enter in lengthy trade-off discussion with both the customer and regulators [93] to be able to apply the risk-based approach.

It is important to avoid mixing risk-based EMC to risk management that is commonly done within rule-based EMC. This risk management has one goal: to reduce commercial risks associated with product development, with an aim to comply with a certain set of EMC standards (i.e. the rules). In the initial phases of development, when no physical prototypes are available, there is a commercial interest to define the length of the product development program as accurately as possible. Fully standard compliant EMC measurements can be done only on final products, and most EMC improvements at that stage involve costly and time-consuming changes. Thus, a risk management approach is used to minimize the possibility of such late problems in the product design, and to meet the time-to-market target for the product. This approach can follow e.g. ISO 31000 risk management process [94] shown in Figure 3.2.

Its core is a **Risk Assessment** process that is divided into three stages:

Risk Identification process collects all the possible ways that the design could fail the applicable standard limits. Then, sources for those failures are described.

Risk Analysis process collects information on the likelihood and severity of the risks identified in the previous step. In addition, it collects possible existing risk controls, like EMC design rules applied during product development.

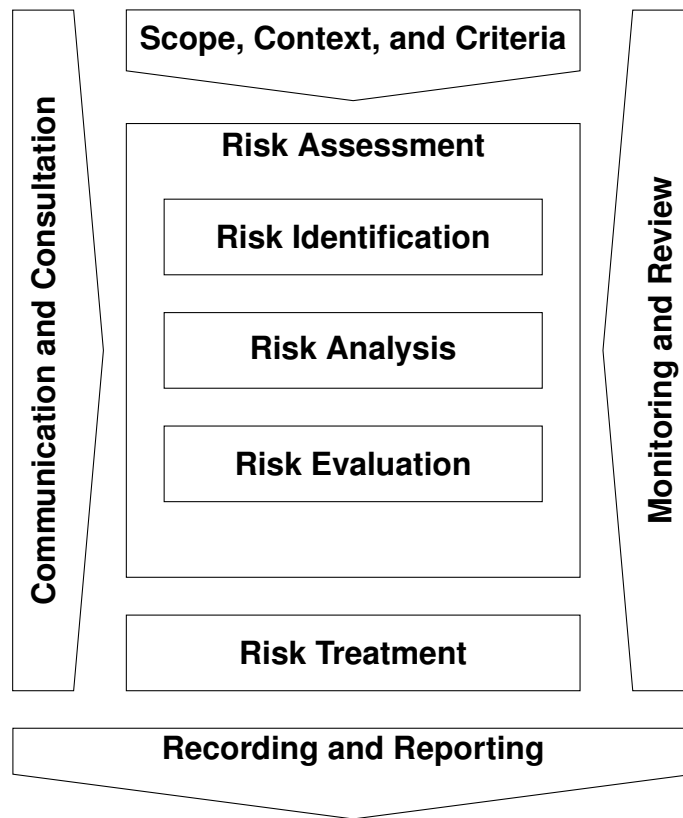


Figure 3.2 – Risk management process according to ISO 31000 [94]

Risk Evaluation combines the information collected in the previous two steps and presents a prioritized overview of EMC compliance risks.

The core assessment process is an effort of an EMC expert group that is usually conducted in a meeting. To be effective in that meeting, some preparatory tasks need to be performed:

Scope, Context, and Criteria define the starting point of the risk management process. For risk management inside rule-based EMC, scope is often predetermined to cover the product under analysis, and the EMC standards it needs to comply with. Context helps to understand the scope, and can provide important details on points to focus. As an example, context information can contain reference products of similar design that have already passed certain or all standard tests defined in the scope. Finally, acceptance criteria for residual risk should be considered beforehand to avoid any decision bias later in the process.

Communication and Consultation plan should be formed before starting the risk assessment process so that all the necessary stakeholders can be kept informed on the risk assessment results, and that all the necessary help on e.g. design details will be received on time.

After the risk assessment process, **Risk Treatment** is performed to do management decisions on handling the risk collection from the evaluation phase. Treatment can include planning of additional verification steps, design changes, or accepting the compliance risks as they are. After the treatment is finished, two tasks are remaining:

Recording and Reporting process is to take care of storing the results of the performed risk management process and distributing them appropriately in reports. The process is generally set within a company as similar risk management tasks exist in e.g. financial domain. Thus, the details on how to do recording and reporting are usually collected during context gathering.

Monitoring and Review is setup to review and update the risk management results regularly to ensure that no late surprises happen as the product development progresses. Most commonly, monitoring is performed at every gate, if a gated product development model [95] is followed.

Two automotive examples on common usage of rule-based EMC, and risk-management within it, are shown in following subsections. Section 3.1.1 discusses an example of a shielded cable used to comply with a bulk current injection (BCI) test, and Section 3.1.2 discusses an example of an electric vehicle (EV) EMI filter design.

The presented use cases are fairly simple, but that is most often the case in rule-based EMC anyway. When faced with a challenge of a large system integration, a completely new type of product, through-life EMC issues, or other area of application, where current standards have deficiencies, it is more efficient to ensure electromagnetic compatibility by applying risk management on the real causes of compatibility problems. This is called risk-based EMC and will be discussed in the next section.

3.1.1 Shielded Cable Connection of a Sensor and an ECU

The shielded cable connection between an automotive sensor and an ECU is meant to be a generic use case of a high-speed communication link in the automotive domain. The sensor can be any component gathering data, like a camera or a radar, and the ECU is a generic data processing unit, like an ADAS domain controller or a vehicle body control

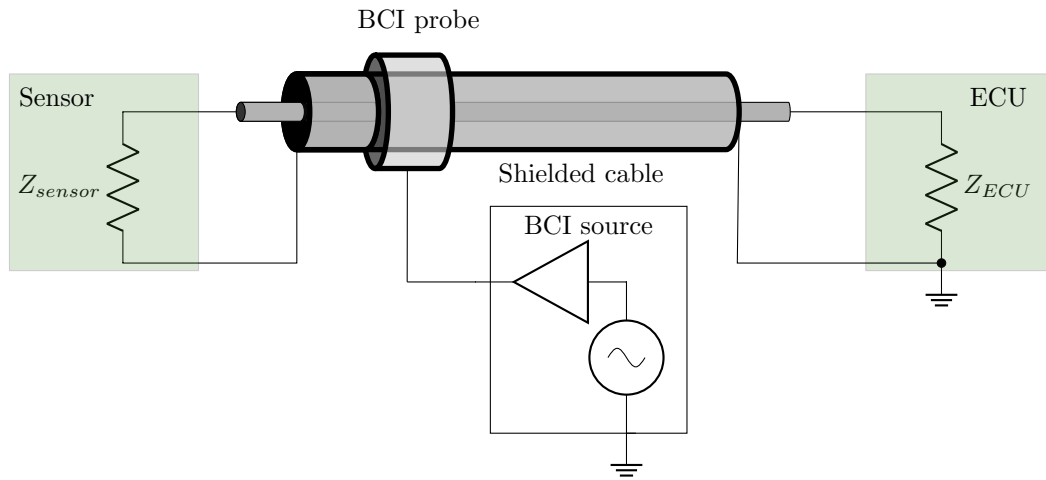


Figure 3.3 – A generic representation of an automotive sensor connected to an ECU with a shielded cable that has disturbances injected to it

module. All these systems can be represented with a generic case in Figure 3.3 which depicts the system with disturbances injected into the cable by a bulk current injection (BCI) probe. Rest of the initial information for the risk management process is gathered in Table 3.1.

The risk assessment process is started with sensitivity analysis. It is a practical way to explore the design space, and to find parameter combinations leading to optimum product performance. This sensitivity analysis can be done over different phases of the product development V-cycle. In concept phase, there can be very different ways to do the cable connection between a sensor and an ECU, and a rough study on different parameters affecting the system immunity can be performed in simulations, including data link architectures with different immunity levels. Then, in development phase some design constraints have been added due to design concept selection. Still, the remaining design freedoms can be explored, now in more detail. As component samples are often available, at least component level tests can be performed. Still, the sensitivity study itself is more efficient to be run in simulation. Statistical studies, like Monte Carlo analyses, are often included to foresee performance variations in production resulting from component tolerances. Finally, in the design verification phase, a limited number of designs can be verified in measurements, and compared to the results of earlier sensitivity studies. Ideally, this last study confirms the earlier simulation results, but in practice, few iterations might need to be done in order to arrive at best designs. When all of the previous steps have

Table 3.1 – Initial information for the risk management of the sensor and ECU case

Item	Details
Scope	BCI-test simulation of a shielded cable connection of a generic sensor to an ECU analysing its sensitivity to changing transfer resistance and inductance of the shielded cable
Context	Product is a concept-level reference design to be used as a design aid by product development teams
Criteria	IC immunity limit of 50 mV is considered across the test frequency spectrum from 1 MHz to 400 MHz. Experience from previous products has shown that the used simulation models underestimate losses compared to real systems, and a passing design in simulation will have enough margin during actual test. Thus, no margin should be required in simulations.
Communication and Consultation	Results of the analysis should be reviewed by the EMC director, and then made available for development teams through the reference design library

been successfully completed, product validation tests will be just about showcasing the product performance.

As specified in Table 3.1, this section illustrates a sensitivity analysis performed in the concept phase of development of a generic shielded cable connection between an automotive sensor and an ECU that has been reported in more detail in [96]. The analysed system is illustrated in Figure 3.3. In the concept phase, the most important task is to find the design parameters that have the largest effect on system performance. Now, the system performance is evaluated against a BCI test. This test can be simulated in SPICE using a simulation circuitry in Figure 3.4. There, the databus is capacitively coupled at the sensor and ECU sides. The BCI probe is positioned at one end of the cable, as the location is not very critical for concept level studies. Moving the probe would mainly have an effect on the system resonance frequencies shifting the highest current peaks in frequency [97]. As a BCI source, a combined signal generator and power amplifier model is used with a level corresponding to an arbitrarily selected OEM requirement. IC immunity models are simplified versions of full models [98] with just a 50-ohm resistor (Z_{sensor} and Z_{ECU}), over which the interference voltage is assessed. Finally, the ground connection wire of an ECU is modelled as an inductance L_{GND} , and the floating sensor has parasitic

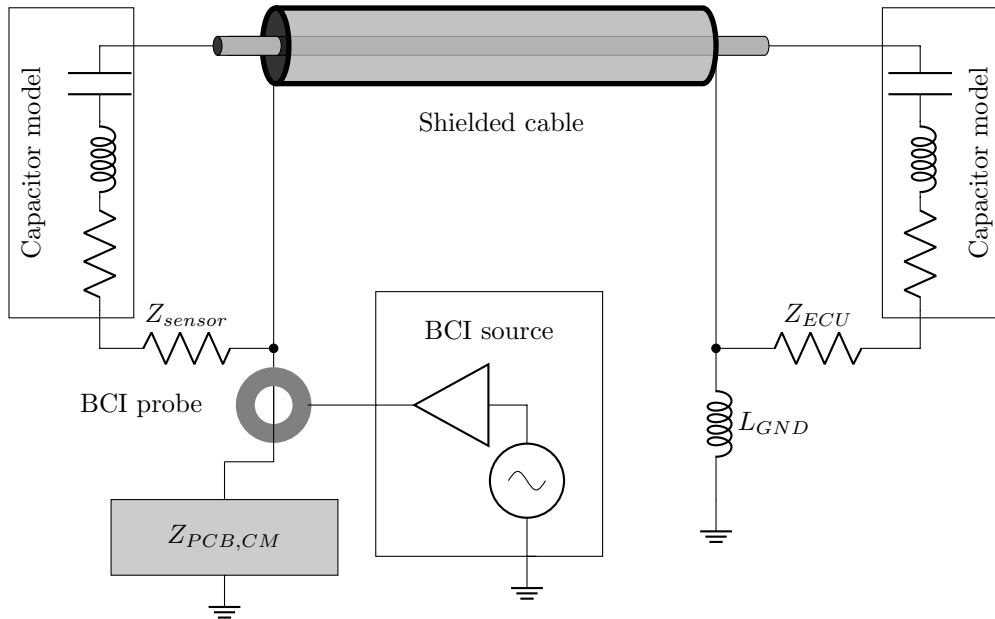


Figure 3.4 – A SPICE circuit model of a BCI test between a sensor and an ECU

ground capacitance that is modelled with an RLC-circuit $Z_{PCB,CM}$ to capture the first ground circuit resonance [98].

Shielded cable model used in these simulations can be formed in a few different ways. A more accurate model can be done with a combination of 2D FEM-simulation of cable cross-section and transmission line equations with a commercial tool like CST Cable Studio, or a more simple model based on characteristic and transfer impedances can be derived. The main advantage of the FEM-based models is that they can take skin-effect and the resulting frequency dependency of transmission line parameters into account. The disadvantage is that doing parametric simulations, like varying length or other physical cable parameters, can be time consuming. On the other hand, the more simple transmission line models are very flexible for parameter changes, but it is complicated to take frequency dependent parameters into account.

The model in Figure 3.5 that is used in this thesis is a simple transmission line model. It consists of a decoupling network that forces all the input current to return through the shield. This is contrary to the low frequency behaviour of a shielded cable system with other ground return paths available [99], but is a valid assumption at high frequencies used during the BCI-test as all the other return paths have much greater inductive impedance. The actual transmission line model of the cable is split into two: first part for the inner

conductor against the shield, and the second part for the shield against the environment. Then, a transfer impedance model is used to couple these two domains together. In this case, an immunity model is used, where the shield current is measured, and a simple transfer impedance model according to Equation 1.10 is injected with this current. Then, the resulting interference voltage is injected to the inner circuit with a help of a voltage controlled voltage source.

Combining the transmission line model with the transfer impedance model forms a distributed element that is then multiplied depending on the desired maximum frequency f_{max} of the analysis as [100]

$$N_{elements} \geq 14.14 f_{max} l \sqrt{LC}. \quad (3.1)$$

Other parameters affecting the number of needed elements are the length of the modelled cable l , and the per-unit-length inductance L and capacitance C of the cable. For the analysed case, $f_{max} = 400$ MHz, and the maximum analysed cable length is 10 m. For cables with a uniform dielectric, the square-root with its contents in Equation 3.1 can be written relative to the phase velocity v_p that can be calculated based on relative permeability μ_r and permittivity ϵ_r of the of the cable dielectric, and the speed of light in vacuum c_0 as [41]

$$\sqrt{LC} = \frac{1}{v_p} = \frac{\sqrt{\mu_r \epsilon_r}}{c_0}. \quad (3.2)$$

Now, as $\mu_r = 1$ and $\epsilon_r = 2.25$ for the selected cable, $\sqrt{LC} \approx 5$ ns/m. The amount of distributed elements needed becomes $N_{elements} \geq 283$. This can be expressed also as an approximate requirement of 30 elements per metre.

Then, a sensitivity analysis of the design EMC performance to cable parameters like length, characteristic impedance, relative permittivity of the dielectric, and transfer impedance can be performed. Here, sensitivity to transfer impedance separating it to transfer resistance and transfer inductance changes is discussed for a cable length $l = 1.7$ m. Results for the rest of the parameters can be found in [96].

Disturbance voltage profile in Figure 3.6 shows a clear system immunity dependency on the transfer resistance of the shielded cable. In this study, transfer inductance of the cable was kept at the value of a coaxial cable ($L_T = 21$ pH/m) as measured in Section 1.4.4. At low, $100 \mu\Omega/\text{m}$ to $1 \text{ m}\Omega/\text{m}$, values transfer resistance does not contribute to the system immunity behaviour, and the immunity curves are superimposed. Around $10 \text{ m}\Omega/\text{m}$, transfer resistance starts to contribute to the immunity profile at low frequencies, but

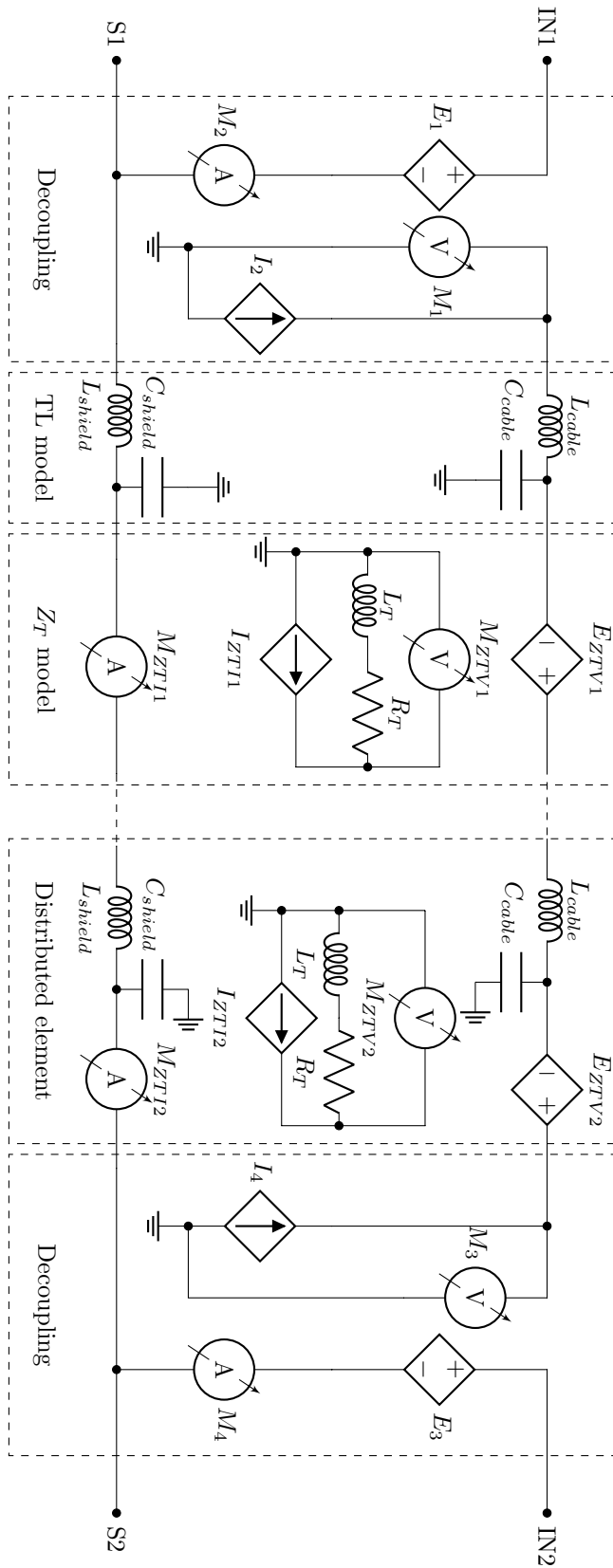


Figure 3.5 – Cable model for BCI sensitivity analysis

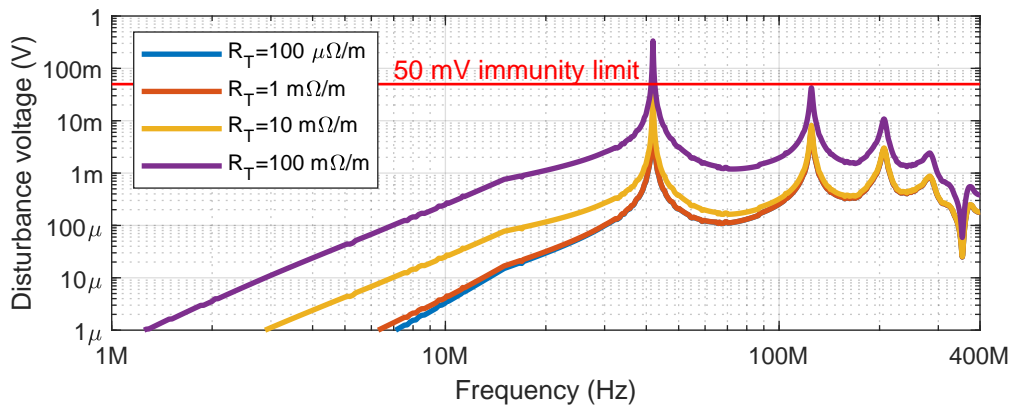


Figure 3.6 – System BCI test sensitivity simulation against transfer resistance with constant $L_T = 21$ pH/m

at the resonance points, where the system is at its weakest, changes are still modest. However, increasing transfer resistance to 100 m Ω /m – a value of a thin shield – immunity performance is worsened significantly. Thus, it can be concluded that for this design, transfer resistance requirement of the cable is 10 m Ω /m or lower.

The results of the other sensitivity study on transfer inductance’s effect on disturbance voltage profile with a constant coaxial cable transfer resistance ($R_T = 10$ m Ω /m) are shown in Figure 3.7. There, a very similar situation compared to transfer resistance sensitivity is observed. Between 1 and 10 pH/m, no significant effect on system immunity performance is seen. Above 10 pH/m, the immunity performance is getting increasingly worse, so that at 100 pH/m the immunity limit is exceeded at 40 MHz resonance peak, and at 1 nH/m the immunity limit is exceeded at multiple resonance locations. Thus, it can be concluded that a transfer inductance requirement of 10 pH/m or lower will yield good system performance for this design.

This sensitivity analysis together with the risk assessment results in Table 3.2 signify the importance of a well-shielded cable for the system design under analysis. However, it was also shown that further improvement of transfer resistance and inductance below 10 m Ω /m and 10 pH/m, respectively, does not give any significant immunity improvement, and is not warranted. This is due to the fact that below those values system performance is not any more given by the cable performance, but other factors, like sensor and ECU grounding. Now, it is evident that if any future product design based on this reference design uses a shielded cable that meets those transfer resistance and inductance specifications does not warrant further BCI-test analyses. In contrary, if lesser performance

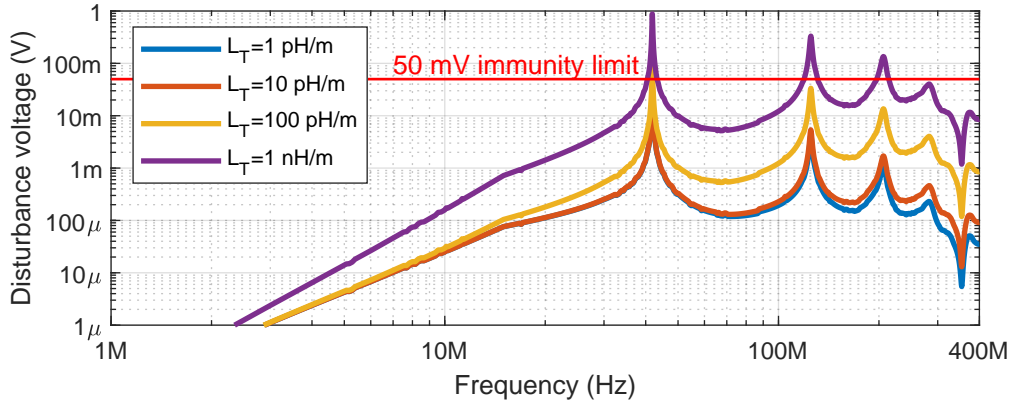


Figure 3.7 – System BCI test sensitivity simulation against transfer inductance with constant $R_T = 10 \text{ m}\Omega/\text{m}$

cable is used, it should trigger additional analysis. After the risk management results are properly stored, and a future review process is setup, this rule-based EMC example is finished.

3.1.2 EMI Filter of a Powertrain Inverter

In the second example, attenuation of an EMI filter for an EV traction inverter is analysed. Initial case information for the risk management process is gathered in Table 3.3. The EMI filter itself is shown in Figure 3.8 with inverter (DC+ and DC-) and battery (B+ and B-) connections highlighted, as well as the available grounding points (M1-M6). It has both differential mode (DM) and common mode (CM) sections, but this study concentrates on CM analysis only with a simplified simulation model developed in the following subsection. Its validity will be studied against voltage transfer function (TF) measurements in the subsequent subsection. Finally, conclusion of the risk management process is given in the last subsection.

Development of the Filter Simulation Model

Filter model development starts always from component identification and characterization. For the CM part of the filter, there were two different capacitors and inductors used. Their descriptions together with their models are gathered in Table 3.4. The models were fitted to impedance measurements of the components. For capacitors, simple RLC-models could be used up to 100 MHz, whereas the inductors needed more complex

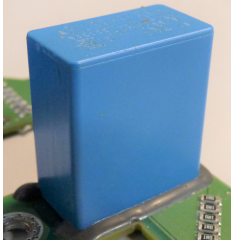
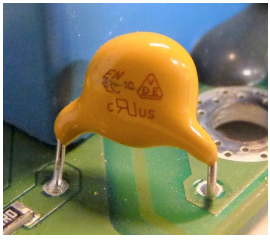
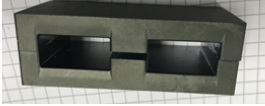

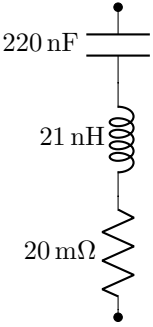
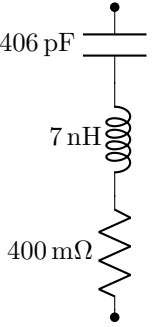
Table 3.2 – Final results for the risk management of the sensor and ECU case

Item	Details
Risk Identification	Too high transfer resistance or inductance can cause the design to fail the immunity limit
Risk Analysis	Designs with cables that have $l \lesssim 2$ m, $r_T \leq 10$ m Ω /m and $l_T \leq 10$ pH/m can be guaranteed to pass the BCI-test
Risk Evaluation	If the reference design is reproduced with cables meeting the criteria recognized during risk analysis, no further cable related BCI-test compliance analysis is needed. In case any of those values is exceeded, an additional analysis on feasibility of the design needs to be conducted.
Risk Treatment	Results were adequate for a reference design, no further actions needed.
Recording and Reporting	The risk assessment results were stored in the reference design library
Monitoring and Review	Process established to link product using the reference design under it in the design library. Critical review of the reference case to be organized at the end of every product development project using it.

Table 3.3 – Initial information for the risk management of the EMI filter case

Item	Details
Scope	EV inverter EMI filter CM attenuation analysis
Context	Product is a concept-level reference design to be used as a design aid by product development teams
Criteria	The following minimum filter attenuation in a 50 Ω system shall be achieved: <ul style="list-style-type: none"> • 20 dB between 100 kHz and 100 MHz • 40 dB between 200 kHz and 30 MHz • 60 dB between 500 kHz and 5 MHz
Communication and Consultation	Results of the analysis should be reviewed by the EMC director, and then made available for development teams through the reference design library

Table 3.4 – EMI filter components and their models

220 nF capacitor	470 pF capacitor	Ferrite	Toroid
			
 <p>220 nF</p> <p>21 nH</p> <p>20 mΩ</p>	 <p>406 pF</p> <p>7 nH</p> <p>400 mΩ</p>	Proprietary model based non-coupled impedance measurement fitting [101]	Proprietary model based non-coupled impedance measurement fitting [101]

proprietary models developed based on theory presented in [101]. The filter is designed as a two-stage low-pass filter as shown in Figure 3.9 with additional damping resistors added in series with the capacitors.

As a filter prototype was available, a reference measurement could be made to compare the attenuation characteristics extracted from the model and measurement. A picture of the measurement setup is provided in Figure 3.10. Due to the dimensions of the filter, connections to the VNA become electrically large at a relatively low frequency, and the maximum analysis frequency was limited to 100 MHz, which was found to be the limit of measurement repeatability.

Building a model based on just the filter component models can work as a first approximation of filter performance. However, as it is shown in Figure 3.11, it cannot capture even the first resonance point due to too low parasitic inductances in the model. To alleviate the issue, some additions to the model are needed. First, the circuit board traces will be modelled by adding 10 nH inductance in series with all the ground connections M2-M5. This starts to direct the simulation result into the right direction as shown by the dashed line in Figure 3.11.

To further improve the simulation model, it is important to note that the circuit board of the EMI filter is mounted on grounding stands that are far away from each

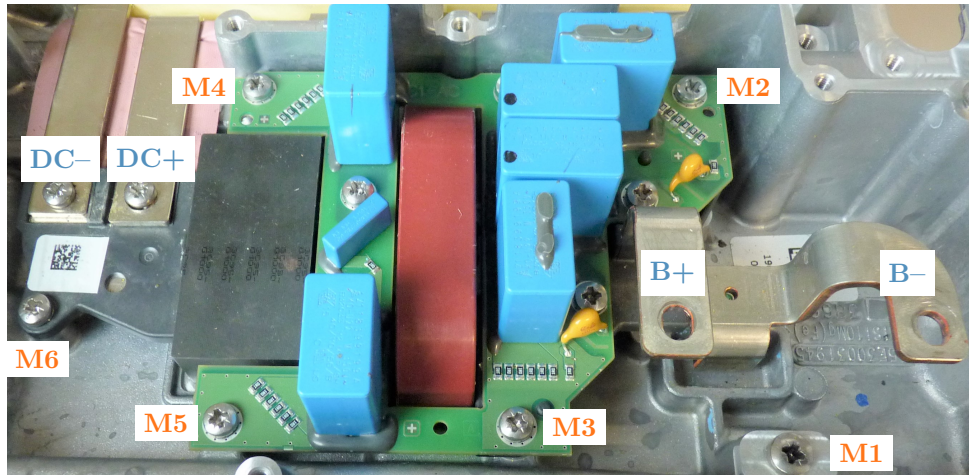


Figure 3.8 – EMI-filter of an EV inverter for the case study

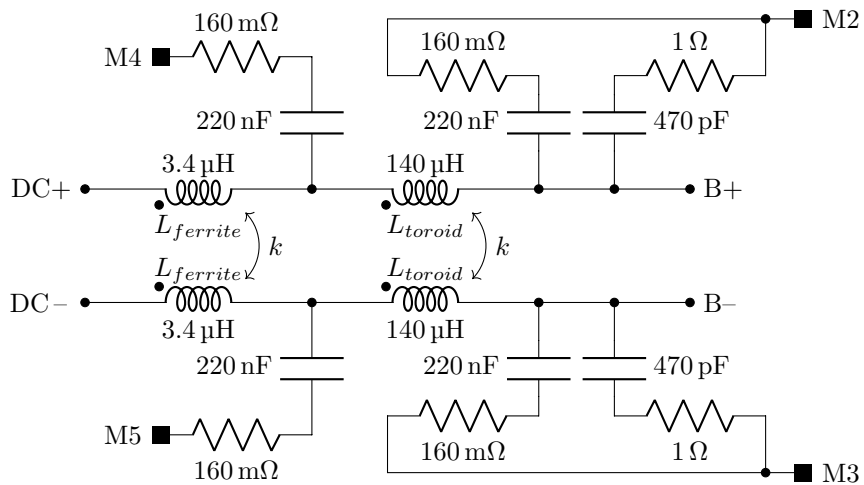


Figure 3.9 – Simplified common-mode schematic of the EMI-filter

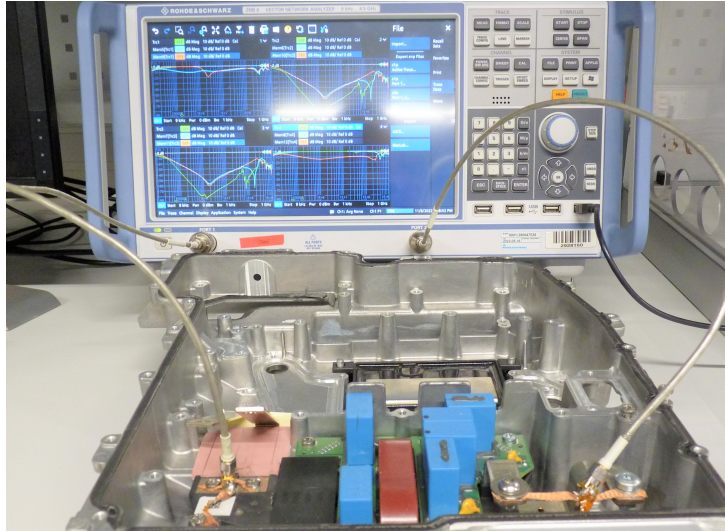


Figure 3.10 – VNA measurement setup for the EMI-filter in its casing

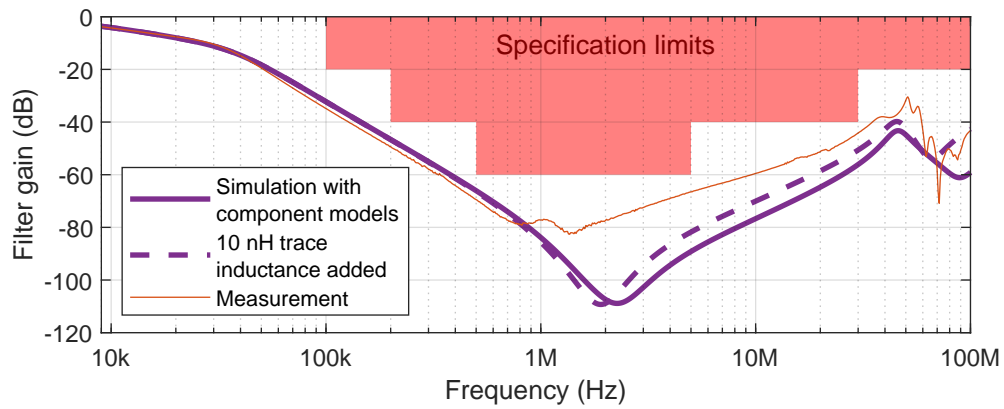


Figure 3.11 – EMI filter attenuation at 50-ohm source and load impedance with a simulation arrangement based on component models only

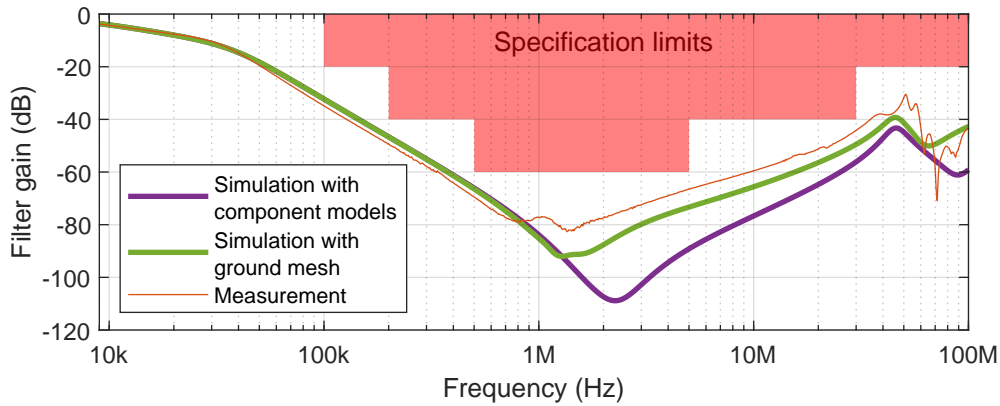


Figure 3.13 – EMI filter attenuation at 50-ohm source and load impedance with a simulation arrangement based on ground mesh

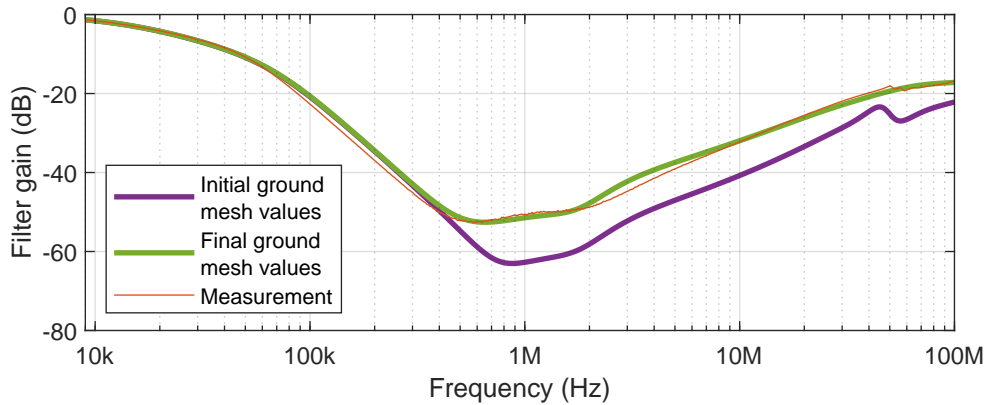


Figure 3.14 – EMI filter attenuation with only M2 and M4 ground points connected

The next step is to extract capacitor-specific stray inductances from the filter layout by measuring each element separately, and adjusting corresponding inductance values in the ground mesh model. To do this properly, a least-squares fitting based method should be developed. However, the work leading to such a method was not in line with the targets of this thesis, and a simplified manual tuning method was used. First, only single grounds between M2-M5 were connected one-at-a-time. Then, all combinations of two and three grounding points were evaluated adjusting the respective inductance elements in the mesh so that the model fits the measurement result. An example of the results of such adjustment is given in Figure 3.14, where the filter attenuation fits the measurement very well after the adjustment.

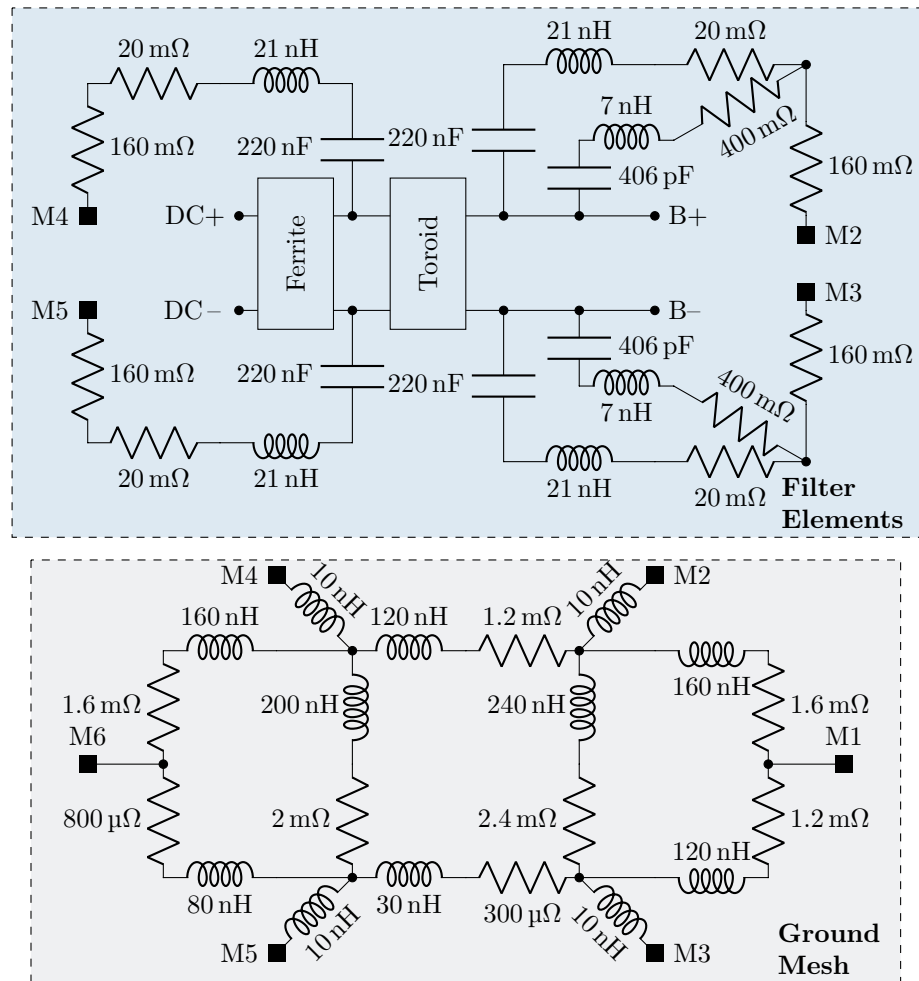


Figure 3.15 – EMI-filter full common-mode schematic

The final filter model is presented in Figure 3.15 so that the component schematic is separated from the ground mesh. It is seen that the complete model is more complex than just a sum of the component models.

Comparison of Measured and Simulated Filter Performance

The voltage transfer function of a fresh filter was measured with a VNA as an S_{21} parameter, and compared to the SPICE simulation model that was built in the previous section. A simplified simulation schematic reproducing the measurement is shown in Figure 3.16. Note, that the presented schematic shows only major filter components, which were modelled with their main parasitic properties included to reach adequate

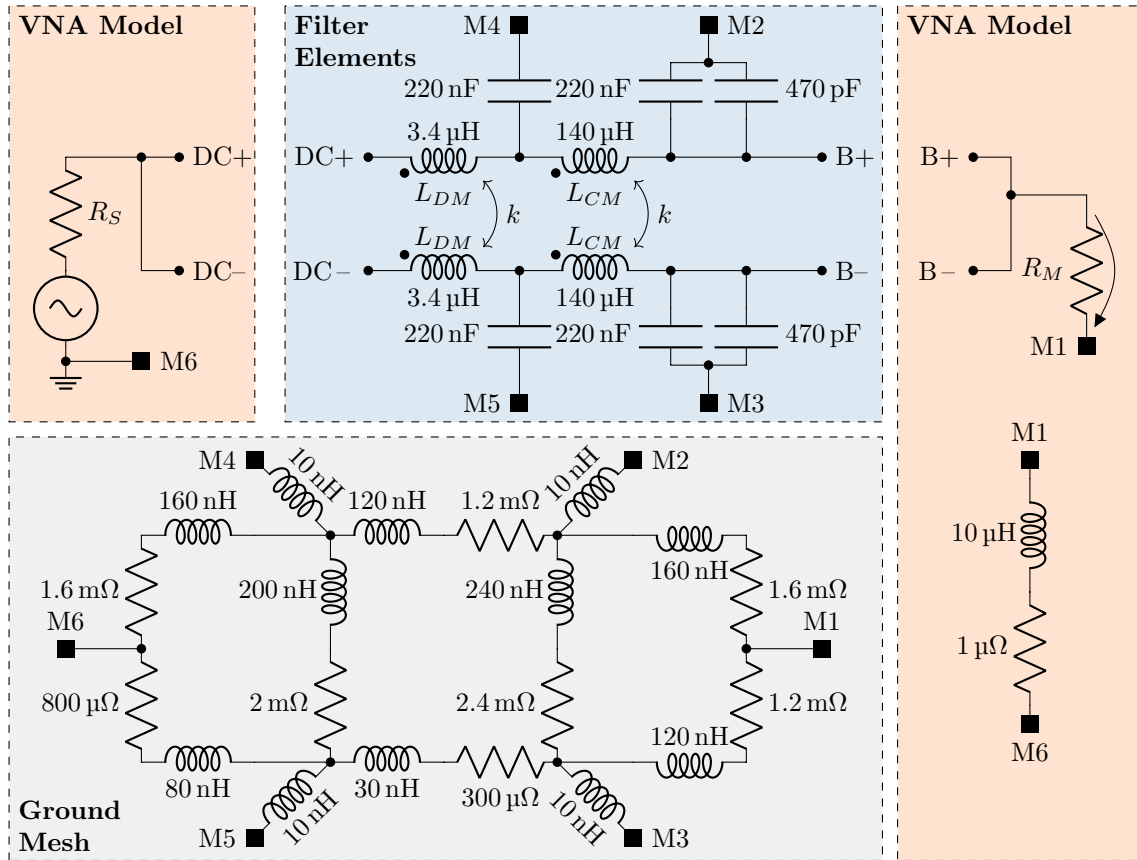


Figure 3.16 – EMI-filter simplified common-mode schematic

models for both capacitors [102], and CM and DM inductors [101]. One of the key points in this section is to see if inter-component coupling [101] needs to be taken into account.

Comparison of measured and simulated filter responses is shown in Figure 3.17. It is seen that the measured and simulated responses do not match exactly, but the simulated response presents the measured one adequately up to 40 MHz. Thus, a simple model without taking into account the inter-component coupling is adequate for this EMI filter.

Filter Performance Risk Management Conclusion

The results shown above signify the importance of not only taking the filter component parasitics into account, but also the parasitic inductances related to the layout of the filter components. Here, a ground mesh approach was used to take the layout parasitics into account. The final risk management results in Table 3.5 highlight this, but also note

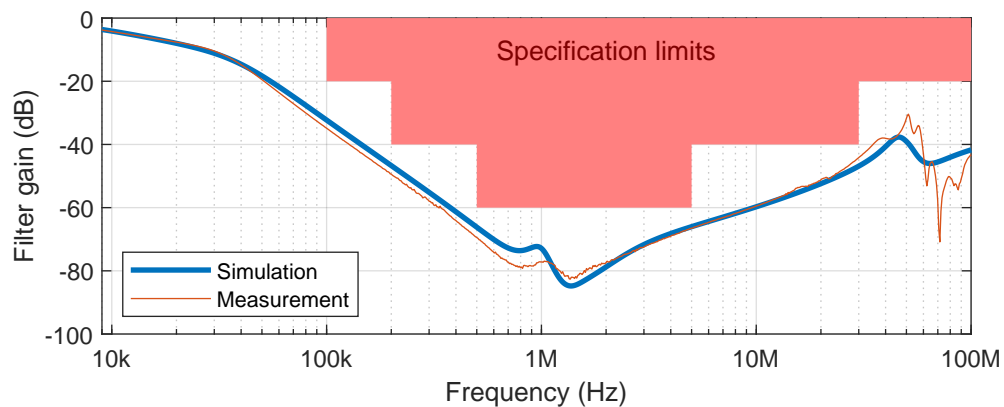


Figure 3.17 – EMI-filter voltage transfer function at 50-ohm source and load impedance

Table 3.5 – Final results for the risk management of the EMI filter case

Item	Details
Risk Identification	Complete filter design can have parasitic inductances that are significantly higher than those of the components
Risk Analysis	Filter arrangement can have a significant effect on its attenuation after the first resonance point. No comprehensive design rules exist. Best practices for filter analysis [101] should be followed.
Risk Evaluation	When the reference design is reproduced, component coupling and ground mesh analysis needs to be redone to ensure adequate filter performance.
Risk Treatment	Results were adequate for a reference design, no further actions needed.
Recording and Reporting	The risk assessment results were stored in the reference design library
Monitoring and Review	Process established to link product using the reference design under it in the design library. Critical review of the reference case to be organized at the end of every product development project using it.

that no comprehensive design rules exist to minimize the effects of the layout. Instead, an iterative approach to optimize the parasitic inductances needs to be used even when using a reference design as a starting point.

This is contrary to the shielded cable case in Section 3.1.1 where clear design rules could be established. Of course, a total parasitic inductance limit could be established

based on the total filter capacitance, but it would not be very helpful for multi-stage filters as the one in this example. In a multi-stage filter, a large inductance on a specific part of a filter does not necessarily mean that the total effective inductance is as large, as it can be paralleled by a smaller inductance reducing the total effective inductance. By this far, no contribution of the environmental stresses is taken into account in the filter performance analysis. In the next section, the risk-based EMC approach takes the intended installation environment better into account including any possible degradation due to environmental stresses.

3.2 Risk-based EMC

Contrary to rule-based EMC, in risk-based EMC, compatibility is assured by conducting a thorough analysis of the product under design and its intended environment, and then applying the necessary measures to achieve electromagnetic compatibility. This process is sometimes called as 'good EMC engineering practice', and it can be divided into four phases as shown in Table 3.6 that is adapted to a product-based view from a systems publication [103].

In the first phase, a director responsible for organizing EMC design activities needs to define the overall project plan and the persons involved in the design. The most important definition is the lead EMC engineer, who needs to define the main design features that

Table 3.6 – Phases of planning in risk-based EMC

EMC Plan	Content	Creator	Audience
Management	Who, what, and when?	Director	Development team (Reduced version to customer)
Control	What needs to be done to achieve EMC?	EMC Engineer	Management & Engineering
Implementation	How the requirements in the control plan are implemented? (Detailed design)	EMC Engineer	Engineers in other domains (electrical, mechanical, etc.)
Verification and Validation	How the effectiveness of the implemented measures is checked?	EMC Engineer	Test Engineer or Technician

ensure achieving necessary EM immunity and low enough emissions. Then, depending on the project size, either the lead EMC Engineer or other EMC Engineers in the project will do the detailed design of the EMC measures for the product. Finally, the engineers need to do a verification and validation plan to ensure that their design is adequately tested. Project management will be responsible on following up that all these plans are executed properly during the project.

In military domain, a risk-based handbook for EMC design [104] has existed for a considerable time, since the beginning of 1970's. Reason for its existence is the design-by-contract (DBC) approach [105] commonly followed in military projects. The handbook provides basics of risk-based EMC to guide any product acquisition project conducted using DBC. In practice, this approach means that the acquisition contract states which EMC requirements the supplier needs to meet but also that any EMC aspect that is not expressly mentioned in the contract is not the responsibility of the supplier or manufacturer of the product. Thus, the organization responsible of the acquisition project has also the final responsibility of the system's EMC. This is in contrast to e.g. EU EMC Directive, where a generic responsibility of the foreseen and unforeseen compatibility problems lies on the manufacturer.

In automotive domain, the need to move to risk-based approach is driven by rapidly developing technologies like electrification, autonomous driving, and vehicle connectivity [90]. A risk-based approach named as 'goal-based' has been proposed that would cover both risk-based EMC and EM resilience [91]. Currently, there is a push to include the risk-based portion of EMC in the automotive systems engineering process, and some examples of how that could be done have been published in [106] and [107].

In the following sections, common challenges necessitating risk-based EMC are discussed. The most prominent ones are cost optimization and breakthrough products discussed in Sections 3.2.1 and 3.2.2, respectively. Their need for risk-based EMC comes from very different starting points, one could say that they are in the opposite ends of the product maturity spectrum. Cost optimization starts from too prescriptive standards that limit innovation and application of EMC engineering to reach best compatibility with lowest cost. On the other hand for innovative products, there might be no existing standards at all, and to guarantee adequate operation of the product, applying risk-based EMC is the only option. In the system level EMC, a specific problem comes from complexity management as discussed in Section 3.2.3. Finally, an emerging topic of software performance updates over the product lifetime, commonly referred to as over-the-air (OTA)

updates, can have an effect on the EMC performance of the product. Thus, the effects of those updates need to be controlled, and a risk-based approach can be used as described in Section 3.2.4. Another emerging issue: environmental stress dependency of EMC solutions is worked through with automotive case examples in Section 3.2.5. To tie all these different aspects together, a conclusion is presented in Section 3.2.6.

3.2.1 Cost Optimization

The starting point of risk-based EMC compliance cost optimization is a situation where it has been recognized that following the currently standardized rule-based approach as described in Section 3.1 results in unnecessary costs for the product. This could be due to product architecture that is different from the average product that the standards were written for, or due to an application of innovative EMC design approach as explained in the naval shipbuilding example below. After the possible cost savings have been identified, it is necessary to do evaluation of additional test and development costs resulting from following the risk-based approach. While there might be no additional cost for special products that are one-off in nature, a mass-produced product with many different foreseeable environments will need more time from EMC experts to generate and justify a proper risk-based approach.

In [90] cost optimization targets were stated in an explicative way. When doing system integration, instead of enforcing similar EMC performance requirements for the components, different requirements are enforced. The complexity and demand level of the requirement depends on the cost and availability of system level mitigation measures and natural protection based on component location. It means that if a component will be placed in a non-protected location with only expensive mitigation means at system level, the component performance requirements will be high. Whereas, if there are plethora of inexpensive mitigation means available at system level, the component performance requirements can be relaxed to obtain an optimum cost solution.

One of the best examples in cost optimization is the application of risk-based EMC in naval shipbuilding [93]. There, strict military standards have been traditionally applied for all equipments integrated into a new-built ship. This approach has worked in the past as most of the electronics innovation has happened first in the military domain, and then brought later into the civil market. However, starting from the late '80s or early '90s, the consumer and industrial electronics innovation has outpaced the rate of military research programs. This has created a need to integrate industrial, and even consumer electronics,

into naval ships. However, EMC requirements for products in the general market are vastly different from those of naval ships that have to withstand electronic warfare in addition to high power radars and communication transmitters. Trying to harden civil products to military standards has resulted cost inflation. Instead, the zoning approach discussed in Section 3.2.3 is to be applied so that just zone boundaries are hardened, and not every product inside the zones. In this way a cost-optimum of the EMC solution will be achieved, which will benefit all stakeholders from customer to society and, of course, the manufacturers.

3.2.2 Breakthrough Products

Breakthrough products are products that create a new and innovative use of electronics in an application that has not existed before, or products that use unforeseen technologies to solve challenges in established applications. What is common for both, is that these new designs might bring new EMC requirements with them that are not covered by any standard or other specification. Thus, pure rule-based EMC approach cannot be conducted.

Instead, a risk-based EMC approach is needed to comply with the EU EMC Directive, and to ensure proper function of the product during its lifetime. Once the products have been established in the market, it is common that standardization process starts in order to enable efficient use of these novel products globally. Normally, the best risk-based approaches are taken as a reference, when the new rules are being made, and compromises made during the process lead to a new rule-based approach for a new standardized product class. Thus, eventually meaning that the breakthrough products have become established, and for which, rule-based EMC will be followed.

3.2.3 Complex Systems

For complex systems, many traditional EMC analysis tools fail to perform adequately. For example, a properly filled source-victim matrix becomes impossible to manage due to its size.

One of the most promising risk-based EMC concepts for managing complex systems is the zoning approach. In fact, it is a legacy approach used in a different context. Zoning is one of the basic methods used in the IEC 61000-series [108] to set EMC limits for different areas of the environment like household vs. industry locations. This kind

of zoning approach works as there are other reasons, like possible pollution, noise, and heavy traffic, due to which industry locations are already geographically zoned away from residential areas. This geographical zoning guarantees some inherent attenuation due to distance between the higher emitting devices in industry, and possibly susceptible low-cost devices used in the residential areas. The same approach is already in use in the civil maritime domain [109], and was proposed to be extended to naval shipbuilding [93].

For automotive domain, the zoning approach could be used with some adaptations. An example of such zoning is given in Figure 3.18:

- Passenger zone is characterized by similar requirements as residential zones of IEC 61000-series for emissions [110] and immunity [111] as it is expected that passengers carry equipment designed for that environment. It is common for people to carry mobile phones while they are travelling, and the mobile phones could operate close to their maximum transmit power when travelling through rural areas. Thus, specific attention needs to be paid to frequencies they commonly use.
- Luggage zone might be a part of passenger zone in some vehicles, like sport utility vehicles (SUVs), where there are no means to implement a zone boundary between them, or it could form a zone of its own in other vehicle types, like sedans.
- Engine zone is where the combustion engine or electric motors reside. In Figure 3.18 this zone is split into two: one for combustion engine in the front of the car, and another for an electric motor at the rear axle of the car.
- Undercarriage zone could be used to connect the different engine zones. It could be built with relative ease in a way that it is well isolated from the passenger zone.
- ADAS zone is an example of a specially protected zone that could be used to house the ADAS controller and related equipment. It is to be noted, that in case of a single controller module, it might be more economical to shield the module alone, whereas with a modular ADAS approach it could make more sense to use simple controller housing inside of a protected ADAS zone.

As the automotive chassis is not RF tight, it is not meaningful to control radiated emissions with the zoning approach, except for ADAS and undercarriage zones. The ADAS zone with relatively small physical dimensions could be made with very good shielding effectiveness (see definition in Section 1.1.1). On the other hand, the undercarriage zone would mostly be utilized for connecting equipment on different high-noise zones together. Design rules could be laid out so that all components are installed behind chassis elements

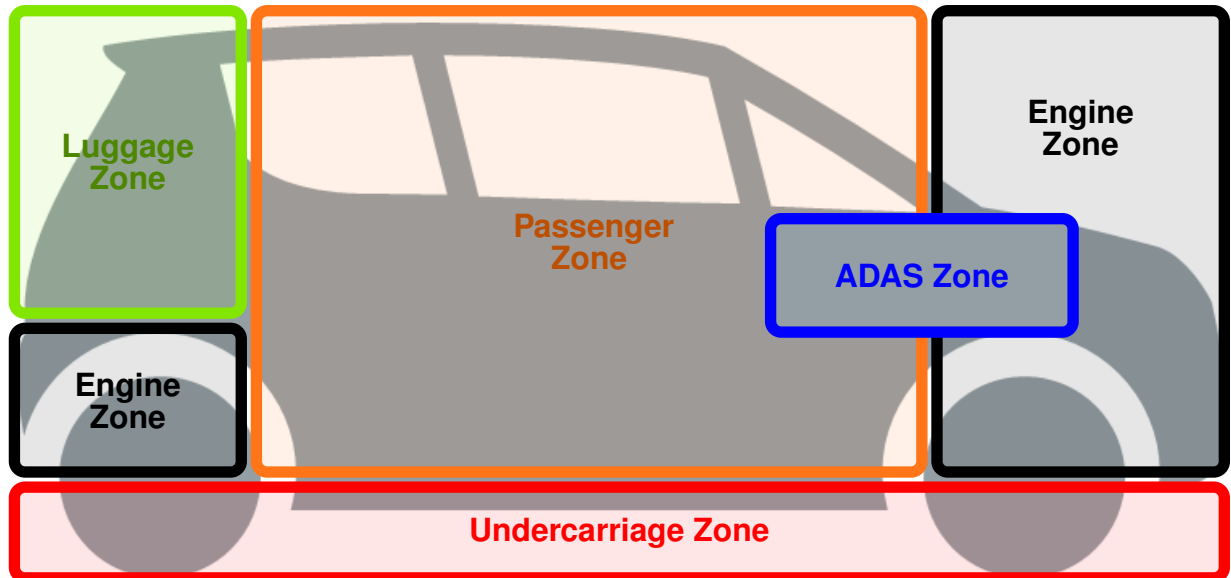


Figure 3.18 – An example of EMC zones in a passenger vehicle

so that they are far away from any openings to achieve an 'effective' shielding effectiveness as observed from the other zones.

In the zoning approach, as well as other approaches for EMC design of complex systems, the most important design aspect is 'divide and conquer'. This makes the complex systems more approachable, and the remaining work can be divided for different teams without too many interdependencies. However, it is rarely meaningful to try to eliminate all interdependencies, but to limit their amount in a way that the remaining ones can be effectively dealt with in systems engineering.

3.2.4 Performance Updates with Software

In the coming years, many products historically relying heavily on complex electronics will be redesigned with a push to increase functionality even further. Most economical way to implement these new functionalities, as well as the old ones, is to use a design where new hardware is increasingly controlled by software, and functions become software dependent. This trend has resulted in software development budgets that exceed those of hardware development [112]. Additional push for fast time-to-market has meant that as soon as hardware design is ready and adequately tested, the product will be shipped to customers. At this time, it might have software features that cover only the basic functionality of the

product. Subsequently, software development continues and new features are introduced little-by-little, and deployed via over-the-air (OTA) updates. This approach can cause a threat to product's EMC performance.

As an example from automotive domain, Tesla is currently following the above described approach with its ADAS system [113]. They have installed hardware capable of advanced ADAS functions to all vehicles they deliver, and are regularly releasing OTA updates to introduce improved ADAS features. Interestingly, there are examples of cases, where they have also downgraded performance [114] and reduced functionality [115] through OTA. An opportunity, which is supposed to be rarely used, although could provide valuable in case of a major EMC issue. From machine building domain, an approach of testing for effects of software changes in EMC performance of variable speed drives (VSDs) has been presented [116] very recently.

One of the largest paradigm shifts that needs to happen in this regard is with EMC testing. Currently, most of certification testing is done when all the product features are ready. However, with the short time-to-market strategies, it will not be possible any more. Instead, EMC engineers need to define new ways to ensure that the product conforms with necessary EMC requirements. Those ways include, among others:

- Using simple test software to test for worst case performance
- Using parametrizable test software to statistically evaluate the EMC performance
- Building a feature roadmap with EMC checkpoints before major feature deliveries with prioritized list of tests to be performed depending on added features
- Using risk management process to initiate further EMC analysis and/or testing, when the residual risk of incompatibility has grown too large

This area of risk-based EMC is rapidly increasing in importance and significant future research efforts are expected to be published covering the subject more in-depth than what was done here.

3.2.5 Environmental Stress Dependency

Moving from rule-based EMC sensitivity analysis to more of a risk-based EMC approach, some additional effects that are not measurable on new product prototypes need to be taken into account. These include parameter variation during production, dependency on environmental stress, and ageing of the components, among other possible influences.

This section studies the effects of environmental stresses to product and system performance with the help of three examples.

In the first example, the effect of temperature dependent transfer impedance of a coaxial cable on system EMC performance is studied. The second example studies the effect of coaxial cable ageing in the same system. Finally, the third example studies the effect of ground contact deterioration on EMI filter attenuation performance.

Effect of Temperature Dependent Transfer Impedance

In this section, the SPICE model of Section 3.1.1 is used to perform sensitivity analysis of the sensor and the ECU system to thermally induced variations in the transfer impedance of the communication cable between them. The linearized dependency of transfer resistance and inductance for coaxial cable in Table 1.7 is used for this purpose. Temperature range from $T_{min} = -40^{\circ}\text{C}$ to $T_{max} = 100^{\circ}\text{C}$ was selected for the analysis covering the range of most automotive applications, except cables placed very close to the combustion engine or its exhaust. The resulting transfer resistances and inductances are shown in Table 3.7.

Plugging in these parameters to the simulation model described in Figure 3.4, the immunity performance result of Figure 3.19 is achieved. It is seen that below 70 MHz, immunity performance with cable at hot temperature is slightly worse, driven by the increased transfer resistance. The highest resonance peak touches the 50 mV immunity limit. Above 70 MHz, immunity performance of the cable at cold temperature is slightly worse. Overall, changes in the immunity performance are so small that similar or larger variation is expected to exist just between different samples of the same cable. Thus, typical design margins would make these variances insignificant.

Effect of Cable Ageing due to Environmental Stresses

In this section, the SPICE model described in Section 3.1.1 is used to perform a sensitivity analysis of the sensor and the ECU system to ageing of its communications cable. Extracted ageing characteristics of a coaxial cable have been taken from Section 1.4.4 to perform the analysis. This work has been reported earlier in a conference publication [9].

The simulation circuit is as described in Figure 3.4, but now the cable model is configured with two different shielding performance figures: between a fresh and an aged cable as shown by the evolution of the transfer impedance parameters in Table 3.8. Ageing of the cable changes the immunity performance of the circuit as shown in Figure 3.20

for an ECU communication link with medium disturbance immunity level of 50 mV. It is clearly seen that the design passes the test with a fresh cable, but fails at three frequency domains: around 40, 120, and 200 MHz with an aged cable.

Based on this case study, it is clear that the environmental stresses can negatively affect immunity performance of a data link made with a coaxial cable. Ageing of the cable shielding needs to be taken into account, when determining the through-life electromagnetic compatibility of systems. As no automotive standards explicitly require taking into account ageing of the shielded cables for EMC-purposes, rule-based EMC cannot be used, and the problematic needs to be treated as an emerging issue of risk-based EMC. In this regard, a simple management plan as shown in Table 3.9 is formed and needs to be followed during product development.

EMI Filter Ground Contact Deterioration Under Environmental Stresses

To highlight the importance of correct ground contact selection for an EMC-filter, the results from Chapter 2 are taken into account and integrated into the simulation model of Section 3.1.2 by adding extra resistance in series with the ground contact points M2-M5 shown in the annotated picture of the filter in Figure 3.8 and in its schematic in Figure 3.15. Then, that resistance is swept from 10 m Ω to 1 k Ω to represent different contact technologies from a qualification limit of the best contacts to a high impedance level representing a damaged contact. Measurement results achieved by adding resistors in series with the contact points are compared to simulation results in Figure 3.21. It is found out that with very small resistances, the simulation model has too pronounced resonance points, but otherwise the results match well. Filter performance starts to deteriorate for values above 1 Ω contact resistance so that at 10 Ω filter performance has deteriorated significantly, and above 100 Ω the filter becomes completely ineffective in its purpose with simulated attenuation less than 20 dB over the analysed frequency spectrum.

The discovered limit contact resistance of 1 Ω is studied further by changing the source and termination impedances to more realistic values for an automotive traction system simulation. Instead of using 50 Ω derived from the VNA port impedance for both source resistance R_S and victim resistance R_M , they are replaced with a source capacitance $C_S = 10$ pF [4] and victim resistance equal to typical lower limit of high voltage system chassis fault of $R_M = 500$ k Ω [117] neglecting any parasitic capacitance. With these more realistic system impedances, the effect of the contact resistances is still the same: above 1 Ω , filter performance starts to deteriorate significantly.

Table 3.7 – Temperature Dependent Transfer Impedance Model Parameters

Parameter	-40°C	20°C	100°C
R_T	8.1 mΩ/m	10 mΩ/m	13 mΩ/m
L_T	27 pH/m	21 pH/m	13 pH/m

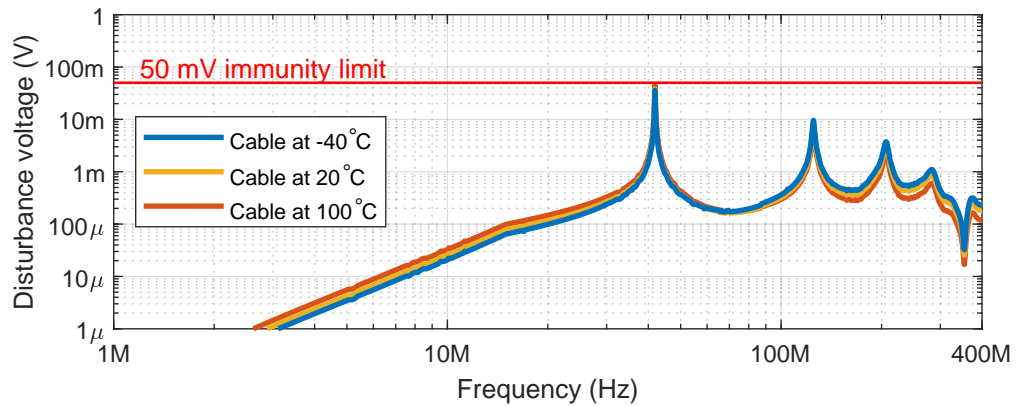


Figure 3.19 – A SPICE simulated BCI test result with temperature dependent coaxial cable transfer impedance

Table 3.8 – Fresh and Aged Cable Transfer Impedance Model Parameters

Parameter	Fresh	Aged
R_T	10 mΩ/m	60 mΩ/m
L_T	21 pH/m	280 pH/m

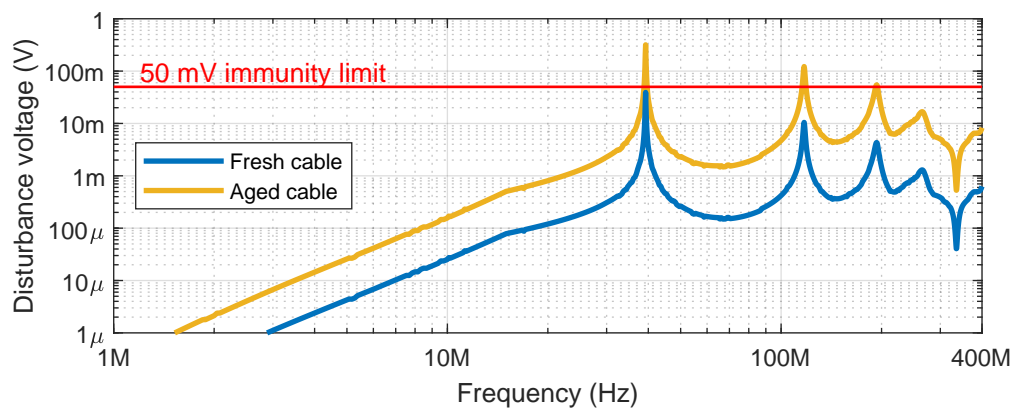


Figure 3.20 – A SPICE simulated BCI test result with a fresh and aged coaxial cable

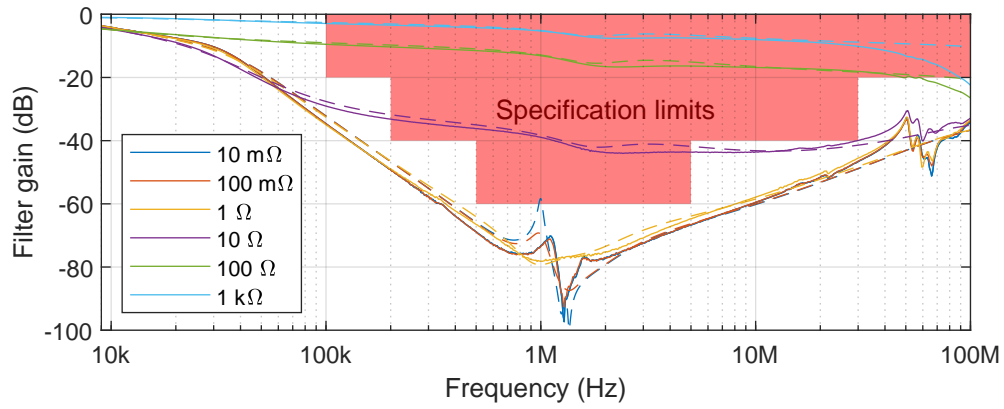


Figure 3.21 – EMI-filter voltage transfer function with swept contact resistance. Measurement results as solid and simulation results as dashed curves.

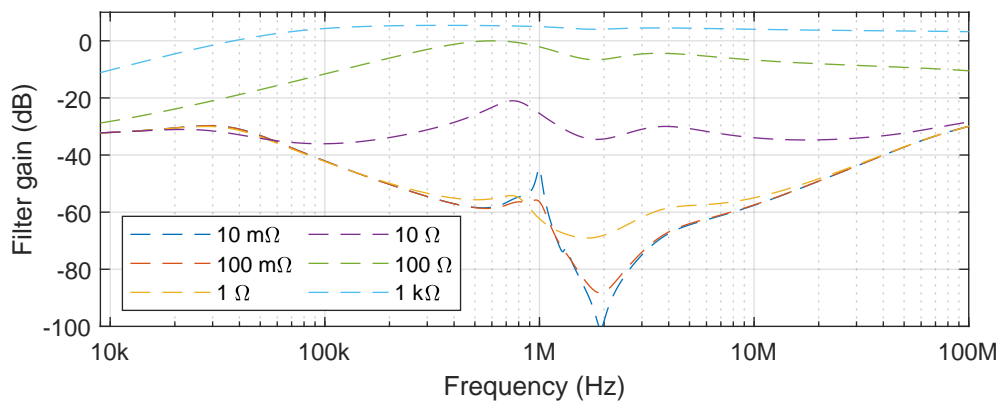


Figure 3.22 – EMI-filter voltage transfer function simulation with swept contact resistance and realistic termination impedances.

Table 3.9 – Risk-based EMC plan for ageing of shielded cables

EMC Plan	Contents
Management	EMC Engineer needs to take ageing of the shielded cables into account during system design
Control	Design needs to pass immunity and emission tests with a shielded cable that has been aged according to system's lifetime environmental stress specification
Implementation	Transfer resistance and inductance values of a cable representative of an aged cable is to be used during system design
Validation and Verification	EMC tests are either done with a cable that has transfer resistance and inductance representative of an aged cable or simulations taking into account cable ageing are performed for tests, where validated simulation models exist.

Based on this case study, it is clear that the environmental stresses can negatively affect EMI filter performance if sensitive ground contacts are used. Ageing of the ground contacts needs to be taken into account when determining the through-life performance of the filter. As no automotive standards explicitly require taking into account ageing of ground contacts for EMC-purposes, rule-based EMC cannot be used, and the problematic needs to be treated as an emerging issue of risk-based EMC. In this regard, a management plan in Table 3.10 needs to be followed during product development.

Table 3.10 – Risk-based EMC plan for ageing of EMI filter ground contacts

EMC Plan	Contents
Management	EMC Engineer needs to take ageing of the EMI filter ground contacts into account during product design
Control	Design needs to conform to the filter attenuation requirements with ground contacts that have been aged according to system's lifetime environmental stress specification
Implementation	Contact resistance values representative of aged contacts are to be used during filter design
Validation and Verification	EMC tests are either done with added resistors in series of the contacts representing aged contacts, or simulations taking into account contact ageing are performed for tests, where validated simulation models exist.

3.2.6 Conclusion on risk-based EMC

Risk-based EMC can be thought to cover the special cases that are too unique to be covered in the standards that rule-based approach consists of. However, this view is too limiting as the flexibility of risk-based EMC approach enables also other dimensions, like ensuring compatibility of different product configurations and emerging issues, like software modifications and effects of environmental stresses. Figure 3.23 visualizes these extensions.

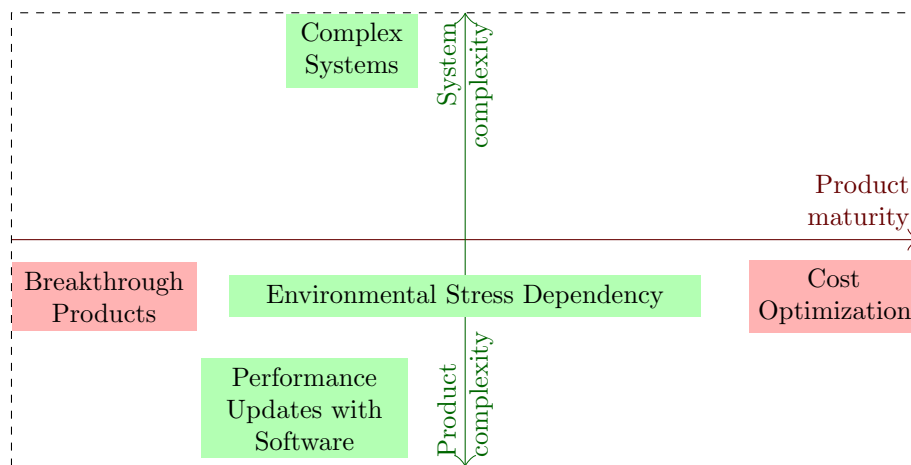


Figure 3.23 – Risk-based EMC extensions and improvements to the rule-based EMC approach lying at the origin of the axes

The horizontal axis represents the maturity level of a product or a system with the main risk-based EMC extensions boxed in red. For novel products, no standards exist, and a rule-based approach cannot be implemented. Instead, a risk-based approach – usually derived from rules, though – is applied to ensure EMC. As the product matures towards the centre of the graph, rules are formed and rule-based EMC becomes the de-facto approach. As the product continues to mature, a point of too restrictive and specific rules can be accrued. To arrive at a cost-optimized product in mature field of technology, a risk-based EMC approach is again needed to make innovative solutions with as good as or better EMC performance as the rule-based EMC would offer.

The vertical axis represents product or system complexity with the main risk-based EMC extensions boxed in green. On the system side, management of the complex systems is impossible or extremely expensive with traditional means, and risk-based EMC is needed as was highlighted in Section 3.2.3. On the product side, complexity is often man-

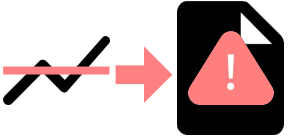

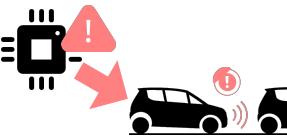
aged by creating simplifications in rule-based EMC domain. However, there are always some emerging issues rising from the introduction of new technologies that need risk-based EMC approach as well as flexible product configuration issues that are common for more mature products being optimized for producing different variants for different customers from same building blocks.

In practice, one of the most effective ways to do risk-based EMC is to create management, control, implementation, and validation and verification plans, and follow them throughout the product development. In addition, EMC zoning is commonly used for complex systems. There, product requirements for each zones are defined independently, applying system-level EMC measures only at the zone borders instead of designing all the equipment to conform with the most stringent specifications. This approach has been already in use, while writing the current standards in the IEC 61000-family as well as for some sector-specific standards like IEC 60533 for maritime industry. However, a formalized generic approach has not existed before, and there is still on-going research to find a generalized approach that fits to everyone's needs. Currently, it seems like there needs to exist a pressing reason to jump from rule-based to risk-based EMC as the latter approach will generate management overhead. One of the reasons shown in Figure 3.23 could provide advantages that offset the increased management costs.

3.3 Conclusion and Perspectives on EMC Risk Management

Traditionally, EMC engineers have only recognized existence of the rule-based EMC. However, with the advent of increasingly complex innovative products, like electrification of many mobility solutions, or the ADAS systems in automotive, different approaches for EMC compliance are needed. This chapter discussed the basics of rule-based EMC and compared it to risk-based EMC. It was found out that risk-based EMC can either be an extension of rule-based EMC to cover more accurately the electromagnetic compatibility problem at hand, or it can be used as a tool to focus on special product design for which standards are too generic. However, rule-based and risk-based EMC are concerned only on the EMC performance of the product. Recently, it has been highlighted that traditional EMC approach is not enough for systems from which high dependability, like functional safety, is needed [118]. EM resilience is brought in to solve this problem. This leads to a completely different approach that is derived from dependability and safety engineering,

Table 3.11 – Summary of EMC risk management objectives

	Rule-based EMC	Risk-based EMC	EM resilience
Applicable to	Standard products and well-known systems	Novel products, complex systems, and emerging issues	Dependable functions of a product or a system
Visual			
Cause	Well-defined EMD	Arbitrary EMD	Arbitrary EMD
Likelihood of	Product EMC performance meeting standard limits	EMI occurring	Malfunctions due to EMI
Consequences	Re-design, Bill-of-materials cost, Time-to-market delay	Product performance failure at customer	Safety or other dependability hazards
Evaluate the severity of	Financial loss	Financial and reputation loss	Accident or other undesired event

not from EMC engineering.

An overview on management of electromagnetic disturbance related risks is given in Table 3.11. From visual summaries, it is seen that rule-based EMC deals with product’s emission and immunity limits compared to standards or other specifications, and optimizes the process of meeting those limits. On the other hand, risk-based EMC is concerned about performance of customer’s process, and about possible EMI induced failures concerning products sold to them. It is common to market many products globally, and thus, the variety of different EM environments that need to be covered can be very large. Finally, EM resilience deals with EMI induced failures in electronic control components that can propagate to dangerous safety failures or other undesired events in highly dependable systems.

For rule-based EMC, the cause that needs to be managed is a well-defined electromagnetic disturbance (EMD) from standards or specifications (i.e. the rules). Engineering decisions need to be taken on the basis of the likelihood of the product to meet its defined EMC performance targets as required by the rules. If those rules are not met, the consequence is re-design need for the product with possibly increased bill-of-materials (BOM)

cost and delay in releasing the product to the market. Failing to manage these aspects properly will cause financial loss for the company developing the product.

In risk-based EMC, the cause to be mitigated is arbitrary EMD depending on the installation location of the product. Instead of being concerned in meeting any standards, the goal in risk-based EMC is to prevent the EMI from occurring, or at least minimize the likelihood of it. The real benchmark on the success of the approach is the amount and severity of product failures at customer installations due to EMI. These failures will lead to financial losses in terms of troubleshooting, repair and product replacement costs. In addition, as the failure happens at the customer application, some reputation loss is evident for the manufacturer. Again, calling for proper management throughout product's lifecycle.

In EM resilience, the cause is the same as for the risk-based EMC, but instead of the likelihood of EMI, it concerns with likelihood of system malfunctions due to that EMI. That is, EMI could occur, and the system could be considered EM resilient if there are no safety or other dependability hazards generated by that EMI. Contrary to the previous cases, financial loss is not evaluated, but the severity of the accident or other undesired event due to the EMI generated hazards is the key aspect to evaluate and manage.

It is easy to see that all the three risk management approaches have their place and time to be applied. Rule-based EMC works well for developing standard products without any special functions. As some innovative solutions are used or the designed system is complex, risk-based EMC can provide a better toolbox to ensure electromagnetic compatibility of the design. Finally, for system requiring high dependability or safety, traditional EMC approach angle is not optimum, but the system design needs to be approached from safety or dependability engineering point of view. This is, where the concepts of EM resilience need to be applied. There is still more research needed to cover the best-practices of risk-based EMC and EM resilience in the best way possible. A small contribution was made in this thesis for EM resilience by showing how one could use goal structuring notation to argue EM resilience of a shielded cable connection in an ADAS system [16]. Most important contributions in this thesis have been for advancement of risk-based EMC by including environmental stresses to analysis of shielded cable connections and EMI filter ground contacts.

CONCLUSION

This thesis studied the environmental stress response and ageing of shielded cable shielding layer and EMI-filter ground contacts. Significance of the stress incurred issues was highlighted by integrating them into automotive case studies. In practice, effectively solving those case studies will need some structures for management of the problem solving process. A contribution to this process was done by collecting and restructuring already published approaches for effective use in automotive and other domains.

The four thesis challenges:

- Evaluate the effect of environmental stresses and ageing on shielded cables and EMI-filter ground connections
- Apply highly accelerated life testing (HALT) to evaluate different cable shielding and ground contact technologies in a rapid fashion.
- Demonstrate the results and their effects to functionality of automotive systems with real-world examples.
- Contribute to the development of risk-based EMC approaches considering multi-parameter influences

were addressed in the main body of the thesis, and the main conclusions for each of them will be presented here. The first challenge is split into two different conclusions: one for shielded cables and one for EMI-filter ground connections.

For shielded cable transfer impedance characterization, a new type of triaxial cell that enables including temperature and vibration stresses during measurements was developed and verified. With it, some cable samples demonstrating different shielding technologies were tested and a following conclusion in their performance was reached:

Shielded cables

Environmental stress can affect the shielding performance of a shielded cable. At low frequencies, the DC-resistance of the shield is temperature dependent up to $0.6\%/^{\circ}\text{C}$. At high frequencies, a well-designed cable will not be susceptible to any environmental stress as its transfer inductance stays constant. However, for cables with design compromises, the following can be observed:

- Braided shields with a flexible jacket will have their transfer inductance dependent on temperature (up to $\pm 0.8\%/^{\circ}\text{C}$ with foil and braid combination) and vibration (up to $0.6\%/g_{rms}$ for a double braided shield) as the shield stretches and contracts
- Foil shields with weak design will exhibit cracks due to thermal and/or vibration stress permanently increasing their transfer inductance up to forty times the original value

Two significant future directions to extend this research are:

1. Developing physics-based equations to explain the measured transfer impedance thermal and vibration dependencies as well as ageing
2. Comparing different foil shield structures, and finding a correct foil structure for robust environmental stress performance.

For EMI-filter ground connection analysis, a generic test setup for any electrical contact from a circuit board to a mounting pole was developed. It is based on 4-wire resistance measurement that can be done either with high-accuracy micro-ohm meter, or with a data acquisition system supporting 4-wire resistance measurement. Generally, a well-designed contact needs to be measured with the micro-ohm meter due to its low resistance. With the test setup a selection of typical automotive circuit board ground contacts were tested, and the following conclusion was reached:

Circuit board ground contacts

Environmental stress can affect the resistance of circuit board ground contacts. Well-designed contacts retain their performance, or even exhibit an improved contact resistance due to combined effect of high mounting force and vibration. However, weak contacts can fail completely during the environmental stress. From the three tested contact technologies, a following conclusion can be given:

- Well-designed screw-contact ($R_{contact} \sim 100 \mu\Omega$) is a reliable mean for both attachment and electrical contact over thermal stress and random vibration
- Swaged contact ($R_{contact} \sim 500 \mu\Omega$) can be a reliable mean for both attachment and electrical contact over thermal stress and random vibration, but its design window is smaller than that of a screw-contact, and it is susceptible to some ageing ($R_{contact} \sim 2 \text{ m}\Omega$ after ageing)
- Spring contact ($R_{contact} \sim 5 \text{ m}\Omega$) can be a reliable mean of electrical contact over thermal stress and light random vibration, but will exhibit failures with moderate to high vibration levels.

Significant future research directions include:

1. Studying different grounding spring topologies to find if some of them can be used under harsher vibration conditions
2. Developing understanding on the design parameters of swaged contacts and improving its manufacturing margins
3. Studying emerging contact technologies, like press-fit pins and foams wrapped in conductive fabrics
4. Developing the test setup further to include electrical connections between different shielding structures, like automotive electronics casings and other support structures

During the shielded cable and ground contact evaluation, fitness of highly accelerated life testing (HALT) to be used for evaluation of these components was implicitly verified. The following conclusion can be drawn based on the experience gained during the tests:

Highly Accelerated Life Testing

Technology evaluations with HALT are feasible, and it is straightforward to use for finding limits of different technologies ought to be used for the same application. However, it does not represent real application stresses and is not fit for estimating the actual lifetime of different solutions in the real application.

Based on this conclusion, the most promising technologies found in HALT could be tested with application representative accelerated tests to find out if similar results of their capabilities are discovered. It is likely that the performance order of the different technologies will be the same, but margins between them could be different.

Two case studies were used to demonstrate the significance of shielded cable transfer impedance change and EMI-filter ground contact resistance change in automotive electronics.

Significance to Automotive Industry

The case studies demonstrated that:

1. Shielded cable deterioration due to environmentally induced ageing can affect the immunity of a camera-to-ECU data link
 - Data link deterioration can have negative consequences on the performance of autonomous driving functions
2. EMI-filter ground contact resistance can increase to a level, where the filter performance is significantly reduced
 - Improper filtering of EV powertrains can lead to system-wide interference problems
 - Proper verification of the ground contacts during and after the environmental stress is needed
 - Cost savings are plausible by moving from screw contacts to swaged contacts

To avoid problems arising from challenges of different magnitude due to the environmental stress susceptibilities of shielded cables and EMI-filter ground connections, proper

risk management is a key task. Risk management strategies can be divided into three levels:

EMC Risk Management

Rule-based EMC is an effective way to ensure EMC performance of standard products

Risk-based EMC is needed for special cases like:

- Breakthrough products
- Product cost control
- Complex system designs
- Emerging issues, like flexible configuration of products

EM resilience is an approach based on dependability engineering practices, and is needed for safety related systems

These management principles are universal to any other EMC challenge as well. The main future research topics lie in the standardization of risk-based EMC approaches that are already in use in the automotive domain, and in EM resilience as it is very immature topic at the moment – especially within the automotive industry.

This thesis brought an important viewpoint on the effects of environmental stresses on EMC related components. It amplifies the message that EMC solutions cannot be just designed to pass relevant EMC tests at the development time of a product, but they need to be designed in so that their performance will be sustained through the product's lifetime. Those, who succeed in doing that will inevitably experience less fault-not-found field failures as it is extremely difficult to pinpoint an EMC failure of a returned product – especially if it is related to an environmental condition other than the laboratory ambient conditions.

BIBLIOGRAPHY

- [1] Ozgur Dedehayir and Martin Steinert, « The Hype Cycle Model: A Review and Future Directions », in: *Technological Forecasting and Social Change* 108 (07/2016), pp. 28–41, ISSN: 00401625, DOI: 10.1016/j.techfore.2016.04.005, URL: <https://linkinghub.elsevier.com/retrieve/pii/S0040162516300270> (visited on 08/11/2022).
- [2] Bill Visnic, « 2020 Hype Cycle for Connected and Smart Mobility », in: *SAE International Newsletter* (11/09/2020), URL: <https://www.sae.org/news/2020/09/2020-hype-cycle-for-connected-vehicles-and-smart-mobility> (visited on 22/08/2022).
- [3] Tancrède Lepoint, *Hype Cycle in TikZ*, GitHub Gist, 14/07/2015, URL: <https://gist.github.com/tlepoint/329dcdf264202cc50b0c>.
- [4] Iqbal Husain et al., « Electric Drive Technology Trends, Challenges, and Opportunities for Future Electric Vehicles », in: *Proceedings of the IEEE* 109.6 (06/2021), pp. 1039–1059, ISSN: 0018-9219, 1558-2256, DOI: 10.1109/JPROC.2020.3046112, URL: <https://ieeexplore.ieee.org/document/9316773/> (visited on 14/11/2022).
- [5] Vinnie Venugopal, *Certain Toyota Corolla, Matrix and Pontiac Vibe Part 573, Defect Information Report*, Defect Information Report for NHTSA, 30/01/2013, URL: <https://static.nhtsa.gov/odi/rc1/2013/RCDNN-13V029-4470.pdf> (visited on 23/08/2022).
- [6] Heinrich Kaden, « L. Schirmung gegen Störströme », in: *Wirbelströme und Schirmung in der Nachrichtentechnik*, Berlin, Heidelberg: Springer Berlin Heidelberg, 1959, pp. 282–341, ISBN: 978-3-540-32570-3, DOI: 10.1007/978-3-540-32570-3, URL: <http://link.springer.com/10.1007/978-3-540-32570-3> (visited on 18/07/2022).

-
- [7] Oskari Leppäaho et al., « Triaxial Cell for Determining Shielded Cable Transfer Impedance During Environmental Stress », in: *IEEE Transactions on Electromagnetic Compatibility* Minor revision submitted (2022).
- [8] T. Kley, « Measuring the Coupling Parameters of Shielded Cables », in: *IEEE Transactions on Electromagnetic Compatibility* 35.1 (02/1993), pp. 10–20, ISSN: 00189375, DOI: 10.1109/15.249391, URL: <http://ieeexplore.ieee.org/document/249391/> (visited on 22/01/2021).
- [9] Oskari Leppäaho et al., « Including Experimental Aging of Shielded Cables into Bulk Current Injection Simulations », in: *2022 Int. Symp. Electromagn. Compat. – EMC Eur. 2022 International Symposium on Electromagnetic Compatibility – EMC Europe*, Gothenburg, Sweden: IEEE, 2022, pp. 811–815, ISBN: 978-1-66540-788-5, DOI: 10.1109/EMCEurope51680.2022.9901089, URL: <https://ieeexplore.ieee.org/document/9901089/>.
- [10] P. Groche et al., « Incremental Bulk Metal Forming », in: *CIRP Annals* 56.2 (2007), pp. 635–656, ISSN: 00078506, DOI: 10.1016/j.cirp.2007.10.006, URL: <https://linkinghub.elsevier.com/retrieve/pii/S0007850607001576> (visited on 24/11/2022).
- [11] Joachim Geiger, *Automated Driving: Between Wish and Reality*, DEKRA solutions, 28/07/2021, URL: <https://www.dekra-solutions.com/2021/07/automated-driving-between-wish-and-reality/?lang=en>.
- [12] Lawrence Burns, Babek Hassibi and Behrooz Rezvani, « Sensing Enters a New Era », in: *Autonomous Vehicle Engineering* 4.3 (07/2022), pp. 4–9, ISSN: 2642-0910.
- [13] Hugo Griffiths, *Advanced Driver Assistance Systems: How the Latest Car Safety Tech Is Tested*, AutoExpress Features, 07/05/2021, URL: <http://www.autoexpress.co.uk/features/354927/advanced-driver-assistance-systems-how-latest-car-safety-tech-tested>.
- [14] Ford Motor Company, *Part 573 Safety Recall Report - 22V-412*, 10/06/2022, URL: <https://static.nhtsa.gov/odi/rc1/2022/RCLRPT-22V412-2331.PDF>.
- [15] Chris Becker et al., *Functional Safety Assessment of an Automated Lane Centering System*, 08/2018.

-
- [16] Oskari Leppäaho et al., « Assuring Shielded Cables as EMI Mitigation in Functional Safety Systems – A Case Study of an Automated Lane Centering System », in: *E-Proceedings of the 31st European Safety and Reliability Conference*, 31st European Safety and Reliability Conference (ESREL 2021), Angers, France, 2021, DOI: 10.3850/978-981-18-2016-8_263-cd.
- [17] Max Chafkin, « Why Intel’s Mobileye Blew a Red Light While Showing Off Its Ride », in: *Bloomberg Technology* (21/05/2018), URL: <https://www.bloomberg.com/news/articles/2018-05-21/why-intel-s-mobileye-blew-a-red-light-while-showing-off-its-ride>.
- [18] ISO, *26262-5:2018 Road Vehicles — Functional Safety — Part 5: Product Development at the Hardware Level*, Geneva, Switzerland: International Organization for Standardization, 12/2018.
- [19] A. Avizienis et al., « Basic Concepts and Taxonomy of Dependable and Secure Computing », in: *IEEE Transactions on Dependable and Secure Computing* 1.1 (01/2004), pp. 11–33, ISSN: 1545-5971, DOI: 10.1109/TDSC.2004.2, URL: <http://ieeexplore.ieee.org/document/1335465/> (visited on 30/08/2022).
- [20] IEEE, *IEEE Std 1848-2020 - IEEE Standard for Techniques and Measurement to Manage Functional Safety and Other Risks with Regards to Electromagnetic Disturbances*, New York, USA: IEEE, 04/06/2020, ISBN: 978-1-5044-6636-3, URL: <https://ieeexplore.ieee.org/servlet/opac?punumber=9052856> (visited on 22/01/2021).
- [21] National Fire Data Center, *Highway Vehicle Fires (2014-2016)*, 07/2018, URL: <https://www.usfa.fema.gov/downloads/pdf/statistics/v19i2.pdf> (visited on 23/08/2022).
- [22] David Jolley, *Shifting to 800-Volt Systems: Why Boosting Motor Power Could Be the Key to Better Electric Cars*, Drivemode News, 13/02/2021, URL: <http://drivemode-h2020.eu/shifting-to-800-volt-systems-why-boosting-motor-power-could-be-the-key-to-better-electric-cars/> (visited on 23/08/2022).
- [23] Alireza Khaligh and Michael D’Antonio, « Global Trends in High-Power On-Board Chargers for Electric Vehicles », in: *IEEE Transactions on Vehicular Technology* 68.4 (04/2019), pp. 3306–3324, ISSN: 0018-9545, 1939-9359, DOI:

-
- 10.1109/TVT.2019.2897050, URL:
<https://ieeexplore.ieee.org/document/8633386/> (visited on 15/11/2022).
- [24] Kirk A. Gray and John James Paschkewitz, *Next Generation HALT and HASS: Robust Design of Electronics and Systems*, Wiley Series in Quality and Reliability Engineering, New York, NY: John Wiley & Sons, 2016, 276 pp., ISBN: 978-1-118-70023-5.
- [25] European Commission, *Horizon 2020 - Pan-European Training, Research and Education Network on Electromagnetic Risk Management*, CORDIS EU reserach results, 22/09/2022, URL: <https://doi.org/10.3030/812790>.
- [26] S. A. Schelkunoff, « The Electromagnetic Theory of Coaxial Transmission Lines and Cylindrical Shields », in: *Bell System Technical Journal* 13.4 (10/1934), pp. 532–579, ISSN: 00058580, DOI: 10.1002/j.1538-7305.1934.tb00679.x, URL: <https://ieeexplore.ieee.org/document/6772273> (visited on 22/01/2021).
- [27] L. Klinkenbusch, « On the Shielding Effectiveness of Enclosures », in: *IEEE Transactions on Electromagnetic Compatibility* 47.3 (08/2005), pp. 589–601, ISSN: 0018-9375, DOI: 10.1109/TEMC.2005.853162, URL: <http://ieeexplore.ieee.org/document/1516231/> (visited on 30/05/2022).
- [28] Eugene Knowles and Lee Olson, « Cable Shielding Effectiveness Testing », in: *IEEE Transactions on Electromagnetic Compatibility* EMC-16.1 (02/1974), pp. 16–23, ISSN: 0018-9375, DOI: 10.1109/TEMC.1974.303318, URL: <http://ieeexplore.ieee.org/document/4090799/> (visited on 21/02/2022).
- [29] M. A. Dinallo et al., « Shielding Effectiveness of Typical Cables from 1 MHz to 1000 MHz », in: *1982 IEEE International Symposium on Electromagnetic Compatibility*, 1982 IEEE International Symposium on Electromagnetic Compatibility, Santa Clara, California: IEEE, 09/1982, pp. 1–5, ISBN: 978-1-5090-3168-9, DOI: 10.1109/ISEMC.1982.7567798, URL: <http://ieeexplore.ieee.org/document/7567798/> (visited on 27/09/2022).
- [30] L.O. Hoefft and J.S. Hofstra, « Measured Electromagnetic Shielding Performance of Commonly Used Cables and Connectors », in: *IEEE Transactions on Electromagnetic Compatibility* 30.3 (08/1988), pp. 260–275, ISSN: 00189375, DOI: 10.1109/15.3304, URL: <http://ieeexplore.ieee.org/document/3304/> (visited on 27/09/2022).

-
- [31] Heinrich Kaden, « H. Durchgriff von elektrischen un magnetischen Feldern durch Löcher », in: *Wirbelströme und Schirmung in der Nachrichtentechnik*, Berlin, Heidelberg: Springer Berlin Heidelberg, 1959, pp. 221–262, ISBN: 978-3-540-32570-3, URL: <https://doi.org/10.1007/978-3-540-32570-3> (visited on 17/06/2022).
- [32] Edward Vance, « Shielding Effectiveness of Braided-Wire Shields », in: *IEEE Transactions on Electromagnetic Compatibility EMC-17.2* (05/1975), pp. 71–77, ISSN: 0018-9375, DOI: 10.1109/TEMC.1975.303389, URL: <http://ieeexplore.ieee.org/document/4090877/> (visited on 22/01/2021).
- [33] T. Kley, « Optimized Single-Braided Cable Shields », in: *IEEE Transactions on Electromagnetic Compatibility 35.1* (02/1993), pp. 1–9, ISSN: 00189375, DOI: 10.1109/15.249390, URL: <http://ieeexplore.ieee.org/document/249390/> (visited on 22/01/2021).
- [34] Edward F. Vance, « Shielding Effectiveness of Braided Wire Shields », Interaction Note 172, Menlo Park, California, 04/1974.
- [35] Nicolas Mora et al., « An Improved Formula for the Transfer Impedance of Two-Layer Braided Cable Shields », in: *IEEE Transactions on Electromagnetic Compatibility 57.3* (06/2015), pp. 607–610, ISSN: 0018-9375, 1558-187X, DOI: 10.1109/TEMC.2015.2388771, URL: <http://ieeexplore.ieee.org/document/7017579/> (visited on 10/06/2022).
- [36] Oussama Gassab et al., « Transmission Line Model for a Shielded TWP With Apertures and Generalization to Braided–Shielded TWP Cables », in: *IEEE Transactions on Electromagnetic Compatibility 63.6* (12/2021), pp. 2115–2123, ISSN: 0018-9375, 1558-187X, DOI: 10.1109/TEMC.2021.3066608, URL: <https://ieeexplore.ieee.org/document/9400790/> (visited on 07/06/2022).
- [37] Yasushi Itani et al., « Aluminum Pipe Shielded High-Voltage Wiring Harness », in: *SEI Technical Review 79* (10/2014), pp. 18–21, ISSN: 1343-4349.
- [38] Madhavi S. Murthy and Guido A. Rasek, « Analytical Determination of Current Distributions in Shielded HV Cables and Ground Systems of Electric Automotive Power Trains », in: *IEEE Transactions on Electromagnetic Compatibility 61.3* (06/2019), pp. 911–918, ISSN: 0018-9375, 1558-187X, DOI: 10.1109/TEMC.2018.2837121, URL: <https://ieeexplore.ieee.org/document/8382295/> (visited on 16/09/2022).

-
- [39] Henrik Wiebe and Matthias Spagele, « EMC Study on Aged Shielded Cables », in: *2022 International Symposium on Electromagnetic Compatibility – EMC Europe*, 2022 International Symposium on Electromagnetic Compatibility – EMC Europe, Gothenburg, Sweden: IEEE, 05/09/2022, pp. 79–83, ISBN: 978-1-66540-788-5, DOI: 10.1109/EMCEurope51680.2022.9901073, URL: <https://ieeexplore.ieee.org/document/9901073/> (visited on 05/12/2022).
- [40] J. Verpoorte, H. Schippers and J.H.G.J. Lansink Rotgerink, « Advanced Models for the Transfer Impedance of Metal Braids in Cable Harnesses », in: *2018 IEEE Int. Symp. Electromagn. Compat. 2018 IEEE Asia-Pacific Symp. Electromagn. Compat. (EMC/APEMC)*, 2018 IEEE International Symposium on Electromagnetic Compatibility and 2018 IEEE Asia-Pacific Symposium on Electromagnetic Compatibility (EMC/APEMC), Singapore: IEEE, 05/2018, pp. 187–192, ISBN: 978-1-5090-5997-3, DOI: 10.1109/ISEMC.2018.8393764, URL: <https://ieeexplore.ieee.org/document/8393764/> (visited on 22/01/2021).
- [41] David M. Pozar, « Chapter 2: Transmission Line Theory », in: *Microwave Engineering*, 3rd ed, Hoboken, NJ: John Wiley & Sons, Inc., 2005, pp. 49–90, ISBN: 978-0-471-44878-5.
- [42] Patrick Deschenes, Rob Bijman and Frank Leferink, « Effect of Gland Quality on the Screening Effectiveness of Cable-Connector Assemblies », in: *2015 IEEE International Symposium on Electromagnetic Compatibility (EMC)*, 2015 IEEE International Symposium on Electromagnetic Compatibility - EMC 2015, Dresden, Germany: IEEE, 08/2015, pp. 62–67, ISBN: 978-1-4799-6616-5, DOI: 10.1109/ISEMC.2015.7256133, URL: <http://ieeexplore.ieee.org/document/7256133/> (visited on 10/06/2022).
- [43] Bernard Démoulin and Lamine Koné, « Shielded Cable Transfer Impedance Measurements in the Microwave Range of 1 GHz to 10 GHz », in: *IEEE Electromagn. Compat. Mag.* 229 (Spr. 2011), pp. 52–61.
- [44] B. Eicher and L. Boillot, « Very Low Frequency To 40 GHz Screening Measurements On Cables And Connectors; Line Injection Method And Mode Stirred Chamber », in: *Int. Symp. Electromagn. Compat.* International Symposium on Electromagnetic Compatibility, Anaheim, CA, USA: IEEE, 1992, pp. 302–307, ISBN: 978-0-7803-0713-1, DOI: 10.1109/ISEMC.1992.626099, URL: <http://ieeexplore.ieee.org/document/626099/> (visited on 04/05/2022).

-
- [45] Zine Eddine Mohamed Cherif et al., « Transfer Impedance Measurement of Shielded Cables Through Localized Injection », in: *IEEE Transactions on Electromagnetic Compatibility* 60.4 (08/2018), pp. 1018–1021, ISSN: 0018-9375, 1558-187X, DOI: 10.1109/TEMC.2017.2760161, URL: <http://ieeexplore.ieee.org/document/8080247/> (visited on 10/06/2022).
- [46] Abid Mushtaq and Stephan Frei, « Transfer Impedance Simulation and Measurement Methods to Analyse Shielding Behaviour of HV Cables Used in Electric-Vehicles and Hybrid-Electric-Vehicles », in: *Advances in Radio Science* 14 (28/09/2016), pp. 139–145, ISSN: 1684-9973, DOI: 10.5194/ars-14-139-2016, URL: <https://ars.copernicus.org/articles/14/139/2016/> (visited on 18/04/2022).
- [47] H. Salt, « The Surface Transfer Impedance of Coaxial Cables », in: *1968 IEEE Electromagnetic Compatibility Symposium Record*, 1968 IEEE Electromagnetic Compatibility Symposium Record, Seattle, WA, USA: IEEE, 07/1968, pp. 198–209, DOI: 10.1109/TEMC.1968.4307135, URL: <http://ieeexplore.ieee.org/document/4307135/> (visited on 01/06/2022).
- [48] IEC 62153-4-3, *Metallic Communication Cable Test Methods – Part 4-3: Electromagnetic Compatibility (EMC) – Surface Transfer Impedance – Triaxial Method*, 2013, ISBN: 978-2-8322-1179-3.
- [49] Rohde & Schwarz, *R&S®ZNL Vector Network Analyzer - Specifications - Data Sheet Version 07.00*, 08/2022.
- [50] bda connectivity, *Short Overview CoMeT*, 01/2020, URL: https://bda-connectivity.com/wp-content/uploads/2020/01/CoMeT-Kurzinformation_20200106_web.pdf (visited on 21/02/2002).
- [51] Neil Storey, « Chapter 9 - Transient Behaviour », in: *Electronics: A Systems Approach*, Sixth edition, Harlow, England London New York Boston San Francisco Toronto: Pearson, 2017, pp. 168–183, ISBN: 978-1-292-11406-4.
- [52] IMI Sensors, *Selecting & Installing Accelerometers*, 2021, URL: https://www.pcb.com/contentstore/mktgcontent/whitepapers/WPL_75_SelectingInstallingAccelerometers.pdf.

-
- [53] Petre G. Stoica and Randolph L. Moses, « Chapter 1: Basic Concepts », in: *Spectral Analysis of Signals*, Upper Saddle River, NJ: Pearson, Prentice Hall, 2005, pp. 1–21, ISBN: 978-0-13-113956-5.
- [54] Petre G. Stoica and Randolph L. Moses, « Chapter 2: Nonparametric Methods », in: *Spectral Analysis of Signals*, Upper Saddle River, NJ: Pearson, Prentice Hall, 2005, pp. 22–85, ISBN: 978-0-13-113956-5.
- [55] Tomasz Gancarz, Przemysław Fima and Janusz Pstruś, « Thermal Expansion, Electrical Resistivity, and Spreading Area of Sn-Zn-In Alloys », in: *Journal of Materials Engineering and Performance* 23.5 (05/2014), pp. 1524–1529, ISSN: 1059-9495, 1544-1024, DOI: 10.1007/s11665-013-0825-3, URL: <http://link.springer.com/10.1007/s11665-013-0825-3> (visited on 12/07/2022).
- [56] Orazio Aiello and Paolo Crovetto, « Characterization of the Susceptibility to EMI of a BMS IC for Electric Vehicles by Direct Power and Bulk Current Injection », in: *IEEE Lett. on Electromagn. Compat. Pract. and Appl.* 3.3 (09/2021), pp. 101–107, ISSN: 2637-6423, DOI: 10.1109/LEMCPA.2021.3085765, URL: <https://ieeexplore.ieee.org/document/9446612/> (visited on 26/10/2022).
- [57] Ragnar Holm and Else Holm, « §1. Introduction. A Simplified Summary of the Theory of Stationary Electric Contacts », in: *Electric Contacts: Theory and Application*, 4th ed., Berlin, Germany: Springer-Verlag, 1967, ISBN: 978-3-662-06688-1.
- [58] Tevis D. B. Jacobs and Ashlie Martini, « Measuring and Understanding Contact Area at the Nanoscale: A Review », in: *Appl. Mech. Rev.* 69.6 (01/11/2017), p. 060802, ISSN: 0003-6900, 2379-0407, DOI: 10.1115/1.4038130, URL: <https://asmedigitalcollection.asme.org/appliedmechanicsreviews/article/doi/10.1115/1.4038130/367044/Measuring-and-Understanding-Contact-Area-at-the> (visited on 13/10/2022).
- [59] David Chapman and Toby Norris, *Copper for Busbars*, 14th revision, Hemel Hempstead, UK: Copper Development Association, 05/2014, 108 pp.
- [60] Nora Dahdah et al., « Influence of the Casting Process in High Temperature Fatigue of A319 Aluminium Alloy Investigated By In-Situ X- Ray Tomography and Digital Volume Correlation », in: *Procedia Structural Integrity* 2 (2016),

-
- pp. 3057–3064, ISSN: 24523216, DOI: 10.1016/j.prostr.2016.06.382, URL: <https://linkinghub.elsevier.com/retrieve/pii/S2452321616304000> (visited on 30/09/2022).
- [61] S. I. Bakhtiyarov, R. A. Overfelt and S. G. Teodorescu, « Electrical and Thermal Conductivity of A319 and A356 Aluminum Alloys », in: *J. Mater. Sci.* 36.19 (2001), pp. 4643–4648, ISSN: 00222461, DOI: 10.1023/A:1017946130966, URL: <http://link.springer.com/10.1023/A:1017946130966> (visited on 29/09/2022).
- [62] M. Braunovic, « Effect of Connection Design on the Contact Resistance of High Power Overlapping Bolted Joints », in: *IEEE Trans. Comp. Packag. Technol.* 25.4 (12/2002), pp. 642–650, ISSN: 1521-3331, DOI: 10.1109/TCAPT.2003.809108, URL: <http://ieeexplore.ieee.org/document/1178768/> (visited on 13/12/2021).
- [63] Ragnar Holm and Else Holm, « §2. The Contact Surface », in: *Electric Contacts: Theory and Application*, 4th ed., Berlin, Germany: Springer-Verlag, 1967, ISBN: 978-3-662-06688-1.
- [64] Kevin H. Brown et al., *Guideline for Bolted Joint Design and Analysis: Version 1.0*, 01/2008, URL: <https://www.osti.gov/servlets/purl/929124>.
- [65] Vadim Shalyt, Mike Ford and Arlene Gleicher, « Advanced Solutions for Measuring Contact Pressure Decrease Defects in Medical Packaging, Molding, and Tooling », in: *Medical Design* (06/2011), pp. 20–24, URL: <http://www.medicaldesign.com/>.
- [66] HBM, *PACeline CLP Piezoelectric Force Washer*, URL: <https://www.hbm.com/fileadmin/mediapool/hbmdoc/technical/B03634.pdf> (visited on 10/10/2022).
- [67] R.L. Jackson, « Significance of Surface Preparation for Bolted Aluminium Joints », in: *IEE Proc. C Gener. Transm. Distrib. UK* 128.2 (1981), p. 45, ISSN: 01437046, DOI: 10.1049/ip-c.1981.0007, URL: <https://digital-library.theiet.org/content/journals/10.1049/ip-c.1981.0007> (visited on 29/09/2022).

-
- [68] R.D. Naybour and T. Farrell, « Degradation Mechanisms of Mechanical Connectors on Aluminium Conductors », in: *Proc. Inst. Electr. Eng. UK* 120.2 (1973), p. 273, ISSN: 00203270, DOI: 10.1049/piee.1973.0060, URL: <https://digital-library.theiet.org/content/journals/10.1049/piee.1973.0060> (visited on 13/12/2021).
- [69] T. Jaglinski et al., « Study of Bolt Load Loss in Bolted Aluminum Joints », in: *J. Eng. Mater. Technol.* 129.1 (01/01/2007), pp. 48–54, ISSN: 0094-4289, 1528-8889, DOI: 10.1115/1.2400262, URL: <https://asmedigitalcollection.asme.org/materialstechnology/article/129/1/48/464937/Study-of-Bolt-Load-Loss-in-Bolted-Aluminum-Joints> (visited on 26/10/2022).
- [70] S. Schoft, « Measurement and Calculation of the Decreasing Joint Force in High Current Aluminum Joints », in: *Proc. 50th IEEE Holm Conf. Electr. Contacts 22nd Int. Conf. Electr. Contacts*, 50th IEEE Holm Conference on Electrical Contacts and the 22nd International Conference on Electrical Contacts, Seattle, WA, USA: IEEE, 2004, pp. 511–518, ISBN: 978-0-7803-8460-6, DOI: 10.1109/HOLM.2004.1353164, URL: <http://ieeexplore.ieee.org/document/1353164/> (visited on 14/12/2021).
- [71] P. Shrotriya and N. R. Sottos, « Creep and Relaxation Behavior of Woven Glass/Epoxy Substrates for Multilayer Circuit Board Applications », in: *Polym. Compos.* 19.5 (10/1998), pp. 567–578, ISSN: 0272-8397, 1548-0569, DOI: 10.1002/pc.10130, URL: <https://onlinelibrary.wiley.com/doi/10.1002/pc.10130> (visited on 12/10/2022).
- [72] Accuratus, *96% Alumina Material Properties*, URL: <http://www accuratus.com/pdf/96aluminaprops.pdf> (visited on 26/10/2022).
- [73] B. N. Roy and T. Wright, « Electrical Conductivity in Polycrystalline Copper Oxide Thin Films », in: *Cryst. Res. Technol.* 31.8 (1996), pp. 1039–1044, ISSN: 02321300, 15214079, DOI: 10.1002/crat.2170310812, URL: <https://onlinelibrary.wiley.com/doi/10.1002/crat.2170310812> (visited on 26/10/2022).

-
- [74] Ragnar Holm and Else Holm, « §27. Fritting of Tarnish Films », in: *Electric Contacts: Theory and Application*, 4th ed., Berlin, Germany: Springer-Verlag, 1967, ISBN: 978-3-662-06688-1.
- [75] E. Yee Kin Choi et al., « Contact Voltage Analysis for Degraded Contact Surfaces by Power Arcing Phenomenon », in: *2014 IEEE 60th Holm Conf. Electr. Contacts Holm*, 2014 IEEE 60th Holm Conference on Electrical Contacts (Holm), New Orleans, LA, USA: IEEE, 10/2014, pp. 1–5, ISBN: 978-1-4799-6068-2, DOI: 10.1109/HOLM.2014.7031023, URL: <http://ieeexplore.ieee.org/document/7031023/> (visited on 13/10/2022).
- [76] Shigeru Sawada et al., « Prediction of Electrical Contact Resistance of Tin-Plated and Silver-Plated Terminals », in: *SEI Tech. Rev.* 71 (10/2010), pp. 37–43, ISSN: 13434349.
- [77] Olof Vingsbo and Staffan Söderberg, « On Fretting Maps », in: *Wear* 126.2 (09/1988), pp. 131–147, ISSN: 00431648, DOI: 10.1016/0043-1648(88)90134-2, URL: <https://linkinghub.elsevier.com/retrieve/pii/0043164888901342> (visited on 22/09/2022).
- [78] Pawel Jedrzejczyk, « Analyse and Quantification of Electrical Contacts Endurance under Fretting Loadings », PhD thesis, Lyon, France: Ecole Centrale de Lyon, 07/2010, 301 pp., URL: <https://tel.archives-ouvertes.fr/tel-01359165>.
- [79] S. El Mossouess et al., « Fretting Corrosion in Power Contacts: Electrical and Thermal Analysis », in: *2014 IEEE 60th Holm Conf. Electr. Contacts Holm*, 2014 IEEE 60th Holm Conference on Electrical Contacts (Holm), New Orleans, LA, USA: IEEE, 10/2014, pp. 1–5, ISBN: 978-1-4799-6068-2, DOI: 10.1109/HOLM.2014.7031058, URL: <http://ieeexplore.ieee.org/document/7031058/> (visited on 29/09/2022).
- [80] Mario Munoz, Hai Chen and Jesus Hernandez, « Tin Plating Investigation as a Potential Alternate to Silver Plating in Plug in Connection for Low Voltage Low Amp Miniature Circuit Breakers », in: *2016 IEEE 62nd Holm Conf. Electr. Contacts Holm*, 2016 IEEE 62nd IEEE Holm Conference on Electrical Contacts (Holm), Clearwater Beach, FL, USA: IEEE, 10/2016, pp. 187–191, ISBN: 978-1-5090-5075-8, DOI: 10.1109/HOLM.2016.7780030, URL: <http://ieeexplore.ieee.org/document/7780030/> (visited on 29/09/2022).

-
- [81] S. El Mossouess et al., « Statistical Analysis of Voltage from Constriction to Micro-Arc Values during Aging by Fretting », in: *2015 IEEE 61st Holm Conf. Electr. Contacts Holm*, 2015 IEEE 61st Holm Conference on Electrical Contacts (Holm), San Diego, CA, USA: IEEE, 10/2015, pp. 304–308, ISBN: 978-1-4673-9341-6, DOI: 10.1109/HOLM.2015.7355113, URL: <http://ieeexplore.ieee.org/document/7355113/> (visited on 29/09/2022).
- [82] S. Fouvry et al., « Fretting Wear of Low Current Electrical Contacts: Quantification of Electrical Endurance », in: *2017 IEEE Holm Conf. Electr. Contacts*, 2017 IEEE Holm Conference on Electrical Contacts, Denver, CO, USA: IEEE, 09/2017, pp. 1–11, ISBN: 978-1-5386-1091-6, DOI: 10.1109/HOLM.2017.8088056, URL: <http://ieeexplore.ieee.org/document/8088056/> (visited on 29/09/2022).
- [83] M. Antler, « Survey of Contact Fretting in Electrical Connectors », in: *IEEE Trans. Comp., Hybrids, Manufact. Technol.* 8.1 (03/1985), pp. 87–104, ISSN: 0148-6411, DOI: 10.1109/TCHMT.1985.1136462, URL: <http://ieeexplore.ieee.org/document/1136462/> (visited on 27/10/2022).
- [84] Thurlby Thandar Instruments, *BS407 - Wide Range Precision Micro-Ohmmeter*, URL: https://resources.aimtti.com/datasheets/AIM-BS407_precision_micro-ohmmeter_data_sheet-Iss1A.pdf (visited on 14/10/2022).
- [85] Keysight, *34980A - Data Acquisition System*, 23/08/2022, URL: <https://www.keysight.com/fr/en/assets/7018-01247/data-sheets/5989-1437.pdf>.
- [86] BK Precision, *DC Resistance Meters - 2840 Series*, 2017.
- [87] Harwin, *Spring Forces of S7041 to S7121 and S1761 Spring Contacts*, 14/03/2019.
- [88] Sofiane El Mossouess et al., « Analysis of Temporal and Spatial Contact Voltage Fluctuation during Fretting in Automotive Connectors », in: The 27th International Conference on Electrical Contacts, Dresden, Germany: VDE Verlag GmbH, 22/06/2014–26/06/2014, pp. 181–185, ISBN: 978-3-8007-3624-9.

-
- [89] Economic Commission for Europe of the United Nations, *Uniform Provisions Concerning the Approval of Vehicles with Regard to Electromagnetic Compatibility*, 20/09/2012, URL: <http://data.europa.eu/eli/reg/2012/10/oj>.
- [90] Alastair R. Ruddle and Anthony J.M. Martin, « The Need for a Risk-Based Systems Engineering Approach in Automotive EMC Engineering », in: *2018 Int. Symp. Electromagn. Compat. EMC Eur.* 2018 International Symposium on Electromagnetic Compatibility (EMC EUROPE), Amsterdam: IEEE, 08/2018, pp. 293–298, ISBN: 978-1-4673-9698-1, DOI: 10.1109/EMCEurope.2018.8485053, URL: <https://ieeexplore.ieee.org/document/8485053/> (visited on 26/08/2022).
- [91] Alastair R. Ruddle, Anthony J.M. Martin and Mark Emery, « Proposals for Change in Automotive EMC Standardization and Engineering Practices », in: *2021 IEEE Int. Jt. EMCSIPI EMC Eur. Symp.* 2021 IEEE International Joint EMC/SI/PI and EMC Europe Symposium, Raleigh, NC, USA: IEEE, 26/07/2021, pp. 1–6, ISBN: 978-1-66544-888-8, DOI: 10.1109/EMC/SI/PI/EMCEurope52599.2021.9559305, URL: <https://ieeexplore.ieee.org/document/9559305/> (visited on 25/08/2022).
- [92] European Parliament and the Council, *Harmonisation of the Laws of the Member States Relating to Electromagnetic Compatibility*, 26/02/2014, URL: <http://data.europa.eu/eli/dir/2014/30/oj>.
- [93] Bart van Leersum, « Requirements with Rationale and Quantitative Rules for EMC on Future Ships », PhD thesis, Enschede, The Netherlands: University of Twente, 05/10/2016, ISBN: 9789036541558, DOI: 10.3990/1.9789036541558, URL: <http://purl.org/utwente/doi/10.3990/1.9789036541558> (visited on 25/08/2022).
- [94] ISO, *31000 -Risk Management: Guidelines*, Geneva, Switzerland: International Organization for Standardization, 2018.
- [95] Robert G. Cooper, « A Process Model for Industrial New Product Development », in: *IEEE Trans. Eng. Manage.* EM-30.1 (1983), pp. 2–11, ISSN: 0018-9391, DOI: 10.1109/TEM.1983.6448637, URL: <http://ieeexplore.ieee.org/document/6448637/> (visited on 14/09/2022).
- [96] Oskari Leppäaho, *PETER Deliverable 3.2 (D8) – Description Methodology for Risk Prediction from IC to System Level*, 10/01/2022.

-
- [97] G. Antonini et al., « Experimental Validation of Circuit Models for Bulk Current Injection (BCI) Test on Shielded Coaxial Cables », in: *2004 Int Symp Electromagn Compat IEEE Cat No04CH37559*, 2004 International Symposium on Electromagnetic Compatibility, vol. 1, Silicon Valley, CA, USA: IEEE, 2004, pp. 63–68, ISBN: 978-0-7803-8443-9, DOI: 10.1109/ISEMC.2004.1349997, URL: <http://ieeexplore.ieee.org/document/1349997/> (visited on 21/02/2022).
- [98] Frédéric Lafon, « Développement de techniques et de méthodologies pour la prise en compte des contraintes CEM dans la conception d'équipements du domaine automobile. : Etude de l'immunité, du composant à l'équipement [Techniques and methodologies development to take into account EMC constraints in Automotive equipment design - Immunity analysis from component until the equipment] », PhD thesis, Rennes, France: INSA Rennes, 19/01/2011, 304 pp.
- [99] Clayton R. Paul, *Applications of Multiconductor Transmission Line Theory to the Prediction of Cable Coupling. Volume VIII. Prediction of Crosstalk Involving Braided-Shield Cables*, 08/1980, URL: <https://apps.dtic.mil/sti/citations/ADA091751>.
- [100] T. Dhaene and D. de Zutter, « Selection of Lumped Element Models for Coupled Lossy Transmission Lines », in: *IEEE Trans. Comput.-Aided Des. Integr. Circuits Syst.* 11.7 (07/1992), pp. 805–815, ISSN: 02780070, DOI: 10.1109/43.144845, URL: <http://ieeexplore.ieee.org/document/144845/> (visited on 23/11/2021).
- [101] Marine Stojanovic, « Study and Modeling of Inter-Component Coupling for Filter Design », PhD thesis, Angers, France: INSA Rennes, 14/09/2018, 180 pp.
- [102] L.D. Smith and D. Hockanson, « Distributed SPICE Circuit Model for Ceramic Capacitors », in: *2001 Proc. 51st Electron. Compon. Technol. Conf. Cat No01CH37220*, 51st Electronic Components and Technology Conference 2001. Proceedings, Orlando, FL, USA: IEEE, 2001, pp. 523–528, ISBN: 978-0-7803-7038-8, DOI: 10.1109/ECTC.2001.927777, URL: <http://ieeexplore.ieee.org/document/927777/> (visited on 03/11/2021).
- [103] Frank Leferink, « Risk-Based vs Rule-based Electromagnetic Compatibility in Large Installations », in: *2018 IEEE 4th Glob. Electromagn. Compat. Conf. GEMCCON*, 2018 IEEE 4th Global Electromagnetic Compatibility Conference (GEMCCON), Stellenbosch, South Africa: IEEE, 11/2018, pp. 1–4, ISBN:

-
- 978-1-5386-5728-7, DOI: 10.1109/GEMCCON.2018.8628505, URL:
<https://ieeexplore.ieee.org/document/8628505/> (visited on 25/08/2022).
- [104] Joint Spectrum Center, *MIL-HDBK-237D Department of Defense Handbook - Electromagnetic Environmental Effects and Spectrum Supportability Guidance for the Acquisition Process*, 20/05/2005.
- [105] Bertrand Meyer, « Design by Contract », in: *Advances in Object-Oriented Software Engineering*, ed. by Dino Mandrioli, Prentice Hall Object-Oriented Series, New York: Prentice Hall, 1992, pp. 1–50, ISBN: 978-0-13-006578-0.
- [106] Mouna Kharrat et al., « EMC Risk Assessment Process through a Topological Analysis », in: *2018 12th Fr.-Jpn. 10th Eur.-Asia Congr. Mechatron.* 2018 12th France-Japan and 10th Europe-Asia Congress on Mechatronics, Tsu: IEEE, 09/2018, pp. 21–26, ISBN: 978-1-5386-2982-6, DOI: 10.1109/MECATRONICS.2018.8495844, URL: <https://ieeexplore.ieee.org/document/8495844/> (visited on 26/08/2022).
- [107] Mouna Kharrat et al., « Integration of Electromagnetic Constraints as of the Conceptual Design Through an MBSE Approach », in: *IEEE Systems Journal* 15.1 (03/2021), pp. 747–758, ISSN: 1932-8184, 1937-9234, 2373-7816, DOI: 10.1109/JSYST.2020.2980144, URL: <https://ieeexplore.ieee.org/document/9062568/> (visited on 15/12/2021).
- [108] IEC, « Section 8 - Classification of Environments », in: *61000-2-5:2017 Electromagnetic Compatibility (EMC): Part 2-5 Environment: Description and Classification of Electromagnetic Environments*, 3.0, Geneva, Switzerland: International Electrotechnical Commission, 2017, pp. 79–101, ISBN: 978-2-8322-3773-1.
- [109] IEC, *60533:2015 Electrical and Electronic Installations in Ships: Electromagnetic Compatibility (EMC): Ships with a Metallic Hull*, 3.0, Geneva: International Electrotechnical Commission, 2015, ISBN: 978-2-8322-2849-4.
- [110] IEC, *61000-6-3:2020 Electromagnetic Compatibility (EMC) – Part 6-3: Generic Standards – Emission Standard for Equipment in Residential Environments*, 3.0, Geneva, Switzerland: International Electrotechnical Commission, 2020, ISBN: 978-2-8322-8661-6.

-
- [111] IEC, *61000-6-1:2016 Electromagnetic Compatibility (EMC) – Part 6-1: Generic Standards – Immunity Standard for Residential, Commercial and Light-Industrial Environments*, 3.0, Geneva, Switzerland: International Electrotechnical Commission, 2016, ISBN: 978-2-8322-3581-2.
- [112] Roger Kulläng, *Best Practices for Software Architecture in Hardware Companies*, Modular Management Blog, URL: <https://www.modularmanagement.com/blog/best-practices-for-software-architecture-in-hardware-companies> (visited on 01/09/2022).
- [113] Tesla, *Autopilot and Full Self-Driving Capability*, URL: <https://www.tesla.com/support/autopilot> (visited on 12/09/2022).
- [114] David Shepardson, « Tesla Agrees to Pay \$1.5 Mln to Settle Claims over Battery Voltage Reduction », in: *Reuters* (29/07/2021), URL: <https://www.reuters.com/business/autos-transportation/tesla-agrees-pay-15-mln-settle-claims-over-temporary-battery-voltage-reduction-2021-07-29/>.
- [115] Alex Ansley, *Pedestrian Warning Sound May Be Obscured/FMVSS 141*, Safety Recall Acknowledgement Letter, 09/02/2022, URL: <https://static.nhtsa.gov/odi/rc1/2022/RCAK-22V063-7336.pdf>.
- [116] Douglas Nascimento et al., « Versatile LabVIEW-FPGA-based Testbench for Electromagnetic Interference Evaluation in VSDs », in: *2022 Int. Symp. Electromagn. Compat. – EMC Eur. 2022 International Symposium on Electromagnetic Compatibility – EMC Europe*, Gothenburg, Sweden: IEEE, 05/09/2022, pp. 764–769, ISBN: 978-1-66540-788-5, DOI: 10.1109/EMCEurope51680.2022.9901037, URL: <https://ieeexplore.ieee.org/document/9901037/> (visited on 13/10/2022).
- [117] Emilio Honey, In-Soo Suh and S. R. Ryu, « Practical Considerations on the Electrical Safety of the High Power System in a Prototype EV », in: *2013 IEEE Veh. Power Propuls. Conf. VPPC*, 2013 IEEE Vehicle Power and Propulsion Conference (VPPC), Beijing, China: IEEE, 10/2013, pp. 1–6, ISBN: 978-1-4799-0720-5, DOI: 10.1109/VPPC.2013.6671699, URL: <http://ieeexplore.ieee.org/document/6671699/> (visited on 14/11/2022).

-
- [118] K. Armstrong, « Why EMC Immunity Testing Is Inadequate for Functional Safety », in: *2004 Int. Symp. Electromagn. Compat. IEEE Cat No04CH37559*, 2004 International Symposium on Electromagnetic Compatibility, vol. 1, Silicon Valley, CA, USA: IEEE, 2004, pp. 145–149, ISBN: 978-0-7803-8443-9, DOI: 10.1109/ISEMC.2004.1350014, URL: <http://ieeexplore.ieee.org/document/1350014/> (visited on 30/09/2022).
- [119] Heinrich Kaden, « G. Durchgriff von elektrischen und magnetischen Feldern durch Spalte (Schlitze) », in: *Wirbelströme und Schirmung in der Nachrichtentechnik*, Berlin, Heidelberg: Springer Berlin Heidelberg, 1959, pp. 203–221, ISBN: 978-3-540-32570-3, DOI: 10.1007/978-3-540-32570-3, URL: <http://link.springer.com/10.1007/978-3-540-32570-3> (visited on 18/07/2022).
- [120] H. A. Bethe, « Theory of Diffraction by Small Holes », in: *Physical Review* 66.7-8 (01/10/1944), pp. 163–182, ISSN: 0031-899X, DOI: 10.1103/PhysRev.66.163, URL: <https://link.aps.org/doi/10.1103/PhysRev.66.163> (visited on 08/06/2022).
- [121] H. Schippers and J. Verpoorte, « Hole Inductance in Braided Cable Shields », in: *2015 IEEE International Symposium on Electromagnetic Compatibility (EMC)*, 2015 IEEE International Symposium on Electromagnetic Compatibility - EMC 2015, Dresden, Germany: IEEE, 08/2015, pp. 56–61, ISBN: 978-1-4799-6616-5, DOI: 10.1109/ISEMC.2015.7256132, URL: <http://ieeexplore.ieee.org/document/7256132/> (visited on 07/06/2022).
- [122] F. De Meulenaere and J. Van Bladel, « Polarizability of Some Small Apertures », in: *IEEE Transactions on Antennas and Propagation* 25.2 (03/1977), pp. 198–205, ISSN: 0096-1973, DOI: 10.1109/TAP.1977.1141568, URL: <http://ieeexplore.ieee.org/document/1141568/> (visited on 22/06/2022).
- [123] C.G. Montgomery, « Chapter 6 - Waveguide Circuit Elements », in: *Principles of Microwave Circuits*, vol. 8, Radiation Laboratory Series, Cambridge, Mass: McGraw-Hill Book Company, Inc., 1948, pp. 162–206.
- [124] Nathan Marcuvitz, « Chapter 1: Transmission Lines », in: *Waveguide Handbook*, Reprinted, IET Electromagnetic Waves Series Volume 21, London: Institution of Engineering and Technology, 2009, pp. 1–54, ISBN: 978-0-86341-058-1.

-
- [125] Nathan Marcuvitz, « Chapter 2: Transmission-line Modes », in: *Waveguide Handbook*, Reprinted, IET Electromagnetic Waves Series Volume 21, London: Institution of Engineering and Technology, 2009, pp. 55–100, ISBN: 978-0-86341-058-1.
- [126] Wang Xiaoling et al., « An Improved Model for the Transfer Impedance Calculations of Braided Coaxial Cables », in: *Proceedings of The 7th International Power Electronics and Motion Control Conference*, 2012 7th International Power Electronics and Motion Control Conference (IPEMC 2012), Harbin, China: IEEE, 06/2012, pp. 1078–1081, ISBN: 978-1-4577-2085-7, DOI: 10.1109/IPEMC.2012.6258960, URL: <http://ieeexplore.ieee.org/document/6258960/> (visited on 05/12/2022).
- [127] H. Schippers and J. Verpoorte, « Uncertainties in Transfer Impedance Calculations », in: *2016 ESA Workshop on Aerospace EMC (Aerospace EMC)*, 2016 ESA Workshop on Aerospace EMC (Aerospace EMC), Valencia, Spain: IEEE, 05/2016, pp. 1–6, ISBN: 978-92-9221-303-9, DOI: 10.1109/AeroEMC.2016.7504589, URL: <http://ieeexplore.ieee.org/document/7504589/> (visited on 30/06/2022).
- [128] Oskari Leppäaho et al., « Sensitivity of Shielded Cable Transfer Impedance Measurement to Triaxial Cell Diameter », in: *2021 Jt. IEEE Int Sym EMC/SIPI EMC Eur.* 2021 Joint IEEE International Symposium on EMC+SIPI and EMC Europe, Raleigh, NC, USA, 2021, pp. 917–921, ISBN: 978-1-66544-888-8, DOI: 10.1109/EMC/SI/PI/EMCEurope52599.2021.9559176.
- [129] Oskari Leppäaho, *D3.2 - Description of Methodology for Risk Prediction from IC to System Level*, 10/01/2022.
- [130] Oskari Leppäaho, *MS18 - HALT Test Report*, 04/04/2022.
- [131] Clayton Paul, « Transmission-Line Modeling of Shielded Wires for Crosstalk Prediction », in: *IEEE Transactions on Electromagnetic Compatibility* EMC-23.4 (11/1981), pp. 345–351, ISSN: 0018-9375, DOI: 10.1109/TEMC.1981.303966, URL: <http://ieeexplore.ieee.org/document/4091491/> (visited on 14/06/2022).
- [132] J.H.G.J. Lansink Rotgerink, H. Schippers and J. Verpoorte, « Multi-Conductor Transmission Line Modelling of Transfer Impedance Measurement Methods », in: *2017 International Symposium on Electromagnetic Compatibility - EMC*

EUROPE, 2017 International Symposium on Electromagnetic Compatibility (EMC EUROPE), Angers, France: IEEE, 09/2017, pp. 1–7, ISBN: 978-1-5386-0689-6, DOI: 10.1109/EMCEurope.2017.8094778, URL: <https://ieeexplore.ieee.org/document/8094778/> (visited on 22/01/2021).

Appendices

TRANSFER INDUCTANCE

This appendix discusses the theoretical derivation of most common transfer inductance parameters concerning shielded cables. Some other definitions do exist. They could be significant for special cable designs, like cables with long slits [119], but they are not discussed in this thesis. First, the helical inductance is discussed in Section A.1, and then the three braid related inductances: hole inductance in Section A.2, braid inductance in Section A.3, and skin inductance in Section A.4 are discussed with specific attention paid to the hole inductance as its state-of-the-art theory is the most refined.

A.1 Helical inductance

Helical inductance is caused by a leakage magnetic field that is formed inside the cable due to an axial magnetic field induced by the shield current component that is travelling circularly in a helically wound shield. It can be calculated as [6]:

$$L_{hel} = \frac{1}{2} \mu_0 \sigma \left(\frac{Dd}{2} - d^2 \right) \cot^2 \alpha_f. \quad (\text{A.1})$$

A typical value of 100 pH/m can be calculated for it by inserting parameters from Table 1.3.

When the winding angle α_f (see Figure 1.3b) approaches zero, the helical inductance tends to infinity as no current would flow towards the axis of the shield. On the other hand, when the winding angle approaches 90° , the helical inductance disappears signifying that if only axial current flow would be achieved, the shield would be effectively a solid shield. Based on this theory, it is evident that most foils are wound with winding angles as close to 90° as possible while maintaining the mechanical integrity of the wound foil.

A.2 Hole inductance

Hole inductance is the fundamental inductance of a braid due to magnetic coupling through holes in braiding. These holes are rhomboidal in nature as was shown in Figure 1.5, and the magnetic coupling through them can be modelled with the help of magnetic polarizability [120], which assumes a uniform shield, and replaces each hole with a magnetic dipole. Then, the complete field solution is a superposition of the solutions with the uniform shield and the individual magnetic dipoles. The more complex boundary conditions due to the holes need to be taken into account only in the latter solution.

The fundamental analysis starts from a tubular shield with circular apertures, and is then extended to cover the specifics of braided shields [34]. The polarizability theory can only be used for electrically small holes with radius r_0 in infinitesimally thin conductors, as the electric and magnetic fields are assumed to be constant over the hole. Thus, for a 1 mm hole diameter, the frequency of analysis needs to be

$$f < \frac{c}{10\lambda} \approx 30\text{GHz}. \quad (\text{A.2})$$

The magnetic field amplitude at the outer edge of the shield is [31]

$$H_0 = \frac{I_{shield}}{\pi D}. \quad (\text{A.3})$$

This magnetic field at a circular hole can be modelled as an equivalent dipole moment [31]

$$m^{circ} = \frac{8\mu_0 r_0^3 H_0}{3}. \quad (\text{A.4})$$

Note that there are different expressions of the dipole moment depending on the units used. E.g. [120] uses non-rational Gaussian units instead of the SI units used in this thesis. Thus, the dipole moment equation found there needs to be multiplied by $4\pi\mu_0$ to obtain Equation A.4. The induced voltage to the centre conductor due to a dipole moment is calculated as [31]

$$U_{ind} = j\omega \frac{m}{2\pi D}. \quad (\text{A.5})$$

The coupling impedance can be calculated by dividing Equations A.5 and A.3, with latter solved for the shield current, and then again dividing by $j\omega$ to obtain hole inductance

$$L_h = \frac{m}{2\pi^2 D^2 H_0}. \quad (\text{A.6})$$

that still depends on the magnetic field amplitude. Inserting Equation A.4 would give the hole inductance for a circular hole, but that of a rhombus is desired.

Now, as the equivalent dipole moment is derived from the magnetic field amplitude at the outer edge of the shield, it is a common practice to derive magnetic polarizability of the hole that can operate on the magnetic field amplitude at the shield edge, and transform it to the magnitude of the dipole moment. Several values exist for it depending on which approximation is taken. It is here, where the methods presented in the earlier literature start to differ. The most common polarizabilities in use are:

$$m_p^{circ} = \frac{m^{circ}}{\mu_0 H_0} = \frac{8r_0^3}{3} \quad (\text{A.7a})$$

$$m_p^{square} \approx \frac{2\sqrt{2}}{\pi\sqrt{\pi}} m_p^{circ} \quad (\text{A.7b})$$

$$m_p^{ellipse} = \frac{2\sqrt{(a')^3}}{3\sqrt{\pi}} \left(\frac{l'}{w'}\right)^{\frac{3}{2}} \left[\frac{e^2}{K(e) - E(e)} \|\mathbf{u}_x\|^2 + \frac{(1-e^2)e^2}{E(e) - (1-e^2)K(e)} \|\mathbf{u}_y\|^2 \right] \quad (\text{A.7c})$$

$$m_p^{rhombus} \approx m_p^{ellipse}(a) \quad (\text{A.7d})$$

for circular [31], square [121], ellipsoidal [122] and rhomboidal [121] holes, respectively. The complete elliptic integrals for first and second kind are defined as

$$K(e) = \int_0^{\pi/2} \frac{d\theta}{\sqrt{1 - e^2 \sin^2(\theta)}} \quad (\text{A.8a})$$

$$E(e) = \int_0^{\pi/2} \sqrt{1 - e^2 \sin^2(\theta)} d\theta, \quad (\text{A.8b})$$

respectively. They can be represented as infinite series, and are to be solved numerically. The eccentricity of the ellipse is

$$e = \sqrt{1 - \frac{(w')^2}{(l')^2}} = \begin{cases} \sqrt{1 - \tan^2(\alpha)}, & \text{if } \alpha < 45^\circ \\ \sqrt{1 - \cot^2(\alpha)}, & \text{if } \alpha > 45^\circ. \end{cases} \quad (\text{A.9})$$

The polarizabilities for square and rhombus are approximated from the circular and ellipsoidal ones, respectively. For square, it is the polarizability of the largest square inscribed in the circle. For rhombus, it is similarly the largest rhombus inscribed in the

ellipse as shown in Figure A.1. For the latter, only the area calculation of the ellipse

$$a' = \frac{\pi w' l'}{4} \quad (\text{A.10a})$$

$$a = \frac{wl}{2} = \frac{(2\pi D \cos \alpha - cNd)^2}{c^2 \sin 2\alpha} \quad (\text{A.10b})$$

is modified to obtain correct area a of the rhombus, and thus, a better polarizability approximation. Before the area calculation, it is recommended to verify the validity range of the calculated polarizability. This can be done by calculating the length and width of the rhomboidal hole, and making sure both are positive values as shown earlier in Figure 1.6.

For ellipse, it is commonplace to assume that the magnetic field is directed along either the major or minor axis. Then, the Equations A.7c and A.7d are split into two partial functions

$$m_{p,major}^{ellipse} = \frac{2\sqrt{A^3}}{3\sqrt{\pi}} \left(\frac{l}{w}\right)^{\frac{3}{2}} \frac{e^2}{K(e) - E(e)} \quad (\text{A.11a})$$

$$m_{p,minor}^{ellipse} = \frac{2\sqrt{A^3}}{3\sqrt{\pi}} \left(\frac{l}{w}\right)^{\frac{3}{2}} \frac{(1 - e^2) e^2}{E(e) - (1 - e^2) K(e)} \quad (\text{A.11b})$$

$$m_{p,major}^{rhombus} \approx m_{p,major}^{ellipse}(A') \quad (\text{A.11c})$$

$$m_{p,minor}^{rhombus} \approx m_{p,minor}^{ellipse}(A') \quad (\text{A.11d})$$

Substituting Equations A.11c and A.11d with basic braid parameters of Figure 1.3, and using Equation A.10b gives the following result:

$$m_{p,major}^{rhombus} \approx \frac{2}{3\sqrt{\pi}} \left(\frac{2\pi D \cos(\alpha) - cNd}{c \cos(\alpha) \sqrt{2}}\right)^3 \frac{e^2}{K(e) - E(e)} \quad (\text{A.12a})$$

$$m_{p,minor}^{rhombus} \approx \frac{2}{3\sqrt{\pi}} \left(\frac{2\pi D \cos(\alpha) - cNd}{c \sin(\alpha) \sqrt{2}}\right)^3 \frac{(1 - e^2) e^2}{E(e) - (1 - e^2) K(e)}. \quad (\text{A.12b})$$

An equation for the rhombus is selected based on the braiding angle. Below 45° , Equation A.11d is used, whereas above 45° , Equation A.11c is used. The magnitude of these polarizabilities is shown in Figure A.2. It is visible that the polarizability of the braiding hole changes as a function of the braiding angle, when other braiding parameters are kept constant. This is partly due to the changing area of the holes in the braiding as the braiding angle is changed. It is also seen that the ellipse assumption of the braiding

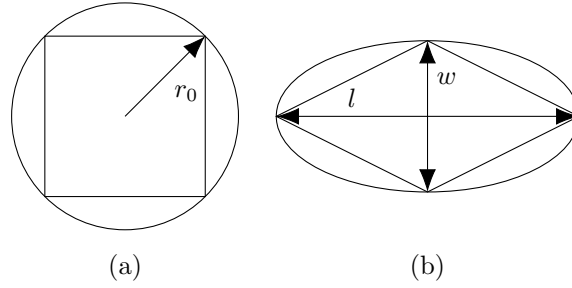


Figure A.1 – Shapes used for polarizability calculations: (a) a circle with an inscribed square and (b) an ellipse with an inscribed rhombus

holes provides constantly nearly twice as large polarizability compared to the rhombus calculation. Meaning in practice that the estimated hole inductance would be doubled. An incredible increase of the hole polarizability is seen around 40° braiding angle. It was verified to exist in plots made directly with equations in [34] and [123]. It is due to a zero of the denominator in Equation A.11b, and could indicate a need for improvement in the polarizability theory of ellipses. This interpretation is supported by a comparison to an equivalent (diameter equal to ellipse axis aligned with the magnetic field) circle polarizability. However, improvements on this level are not in the scope of this thesis.

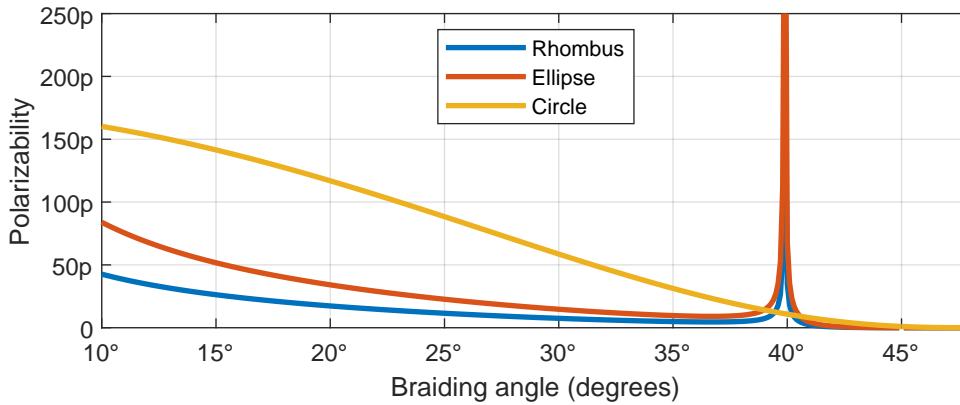


Figure A.2 – Magnitude of rhombus polarizability as a function of braiding angle for $D = 2.95$ mm, $d = 110$ μ m, $N = 7$, $c = 16$

After obtaining a satisfactory approximation of the rhombus polarizability, the next issue is to take into account is the curvature of the braid, as the previous polarizabilities were developed for a planar shield. No proper theoretical treatment exists, but an exper-

imental curvature coefficient $C = 0.875$ has been established [33]. It will be used in the frame of this thesis. Second assumption to unravel is on infinitesimal shield thickness. There is a specific field amplitude dampening happening as the shield thickness increases. This is called as chimney effect [31], and it has been adopted to be used with shielded cables [33].

Chimney effect is a term that is slightly misleading as the phenomenon is more about forming a small waveguide at the hole of the shield, that is always operated well below its first mode. In this case, it is a valid approximation to assume that the sum of the field components passing through is equal to the component of the first mode, as all the higher modes are attenuated significantly more [31]. This brings the so called chimney effect coefficient, here called as the hole cut-off, as

$$h_{cut-off} = e^{-\kappa d}. \quad (\text{A.13})$$

For circular holes, the attenuation coefficient is [31]

$$\kappa^{circ} = \frac{1.84}{r_0}, \quad (\text{A.14})$$

and for rhomboidal holes [121] it is estimated based on an attenuation constant [124] derived for a first dominant mode cut-off frequency of a rectangular waveguide [125]

$$\kappa^{rhombus} = \pi \sqrt{\frac{2}{wl}} = \frac{\pi c \sqrt{\sin 2\alpha}}{2\pi D \cos \alpha - cNd}. \quad (\text{A.15})$$

The results of the Equation A.13 using the two attenuation constants of Equations A.14 and A.15 are plotted in Figure A.3. It is seen that with small braiding angles, when the rhomboidal hole is long, the circular approximation overestimates the waveguide cut-off effect of the holes. However, with typical braiding angles closer to 45° the error is negligible. A significant feature of the hole cut-off is that it becomes very dominant, when the hole diameter becomes smaller than the braid-wire thickness. This point is around 43° in Figure A.3.

Now, the equation for a single hole at one braid crossing, as shown in Figure 1.5, is

$$L_{h,single} = \frac{\mu_0 m_p^{rhombus}}{2\pi^2 D^2} C h_{cut-off}. \quad (\text{A.16})$$

The effect of the curvature coefficient C and the hole cut-off can be seen in Table A.1,

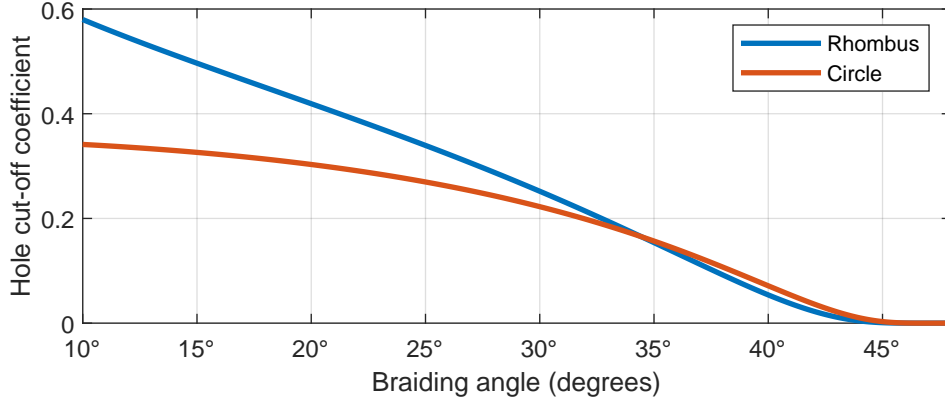


Figure A.3 – Hole-cut off coefficient as a function of braiding angle for $D = 2.95$ mm, $d = 110$ μm , $N = 7$, $c = 16$

where the single hole leakage inductance with typical braid parameters is plotted with and without their effect.

Table A.1 – Single hole inductance in a braid for $D = 2.95$ mm, $d = 110$ μm , $N = 7$, $c = 16$, $\alpha = 35^\circ$

Characteristic	Basic	With curvature	With curvature and cut-off
Hole Inductance	36 fH	31 fH	4.8 fH

To combine the effect of single holes, it is assumed that their contributions can be simply superimposed together. Thus, a multiplication factor is developed as [34]:

$$\nu = \frac{2\pi D \sin(\alpha) \cos(\alpha)}{H^2} = \frac{c^2 \tan \alpha}{2\pi D}. \quad (\text{A.17})$$

This equation signifies that the number of holes for given braiding parameters varies with braiding angle. Figure A.4 shows a typical dependency, where the hole amount can be almost decade larger between meaningful braiding angle extremes.

Now, a final equation for the hole inductance of a braid is

$$\begin{aligned} L_h &= \nu \frac{\mu_0 m_p^{rhombus}}{2\pi^2 D^2} C h_{cut-off} \\ &= C \frac{c^2 \mu_0 m_p^{rhombus}}{4\pi^3 D^3} \tan(\alpha) e^{-\frac{\pi c d \sqrt{\sin(2\alpha)}}{2\pi D \cos(\alpha) - c N d}}. \end{aligned} \quad (\text{A.18})$$

This leads to total hole inductance of the example cable as shown in Table A.2 with the

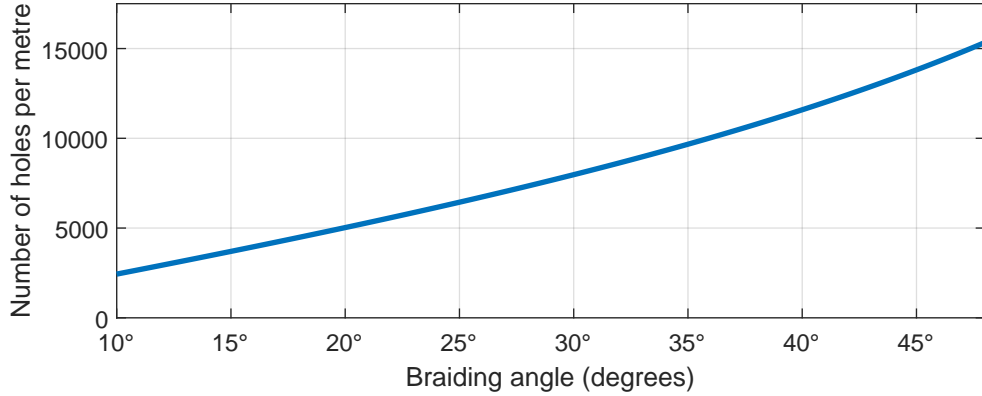


Figure A.4 – Number of holes per metre as a function of braiding angle for $D = 2.95$ mm, $d = 110$ μm , $N = 7$, $c = 16$

basic hole inductance, curvature, and cut-off effects separated.

Table A.2 – Total hole inductance in a braid for $D = 2.95$ mm, $d = 110$ μm , $N = 7$, $c = 16$, $\alpha = 35^\circ$

Characteristic	Basic	With curvature	With curvature and cut-off
Hole Inductance	350 pH	300 pH	47 pH

A.3 Braid inductance

Braid inductance is used to model the differential inductance caused by coupling of the external magnetic field to the top and bottom braid wire bundles at their crossing. Ideally, the external magnetic field would couple an equal current to both of the braid wires at the crossing, but that is possible only if they would be placed exactly on top of each other. In practice, the external flux induces currents of different amplitudes at the crossing braids that then cause a magnetic flux coupling to the inner conductor. The effect is minimized when the braids are crossing each other at straight angle, i.e. $\alpha = 45^\circ$.

The magnetic field generated at the braid crossing can be approximated as that of a solenoid with N turns [40]

$$H_{bc} \approx \frac{I_{shield}}{cNd}, \quad (\text{A.19})$$

where the equivalent solenoid length is estimated as the width of the single braid carrier Nd . Note, that the braiding angle is not taken into account, when determining the

equivalent length. Then, the magnetic flux through the opening at the braid crossing is

$$\Phi_{bc} = \mu_0 \mathbf{H}_{bc} \cdot \mathbf{S}_{bc} = -\frac{\mu_0 I_{shield} A_{bc}}{cNd} \cos(2\alpha), \quad (\text{A.20})$$

where $\mathbf{S}_{bc} = A_{bc} \hat{\mathbf{n}}$ is the braid crossing surface area multiplied with its normal vector. A satisfactory approximation of the braid crossing surface area is given by

$$A_{bc} \approx Ndh' + \frac{(H - Nd)d}{2} \left(1 - \frac{(h')^2}{d^2}\right) + Nd^2 \left(1 - \frac{\pi}{4}\right), \quad (\text{A.21})$$

where h' is the height of the empty area between the top and bottom braids. It is approximated by

$$h' \approx \frac{2d^2}{d + H - Nd}. \quad (\text{A.22})$$

Equation 1.26d could be inserted into Equation A.22 that could then again be inserted into Equation A.21, but few of the terms can be reduced, and the resulting equation would be too complex. Thus, it is preferable to use h' and H as help variables here.

The braid inductance then becomes

$$L_b \approx \frac{\Phi_{bc}}{I_{shield}} = -\frac{\mu_0 A_{bc}}{cNd} \cos(2\alpha). \quad (\text{A.23})$$

Currently, the state-of-the-art of braid inductance derivation lacks similar rigour as has been presented for hole inductance by Kaden [31]. This is likely due to complexity of the braid analysis which has seen fairly recent improvements [40], like the one from Xiaoling [126]. In the future, it would be beneficial to derive the basic braid inductance equations with rigour equivalent to hole inductance, but it is not attempted in the frame of this thesis.

As it is highlighted in [127], the height between the braid wires at the crossing point will have a significant effect on the amplitude of the braid inductance. This phenomenon makes it virtually impossible to model the transfer inductance for all braids with good accuracy. Exception being the ones, where the estimate of h with Equation A.22 happens to give close-enough value to reality, and of course, the braids that are crossing each other at a straight angle. In practice, one needs to measure the transfer impedance of a cable, and then select the correct average height to arrive at matching magnitude of braid inductance, and a reasonable model.

A.4 Skin inductance

Skin inductance is brought to compensate for some additional errors due to the infinitely thin shield assumption made during hole inductance calculation [33]. One can note that the basic effect of field intensity reduction was already discussed during hole inductance treatment. However, there is a secondary effect coming up from the hole: the magnetic field penetrates the lateral area of the hole surface, and causes eddy currents in the shield. These eddy currents cause additional losses, and change the coupling inductance slightly. Similar effect happens also with the field generated between the two braid carrier crossings. Skin inductance is the imaginary part of a simplified high-frequency equation for these skin-effects:

$$L_s = \frac{1}{2\pi^2 f \sigma \delta} \left(\frac{1}{D_L} + \frac{1}{D_G} \right) = \text{Im} \left\{ \frac{\gamma}{2\pi^2 f \sigma} \left(\frac{1}{D_L} + \frac{1}{D_G} \right) \right\}. \quad (\text{A.24})$$

with two effective diameters D_L and D_G representing the contribution from the eddy currents around the braid holes and braid carrier crossings, respectively. The effective diameter estimations have been found from experimental data as [33]

$$D_L \approx \frac{D}{10\pi G_0^2 (1-G) \cos(\alpha) e^{-\tau_E}} \quad (\text{A.25a})$$

$$D_G \approx \frac{2\pi D G_0}{3.3 \cos(2k_2 \alpha)}, \quad (\text{A.25b})$$

where

$$G_0 = \frac{cNd}{2\pi D} \quad (\text{A.26a})$$

$$G = \frac{G_0}{\cos(\alpha)} \quad (\text{A.26b})$$

$$B = G(2-G) \quad (\text{A.26c})$$

$$\tau_E = 12G \sqrt[3]{\frac{B^2 d}{D}} \quad (\text{A.26d})$$

$$k_2 = \frac{\pi}{4} \left(\frac{2G_0}{3} + \frac{3}{8} \right)^{-1}. \quad (\text{A.26e})$$

FIELD STRENGTHS AT CIRCULAR TRIAXIAL CELL CROSS-SECTION

In this Appendix, the electric and magnetic field strengths on a cross-sectional line of circular triaxial cell are calculated according to theory presented in [41]. The theoretical results are compared to 3D-FEM simulations in Figure 1.17. Parts of this analysis have been previously published in [7].

The E-field strength

$$E(z, \rho) = -\nabla_t \Phi(z, \rho) \quad (\text{B.1})$$

is calculated with the help of scalar potential

$$\Phi(z, \rho) = \frac{V(z) \ln \frac{b}{2\rho}}{\ln \frac{b}{a}}, \quad (\text{B.2})$$

where ρ is the distance from the center of the cell, b is the inner diameter of the triaxial cell, and a is the diameter of the copper rod. To arrive at the correct voltage $V(z)$ along the line, the incident voltage wave amplitude needs to be calculated as

$$V^+ = \frac{V(z)}{e^{-j\beta z} - e^{j\beta z}} = \frac{2P_{in}Z_0}{e^{-j\beta z} - e^{j\beta z}}, \quad (\text{B.3})$$

where $z = -385\text{mm}$, input power $P_{in} = 1\text{W}$, and $Z_0 = \sqrt{L/C}$, $\beta = 2\pi f\sqrt{LC}$ are the characteristic impedance and propagation constant of the triaxial cell configuration, respectively. The distributed inductance and capacitance are calculated as

$$L = \frac{\mu_0}{2\pi} \ln \frac{b}{a} \quad (\text{B.4a})$$

$$C = \frac{2\pi\epsilon_0}{\ln \frac{b}{a}}, \quad (\text{B.4b})$$

respectively, with μ_0 and ϵ_0 as vacuum permeability and permittivity.

Then, the voltage $V(z)$ in (B.2) can be calculated as

$$V(z) = V^+ (e^{-j\beta z} - e^{j\beta z}), \quad (\text{B.5})$$

and the field strength in Fig. 1.17a can be calculated by setting $z = -195\text{mm}$ and sweeping ρ .

The H-field strength in the cell is

$$H(z, \rho) = \frac{I(z)}{2\pi\rho}, \quad (\text{B.6})$$

where

$$I(z) = \frac{V^+}{Z_0} (e^{-j\beta z} + e^{j\beta z}), \quad (\text{B.7})$$

is the current travelling along the copper rod. Again, setting $z = -195\text{mm}$ and sweeping ρ , the H-field strength in Figure 1.17b can be calculated.

As seen in Fig. 1.17, the analytical results for E-field match perfectly with the FEM-simulation results, but the H-field results have an offset. This is related to the rapidly changing characteristic impedance of the formed coaxial resonator. Thus, even a small inaccuracy in meshing or boundary conditions renders a pointwise result with an offset. A boundary condition that would yield equal theoretical and simulation results was not found.

LIST OF PUBLICATIONS

All scientific and project publications related to this thesis are listed in here. In total, there was one journal level publication, three conference level publications, and two project related publications. The scientific publications were peer-reviewed, whereas the project publications were not.

Journal Publications

1. Oskari Leppäaho et al., « Triaxial Cell for Determining Shielded Cable Transfer Impedance During Environmental Stress », in: *IEEE Transactions on Electromagnetic Compatibility* Minor revision submitted (2022)

Conference Publications

1. Oskari Leppäaho et al., « Sensitivity of Shielded Cable Transfer Impedance Measurement to Triaxial Cell Diameter », in: 2021 Joint IEEE International Symposium on EMC+SIPI and EMC Europe, Raleigh, NC, USA, 2021, pp. 917–921, ISBN: 978-1-66544-888-8, DOI: 10.1109/EMC/SI/PI/EMCEurope52599.2021.9559176
2. Oskari Leppäaho et al., « Assuring Shielded Cables as EMI Mitigation in Functional Safety Systems – A Case Study of an Automated Lane Centering System », in: 31st European Safety and Reliability Conference (ESREL 2021), Angers, France, 2021, DOI: 10.3850/978-981-18-2016-8_263-cd
3. Oskari Leppäaho et al., « Including Experimental Aging of Shielded Cables into Bulk Current Injection Simulations », in: 2022 International Symposium on Electromagnetic Compatibility – EMC Europe, Gothenburg, Sweden: IEEE, 2022, pp. 811–815, ISBN: 978-1-66540-788-5, DOI: 10.1109/EMCEurope51680.2022.9901089

Project Publications

1. Oskari Leppäaho, *D3.2 - Description of Methodology for Risk Prediction from IC to System Level*, 10/01/2022
2. Oskari Leppäaho, *MS18 - HALT Test Report*, 04/04/2022

AVIS DU JURY SUR LA REPRODUCTION DE LA THESE SOUTENUE

Titre de la thèse:

Evaluation of System-level Electromagnetic Hazards due to Environmental Stresses and Ageing # Application to Shielded Cables and EMI-filter Ground Connections

Nom Prénom de l'auteur : LEPPÄHO OSKARI

Membres du jury :

- Monsieur DEUTSCHMANN Bernd
- Monsieur LEFERINK Frank
- Monsieur RAMDANI Mohamed
- Monsieur MAURICE Olivier
- Madame PALADIAN Françoise
- Monsieur BESNIER Philippe
- Monsieur LAFON Frédéric
- Monsieur PISSOORT Davy

Président du jury :

Date de la soutenance : 10 Mars 2023

Reproduction de la these soutenue

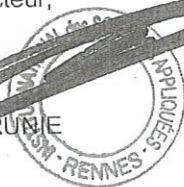
- Thèse pouvant être reproduite en l'état
 Thèse pouvant être reproduite après corrections suggérées

Fait à Rennes, le 10 Mars 2023

Signature du président de jury

Le Directeur,

Vincent BRUNIE



A handwritten signature in blue ink, consisting of several loops and a long horizontal stroke, positioned below the text 'Signature du président de jury'.

Titre : Évaluation des risques électromagnétiques au niveau du système dus aux contraintes environnementales et au vieillissement - Application aux câbles blindés et aux connexions de masse des filtres CEM

Mots clés : CEM, HALT, Câbles blindés, Impédance de transfert, Résistance de contact

Résumé : L'électronique automobile d'aujourd'hui évolue rapidement vers des solutions d'assistance à la conduite et de propulsion électrique. Pour industrialiser ces solutions, les problématiques de compatibilité électromagnétique (CEM) liées au vieillissement d'un équipement doivent être résolues. Cette thèse aborde deux points techniques clés : l'impédance de transfert des câbles blindés et la résistance de contact des connexions de masse des filtres CEM.

Dans ce cadre, une méthode d'essai pour les tests de vieillissement hautement accélérés (HALT) a été développée dans le but de caractériser l'impédance de transfert et la résistance de contact. De ce fait, un

ensemble représentatif de câbles blindés et de contacts de mise à la masse de circuits imprimés ont été caractérisés. Ainsi, il a été mis en évidence que les blindages avec tresse résistent mieux aux contraintes HALT que les blindages avec feuillard. Concernant les contacts de masse, des différences ont également pu être mises en évidence : les contacts à vis résistent à l'intégralité des contraintes HALT, les contacts sertis résistent aux contraintes HALT jusqu'à un niveau modéré de vibration, finalement, les contacts à ressort résistent aux contraintes thermiques, mais sont très sensibles aux vibrations.

Title: Evaluation of System-level Electromagnetic Hazards due to Environmental Stresses and Ageing - Application to Shielded Cables and EMI-filter Ground Connections

Keywords : EMC, HALT, Shielded cables, Transfer impedance, Contact resistance

Abstract: Today's automotive electronics is developing rapidly towards more complex solutions for automated driving assistance and electric propulsion. To properly industrialize these solutions, the problematic of through-life electromagnetic compatibility (EMC) needs to be solved. This thesis discusses two technical domains of the problematic: transfer impedance of shielded cables and contact resistance of EMI-filter ground connections.

A test setup for highly accelerated life tests (HALT) is developed for both transfer

impedance and contact resistance characterisation. A representative set of shielded cables and circuit board ground contacts are then characterized. It is found out that braided shields withstand HALT-stress better than foil shields in cables. For ground contacts, a clear distinction is also found: screw contacts withstand all the HALT stresses, swaged contacts withstand all the HALT stresses up to medium vibration level, and spring contacts withstand thermal stresses, but show great variation in vibration withstand.